

UNIVERSITY OF OXFORD

Internalising Radioimmunoconjugates to Target KRas Cancer Cells for Simultaneous Radio-Ligand Therapy and Radiosensitisation

João Lourenço

St Cross College

Department of Oncology

University of Oxford

Michaelmas Term

A thesis submitted to the Medical Sciences Division of the University of Oxford in partial fulfilment of the requirements for the degree of Doctor of Philosophy

Abstract

The intracellular environment hosts many cancer-relevant proteins. Among them, Ras plays an important role and is frequently activated in cancers of unmet need, such as pancreatic ductal adenocarcinoma (PDAC), non-small cell lung cancers (NSCLC) and colorectal carcinoma (CRC). Despite years of extensive research, PDAC is associated with poor survival (5-year survival rate of 7%), and in most cases (90-95%), it is driven by oncogenic mutant KRas. Direct inhibition of KRas has proven extremely difficult, with the scientific community labelling KRAS as "undruggable" for many years. In 2013, deeper insights into the structure of RAS stimulated a race to find direct inhibitors. This resulted in the approval of two small molecule inhibitors against KRAS *p.G12C* for the treatment of advanced NSCLC – Sotorasib and Adagrasib. However, reports of acquired resistance rapidly emerged. Additionally, $KRas^{G12C}$ mutations are rare in PDAC, with less than 5% of the reported cases showing this mutation. Therefore, despite promising candidates being reported, the development of new and innovative targeted therapies is still urgently needed.

This thesis focuses on a novel approach to target KRas-mutant PDAC cells by combining engineered mutant-specific anti-KRas antibodies, including DARPin K19 and scFv Y6-cFarn, with a newly developed TAT-derived cell-penetrating peptide – Tri-cTAT B. The main goal is that the disruption of KRAS results in the downregulation of proteins that are critical in stimulating cell growth and proliferation whilst radiosensitising PDAC cell lines. Initial experiments using live-cell confocal microscopy showed the ability of Tri-cTAT B to transfect mCherry-labelled anti-KRas macromolecules, up to 70 kDa, in 2D and 3D PDAC cell models. Cellular uptake of anti-KRas macromolecules was followed by prominent accumulation in the nucleus and nucleoli, raising concerns about potential off-target effects since KRas is located primarily at the inner leaflet of the cell membrane.

To address this, DARPin K19 and scFv Y6 were modified by attachment of a farnesyl group, acting as an anchor to the cell membrane. Live-cell images with the modified anti-KRas-cFarn macromolecules revealed clear accumulation at the inner aspect of the cell membrane. This modification led to the development of other variations, including the addition of a VHL E3 ligase degrader. The downregulation of phosphorylated ERK and MEK proteins, kinases that are involved in the proliferation and replication of cells was observed, with consequent loss of cell viability 48 h after treatment. In contrast, internalised DARPin K19-cFarn and scFv Y6-cFarn did not lead to the downregulation of phosphorylated ERK and MEK or loss of viability in BxPC-3 cells, a wild-type (WT) KRAS PDAC cell line. Finally, the effect of the downregulation of KRas signalling on the radiosensitisation of PDAC cells was explored. For that purpose, following the co-delivery of scFv Y6-cFarn, cells were subjected to increasing doses of radiation. Concomitantly, the radiosensitisation of PDAC cells was also studied in a more targeted approach. To do so, anti-KRas immune molecules were radiolabelled with [^{123}I] and co-delivered with Tri-cTAT B, aiming for a dual-effect therapy. In both approaches, cell survival was assessed using clonogenic assays. Overall, this work showcases a new state-of-the-art methodology to address KRas mutations while improving the efficacy of radiotherapy in PDAC treatment. Additionally, the use of engineered anti-KRas antibodies that are not limited to a particular KRas mutation, broadens their therapeutic window in a precise and functionally targeted approach.

Acknowledgments

First and foremost, I would like to express my sincere gratitude to Professor Katherine Vallis for making a childhood dream come true – to study at the University of Oxford. Without her guidance and support, this thesis would not have been possible.

What a ride these past three years were! Alongside starting a DPhil amid a global pandemic and having two and a half years to finish it was incredibly challenging. However, this surely allowed me to grow and develop myself! Unquestionably, this would have been much more difficult without members of the Vallis Lab. My biggest thanks go to Sarah for teaching a Chemist how to work in a Biochemistry Lab. To Fernando, for his constant advice and for helping me go through the ”why is this not working?” moods. To Yi-Jhih, for his companionship in the Lab and for the longer hours discussing science (and football). To Gemma, for your massive support in ordering batches of [^{123}I] urgently and helping me design never-ending clonogenic experiments. To Ole, Irini, Rachel, Swati and Anna – thank you all for your help and support!

Equally, this would not be possible without my funding entity – the EU Marie Curie Actions, particularly the THERADNET. It was an amazing experience and belonging to this network has allowed me to live moments that I will definitely remember for the rest of my life! I would like to particularly thank Professor Martin Pruschy and Professor Geoffrey Higgins.

During these past three years, I was able to live with amazing people who made this journey more pleasant. To Bav, Paula and Grace for your companionship, relaxation trips to Bicester Village and for hearing me endlessly about watches and wine!

Importantly, to my parents, who have given me the opportunity to find my own path in life. To my brother, who has shown me the importance of working hard and having high standards to be the best in business.

Lastly, my partner, Mafalda, who despite the long-distance relationship, always supported my decisions. Thank you for understanding my “I can’t go on holiday because I have important experiments to do”. I promise next year, I will try to take you on vacation!

Abbreviations

PDAC	Pancreatic Ductal Adenocarcinoma
NSCLC	Non-Small Cell Lung Cancer
CRC	Colorectal Carcinoma
PanIn	Pancreatic Intraepithelial Neoplasia
IPMNs	Intraductal Papillary Mucinous Neoplasms
TGF-$\boldsymbol{\beta}$	Transforming Growth Factor Beta
EGFR	Epidermal Growth Factor Receptor
DBS	Double-Strand Breaks
MSV	Harvey Murine Sarcoma Virus
GAP	GTPase-activating Protein
GEF	Guanidine Nucleotide-Exchange Factors
SOS	Son of Sevenless
MEK	Mitogen-activated Kinases
MAPK	Mitogen-activated Protein Kinases
ERK	Extracellular Signal-Regulated Kinases
PI3K	Phosphatidylinositol 3-Kinase
PDK1	3-Phosphoinositide-dependent Protein Kinase 1
RAC	RAS-related C3 Botulinum Substrate
NF-$\boldsymbol{\kappa}$B	Nuclear Factor – $\boldsymbol{\kappa}$B
PLC$\boldsymbol{\varepsilon}$	Phosphoinositide-specific Phospholipase C
PKC	Protein Kinase C
WT	Wild-Type
HVR	Hypervariable Region
FTase	Farnesyltransferase
FTIs	FTase Inhibitors
GGTase I	Geranylgeranyltransferase I
RCE1	RAS Converting CAAX Endopeptidase 1
ICMT	Protein-*S*-isoprenylcysteine *O*-methyltransferase
S-IIP	Switch-II Pocket
TME	Tumour Microenvironment
IL	Interleukin
CXCR	C-X-C Chemokine Receptor

ICAM-1	Intercellular Adhesion Molecule 1
TNF	Tumour Necrosis Factor
TTP	Tristerrolin
ROS	Reactive Oxygen Species
MHC	Major Histocompatibility Complex
GM-CSF	Granulocyte-Macrophage Colony Stimulating Factor
MDSC	Myeloid-derived Suppressor Cells
IRF2	Interferon Regulatory Factor 2
ATM	Ataxia-Telangiectasia Mutated
CHK	Checkpoint Kinase
HRR	Homologous Recombination Repair
NHEJ	Non-Homologous End Joining
EBRT	External Beam Radiation Therapy
5-FU	5-Fluorouracil
dTTP	Deoxythymidine Triphosphate
dATP	Deoxyadenosine Triphosphate
PDXs	Patient-derived Xenografts
mAbs	Monoclonal Antibodies
FDA	Food and Drug Administration
HER2	Human Epidermal Growth Factor Receptor 2
scFv	Single-Chain Fv
DARPin	Designed Ankyrin Repeat Proteins
CPP	Cell-Penetrating Peptide
HSPGs	Heparin Sulfate Proteoglycans
SAP(E)	Sweet Arrow Peptide Derivative
MAP	Model Amphiphatic Peptide
GAGs	Glycoaminoglycans
RTKs	Receptor Tyrosine Kinases
[^{123}I]	Iodine-123
PLA	Proximity-Ligation Assays
QTOF	Quadrupole Time-of-Flight
HPLC	High-Pressure Liquid Chromatography
CuAAC	Cooper(I)-Catalysed Azide-Alkyne [3+2] Cycloaddition
ROI	Region of Interest

Table of Contents

Chapter 1 Introduction *1*

1.1. The Pancreas: Anatomy and function **1**

1.2. Pancreatic Cancer **2**

1.2.1. Introduction **2**

1.2.2. Development of Pancreatic Cancer **2**

1.2.3. Histological Classification of Pancreatic Cancer **5**

1.2.4. Treatment Strategies for PDAC **6**

1.3. The Biology of RAS Oncogenes **9**

1.3.1. The Discovery of RAS Oncogenes **9**

1.3.2. Mechanisms and Role of RAS Oncogenes **11**

1.3.3. Ras Structure **15**

1.3.4. Ras Mutations **17**

1.3.5. KRas Inhibitors **19**

1.3.5.1. Indirect KRas Inhibitors **20**

1.3.5.2. Direct KRas Inhibitors **22**

1.4. Tumour Microenvironment **28**

1.4.1. Introduction **28**

1.4.2. Effect of KRas Mutations in the Tumour Microenvironment **29**

1.5. Radiation and Targeted Therapies **31**

1.5.1. Introduction **31**

1.5.2. Radiation-induced DNA Damage **32**

1.5.3. Radiosensitising Agents **33**

1.5.4. Antibody-based Therapies **35**

1.6. Cell-Penetrating Peptides **36**

1.6.1. Introduction **36**

1.6.2. Classes of Cell-Penetrating Peptides **37**

1.6.2.1. Positively-charged Cell-Penetrating Peptides **37**

1.6.2.2. Negatively-charged Cell-Penetrating Peptides **38**

1.6.2.3. Amphipathic Cell-Penetrating Peptides **39**

1.6.3. Cellular Uptake Mechanisms **40**

1.6.3.1. Energy-dependent Mechanisms **40**

1.6.3.2. Energy-independent Mechanisms **42**

1.7. Research Objectives **43**

Chapter 2 Materials and Methods *45*
2.1. Synthesis of Optimised Trimeric CPPs **45**
2.1.1. cTAT$_3$-Alkyne **45**
2.1.2. Tri-cTAT B – Alexa Fluor™ 488 ..... **45**
2.2. Cell Culture **46**
2.2.1. 2D Cell Culture **46**
2.2.2. 3D Cell Culture **47**
2.3. Live-Cell Confocal Microscopy **47**
2.4. Proximity Ligation Assay **48**
2.5. Western Blotting **49**
2.6. Radiochemistry **51**
2.7. Retention Assay **52**
2.8. Fractionation Assay **52**
2.9. Clonogenic Assays **53**
2.9.1. *In Vitro* Irradiations **53**
2.9.2. Co-Delivery of [^{123}I]I-anti-KRas Macromolecules **53**
2.9.3. Cell Staining **54**
2.10. *In Vivo* Experiments **54**
2.10.1. Animals and Husbandry **54**
2.10.2. Tumour Inoculation **54**
2.10.3. Treatment **55**
2.10.4. *In Vivo* Bioluminescence Imaging **55**
2.10.5. SPECT/CT **56**
2.10.6. SPEC/CT *Ex Vivo* Biodistribution **56**
2.11. Statistical Analysis **56**
Chapter 3 Synthesis of Tri-cTAT B and Co-Delivery of Anti-KRas Molecules *57*
3.1. Introduction **57**
3.1.1. Novel TAT-derived Cell-Penetrating Peptide **57**
3.1.2. Anti-KRas Immune Molecules **59**
3.2. Aims **60**
3.3. Results **61**
3.3.1. Synthesis of Tri-cTAT B through Microwave-Assisted Chemistry **61**
3.3.2. Tri-cTAT B Transfection in PDAC Cell Lines **68**
3.3.3. Co-Delivery of Anti-KRas Immune Molecules with Tri-cTAT B **70**

3.3.4. Co-Delivery of Anti-KRas^{G12D} Antibody Interacts with KRAS 89

3.3.5. *In vivo* Uptake of Tri-cTAT B 92

3.4. Discussion 94

3.4.1. Tri-cTAT B Mediates the Delivery of Anti-KRas Macromolecules in Cells 95

3.4.2. Tri-cTAT B Enables Intact Co-Delivery of DARPin K19 in 3D Spheroids 97

3.4.3. Tri-cTAT B Facilitates the Interaction of a KRas^{G12D} IgG with KRas 98

3.4.4. Tri-cTAT B Demonstrates Multi-Organ Uptake *In Vivo* 99

Chapter 4 Biological Effect of the Co-Delivery of Anti-KRas Immune Molecules in PDAC Cancer Cells 100

4.1. Introduction 100

4.2. Aims 102

4.3. Results 103

4.3.1. Downregulation of KRas-mediated Kinases 103

4.3.2. Downregulation of KRas Affects the Viability of PDAC Cell Lines 114

4.3. Discussion 118

4.3.1. Co-Delivery of Anti-KRas Macromolecules Causes ERK/MEK Suppression 118

4.3.2. Co-Delivery of Anti-KRas Macromolecules Impairs PDAC Cell Viability 122

Chapter 5 Internalisation of Radiolabelled Anti-KRas Macromolecules for Radionuclide Therapy 125

5.1. Introduction 125

5.1.1. Targeted Radiation Delivery 125

5.1.2. External Beam Radiation and Radiosensitisation of Cancer Cells 127

5.2. Aims 129

5.3. Results 129

5.3.1. Radiolabelling of anti-KRas macromolecules with [^{123}I] 129

5.3.2. Distribution of [^{123}I]I-Anti-KRas Macromolecules in PANC-1 Cells 132

5.3.3. Intracellular Retention of [^{123}I]I-DARPin K19-cFarn 136

5.3.4. Cytotoxicity of [^{123}I]I-DARPin K19-cFarn-internalised Macromolecules 137

5.3.3. KRas-mediated Radiosensitisation of PANC-1 Cells 139

5.3.4. Evaluation of the Biosdistribution of [^{123}I]I-anti-KRas IgG *in Vivo* by SPECT/CT. 140

5.4. Discussion 146

5.4.1. Radioiodination of Anti-KRas Macromolecules 146

5.4.2. Radioiodination of Farnesylated Anti-KRas Macromolecules Follows Live-Cell Microscopy Data 146

5.4.3. Downregulation of KRas-Mediated Kinases Causes Radiosensitisation..... 147

5.4.4. Co-Delivery of Anti-KRAS IgG *In Vivo* Demonstrates Limited Effects 149

***Chapter 6 Concluding Remarks*.....151**

6.1. Synopsis 151

6.2. Study Limitations 154

6.3. Future Perspectives..... 157

***Chapter 7 Bibliography*.....161**

List of Figures

Figure 1.1 - Anatomy and histology of the pancreas. 1

Figure 1.2 - Histological and genetic progression model of the development of pancreatic carcinogenesis. 5

Figure 1.3 - Schematic representation of KRas activation. 12

Figure 1.4 - Signalling downstream of Ras. 14

Figure 1.5 - Structure of KRas. 16

Figure 1.6 - KRas undergoes conformational changes upon GTP hydrolysis. 17

Figure 1.7 - Common KRas substitutions in lung, pancreas and large intestine tumours. 18

Figure 1.8 - Frequency and distribution of RAS mutations in human cancers. 19

Figure 1.9 - Downstream approaches to targeting KRas.. 21

Figure 1.10 - The hallmarks of cancer. 28

Figure 1.11 - KRas-mediated immune escape in the tumour microenvironment. 30

Figure 3.1 - Chemical Structure of Tri-cTAT B. 58

Figure 3.2 - DARPin K19 binds KRas at an allosteric site. 60

Figure 3.3 - Tri-cTAT B-related chemical structures. 61

Figure 3.4 - Reaction products. 63

Figure 3.5 - Tri-cTAT B synthesis.. 64

Figure 3.6 - Microwave-assisted "click" chemistry. 66

Figure 3.7 - Synthesis of Tri-cTAT B - AlexaFluor™ 488 67

Figure 3.8 - Live-cell confocal microscopy of linear and cyclic TAT trimers in PANC-1 and PSN-1 cells 70

Figure 3.9 - Co-delivery of DARPin K19 in PDAC cell lines using Tri-cTAT B 73

Figure 3.10 - Time-course uptake of DARPin K19 and Tri-cTAT B in PSN-1 cells. 76

Figure 3.11 - Co-delivery of DARPin K19 confirmed by western blotting. 78

Figure 3.12 - Morphology of PANC-1 spheroids 80

Figure 3.13 - Co-delivery of DARPin K19 in PANC-1-derived spheroids using Tri-cTAT B. 82

Figure 3.14 - DARPin K19 accumulation in PDAC cells. 83

Figure 3.15 - Co-delivery of modified anti-KRas macromolecules in PDAC cell lines using Tri-cTAT B 86

Figure 3.16 - Re-distribution of farnesylated anti-KRas macromolecules over 48 h 88

Figure 3.17 - Proximity ligation assays (PLA)..... 90

Figure 3.18 - AF488-conjugated Tri-cTAT B uptake in vivo models. 94

Figure 4.1 - Treatment of PANC-1 cells using Condition 3 causes limited pERK downregulation. 104

Figure 4.2 - Treatment of PANC-1 cells using Condition 4 reveals extensive pERK downregulation. 105

Figure 4.3 - Efficacy of DARPin K19-cFarn in downregulating pERK after 24 h incubation. 106

Figure 4.4 - DARPin K19-cFarn-VHL downregulates the MAPK signalling pathway of KRas. 108

Figure 4.5 - Treatment of PANC-1 cells with scFv-Y6-cFarn impairs pERK.. 109

Figure 4.6 - pERK downregulation in PSN-1 cells appears to be limited.. 113

Figure 4.7 - Co-delivery of anti-KRas macromolecules with Tri-cTAT B, impairs the viability of PANC-1 cells. 115

Figure 4.8 - Co-delivery of anti-KRas macromolecules with Tri-cTAT B, impairs the viability of PSN-1 cells..... 116

Figure 4.9 - Co-delivery of anti-KRas macromolecules with Tri-cTAT B has no effect on the viability of BxPC-3 cells. 117

Figure 5.1 - Labelling of anti-KRas macromolecules with [^{123}I]. 132

Figure 5.2 - Fractionation of PANC-1 cells...... 133

Figure 5.3 - Western blotting validation of PANC-1 cells fractionation. 135

Figure 5.4 - Retention of [^{123}I]I-DARPin K19-cFarn in PANC-1 and PSN-1 cells as a function of time. 136

Figure 5.5 - Internalisation of [^{123}I]I-DARPin K19-cFarn impairs the survival of PANC-1 cells...... 138

Figure 5.6 - Downregulation of KRAS signalling pathways radiosensitises PANC-1 cells 139

Figure 5.7 - Anti-KRas IgG Radiolabelling and Serum-Stability Assay..... 142

Figure 5.8 - In vivo imaging of anti-KRas IgG in PSN-1 tumours. 145

List of Tables

Table 1.1 - Types of pancreatic precursor lesions 3

Table 1.2 - Stages of PDAC according to the American Cancer Society 7

Table 1.3 - Current treatment options for PDAC according to the type of tumour 8

Table 1.4 - Selected KRas-directed therapies 26

Table 2.1 - List of antibodies 50

Table 3.1 - Cooper(I)-catalysed azide-alkyne [3+2] cycloaddition (CuAAC) conditions 62

Table 3.2 - PDAC cell lines and respective alterations 68

Table 4.1 - Conditions used for the downregulation of KRas-mediated kinases 103

Chapter 1 Introduction

1.1. The Pancreas: Anatomy and function

The pancreas is a gland located in the abdomen, about six inches long and with important digestive functions. It is an elongated, tapered organ, and it is divided into three segments – the head (right side), the tail (left side), and the neck and body (middle section). Anatomically, it is surrounded by the stomach, small intestine, liver, spleen, gallbladder, and two major blood vessels, the superior mesenteric artery and superior mesenteric vein.

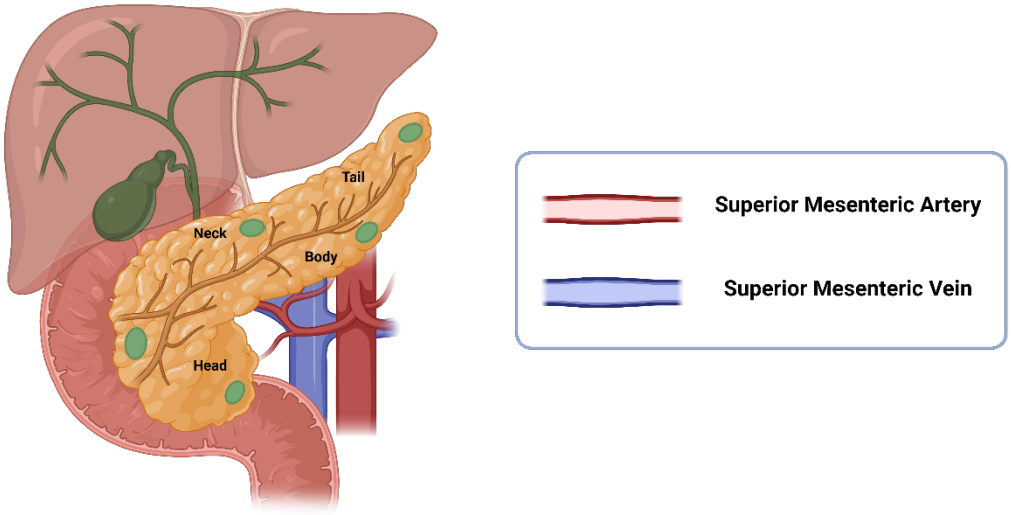


Figure 1.1 - Anatomy and histology of the pancreas.

As a gland, the pancreas has exocrine and endocrine functions, although the majority of the pancreas (95%) is occupied by exocrine tissue that produces pancreatic enzymes for digestion. These include amylase for the digestion of carbohydrates, trypsin to digest proteins, and lipase to break down fat. The remaining tissue, also known as islets of Langerhans, are endocrine cells whose function is the production of two main hormones for the regulation of blood sugar levels: insulin, promoting the decrease of blood sugar, and glucagon, acting to increase blood sugar[1].

1.2. Pancreatic Cancer

1.2.1. Introduction

Pancreatic ductal adenocarcinoma (PDAC), more commonly referred to as pancreatic cancer, is the 12th most common cancer worldwide, with more than 495,000 new cases diagnosed in 2020[2]. In the UK, pancreatic cancer is the 10th most common cancer, accounting for 3% of all new cancer cases between 2016-2018 [3]. PDAC is also responsible for almost 10,000 deaths in the UK, making it the 5th most common cause of cancer death. The five- and ten-year survival rates are 7.3% and 5%, respectively, making it one of the most fatal malignancies. Shockingly, these figures have shown the same trend since the early 70s, with no significant increase in either men or women, whilst cases rose by 17% since the 1990s[4].

Pancreatic cancer is primarily a disease associated with older adults, with peak incidence being currently between 85 and 89 years old for females and 90+ years old for males[5]. Often, the development of PDAC arises as a consequence of acquired mutations in cancer-associated genes[6]. However, environmental factors such as smoking, chronic pancreatitis and diabetes mellitus are also strong aetiological factors[7–10].

PDAC often presents late when the disease carries a high mortality rate, although, if detected early, patients can experience a positive prognosis[11]. However, patients often only start to develop symptoms when the disease is at an advanced stage, often when distant metastases have already developed, and when there are very limited treatment options.

1.2.2. Development of Pancreatic Cancer

In a pattern analogous to that seen in other tumours, pancreatic cancer arises from a progressive accumulation of genetic changes in the pancreatic epithelium, evolving from non-neoplastic to non-invasive precursor lesions to invasive carcinoma[6]. Frequently, the

lesions associated with the development of PDAC occur in small ducts and ductules and are called pancreatic intraepithelial neoplasia (PanIn)[12]. However, larger precursor lesions such as intraductal papillary mucinous neoplasms (IPMNs) and mucinous cystic neoplasms are also often reported.

The progression from normal epithelium to invasive carcinoma involves a stepwise transition that is classified as low-grade and high-grade. While the former is divided between PanIN-1A, PanIN-1B and PanIN-2, the latter includes PanIN-3 lesions. Table 1.1 describes the different pancreatic precursor lesions and their characteristics.

Table 1.1 - Types of pancreatic precursor lesions

Grade	Stage	Cytological Structural Atypia	Characteristics
Low	PanIN-1A	Minimum	Flat epithelial lesions. The nuclei are small and round to oval.
	PanIN-1B	Minimum	Lesions with papillary, micropapillary or basally, pseudostratified architecture.
	PanIN-2	Mild-Moderate	Lesions can be flat or papillary. Presence of nuclear abnormalities. Mitoses are rare.
High	PanIN-3	Severe	Lesions are usually papillary or micropapillary. Presence of small clusters of epithelial cells and luminal necroses. Loss of nuclear polarity.

The development of PDAC also involves a stepwise genetic transition that includes the four most commonly mutated genes – KRAS, TP53, SMAD4 and CDKN2A/p16[13–17]. Among these, KRAS is one of the most frequently altered oncogenes, and its mutations

are present in greater than 90% of PDAC cases. KRas mutations are related to the intrinsic GTPase activity of the KRas protein, which is represented by the continuous activation of the protein, resulting in the stimulation of intracellular signalling pathways that promote carcinogenesis[18]. TP53, considered to be the guardian of the genome, is a tumour suppressor gene whose mutation is found in 50% to 70% of pancreatic cancers and is responsible for stimulating cell-cycle checkpoints as well as inducing apoptosis and senescence of cells[19,20]. The CDKN2A/p16 gene, which acts as a tumour suppressor, is inactivated in almost 95% of PDAC cases, blocking important cell checkpoints[21]. Lastly, the suppression of the SMAD4 gene, deactivated in 55% of pancreatic cancers, acts as a mediator of the transforming growth factor beta (TGF-β), playing an important role as a tumour suppressor in early-stage PDAC[22].

The progression of pancreatic lesions from normal epithelium to invasive carcinoma is often accompanied by an accumulation of the four most mutated genes that arise at specific stages (Figure 1.2). Mutation of KRAS oncogene is the first one to occur and appears at early stages (between PanIN-1A and PanIN-1B), while the inactivation of the CDKN2A/p16 tumour suppressor gene occurs at intermediate stages (PanIN-2)[23]. Deactivation of TP53 and SMAD4 are later events (PanIN3)[24–26].

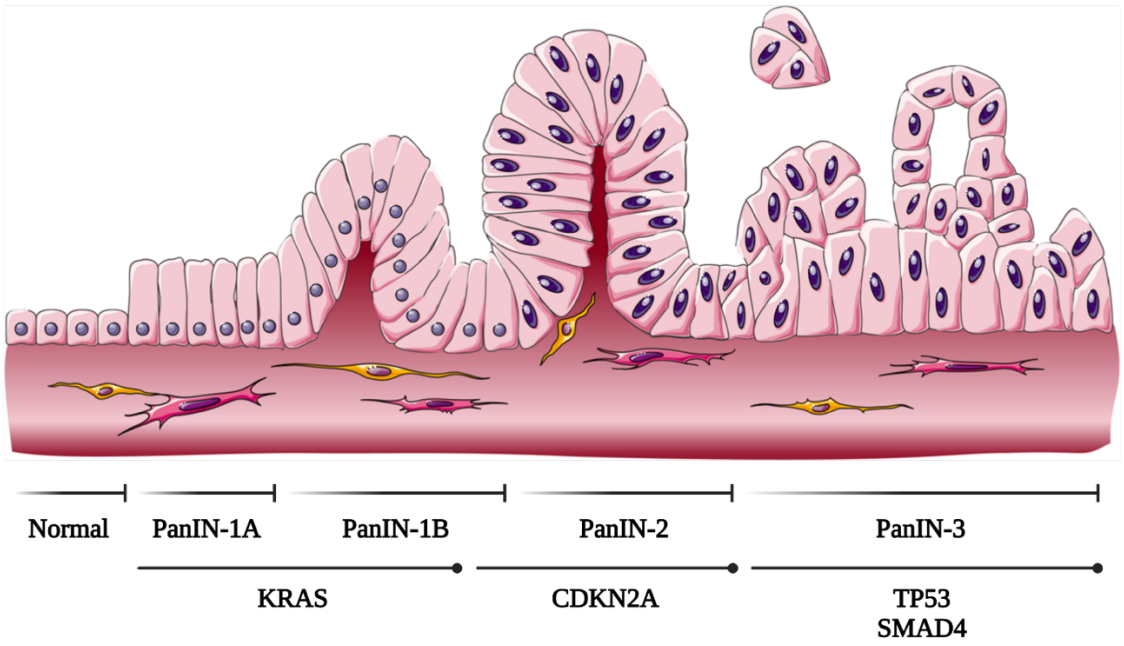


Figure 1.2 - Histological and genetic progression model of the development of pancreatic carcinogenesis. The occurrence of precursor lesions results in pancreatic cancer in a multistage process that is mediated by consecutive genetic alterations. Initial mutations involve the oncogene KRAS, while later mutations include CDKN2A, TP53, and SMAD4, resulting in the silencing of these tumour suppressors.

1.2.3. Histological Classification of Pancreatic Cancer

Pancreatic cancer is categorised into two major types, depending on the cell of origin and location within the pancreas. As a result, pancreatic cancer can be classified as exocrine pancreatic cancer and neuroendocrine pancreatic cancer.

Exocrine pancreatic cancer accounts for more than 95% of all cancers of the pancreas and is subdivided into four different types – adenocarcinoma, squamous cell carcinoma, adenosquamous carcinoma and colloid carcinoma.

Pancreatic ductal adenocarcinoma occurs in the duct of the pancreas and is the most common form of pancreatic cancer. It carries a high mortality rate, and common symptoms include abdominal pain, nausea, and weight loss[27]. Conversely, pancreatic squamous cell carcinoma and pancreatic adenosquamous carcinoma are rare, and their biology is poorly understood[28–30]. Additionally, they have a worse survival rate than

PDAC[31–33]. Although also rare, pancreatic colloid carcinoma has a much better prognosis than other types of exocrine pancreatic cancer since it is less likely to spread to neighbouring tissues. This type of pancreatic cancer arises from IPMN lesions[34].

Neuroendocrine pancreatic cancer develops from cells in the endocrine gland of the pancreas, forming clusters of cells named islets[35]. Malignant tumours that occur in these clusters of cells are called pancreatic neuroendocrine tumours (NETs) or islet cell carcinoma. These tumours are rarer than exocrine tumours and have a better prognosis, with some studies reporting a 1-year survival rate of 77% and a 10-year survival rate of 31%[36,37].

1.2.4. Treatment Strategies for PDAC

Surgery, followed by chemotherapy, remains the commonest treatment approach for PDAC[38]. However, this option can only be implemented in patients whose disease is detected at stages I-II. Consequently, only a fraction of patients undergoes surgery as the majority of cases are detected at stage III-IV, when there has already been spread to lymph nodes and/or other organs[39,40]. Table 1.2 summarizes how the different stages of PDAC are classified by the American Cancer Society[41].

Table 1.2 - Stages of PDAC according to the American Cancer Society

Stage	Stage Grouping	Stage Description
0	Tis N0 M0	The cancer is confined to the top layers of pancreatic duct cells and has not invaded deeper tissues. It has not spread outside of the pancreas. Also referred to as carcinoma in situ (Tis). It has not spread to nearby lymph nodes (N0) or distant sites (M0).
IA	T1 N0 M0	The cancer is confined to the pancreas and is no bigger than 2 cm across (T1). It has not spread to nearby lymph nodes (N0) or distant sites (M0).
IB	T2 N0 M0	The cancer is confined to the pancreas and is larger than 2 cm but no more than 4 cm across (T2). It has not spread to nearby lymph nodes (N0) or distant sites (M0).
IIA	T3 N0 M0	The cancer is confined to the pancreas and is bigger than 4 cm across (T3). It has not spread to nearby lymph nodes (N0) or distant sites (M0).
IIB	T1 N1 M0	The cancer is confined to the pancreas and is no bigger than 2 cm across (T1) **AND** it has spread to no more than 3 nearby lymph nodes (N1). It has not spread to distant sites (M0).
	T2 N1 M0	The cancer is confined to the pancreas and is larger than 2 cm but no more than 4 cm across (T2) **AND** it has spread to no more than 3 nearby lymph nodes (N1). It has not spread to distant sites (M0).
	T3 N1 M0	The cancer is confined to the pancreas and is bigger than 4 cm across (T3) **AND** it has spread to more than 3 nearby lymph nodes (N1). It has not spread to distant sites (M0).
III	T1 N2 M0	The cancer is confined to the pancreas and is no bigger than 2 cm across (T1) **AND** it has spread to 4 or more nearby lymph nodes (N2). It has not spread to distant sites (M0).
	OR	
	T2 N2 M0	The cancer is confined to the pancreas and is larger than 2 cm but no more than 4 cm across (T2) **AND** it has spread to 4 or more nearby lymph nodes (N2). It has not spread to distant sites (M0).
	OR	
	T3 N2 M0	The cancer is confined to the pancreas and is bigger than 4 cm across (T3) **AND** it has spread to 4 or more nearby lymph nodes (N2). It has not spread to distant sites (M0).
	OR	
	T4 Any N M0	The cancer is growing outside the pancreas and into nearby major blood vessels (T4). The cancer may or may not have spread to nearby lymph nodes (Any N). It has not spread to distant sites (M0).
IV	Any T Any N M1	The cancer has spread to distant sites such as the liver, peritoneum, lungs or bones (M1). It can be any size (Any T) and might or might not have spread to nearby lymph nodes (Any N).

In other cases, one option is neoadjuvant therapy, usually chemotherapy alone. For this purpose, a cocktail of cytotoxic drugs comprised of folinic acid, fluorouracil, irinotecan and oxaliplatin is widely used and named FOLFIRINOX[42]. Gemcitabine, in combination with the albumin-conjugated drug paclitaxel, or with the epidermal growth factor receptor (EGFR) inhibitor erlotinib, is also commonly used for the treatment of PDAC[43,44]. Table 1.3 describes frequent treatments currently employed in PDAC patients according to the type of tumour[45].

Table 1.3 - Current treatment options for PDAC according to the type of tumour

Tumour Type	First-Line Treatment	Second-Line Treatment	Median Survival
Resectable Tumour	Pancreatic Resection	Adjuvant Chemotherapy: Gemcitabine-Capecitabine or FOLFIRINOX	26 Months
Nonresectable Borderline and/or Nonresectable Locally Advanced Tumour (ECOG Score 0/1)	Neoadjuvant Radiotherapy or Chemotherapy	Stable or Response: Surgical Exploration or Continued Chemotherapy; Progression: Gemcitabine or FOLFOX or Nanoliposomal Irinotecan + 5FU	6-18 Months
Nonresectable Borderline and/or Nonresectable Locally Advanced Tumour (ECOG Score 2)	Gemcitabine; BSC if ECOG Score > 2	FOLFOX or Nab-Paclitaxel + Gemcitabine or Nanoliposomal Irinotecan + 5FU or BSC	6-8 Months
Metastatic Tumour	ECOG Score 0/1: FOLFOX or Nab-Paclitaxel + Gemcitabine or Nab-Paclitaxel + Erlotinib ECOG Score 2: Gemcitabine; ECOG Score > 2: BSC	FOLFOX or Nab-Paclitaxel + Gemcitabine or Nanoliposomal Irinotecan + 5FU or BSC	6-11 Months

Radiotherapy produces DNA lesions, of which double-strand breaks (DSB) are the most deleterious. Consequently, cells that are affected by ionizing radiation, including photon therapy, initiate a molecular process whose objective is the maintenance of genome integrity and support of normal functions of the cell – DNA Damage Response. Failure to repair DNA efficiently leads to cell death, the desired outcome of radiotherapy. However, tumours have mechanisms by which they can evade the desired radiotherapy effect. Desmoplasia, hypoxia, inflammation and altered response to oxidative stress are well-known hallmarks of PDAC radioresistance, and all contribute to the poor response rate to radiotherapy. For that purpose, radiosensitisation remains a feasible solution and the development of novel techniques to sensitise cancer cells while maintaining healthy cells "untouched" continues to be an exciting and promising field. To date, gemcitabine, capecitabine and 5-FU are used as radiosensitiser agents, and they are often combined with radiotherapy. However, similar to other approaches, the use of these radiosensitisers offers only modest survival benefits, both in resectable disease and locally advanced disease. In the 2019 American Society for Radiation Oncology guidelines, the use of fractionated RT and SBRT for patients with borderline/ locally advanced PDAC is conditionally recommended with moderate quality of evidence[46].

1.3. The Biology of RAS Oncogenes

1.3.1. The Discovery of RAS Oncogenes

RAS family members are the most commonly mutated oncogenes in human cancer. The beginning of RAS research started in 1964 when Jennifer Harvey observed that a viral preparation from a leukemic rat induced sarcomas in rodents, defined as Harvey Murine Sarcoma Virus (Ha-MSV)[47,48]. Later on, three additional viruses with similar tumorigenic properties were identified, including the Kirsten Murine Sarcoma Virus (Kirsten-MSV)[48], the BALB Murine Sarcoma Virus (BALB-MSV)[49], and the Rasheed strain of rat sarcoma

virus[50]. In 1975, Ed Scolnick and colleagues demonstrated that the Ha-MSV and Ki-MSV strains contained genomic sequences derived from the rat genome, today known as HRas and KRas respectively[51].

The linkage between retroviral oncogenes and their molecular nature was reported in 1982 by Channing Der and colleagues. In this study, DNA extracted from NIH 3T3 cells was modified with human tumour DNA hybridized to probes specific for the v-h-ras and v-k-ras[52]. Later in the same year, two other studies confirmed the same findings. In 1983, a new human transforming gene that belongs to the RAS gene family was identified in a neuroblastoma cell line and designated as NRAS[53,54].

To further comprehend the biology of RAS oncogenes, the normal human HRAS gene was compared with its oncogenic form, allowing the identification of single-point mutations[55–57]. Additionally, it was shown that RAS oncogenes were not able to transform primary cells into malignant forms. However, this transformation was possible when RAS oncogenes cooperated with other oncogenes (i.e. MYC) or when inactivation of a tumour suppressor gene occurred (i.e. p53)[58–60].

In 1984, mutant KRas was, for the first time, identified in a tumour biopsy from a lung cancer patient. However, these mutations were not observed in cells from healthy tissue[61]. Over the next few years, new Ras mutations were found in other tumours such as colon and pancreatic carcinomas[13,62,63].

In vitro, translation of HA-MSV and KI-MSV RNA resulted in a 21 kDa polypeptide, at that time designated as p21[64]. The analysis of cells transformed by a temperature-sensitive mutant of Ki-MSV, later known as KRas, allowed scientists to identify that the p21 peptide was the product of this oncogene[65]. During the late 1970s, new results allowed the identification of two characteristics that would become critical in understanding the

mechanism of activation of these proteins. Firstly, the affinity of these p21 proteins towards guanine-containing nucleotides, and secondly, the identification of p21 proteins located on the inner side of the plasma membrane[66,67].

1.3.2. Mechanisms and Role of RAS Oncogenes

The starting point of understanding the biological function of Ras began in 1984 when three articles reported that Ras proteins were GTPases. Together with the observed structural homologies between Ras and the alpha unit of G proteins, suggestions emerged concerning the role of Ras proteins as mediators of signal transduction. The first evidence was provided by Kamata and Feramisco ,who observed that the transmembrane protein, epidermal growth factor receptor (EGFR), stimulated GTP binding to Ras proteins, resulting in their activation[68].

As insights into the molecular activation of Ras grew, a soluble cytosolic protein responsible for the stimulation of GTPases - a GTPase-activating protein (GAP) was identified[69]. It was concluded that GAPs such as p120 Ras-GAP could stimulate the binding of GTP to Ras proteins, leading to activation. How upstream signals induced GTP binding remained unanswered until 1990, when mammalian cytosolic factors that accelerate the release of GDP from RAS p21 proteins were reported, becoming known as guanidine nucleotide-exchange factors (GEFs)[70]. In 1992, mammalian Ras-GEFs were isolated for the first time by functional complementation of *CDC25* or by sequence homology, resulting in the discovery of SOS1, SOS2, and Ras-GRF[71–73].

In the same year, another important piece of the puzzle was revealed by an investigation of the interaction between tyrosine-kinase cell surface receptors and Ras-GEFs. Through protein screening, GRB2 was identified, a protein that can bind the autophosphorylated tail of EGFR through their respective SH2 domains. Additionally, GRB2 contains two SH3 domains capable of binding GEFs such as SOS1. As a result, GRB2 acts as an

intermediary between EGFR and KRas proteins, indicating how signals are transmitted from outside to inside the cell[74,75].

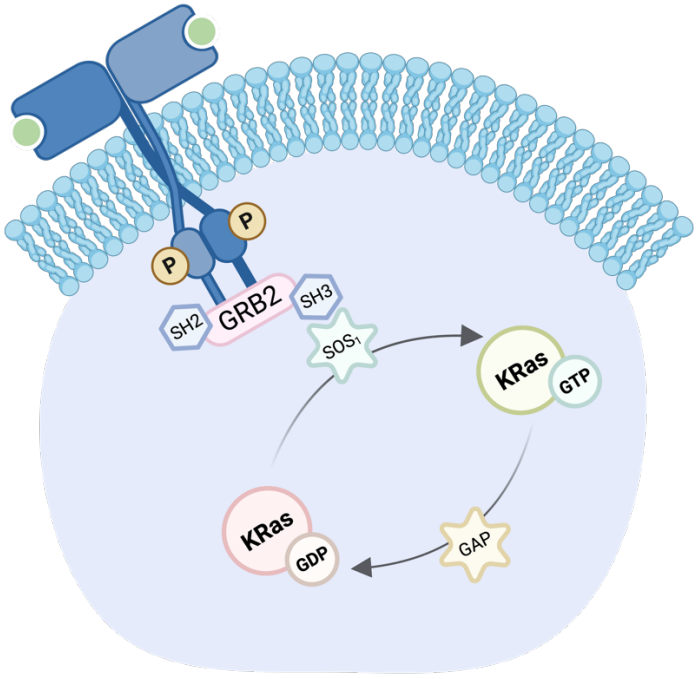


Figure 1.3 - Schematic representation of KRas activation. Ras proteins are activated by various extracellular stimuli, which are mediated by among others, receptor tyrosine kinases (RTK) and G proteins. Briefly, GRB2 binds to activated receptors via the SH2 domain while SH3 domains interact with guanine nucleotide-exchange factors (e.g., SOS1), promoting the GDP-GTP exchange on KRas. The presence of GTPase-activating proteins (GAPs) promotes the downregulation of KRas by catalysing the GTP hydrolysis.

Next, attention was focused on identifying downstream mediators of Ras. Briefly, RAF, a serine/threonine kinase, was found to interact with activated Ras proteins[76–79]. This interaction was found to activate three proteins, c-RAF1, BRAF and ARAF, resulting in the translocation of RAF to the plasma membrane[80,81]. Once activated, RAF phosphorylates and activates mitogen-activated kinases 1 and 2 (MEK1 and MEK2), resulting in phosphorylation and activation of the mitogen-activated protein kinases (MAPK) and extracellular signal-regulated kinases 1 and 2 (ERK1 and ERK2). The activation of ERK1/2 influences the regulation of transcription factors, stimulating key

cell-cycle regulatory proteins that enable the cell to transit through the G1 phase of the cell cycle[82,83].

Next, the role of Ras proteins in stimulating the phosphatidylinositol 3-kinase (PI3K) protein, resulting in the activation of the lipid kinase as a result of its translocation to the membrane, was uncovered[84,85]. Attention was centred on the 3-phosphoinositide-dependent protein kinase 1 (PDK1) and AKT due to their roles in anti-apoptotic functions[86]. PI3K activation also stimulates the Ras-related C3 botulinum substrate (RAC), a protein that belongs to the RHO family of GTPases and whose function is to regulate the actin cytoskeleton and activate transcription factor pathways such as the nuclear factor – κB (NF-κB), responsible for several biological processes, including inflammation, tumour promotion and metastasis[87,88].

Ras is equally associated with a third signalling pathway via three exchange factors for the Ras-related RAL proteins – the RAL guanine nucleotide dissociation stimulator (RALGDS), the RALGDS-like gene (RGL/RSB2), and the RGL2/RLF. Through RAL, RAS can stimulate the inhibition of forkhead transcription factors associated with cell-cycle arrest through the induction of the cyclin-dependent kinase KIP1[89].

More recently, a fourth Ras effector protein was identified – the phospholipase Cε. Known as the fourth class of mammalian phosphoinositide-specific phospholipase C (PLC), PLCε contains a GEF domain, GRF CDC25, and two c-terminal Ras-binding domains, RA1 and RA2. PLCε stimulation results in the activation of protein kinase c (PKC), a group of enzymes that controls proteins through the phosphorylation of other serine/threonine amino acid residues. Among others, the intracellular level of Ca^{2+} appears to be influenced by this stimulation, resulting in its mobilization. However, evidence also shows the role of Ca^{2+} in stimulating Ras activation in a Ca^{2+}-dependent

manner, indicating the possibility of PLCε signalling upstream and downstream of Ras activation[90].

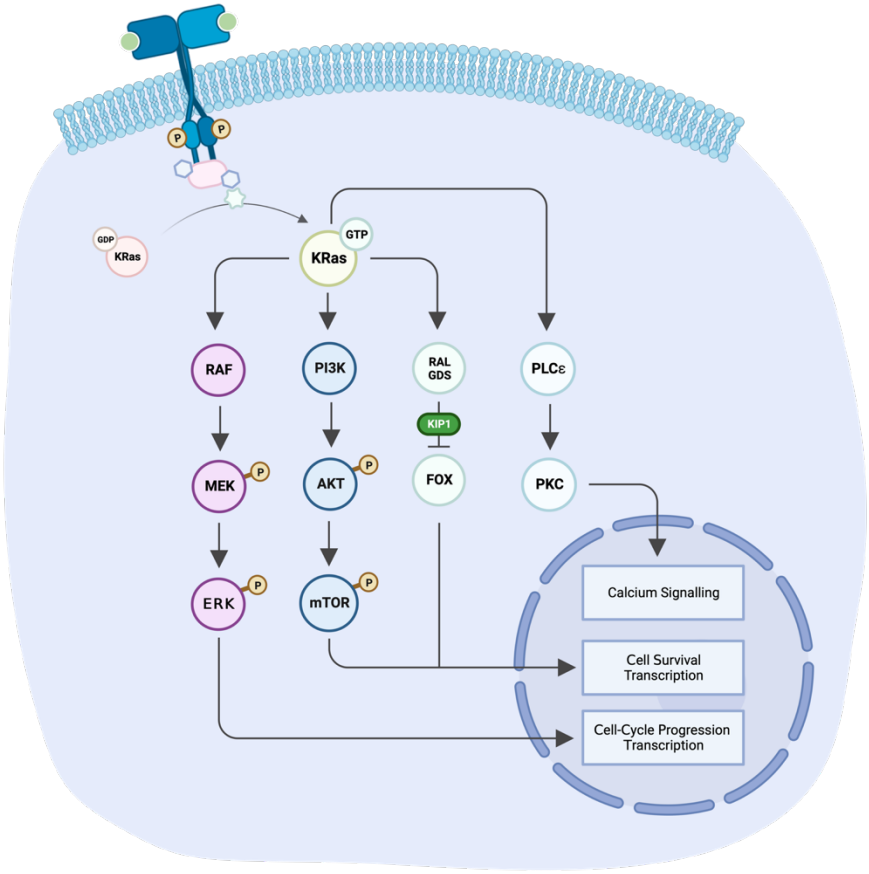


Figure 1.4 - Signalling downstream of KRas. Once in its active, GTP-bound state, Ras interacts with several families of effector proteins, resulting in their stimulation. Among others, KRas leads to the activation of RAF protein kinases, initiating the mitogen-activated protein kinase (MAPK) cascade and ultimately resulting in the phosphorylation of ERK. Once active, ERK regulates multiple transcription factors, including ELK1, that regulate cell-cycle progression. Additionally, KRas interacts with type I phosphoinositide 3-kinases (PI3K), which results in the phosphorylation of phosphatidylinositol-4,5-biphosphate (PtdIns(4,5)P2) into a second-messenger lipid that through AKT/mTOR proteins regulate the survival of cells. A third signalling pathway controlled by KRas comprises three exchange factors for the Ras-related RAL proteins. Through these proteins, KRas stimulates RAL, resulting in the inhibition of forkhead transcription factors. Finally, KRas also controls the activity of phospholipase Cε (PLCε) that catalyses the hydrolysis of phosphatidylinositol-4,5-biphosphate to diacylglycerol and inositol triphosphate, leading to the activation of protein kinase C (PKC) and ultimately calcium mobilisation.

Overall, the combined action of these effector proteins, when activated by mutant-KRas, is the promotion of tumorigenesis by stimulating cell proliferation and anti-apoptotic signals. As a result, for many years, targeting these proteins was considered a valid approach to indirectly target KRas.

1.3.3. Ras Structure

In the late 1980s, the first structure of Ras was published by Sung-Ho Kim and Fred Wittinghofer[91,92]. These early studies resulted in two important discoveries about the function of these GTPases. Firstly, the understanding that the crystal structure of mutant Ras was identical to wild-type (WT) forms[93,94]. Yet, at residue 12, a known hot spot of RAS mutations, the insertion of an amino acid other than glycine (present in WT) results in the addition of a side chain that sterically interferes with the geometry of the GTP transition state[93–95]. Secondly, the role of the glutamine residue at position 61 (Gln61). Known as another hot spot for RAS mutations, Gln61 plays an important role in catalysis, as it forms a hydrogen bond with the Arg789 residue from GAP p120, allowing the nucleophilic attack of water, a crucial step for GTP hydrolysis [93–95].

Structurally, Ras proteins have three key regions – a highly conserved effector lobe, an allosteric lobe, and a hypervariable region (HVR). The combination of the effector and allosteric lobes constitutes the G domain (aa 1-166), whilst the HVR varies between different Ras isoforms, thus being the least conserved region of the protein.

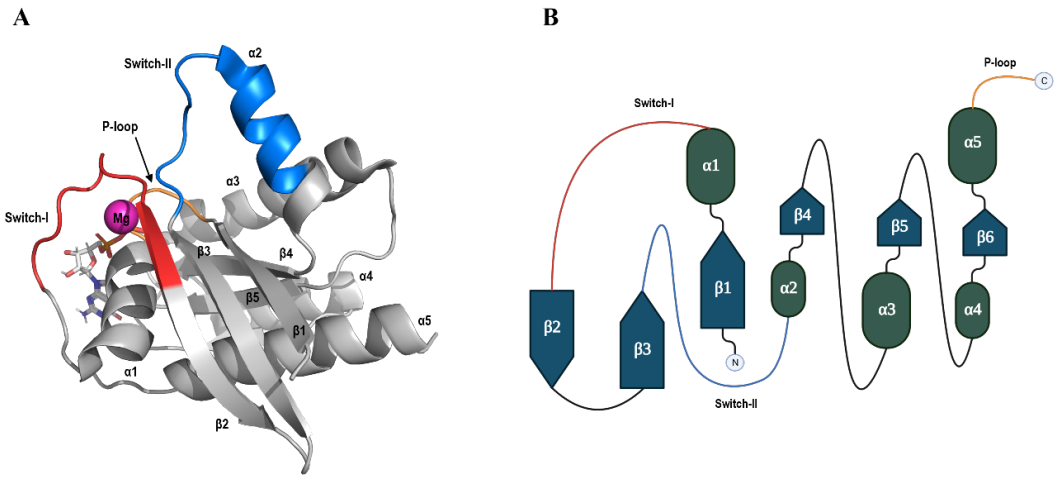


Figure 1.5 - Structure of KRas. (A) Crystal structure of wild-type (WT) KRas in the GDP-bound conformation (PDB ID: 4OBE). **(B)** 2D illustration of the secondary structure of KRas encompassing five alpha-helices and six beta-strands. Some structures were highlighted to identify key regions. These include the P-loop (aa 10-14) – orange, the switch-I region (aa 30-40) – red, and the switch-II region (aa 58-72) – blue.

The G domain, responsible for the basic biological activity of Ras proteins, encompasses six beta-strands surrounded by five alpha-helices. Additionally, the G-domain contains two regions that are critical for the functioning of Ras proteins, named switch-I (S-I) and switch-II (S-II). These regions form the binding interface for effector proteins to bind and activate the signalling pathways Ras mediates. Moreover, this is also the location where RAS regulators, such as GAPs and GEFs bind, allowing the activation and deactivation of GTPases[96]. The HVR, on the other hand, provides GTPases flexibility through the C-terminal element, an important element in anchoring Ras to the membrane[97].

More recent x-ray studies involving KRas revealed conformational changes during the conversion of the GDP-bound state to a GTP-bound state at the level of the switch regions[98]. When active, KRas presents one pocket below the S-I region, the location where GTP binds. However, when inactive GDP binds in the same pocket, yet results in the formation of a second pocket, the S-II pocket.

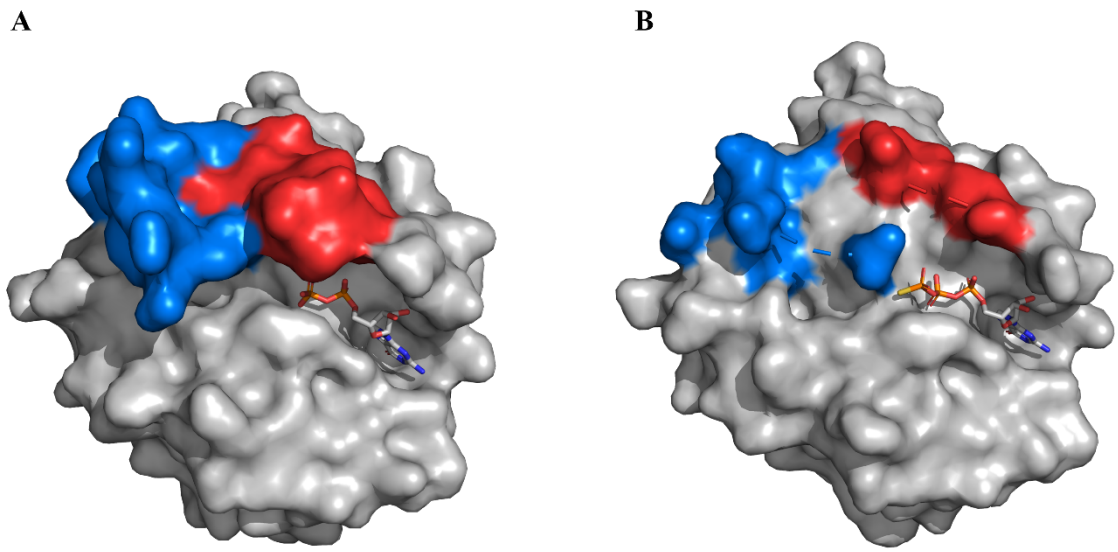


Figure 1.6 - KRas undergoes conformational changes upon GTP hydrolysis. Comparison between the crystal structure of mutant KRas with GDP-bound **(A)** (PDB ID: 4LDJ) and mutant KRas with GTP-bound **(B)** (PDB ID: 5USJ) shows the formation of a second pocket in (A) under the S-II region (blue) and named switch-II (S-II) pocket. Other regions highlighted include the S-I region (red).

1.3.4. Ras Mutations

The frequency of Ras mutations varies across different datasets, resulting in a lack of consensus on the real number of mutations of a particular protein. However, according to the Catalogue of Somatic Mutations in Cancer (COSMIC), RAS mutations are the most mutated oncogene in cancer, accounting for 27% of all mutations present in human cancers[99]. Additionally, based on the American Cancer Society, in 2018 approximately 1.7 million new cases of cancer were detected in the United States, with almost a fifth harbouring a Ras mutation. In 2023, more than 1.9 million new cancer cases are expected to occur[100]. Therefore, a high number of Ras-mutant cases is also expected. Consideration of the different Ras isoforms shows that KRas mutations are reported in 75% of cases, followed by NRas (17%) and HRas (7%)[99]. The position of these alterations is also an important characteristic of Ras proteins with 97-99% of mutations occurring at codons 12, 13, or 61, resulting in the possible conversion to seven other amino acids via single

base substitutions. When looking into KRas, 43% of all mutations are produced by G → A transitions at the second base of codons 12 or 13, yielding G12D or G13D mutations, followed by G → T transversion at the second base of codon 12, resulting in G12V mutations. However, a special case occurs in NSCLC where a G → T transition at the first base of codon 12 produces G12C mutations. Although not frequent, G → T substitutions are also possible, leading to G12R and G12A mutations[101].

Although not fully understood, different mutations are more frequent in some tumours than others. For instance, while KRAS^{G12C} mutations are common in NSCLC (13%), they are rare in PDAC (2%). Conversely, even though KRAS^{G12R} mutations are scarce in NSCLC and CRC (~1%), they are the third most common KRAS mutation in PDAC (Figure 7)[102,103].

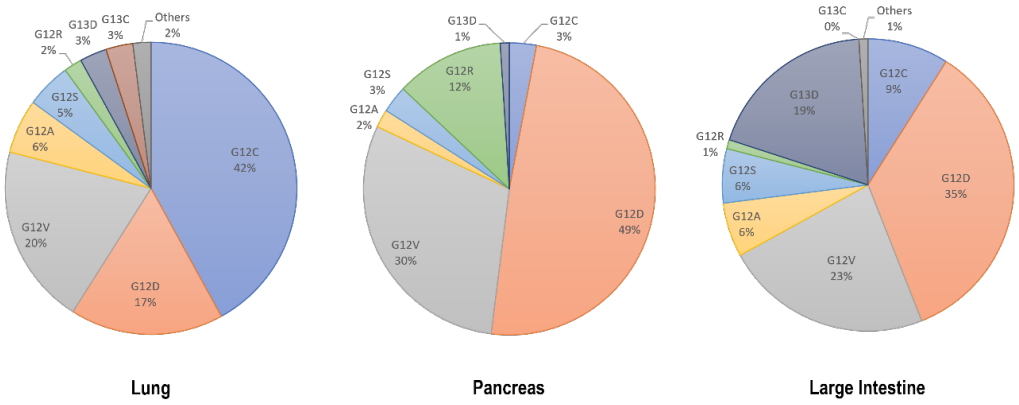


Figure 1.7 – Common KRAS substitutions in lung, pancreas and large intestine tumours.

Similar to the frequency of Ras mutations, the rate of mutant-Ras isoforms in different tumours is also not uniform. There is a general understanding that KRas mutations are most common in the pancreas, with reported frequencies between 75-95%. KRas mutations are less common in bowel (30-50%) and lung cancer (20-40%).

a

Cancer tissue	Frequency of mutation (%)		Death rate per year
Biliary tract	23.3	*KRAS*: 20	6.6
		NRAS: 1.9	
		HRAS: 1.4	
Bowel	51.5	*KRAS*: 49.7	13.7
		NRAS: 1.6	
		HRAS: 0.2	
Cervix	17.1	*KRAS*: 13.8	2.2
		NRAS: 0.9	
		HRAS: 2.4	
Lung	20.9	*KRAS*: 20.1	38.5
		NRAS: 0.6	
		HRAS: 0.2	
Myeloid	21.4	*KRAS*: 5.5	3.2
		NRAS: 11.1	
		HRAS: 4.8	
Ovary/ Fallopian tube	15	*KRAS*: 13.9	6.7
		NRAS: 1	
		HRAS: 0.1	
Pancreas	79.2	*KRAS*: 78.7	11
		NRAS: 0.4	
		HRAS: 0.1	
Skin	18.9	*KRAS*: 1.3	2.3
		NRAS: 14.2	
		HRAS: 3.4	
Testis	19.5	*KRAS*: 14.4	0.3
		NRAS: 4.4	
		HRAS: 0.7	
Uterus	19.4	*KRAS*: 16.7	4.9
		NRAS: 2	
		HRAS: 0.7	
Vulva/vagina	16.4	*KRAS*: 8.6	0.6
		NRAS: 2.7	
		HRAS: 5.1	

b

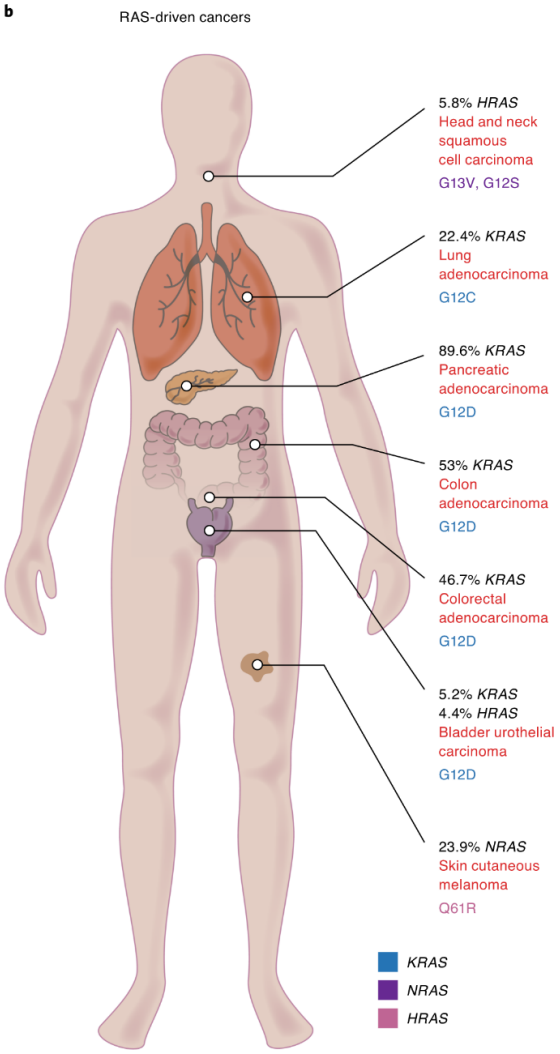


Figure 1.8 - Frequency and distribution of Ras mutations in human cancers. (A) Frequency of the different RAS isoforms across the different organs of the human body. The death rate per year (%) is based on the death rate per 100,000 men and women. **(B)** Types of tumours frequently associated with RAS mutations. For each tumour type, the described RAS isoform is the most commonly mutated RAS gene. Additionally, each site shows the most common amino acid alteration.

1.3.5. KRas Inhibitors

Since the discovery of KRas mutations and their prevalence in human cancer, intensive efforts have been made to target these proteins. Often, these are classified as direct or indirect approaches, and their classification is based on whether they target KRas or another protein that is related to Ras.

1.3.5.1. Indirect KRas Inhibitors

One of the first approaches was to look upstream of KRas. As previously mentioned, KRas activation is dependent on its association with the plasma membrane, a process that involves a series of posttranslational modifications at Ras c-terminal CAAX motifs[104]. Consequently, targeting this association looked like a logical approach for anti-Ras therapeutics. The inhibition of farnesyltransferase (FTase), an irreversible step of CAAX anchoring, was one of the first targets to be explored, and after extensive compound screening and drug design, two compounds reached clinical trials – lonafarnib and tipifarnib. However, both failed to show efficacy against KRas-driven cancers[105,106]. The explanation for this came a few years later when studies showed that in the presence of FTase inhibitors (FTIs), NRas and KRas, but not HRas, have the ability to bind to the membrane through an alternative enzyme – geranylgeranyltransferase I (GGTase I)[107,108]. As a result, new efforts were made to target this substrate, but once again without success since the only ones that reached the clinic were unacceptably toxic[109,110].

The postprenylation process was also explored to find suitable therapeutic targets. Among them, the Ras Converting CAAX Endopeptidase 1 (RCE1) and Protein-*S*-isoprenylcysteine *O*-methyltransferase (ICMT), two enzymes that are known to be involved in the prenylation of proteins to the cellular membrane appeared as favourite targets. However, scientists failed to understand if they were critical for the activation of KRas. Additionally, many drugs that were created to target RCE1 failed due to cardiac toxicity, a biological effect of *Rce1* depletion[111].

Although the initial opportunity to target upstream of KRas seemed encouraging, over time, the interest in targeting substrates associated with Ras prenylation processes started to fade. As a result, scientists started to look downstream of KRas. As previously mentioned, in its active form, KRas stimulates a series of effector proteins that result in

signals that, among others, are critical for the proliferation of cells. Thus, targeting proteins mainly from the MAPK and PI3K pathways looked like a rational approach. As a result, over the years, extensive efforts were made in this direction, resulting in the development of several kinase inhibitors.

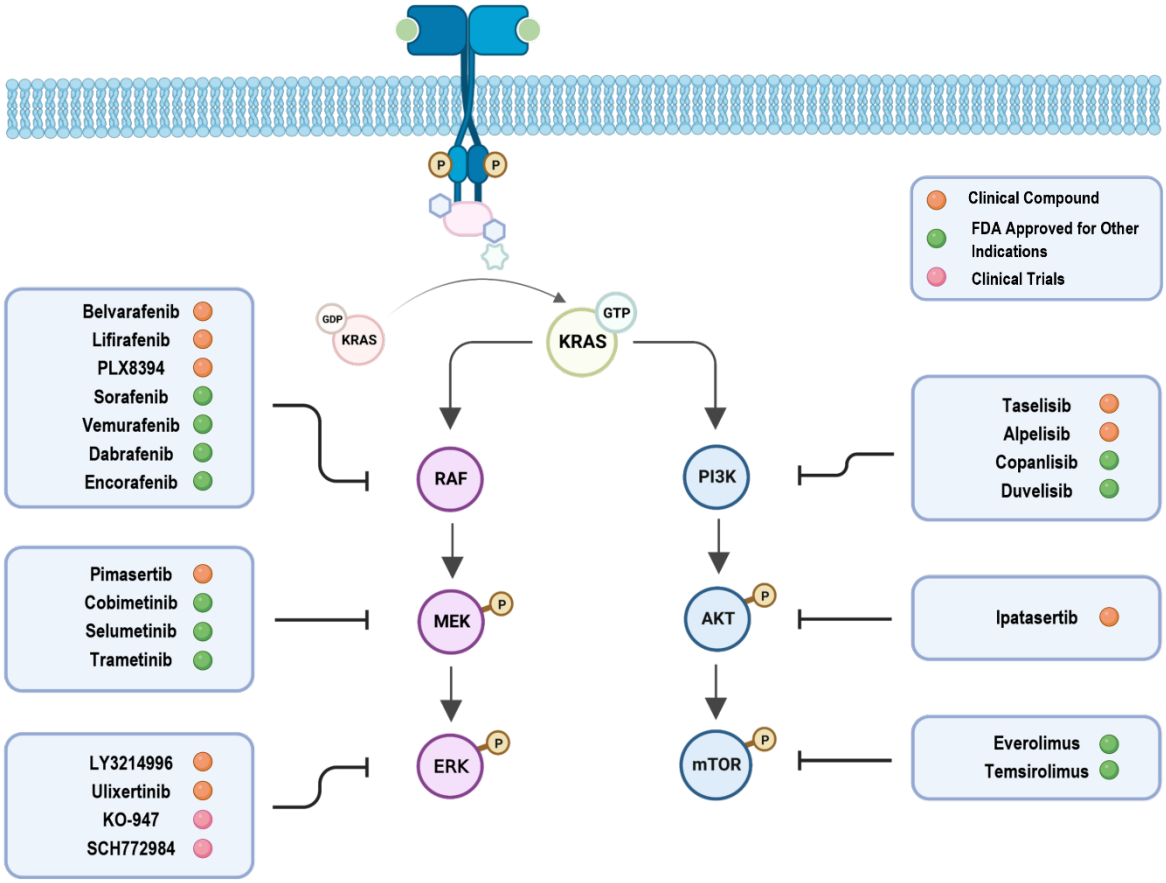


Figure 1.9 – Downstream approaches to targeting KRas. The Ras signalling pathway contains numerous targets that can be used to indirectly target KRas and thus limit its biological influence.

Even though the development of these drugs seemed encouraging, it is predictable that their therapeutic efficacy varies between different KRas-driven tumours. As an example, while RAF is essential for the development of $KRas^{G12D}$-driven NSCLC, its role in $KRas^{G12D}$-driven PDAC appears to be minimal[112–114]. Conversely, while $KRas^{G12D}$-driven PDAC is dependent on signalling via the PI3K effector, *Pdk1*, $KRas^{G12D}$-driven NSCLC is unaffected by the loss of *Pdk1*[114]. Furthermore, this therapeutic approach is often seen

as a temporary solution due to the well-known inhibitory cross-talk between the MAPK and PI3K pathways[115]. As a result, the combination of different kinase inhibitors targeting multiple signalling pathways is currently being investigated. However, dual-pathway inhibition has been shown in the past to be more toxic than single-agent therapies[116].

Overall, targeting KRas via an indirect approach has proven to be unfeasible or limited over time. Hence, a third and probably more rational approach was attempted – the direct inhibition of KRas. In fact, similar to other GTPases, the direct inhibition of KRas was probably the first tried method, but after years of experiments, no drug reached the clinic, resulting in the labelling of KRas as an "undruggable" target[117]. Over the years, the discovery of new characteristics of KRas allowed the scientific community to understand why targeting this GTPase was so challenging. Through the development of crystals, it was possible to conclude that the protein has a smooth surface, lacking binding pockets other than the GDP/GTP binding site. However, competing with these proved to be profoundly challenging due to the picomolar affinity between KRas and GDP/GTP[118].

1.3.5.2. Direct KRas Inhibitors

In 2013, the direct inhibition of KRas became a possibility when Shokat and colleagues reported that when bound to GDP, KRas undergoes a conformational change that results in the formation of an allosteric binding pocket behind the SW-II region – the switch-II pocket (S-IIP)[98,119,120]. The same article reported the development of small molecules that could irreversibly and specifically bind to $KRas^{G12C}$ by targeting the S-II region, favouring GDP binding over GTP. Targeting the S-IIP also resulted in a decrease in interactions with effector and regulatory proteins, lower cell viability and increased apoptosis. This breakthrough discovery led to a race to develop small-molecule drugs that could target the S-IIP, including ARS-853 and ARS-1620[119,120].

Molecules that target the S-IIP of KRas share an acrylamide moiety in their structure, a critical but not unique characteristic for the inhibition of KRAS. Equally, the type of KRAS mutation is crucial for the outcome of the biological response since this class of molecules is only effective against *KRAS p.G12C*. Historically, cysteine residues are desirable targets for drug discovery due to their intrinsic reactive nature. Thus, this approach exploits the reaction between the cysteine residue present at codon 12 in *KRAS p.G12C* and the acrylamide tag that exists in this class of molecules, resulting in the formation of an irreversible covalent bond that blocks the conversion of GDP to GTP[98]. Ultimately, this impedes KRas from becoming active.

The discovery provided by Shokat and colleagues revealed it to be a game-changer in the race against the direct inhibition of KRas, resulting for the first time in drugs reaching advanced stages of clinical trials.

One of these drugs, developed by Amgen, is AMG 510[121,122]. In their original article, Canon and colleagues reported for the first time the efficacy of a $KRas^{G12C}$ direct inhibitor in an immune-competent murine cancer model developed from the murine CT-26 CRC cell line using CRISPR technology to replace both *KRAS p.G12D* alleles with *p.G12C*. In 2021, the FDA granted accelerated approval for AMG 510, clinically called Sotorasib. This approval, based on a study involving 126 people with $KRAS^{G12C}$-mutant NSCLC, reported complete tumour disappearance in 4 patients and partial shrinkage in 42 people, whereas 54 patients had stable disease. Although the approval of the first KRas-direct inhibitor was a historic milestone, participants had a median of only 6.8 months of progression-free survival, a worse outcome than for other targeted therapies for NSCLC.

Alongside AMG 510, Mirati Therapeutics Inc. reported the development of another promising $KRAS^{G12C}$ inhibitor, MRTX849[123]. In 2022, the FDA granted accelerated

approval to MRTX849, clinically known as Adagrasib, for the treatment of NSCLC, thus becoming the second $KRas^{G12C}$ inhibitor available in the clinic. Similar to Sotorasib, Adagrasib also shows an insufficient progression-free survival median of only 6.5 months.

Although progress has been made over the last few years in the direct inhibition of KRas, it is fair to say that the job is far from being done. Not only do these drugs only cover a fraction of KRAS mutations, but the response seems to be limited.

Shortly after the FDA granted accelerated approval of Sotorasib, the New England Journal of Medicine (NEJM) released an article about the acquired resistance to $KRas^{G12C}$ inhibitors[124]. In this study, including 38 patients with acquired resistance to Sotorasib, the authors were able to hypothesize, based on DNA sequencing of tumour-biopsy samples or ctDNA, mechanisms of resistance for 17 patients (45%). Surprisingly, along with other categories, Awad and colleagues reported the occurrence of new secondary KRas mutations, including G12D/R/V/W, G13D and Q61H. The activation of the RTK-RAS signalling pathway by other oncogenes and histologic transformation from lung adenocarcinoma to squamous-cell carcinoma were also detected.

Despite the exciting clinical benefits, it is predictable that most patients will develop acquired resistance to these drugs. Yet, KRas inhibitors are a recent class of drugs whose resistance mechanisms were never before studied. As a result, despite valuable initial insights, additional studies are needed to consolidate the knowledge regarding the underlying mechanisms behind the acquired resistance of $KRas^{G12C}$ inhibitors.

Nevertheless, the last decade saw an important improvement in the development of new therapies, not only for $KRas^{G12C}$-mutant tumours but also for other mutations. Recently, Mirati Therapeutics Inc. reported, for the first time, the synthesis of a small molecule that

interacts with $KRAS^{G12D}$-mutant models with picomolar affinity[125]. Besides classical targeting approaches, other technologies are being investigated, including using siRNA, PROTACs, and immune cell therapy. Table 1.4 describes a summary of some KRAS targeting strategies currently in preclinical or clinical studies.

Table 1.4 - Selected KRas-directed therapies

Target	Agent	Phase of Development
Mutant-Specific KRas Inhibitors		
$KRAS^{G12C}$	Sotorosib (AMG 510)	Approved. Multiple Clinical Trials Ongoing (NCT04380753, NCT04625647, NCT05180422, NCT04303780, NCT05398094, NCT04933695, NCT05638295, NCT03600883, NCT04667234, NCT05074810, NCT05054725, NCT05273047, NCT05198934, NCT05451056, NCT05118854, NCT05347797).
	Adagrasib (MRTX849)	Approved. Multiple Clinical Trials Ongoing (NCT05263986, NCT05634525, NCT05722327, NCT05162443, NCT04685135, NCT04613596, NCT03785249, NCT04330664, NCT04793958, NCT05178888, NCT05472623, NCT05578092).
	JAB-21822	Multiple Clinical Trials Ongoing (NCT05009329, NCT05194995, NCT05002270, NCT05276726, NCT05288205).
	D-1553	Multiple Clinical Trials Ongoing (NCT05383898, NCT05492045, NCT04585035, NCT05379946).
	JDQ443	Multiple Clinical Trials Ongoing (NCT05132075, NCT05445843, NCT05358249, NCT04699188).
	GDC-6036	Multiple Clinical Trials Ongoing (NCT04449874, NCT04929223 NCT03178552).
	LY3537982	Clinical Trials (NCT04956640).
	BI1823911	Clinical Trials (NCT04973163).
	MK-1084	Clinical Trials (NCT0506723).

Target	Agent	Phase of Development
Mutant-Specific KRAS Inhibitors		
$KRAS^{G12D}$	MRTX1133	Clinical Trials (NCT05737706).
	JAB-22000	Preclinical Studies.
	RM-036	Preclinical Studies.
$KRAS^{G12V}$	JAB-23000	Preclinical Studies.
$KRAS^{G13C}$	RCM-8839	Preclinical Studies.
$KRAS^{MULTI}$	JAB-23400	Preclinical Studies.
Pan-RAS Inhibitors		
RAS^{MULTI}	RMC-6236	Clinical Trials (NCT05379985).
RAS^{MULTI}	BBP-454	Preclinical Studies.
KRAS	Pan-KRASi	Preclinical Studies.
RAS Degraders		
$KRAS^{G12C}$	LC-2	Preclinical Studies.
$KRAS^{MULTI}$	K27-SPOP	Preclinical Studies.
Immune Cell Therapy		
$KRAS^{G12V}$	T-Cell Receptor	Clinical Trials (NCT04146298).
$KRAS^{G12D}$	T-Cell Receptor	Preclinical Studies.
Cancer Vaccines		
$KRAS^{G12D}$ $KRAS^{G12R}$	ELI-002 2P	Multiple Clinical Trials Ongoing (NCT04853017, NCT05726864)
$KRAS^{MULTI}$	mRNA-5671/V941	Clinical Trials (NCT03948763).
$KRAS^{MULTI}$	KRAS Long Peptide	Clinical Trials (NCT04117087).
$KRAS^{MULTI}$	mDC3/8-KRAS	Clinical Trials (NCT03592888).
KRAS siRNA		
$KRAS^{G12D}$ mRNA	iExosomes	Clinical Trials (NCT03608631).

1.4. Tumour Microenvironment

1.4.1. Introduction

While previous chapters were focused on the intrinsic biologic side of cancer development, other factors, such as the tumour microenvironment (TME), highly influence their growth, invasion, and metastasis[126–128]. In fact, together with the genetic/ epigenetic modifications that cells undergo, the rearrangement of the components of TME comprises the overall process of tumour formation and progression.

The TME is a highly dynamic and complex system that is composed of different components that are often represented in the hallmarks of cancer, including blood vessels, the tumour stroma, inflammatory cells, immune cells, and others[129].

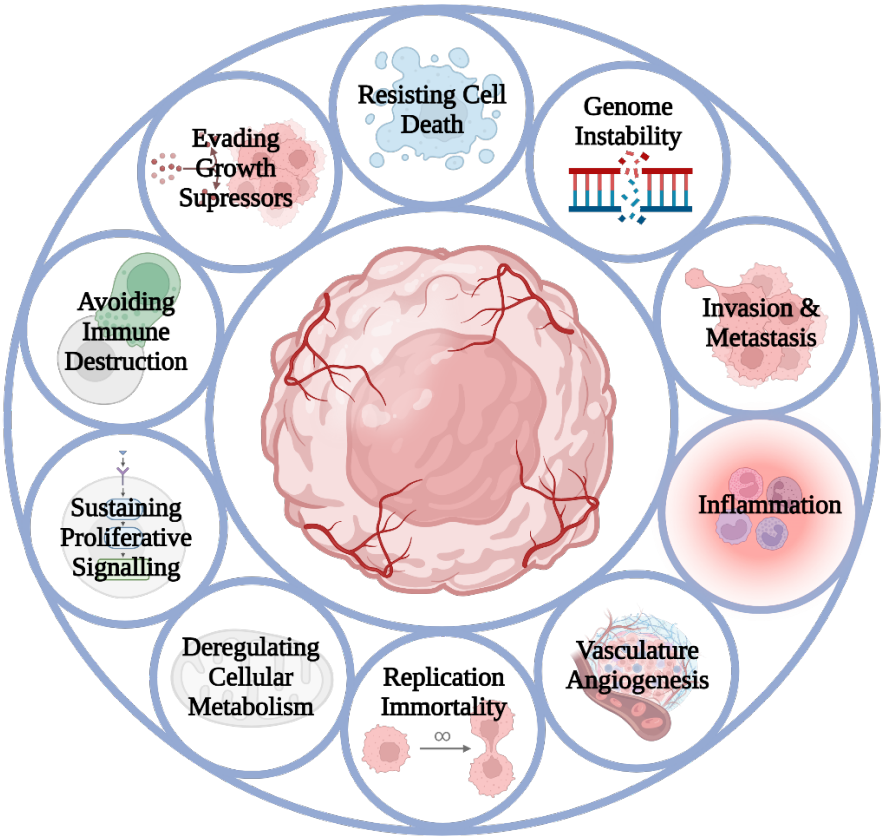


Figure 1.10 - The hallmarks of cancer.

1.4.2. Effect of KRas Mutations in the Tumour Microenvironment

Although the study of TME dates back to 1863 when Virchow proposed the relationship between inflammation and cancer, the study of links between KRas and components of TME was rare[130]. However, over the past few years, there has been an increased interest in this theme, with growing evidence that certain genetic changes influence the immune environment of cancer.

In the presence of KRas mutations, the TME is inflammatory and infiltrated with several immune cells that are facilitated by various cytokines and chemokines, including interleukin-6 (IL-6) and interleukin-8 (IL-8)[131–133]. In PDAC, besides promoting tumour progression, IL-6 also promotes the synthesis of reactive oxygen species through the ERK pathway[134]. Similarly, IL-8 plays an important role in the inflammatory process of the TME as a C-X-C motif chemokine receptor 2 (CXCR2) ligand. Through the MAPK and PI3K pathways, KRas induces the activation of IL-8, leading to the promotion of tumour angiogenesis, inflammation, and the recruitment of endothelial cells[135,136]. In addition, the presence of KRAS mutations in pancreatic cells leads to the upregulation of intercellular adhesion molecule 1 (ICAM-1), thus inducing macrophage polarization[137]. Ultimately, this contributes to an inflammatory environment.

While inflammation is a key aspect of tumour progression, other factors highly contribute to this outcome (Figure 1.10). When looking at KRas, studies show that KRas-driven tumours mainly evade the immune system by upregulating the expression of PD-L1 cells[138].

KRas-induced PD-L1 expression results from the Ras-MEK signalling pathway, where MEK phosphorylates tristerrolin (TTP), impeding TTP binding to AU-rich elements in the *PD-L1* mRNA 3'UTR, and thus blocking the possibility of PD-L1 degradation[139].

Hence, TTP phosphorylation by MEK promotes the stability of mRNA *PD-L1*. More recently, Glorieux and colleagues suggested an alternative method of PD-L1 expression in $KRas^{G12V}$ mutations through a redox-mediated process by the generation of reactive oxygen species (ROS) and FGFR1 expression[140]. In specific CRC models, studies associate the role of KRas in evading the immune system by downregulating the expression of molecules from the major histocompatibility complex (MHC) class I, a set of cell-surface receptors that are critical for antigen presentation and antigen recognition by T cells. As a result, the downregulation of MHC class I leads to the mitigation of specific T cells, including cytotoxic $CD8^+$ T cells[141].

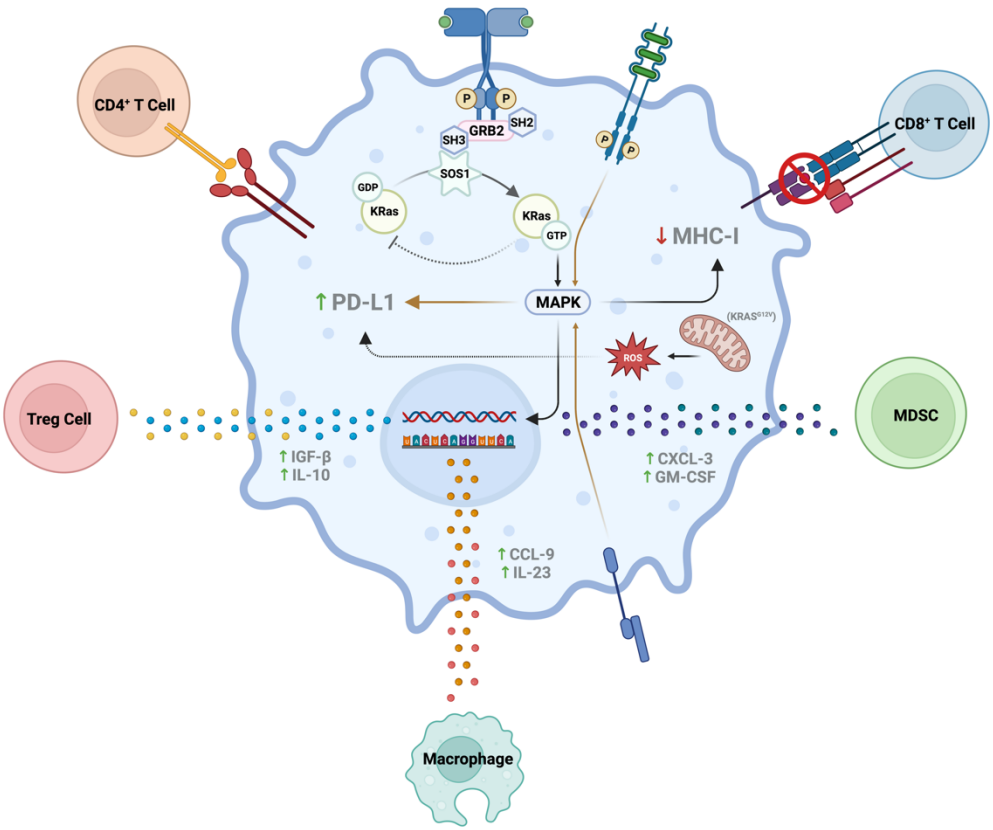


Figure 1.11 - KRas-mediated immune escape in the tumour microenvironment. KRas mediates immune escape in the tumour microenvironment by upregulating PD-L1 expression, downregulating MHC-I expression and stimulating the secretion of cytokines and chemokines that promote tumour evasion. Treg cell: regulatory T cells; MDSC: myeloid-derived suppressor cells; IL-10: interleukin-10; IL-23: interleukin-23; TGF-β: transforming growth factor-β; GM-SCF: granulocyte-macrophage colony stimulating factor; CXCL-3: chemokine (C-X-C motif) ligand 3.

The development of $KRas^{G12C}$ inhibitors opened a new subset of research by studying the immunogenic response resulting from the inhibition of KRas. In a recent study, Zhang and colleagues reported that the treatment of $KRas^{G12C}$-bearing cell lines with ARS-1620 resulted in the formation of ARS-1620-modified peptides that could act as haptens to generate specific MHC-I restricted neoantigens[142]. Hence causing the production of cytotoxic T-cell responses against $KRAS^{G12C}$ cells.

Besides affecting tumour cells, KRAS mutations can also influence the role of immune cells involved in the immune evasion of the TME. In CRC models, KRas mutations promote the secretion of interleukin-10 (IL-10) and tumour growth factor-β1 (TGF-β1) via the MAPK signalling pathway, resulting in the production of immunosuppressive Treg cells by $CD4^+$ T cells[143]. In PDAC, $KRas^{G12D}$ mutations upregulate the production of granulocyte-macrophage colony-stimulating factor (GM-CSF), a cytokine that promotes the development of myeloid-derived suppressor cells (MDSC)[144]. Additionally, $KRas^{G12D}$ mutations also promote the release of CXCL3, thus leading to the migration of MDSC to the TME[145]. Overall, MDSCs act as potent immune suppressive agents.

1.5. Radiation and Targeted Therapies

1.5.1. Introduction

DNA is constantly being damaged during normal cellular processes. Yet, cells have intrinsic processes to repair these errors, including cell cycle checkpoints and DNA repair mechanisms. Naturally, these are powerful tools to avoid the formation of mutations that can lead to the development of genetic disorders. However, in special cases, the development of unrepairable cell damage is extremely beneficial. As a result, the use of targeted therapies to induce DNA damage in tumour cells is a key approach and is the foundation of radiotherapy.

1.5.2. Radiation-induced DNA Damage

Radiation can be administered to cells either in the form of photons, through x-rays and γ-rays, or particles, *via* protons, neutrons, and electrons. The interaction with cells results in the absorbance of energy by DNA, promoting its ionization. Additionally, radiation can interact with water, the major constituent of cells, generating free radicals that equally induce DNA ionization[146].

Ionizing radiation-induced DNA damage promotes replication errors that can be repaired through multiple cell cycle checkpoints. Generally, these events occur in three stages of the cell cycle, including at the border between the G1 phase and S phase, the intra-S phase, and the border between the G2 phase and mitosis. At this level, ataxia-telangiectasia mutated (ATM), a serine/threonine kinase, plays a fundamental role in inducing these cell cycle checkpoints[147]. For instance, the replication of cells with damaged DNA in the G1 phase is arrested at the G1/S interface through ATM-dependent activation of p53 and p21. Similarly, DNA-damaged cells at the S phase are arrested by the activation of checkpoint kinase (CHK) 2, leading to the inhibition of CDK2, whereas DNA-damaged cells at the G2 phase are prevented from entering mitosis by the activation of CHK1, and consequently, inhibition of CDK1[148].

Ionizing radiation causes, among others, DNA single-strand (SS) and double-strand breaks (DSB), where the latter is the main event that leads to cell inactivation and cell killing[149]. However, similar to cell cycle checkpoints, DNA also has intrinsic mechanisms of repair. One of the first events that occur in response to DNA double-strand breaks is the ATM-mediated phosphorylation of H2AX to become γ-H2AX, forming multiprotein complexes, known as *foci*, that promote the recruitment of additional ATM molecules and other repair factors[150]. In eukaryotic cells, DNA double-strand breaks are repaired by two processes – homologous recombination repair (HRR), which requires an undamaged

DNA strand and non-homologous end joining (NHEJ), which mediates end-to-end joining[151]. In mammalian cells, the mechanism by which damaged DNA is repaired is dependent on the phase of the cell cycle. Whilst HRR is primarily used in the late S/G2 phase, in the G1 phase, NHEJ is the preferred mechanism of DNA repair[152].

1.5.3. Radiosensitising Agents

Since its discovery in the late 19th century, external beam radiation therapy (EBRT) has become a hallmark of oncology treatment[153]. According to NIH, close to 50% of patients receive radiation therapy at some point during their treatment plan. Due to its clinical importance, over the years, efforts have been made to increase the efficacy of the treatment whilst reducing its side effects[154]. These include improvements in dose delivery, allowing more precisely the delivery of high-dose radiation in tumours with reduced injury on healthy tissues, and the development of radiosensitiser agents.

At this level, several classes of chemotherapeutic agents are used as radiosensitisers, including antimetabolites, platin-derived chemicals, and other molecular targeted agents. 5-Fluorouracil (5-FU) is one of the most common antimetabolite drugs used as a radiation sensitiser. Initially discovered in the 1950s, the combination of 5-FU with radiation has led to several clinical improvements, including in head and neck, breast, and colorectal cancers[155–157]. The ability of 5-FU to radiosensitise cells is related to its ability to inhibit thymidylate synthase, leading to the depletion of deoxythymidine triphosphate (dTTP) and consequently altering the synthesis of DNA[158]. Gemcitabine is another well-known antimetabolite with radiosensitising properties. Primarily used as a first-line treatment for PDAC, gemcitabine influences the depletion of deoxyadenosine triphosphate (dATP), a nucleotide used in cells for DNA synthesis, as well as the redistribution of cells into the early S phase[159,160].

Cisplatin is likely the most commonly used chemotherapeutic drug in combination with radiation. Initially synthesised in 1844 by M. Peyrone, cisplatin only garnered the attention of the scientific community in the 1960s when Rosenberg and colleagues discovered that in the presence of certain transition metal compounds, the cell division of *Escherichia Coli* was severely affected[161]. Alongside being used in PDAC, cisplatin and other platin-derived agents, such as carboplatin, are heavily used in other malignancies, including leukaemia, lymphomas, breast, testicular, ovarian, head and neck, and cervical cancers[162]. The ability of cisplatin to radiosensitise cancer cells is related to its capacity to cause inter- and intrastrand DNA cross-links, altering the DNA structure and thereby inhibiting its replication and transcription[163]. Additionally, cisplatin appears to interfere with the mechanisms of DNA repair resulting from the radiation-induced DNA double-strand breaks[164].

Despite its clinical benefits, the use of conventional chemotherapeutic agents is often associated with high levels of toxicity[165]. Alternatively, molecularly targeted agents are a viable option due to their low toxicity and high specificity. At this level, the EGFR has been intensely pursued as a target, resulting in the development of erlotinib and cetuximab[166–169]. Despite its use in PDAC and NSCLC, combining radiotherapy with EGFR inhibitors is more beneficial in head and neck cancers[170,171]. Similarly, targeting the response to DNA damage also results in the radiosensitisation of cancer cells. The inhibition of WEE1, a kinase involved in the G2-M cell-cycle checkpoint, in combination with radiation, resulted in decreased tumour growth, both in xenografts and in patient-derived xenografts (PDXs)[172–174]. Concomitantly, the inhibition of proteins activated by KRas leads to the radiosensitisation of cancer cells. In a study conducted by Fokas and colleagues, the dual inhibition of the PI3K/mTOR pathway increased the tumour radiosensitivity through the vascular normalisation of blood vessels[175].

1.5.4. Antibody-based Therapies

Considered by many the "Holy Grail" of cancer therapy, the interest in the development of immunotherapy agents has risen over the past few years. Since the development of the hybridoma technique to produce monoclonal antibodies (mAbs) by Köhler and Milstein in 1975, the FDA approved more than 100 mAbs for treating different human diseases, including cancer and autoimmune diseases[176,177].

Between several advantages, using macromolecules, such as mAbs, offers high specificities and long half-lives, resulting in higher approval rates than new chemical entities[178–180]. As an example, the development of trastuzumab, a mAb used in patients with human epidermal growth factor receptor 2 (HER2)-positive, dramatically improved the outcomes of early breast cancer patients by reducing the risk of mortality by more than 30%[181].

Besides generic antibodies, other immune molecules were developed to present higher specificities but also better pharmacokinetics and pharmacodynamics properties[182]. These include antibody-derived structures such as scFv and Fab fragments, diabodies, VHH domains and others. However, in recent years, the advancement of *in vitro* technologies, namely phage display and ribosome display, allowed the development of specific binders other than immunoglobulins. Designed ankyrin repeat proteins (DARPins), derived from one of the most common binding proteins in the human genome, are a class of small and single domain proteins[183]. Composed of a varying number of ankyrin motifs (repeats), they can be engineered to interact with any given target with high specificity and affinity[184]. Additionally, they can be used to carry various effector functions, making them powerful prospective drug candidates[185]. Despite its potential, to this date, no DARPin has been approved by any governmental agency, with the FDA rejecting the

approval of a DARPin for age-related macular degeneration (AMD) after 15% of the volunteers exhibited intraocular inflammation[186].

The development of targeted therapies based on immunotherapy agents revolutionized the treatment of several malignancies, resulting in a viable alternative to the classical drug discovery process. As previously mentioned, KRas inhibition has proven difficult to achieve with small molecules due to its lack of targetable pockets and high affinity towards GDP/GTP[187]. Yet, during the last decade, several immunotherapy agents were developed to target mutant KRas, resulting in the synthesis of antibody fragments and DARPins with high specificity and affinity[188,189]. However, while the use of antibody-based agents against extracellular targets is feasible, its use against intracellular targets is limited due to the inability to cross cell membranes, therefore restricting the applicability of this approach to a small number of cancer-associated antigens[190].

1.6. Cell-Penetrating Peptides

1.6.1. Introduction

The hydrophobic nature of cell membranes hinders cells from internalising exogenous bioactive molecules, such as peptides, proteins, and oligonucleotides. In addition, based on the permeability of cell membranes, compounds with molecular weights above 1000 Da experience a steep drop-off in membrane penetrance, limiting the intracellular delivery of macromolecules[191]. To tackle this problem, over the years, several strategies have been developed, including microinjection and electroporation[192,193]. However, these have been proven ineffective due to their low efficiency, high toxicity, poor specificity and lack of in vivo translatability. Alternatively, another strategy arose unexpectedly in 1988, with the discovery of the HIV TAT transactivating factor, and in 1994, with the finding of the *Drosophila* Antennapedia transcription factor[194–196]. In these studies, scientists noticed the ability of these constructs to transfer across the cell membrane, with

further evidence suggesting that only a short sequence taken from these proteins was needed to exert membrane-penetrating properties. The discovery of these two peptides, later named TAT and Penetratin, would become the foundation for the development of a new class of intracellular carriers – cell-penetrating peptides (CPPs).

1.6.2. Classes of Cell-Penetrating Peptides

CPPs are often classified based on their charge and hydrophobicity, which are directly related to their cell penetration mechanisms. As a result, CPPs are divided into three main categories – positively charged, negatively charged, and amphipathic.

1.6.2.1. Positively-charged Cell-Penetrating Peptides

This includes CPPs that, at physiological conditions, carry an overall positive charge and involve the majority of CPP sequences. This class of CPPs takes advantage of positively charged amino acids to interact with the negatively charged heparin sulfate proteoglycans (HSPGs) present in the plasma membrane[197]. Additionally, the electrostatic interaction between CPPs and elements of the cell membrane induces the uptake of these peptides via endocytosis or direct membrane penetration[198].

The efficacy of CPPs is highly dependent on their amino acid sequence. For this class of CPPs, lysine (Lys, K) and arginine (Arg, R) residues are often used due to their pK_a value at physiological pH conditions – 10.3 and 12.5, respectively. However, despite both having positively charged side chains, some amino acids present better physicochemical characteristics than others. While Arg residues have a guanidinium group in the side chain, Lys residues contain an ammonium group. As a result, Arg residues have stronger electrostatic interactions with the phosphate group of phospholipids than Lys residues due to the stronger bidentate bonds that the guanidinium moiety allows[199]. Moreover, Arg-based CPPs also present stronger interactions with negatively charged membrane-associated carbohydrates than Lys residues[200].

The length of CPPs can also influence their uptake into cells[201]. Based on the analysis of arginine-rich peptides of different lengths (4-16), Nakase and colleagues demonstrated that R4 peptides showed little internalization compared to R6 and R8 peptides[202]. However, the continuous addition of amino acids leads to a prejudicial overall effect due to increased cell cytotoxicity[203].

1.6.2.2. Negatively-charged Cell-Penetrating Peptides

Based on the negatively charged nature of cell membranes, the use of positively charged CPPs is thermodynamically more favourable than negatively charged CPPs. As a result, the use of negatively charged CPPs often leads to electrostatic repulsions, with additional energy needed for CPPs to enter.

Despite the challenges, some negatively charged peptides are capable of crossing the cell membrane and are thus classified as CPPs. For instance, the azurin-derived CPP p28 has been shown to penetrate cells in an energy-dependent manner[204]. Additionally, p28 possesses anticancer activity since it mitigates the proteasomal degradation of p53, thus inhibiting the growth of cancer cells[205]. Lastly, p28 also has an anti-angiogenic action by inhibiting the phosphorylation of VEGFR-2, FAK, and AKT[206].

The sweet arrow peptide (SAP) derivative, SAP(E), is another example of a negatively charged CPP. Based on the proline-rich SAP CPP, Martín and colleagues substituted three Arg amino acids with negatively-charged glutamic acid (Glu, E) residues, resulting in retained cell-penetrating activity of similar efficiency[207]. Although some groups attempted to study the entry mechanism of SAP(E), its interaction with cell membranes is not yet fully understood. However, a report from Franz and colleagues suggests that SAP(E) suffers structural modifications at membrane interfaces, either by refolding or self-association. Additionally, the authors also show that the interaction between SAP(E) and components of the cell membrane is limited.

1.6.2.3. Amphipathic Cell-Penetrating Peptides

Similar to negatively charged CPPs, amphipathic CPPs are also uncommon. However, in this category, it is possible to find a well-known CPP – penetratin. Composed of a total of 16 amino acids, penetratin contains seven positively charged residues and six hydrophobic amino acids, including tryptophan (Trp, W), isoleucine (Ile, I), phenylalanine (Phe, F), and methionine (Met, M). The combination of positively charged residues and hydrophobic amino acids results in an amphipathic CPP.

The design of amphipathic CPPs, such as MPG or VT5, often includes the separation of cationic and hydrophobic sequences to increase their cellular uptake. Similar to positively charged CPPs, the cationic residues interact with negatively charged components of the plasma membrane, while the hydrophobic sequences interact with hydrophobic lipid tails, inducing the reorganization of membranes[208].

The use of intermingled cationic and hydrophobic sequences is an additional strategy for the synthesis of amphipathic CPPs. In this scenario, CPPs suffer structural modifications upon exposure to cell membranes[209]. The model amphipathic peptide (MAP) falls into this category through the incorporation of repeated sequences of lysine-leucine-alanine (Lys-Leu-Ala, or K-L-A) amino acids[210]. Upon interaction with the membrane, MAP forms an α-helix composed of positively charged Lys residues and hydrophobic Leu amino acids, inducing cell uptake through the lipid layer.

The use of hydrophobic amino acids can be used as an alternative approach for the synthesis of CPPs, whose mechanism lies in the interaction with hydrophobic moieties of cell membranes. Often, the insertion of amino acids with aromatic side chains is used to increase lipid affinity[211]. In fact, it is thought that the use of tryptophan (Trp, W) amino acids enhances cellular uptake of amphipathic CPPs by interacting with cell-surface-

exposed glycosaminoglycans (GAGs), a polysaccharide involved in the endocytic uptake of CPPs[212]. Nevertheless, the design of amphipathic CPPs involves a cautious addition of hydrophobic amino acids since its insertion inevitably reduces the aqueous solubility and increases cytotoxicity[213].

1.6.3. Cellular Uptake Mechanisms

Although various mechanisms have been suggested for the cellular uptake of CPPs, they are still not fully understood. However, these are normally categorized as energy-dependent and energy-independent mechanisms.

1.6.3.1. Energy-dependent Mechanisms

Most reported CPPs enter cells via endocytosis, a process involving ATP to form vesicular structures called endosomes[214]. Several forms of endocytosis have been described, including phagocytosis, macropinocytosis, clathrin-mediated and caveolae/ lipid raft-mediated endocytosis[215].

Phagocytosis typically takes place in scavenger cells, such as macrophages and dendritic cells, and is responsible for engulfing particles more than 0.5 μm in size through vesicles called phagosomes[216]. Although a critical tool of the innate immune system, phagosomes are not the main uptake pathway of CPPs since these are used to maintain the homeostasis of cells by deleting microorganisms, apoptotic cells, and cell debris[217,218].

In non-phagocytic cells, other endocytic pathways are used, including macropinocytosis. In these cases, particles are surrounded by an extended plasma membrane and internalized through macropinosomes[219]. Additionally, macropinocytosis is often stimulated through external factors that trigger the activation of receptor tyrosine kinases (RTKs), leading to the promotion of signalling cascades controlled by GTPases such as RAS. Activation of the RAS signalling pathway *via* PI3K induces changes in the dynamics of actin filaments and ultimately disturbs the plasma membrane[220]. In special circumstances, including the

atypical *KRAS p.G12R*, the basal level of proteins involved in the PI3K signalling pathway is downregulated due to structural disruptions in the SII region of KRAS, resulting in impaired macropinocytosis events[221].

Other well-known internalization mechanisms involve clathrin-mediated and caveolae/ lipid-raft-mediated endocytosis. Although initially described over five decades ago, the mechanisms of clathrin-mediated endocytosis are still a hot topic of research, with more than 50 other cytosolic proteins known to be involved in the formation of clathrin-coated endocytic vesicles[222–224]. Similarly, caveolae/ lipid raft endocytosis, also known as a clathrin-independent endocytic process, is a well-studied mechanism of internalization of macromolecules and involves the invagination of glycolipid rafts in a cholesterol-dependent manner. Clathrin-coated endosomes are larger, with sizes ranging from 50-150 nm in diameter, whereas caveolin-coated endosomes range from 50-80 nm[225]. Additionally, endocytosis through clathrins occurs more often than caveolae-mediated endocytosis since the latter occurs in lipid rafts, a specialized part of the cellular membrane[226].

Besides these, evidence shows that CPPs can induce endocytosis without a specific ligand. As an example, the heparan sulfate proteoglycan receptor (HSPG), a type of glycoprotein found in the extracellular matrix of cells, presents a global negative charge structure due to the sulfated and carboxylated repeats of glucuronic acid and *N*-acetylglucosamine[227]. As a result, these can interact with positively charged CPPs, inducing their endocytosis[228].

Following endosome formation, macromolecules, including CPPs and antibodies, face a critical step in their release into the cytosol – to escape endosomal entrapment. Due to the ATP-driven proton pump present in the endosomal membrane, endosomes experience

a decrease in their pH[229]. Additionally, the acidified endosomes fuse with lysosomes, resulting in the degradation of macromolecules[230]. Some CPPs, such as R_8 and K_8, have intrinsic endosomal escape activity through destabilisation of the endosomal membrane, whereas others, including some amphipathic CPPs, remain trapped in these vesicles[231,232]. To overcome this problem, the use of endosomal acidifier inhibitors, such as chloroquine (CQ), is often employed due to its role as a proton sponge. Consequently, this results in an increase in the osmotic pressure, leading to disruption of the endosomal membrane[233].

1.6.3.2. Energy-independent Mechanisms

ATP is critical to support the different stages of the endocytic process. However, on some occasions, CPPs can directly transfect the cellular membrane by interacting with the phospholipid bilayers and disrupting their integrity. To support this thesis, three energy-independent mechanisms have been proposed, including the inverted micelle model, the pore formation model, and the carpet model.

Arg-rich peptides, such as TAT, use their positively charged motifs to interact with the negatively charged moieties of the cell membrane, creating guanidine-phosphate interactions. These interactions result in the formation of an inverted micelle, allowing the encapsulation of Arg-rich CPPs into cells[234]. Additionally, the interaction with the membrane destabilises and permeabilises the planar phospholipid bilayer, resulting in the formation of pores, allowing TAT to enter cells by diffusion[235,236]. Other CPPs, such as TP10, create a parallel carpet-like deposition on the membrane, softening the lipidic bilayer and permitting the transfection of CPPs[237].

Most CPPs transfect cells through more than one mechanism in a process where concentration, temperature and cargo-molecule size affect the preferred mechanism of internalisation. For instance, while TAT, at low concentrations, transfects HeLa cells primarily by energy-dependent mechanisms, at higher concentrations, energy-

independent mechanisms appear to be favoured[238]. Additionally, whereas at physiological temperature, CPPs enter cells *via* both energy-dependent and energy-independent mechanisms, at low temperatures, energy-independent processes are the exclusive mechanism of transfection[239].

1.7. Research Objectives

This thesis focuses on a new approach to target KRas-mutant PDAC cells by combining engineered anti-KRas antibodies with a novel TAT-derived cell-penetrating peptide – Tri-cTAT B. The main goals of this work were to investigate the use of CPPs to internalise anti-KRas antibodies into PDAC cells, to explore whether the subsequent downregulation of proteins activated by KRas results in the radiosensitisation of PDAC cells and whether this platform could be exploited for anti-PDAC radionuclide therapy. To do so, this thesis is divided into three experimental parts. **Chapter 3** focuses on the ability of Tri-cTAT B to co-deliver anti-KRas immune molecules in PDAC cells *via* live-cell confocal microscopy. For that purpose, Tri-cTAT B was conjugated with an AlexaFluor™ (AF)-488 fluorophore, whilst anti-KRas macromolecules were labelled with a mCherry fluorescence protein marker. Additionally, the uptake of anti-KRas macromolecules with Tri-cTAT B was assessed in more complex environments, including 3D cell models. Concomitantly, this part of the project studies whether the co-delivery of functional anti-KRas immune molecules results in its interaction with KRas. For that purpose, Proximity-Ligation Assays (PLA), following the co-delivery of an anti-$KRas^{G12D}$ antibody with Tri-cTAT B, were explored in PANC-1 cells. **Chapter 4** reports the biological consequences of the co-delivery of functional anti-KRas immunes molecules with Tri-cTAT B. To do so, the downregulation of proteins activated by KRas, including phosphorylated ERK and MEK, was assessed *via* western blot analysis. Additionally, the viability and proliferation of cells following the downregulation of KRas were explored using cell viability assays.

Chapter 5 answers the ultimate goal of this thesis by assessing if the downregulation of proteins activated by KRas results in the radiosensitisation of PDAC cells. To this end, two approaches were explored, including using EBRT or co-delivering [^{123}I]I-anti-KRas immune molecules with Tri-cTAT B. While the former was performed following the treatment of cells with Tri-cTAT B + anti-KRas macromolecules, the later explored the downregulation of proteins activated by KRas whilst radiosensitises cells, resulting in a dual-approach therapy. Following the radiolabelling of anti-KRas macromolecules with [^{123}I], **Chapter 5** further studies the uptake of radiolabelled anti-KRas immune molecules within the different organelles of cells *via* fractionation assays. Still in **Chapter 5**, the first steps were taken towards co-delivering [^{123}I]I-anti-KRas macromolecules with Tri-cTAT B *in vivo*, using PET/SPECT.

Chapter 2 Materials and Methods

2.1. Synthesis of Optimised Trimeric CPPs

2.1.1. cTAT$_3$-Alkyne

$CuSO_4$ (177 µg, 4 eq) and THPTA (2427 µg, 20 eq) were dissolved in H_2O and mixed for 5 minutes in a MW reaction vial. Tetrakis(2-propynuloxymethyl)methane (80 µg, 1 eq) and azidolysine-cyclicTAT-NH_2 (cTAT Azide (49-57)) (Cambridge Peptide, UK) (1600 µg, 4.2 eq)) were dissolved in DMSO and H_2O, respectively and allowed to react for 5 minutes. The solution containing the mixture of cTAT Azide and Tetrakis(2-propynuloxymethyl)methane was added to the MW reaction vial, together with sodium ascorbate (442 µg, 8 eq) and aminoguanidine hydrochloride (370 µg, 12 eq). After vortexing, the resulting solution was dissolved in 30% DMSO/PBS and heated at 70 °C for 20 minutes in a MW reactor. The resulting mixture was purified by HPLC. HPLC Retention Time R_t = 5.22 minutes; MS QTOF [ES^+]: 5100.32 (MW calculated: 5100.14 for $C_{209}H_{386}N_{108}O_{43}$).

2.1.2. Tri-cTAT B – Alexa Fluor™ 488

cTAT$_3$-Alkyne (1 mg, 1 eq) and Alexa Fluor™ 488 5-Carboxamido Azidohexanyl), Bis(Triethylammonium Salt), 5-isomer (AF488-Azide) (Thermo Fischer Scientific) (337 µg, 2 eq) were dissolved in H_2O and allowed to react for 5 minutes. $CuSO_4$ (31 µg, 1 eq) and THPTA (49 µg, 5 eq) dissolved in H_2O were mixed for 5 minutes followed by the addition of sodium ascorbate (77 µg, 2 eq) and aminoguanidine hydrochloride (64 µg, 3 eq). The mixture of cTAT$_3$-Alkyne and AF488 was transferred to the THPTA mixture and the resulting solution was dissolved in 30% DMSO/PBS and heated at 40 °C for 1 h. The product was purified by HPLC. HPLC Retention Time R_t = 5.23 minutes; MS QTOF [ES^+]: 5759.09 (MW calculated: 5758.79 for $C_{236}H_{412}N_{114}O_{53}S_2$).

2.2. Cell Culture

2.2.1. 2D Cell Culture

PSN-1 and AsPC-1 pancreatic cell lines were a kind gift from Dr Bart Cornelissen (University of Oxford), while BxPC-3 and PANC-1 pancreatic cancer cells were purchased from ATCC. AsPC-1, PSN-1 and BxPC-3 cells were maintained in Roswell Park Memorial Institute 1620 (RPMI 1620) medium (Thermo Fischer Scientific, UK) and supplemented with 10% (v/v) fetal bovine serum (FBS) (Invitrogen, UK), and 1% (v/v) penicillin/streptomycin/ glutamine (PSG) (Invitrogen, UK). CFPAC-1 cells were grown in Iscove's Modified Dulbecco's Medium (IMDM) (Thermo Fischer Scientific, UK) and supplemented with 10% (v/v) FBS (Invitrogen, UK), and 1% (v/v) penicillin/streptomycin PSG (Invitrogen, UK). PANC-1 cells were grown in Dulbecco Modified Eagle Medium (DMEM) (Thermo Fischer Scientific, UK) and supplemented with 10% (v/v) FBS (Invitrogen, UK), and 1% (v/v) penicillin/streptomycin PSG (Invitrogen, UK). All cell lines were grown at 37 °C, 5% CO_2. When cells reached 90% confluency, they were washed in phosphate buffer saline (PBS) (37 mM NaCl; 2.7 mM KCl; 4.3 mM Na_2HPO_4; 1.47 mM KH_2PO_4; pH 7.4) and detached from the culture flask using trypsin-ethylenediaminetetraacetic acid (Trypsin-EDTA) (Thermo Fischer Scientific, UK). Detached cells were transferred to a falcon tube and centrifuged at 1000 x rpm for 5 minutes in a Heraeus™ Megafuge™ 40 centrifuge (Thermo Fischer Scientific, UK). Following the removal of the supernatant, cells were resuspended in fresh culture medium and transferred to a new flask. Cells were kept for up to 20 passages, and tested every 4 weeks for mycoplasma using a MycoAlert® testing kit (Lonza, UK), according to the manufacturer's instructions.

2.2.2. 3D Cell Culture

As for 2D cell culture, PANC-1 cells were grown in DMEM (Thermo Fischer Scientific, UK) and supplemented with 10% (v/v) FBS (Invitrogen, UK), and 1% (v/v) PSG (Invitrogen, UK). On the day of spheroid generation, cells were washed in PBS and detached from the culture flask using Trypsin-EDTA (Thermo Fischer Scientific, UK). Detached cells were transferred to a falcon tube and centrifuge at 1000 x rpm for 5 minutes in a Heraeus™ Megafuge™ 40 centrifuge (Thermo Fischer Scientific, UK). Following removal of the supernatant, cells were resuspended in 1 mL of fresh culture medium and counted using a Countess II Automated Cell Counter (Thermo Fischer Scientific, UK). Cells were seeded in different seeding densities in a Nunclon™ Sphera™ 96-Well, Nunclon Sphera-Treated, U-Shaped-Bottom Microplate (Thermo Fischer Scientific, UK) containing 200 µL of DMEM (Thermo Fischer Scientific, UK) supplemented with 10% (v/v) FBS (Invitrogen, UK), and 1% (v/v) PSG (Invitrogen, UK). Plates containing cells were centrifuged at 1500 x rpm for 10 minutes at room temperature and incubated at 37 °C, 5% CO_2. The day on which cells were seeded was counted as day 0. Cells were kept up to day 6 without any medium replacement.

2.3. Live-Cell Confocal Microscopy

Cells were seeded onto a Greiner 75/25 mm glass bottom CELLview™ cell culture slide (Greiner Bio-One, UK), allowed to adhere for 24 h and washed with serum-free medium (3x). Next, Tri-cTAT B (1-3 µM) was added to the cells in serum-free medium and incubated at 37 °C in an atmosphere of 5% CO_2. After 1 h, cells were washed with serum-supplemented medium (3x). Some experiments involved the need to internalize Tri-cTAT B in combination with cargo molecules. In these cases, Tri-cTAT B was first mixed with the cargo molecule in an Eppendorf tube and allowed to react for 15 minutes at 37 °C. Then, serum-free medium was added, and the resulting mixture was combined with pre-

washed cells. After the desired incubation period, cells were washed with serum-supplemented medium (3x). Cells were visualised under a Zeiss 880 NLO Inverted Confocal Microscope fitted with a Plan-Apochromat 63x / 1.40 Oil DIC M27 objective. Images were collected using a laser strength of 1% with gains between 400 and 600. Pinhole sizes of 0.7 µm and 0.9 µm were used for the green and red channels, respectively. Bright-field images were collected using a transmission detector and the 458 laser lines. Images were analysed using ImageJ software.

2.4. Proximity Ligation Assay

The Duolink® *In Situ* Red Starter Kit (Sigma Aldrich, UK) was used with mouse/rabbit secondary detection antibodies. The protocol recommended by the manufacturer was followed . Briefly, PANC-1 cells were seeded at a density of $20x10^3$ cells in Greiner 75/25 mm glass bottom CELLview™ cell culture slides (Greiner Bio-One, UK) and allowed to adhere overnight. Cells were treated with AF488-conjugated Tri-cTAT B (1 µM) + AF647-labelled anti-$KRas^{G12D}$ IgG (166 nM) for 1 h at 37 °C, 5% CO_2. Following treatment, cells were washed thoroughly with PBS (37 mM NaCl; 2.7 mM KCl; 4.3 mM Na_2HPO_4; 1.47 mM KH_2PO_4; pH 7.4), fixed for 15 minutes using 4% paraformaldehyde (Thermo Fischer Scientific, UK) and permeabilised using Triton™ X-100 (0.1%) (Sigma Aldrich, UK) for 10 minutes at room temperature. After washing with PBS (37 mM NaCl; 2.7 mM KCl; 4.3 mM Na_2HPO_4; 1.47 mM KH_2PO_4; pH 7.4), cells were incubated with Duolink® Blocking Solution for 1 h at 37 °C, 5% CO_2. Anti-KRas 9.13 IgG was incubated at 1:1000 dilution for 1 h, followed by the incubation of secondary antibodies (Duolink® *In Situ* PLA® Probe Anti-Mouse PLUS and Anti-Rabbit Minus) for 1 h at 37 °C, 5% CO_2. Ligation was carried out for 30 minutes and amplification for 3.5 h at 37 °C. After final washes, cells were stained with BioTracker 400 (7 µL component A + 7 µL component B in 1 mL PBS) for 30 minutes and Hoechst (1 $\mu L \cdot mL^{-1}$) for 10 minutes.

2.5. Western Blotting

Cells were seeded in 6- or 12-well plates (Greiner Bio-One) and incubated for 24 h to allow them to adhere. On the following day, cells were washed with PBS and treated according to the experimental plan for a given period at 37 °C, 5% CO2. Cells were washed with PBS and lysed with RIPA buffer (Sigma Aldrich, UK) containing cOmplete™ Mini protease inhibitors cocktail (Roche) or with a protease and phosphatase inhibitor cocktail (Abcam, UK) for 5 minutes. Cell lysates were scraped and transferred to Eppendorf tubes and centrifuged at 14,000 x g for 10 minutes at 4 °C. The supernatants were harvested and the protein concentration of each sample was determined using a bicinchoninic acid (BCA) Protein Assay Kit (Thermo Fischer Scientific, UK). The resulting absorbance was measured through an Infinite 200 Pro plate reader (Tecan, Germany). Equal amounts of protein (15-20 µg) were mixed with 4 µL of LDS loading buffer (Invitrogen, UK) and 2 µL of NuPAGE™ reducing agent (Thermo Fischer Scientific, UK). Samples were then heated at 80 °C for 10 minutes, and subsequently loaded on a 4-12% Bis-Tris Gel (10- or 12-well, NuPage™ Novex™, Thermo Fischer, UK) in an XCell SureLock™ Mini-cell system (Thermo Fischer Scientific, UK) with NuPAGE™ MOPS SDS running buffer (Thermo Fischer Scientific, UK) in a ratio of 1:20 in deionised water. SeeBlue™ Plus2 Pre-stained Protein Standard (Thermo Fischer Scientific, UK) and MagicMark™ XP Western (Thermo Fischer Scientific, UK) were used as standard marker. Gels were allowed to run for 1 h at 165 V, using a PowerPac™ High Current power supply (Bio-Rad Laboratories Ltd., UK). Next, proteins were transferred onto a nitrocellulose membrane (GE Healthcare) using NuPAGE™ Transfer Buffer in a ratio of 1:20 in deionised water and 20% (v/v) methanol at 100V for 1 h. Membranes were blocked in 5% bovine serum albumin (BSA) (Sigma Aldrich, UK) in TBS-0.1% Tween20 for 1 h and incubated overnight with primary antibodies (Table 2.1)

diluted in blocking buffer at 4 °C. Blots were washed 3 x 5 min with PBS-T and incubated with secondary horseradish peroxidase (HRP) conjugated antibody for 1 h, followed by washing 3 x 5 min with PBS-T. Membranes were developed using Pierce™ ECL Western Blotting Substrate (Thermo Fischer Scientific, UK) and detected using a LI-COR C-DiGit Blot Scanner (Li-COR, USA).

Table 2.1 – List of antibodies

Antibody	Species	Cat. Number	Manufacturer	Dilution
Phospho-p44/42 MAPK (pERK1/2)	Rabbit	9101S	Cell Signalling Technology	1:1000
p44/42 MAPK (total ERK1/2)	Rabbit	9102S	Cell Signalling Technology	1:1000
Phospho-p44/42 MAPK (EKR1/2) (Thr202/Thr204) (D13.14.4E) XP® (HRP)	Rabbit	8544S	Cell Signalling Technology	1:1000
p44/42 MAPK (EKR1/2) (Thr202/Thr204) (D13.14.4E) XP® (HRP)	Rabbit	4348S	Cell Signalling Technology	1:1000
Phospho-MEK1/2 (Ser217/221)	Rabbit	9121	Cell Signalling Technology	1:1000

Antibody	Species	Cat. Number	Manufacturer	Dilution
MEK1/2	Rabbit	9122	Cell Signalling Technology	1:1000
mCherry	Rabbit	E5D8F	Cell Signalling Technology	1:1000
Cyclophilin A	Rabbit	PA-1025	Thermo Fischer Scientific	1:1000
β-Actin (HRP)	Rabbit	5125	Cell Signalling Technology	1:1000
Sodium Potassium ATPase	Rabbit	Ab76020	Abcam	1:1000
Lamin B1	Rabbit	12586	Cell Signalling Technology	1:1000
Goat anti-rabbit IgG (H+L) (HRP)	Goat	31460	Thermo Fischer Scientific	1:10,000

2.6. Radiochemistry

The protein to be iodinated (10 µL, 1.5 mg/mL) was added Na[^{123}I] (5 µL) to an Eppendorf tube, followed by 50 µL of sodium phosphate buffer (0.5 M, pH 7.4) and 25 µL of chloramine-T (2 mg·mL^{-1}) dissolved in sodium phosphate buffer (0.05 M, pH 7.4). The resulting mixture was allowed to react for 5 minutes at room temperature and quenched by the addition of 500 µL of sodium metabisulfite (1 mg·mL^{-1}) dissolved in sodium phosphate buffer containing1M NaCl, 0.1% BSA and 1% KI. Next, the resulting solution was loaded onto a 7K MWCO Zeba™ Spin Desalting Columns (Thermo Fischer Scientific, UK), transferred to a Pico™ 17 Microcentrifuge and spun at 1500 x g for 2 minutes to obtain pure [^{123}I]I-anti-KRas proteins.

2.7. Retention Assay

PANC-1 and PSN-1 cells ($2x10^5$) were seeded into 24-well plates and allowed to attach overnight. On the following day, cells were washed 3x with serum-free medium and treated with Tri-cTAT B (1 μM) + [^{123}I]I-DARPin K19-cFarn (1 MBq·μg^{-1}) for 1 h at 37 °C, 5% CO_2. Cells were washed with PBS and resuspended in medium, supplemented with 10% (v/v) FBS (Invitrogen, UK) and 1% (v/v) PSG (Invitrogen, UK). At selected time points, medium was removed, and cells were washed with PBS followed by Glycine (0.1 M, pH 2.5) for 6 minutes at 4 °C. The resultant supernatant was removed, and cells were washed with PBS and lysed with NaOH (500 μL, 0.1 M) for 15 minutes. Cell lysates were transferred to a counting tube, and radioactivity was recorded using a γ counter (PerkinElmer 2480 Automatic Wizard 2).

2.8. Fractionation Assay

PANC-1 cells ($2x10^6$) were seeded into 6-well plates and allowed to attach overnight. On the following day, cells were washed 3x with serum-free medium and treated according to the treatment plan for 1 h at 37 °C, 5% CO_2. Cells were washed with PBS harvested with Trypsin-EDTA and spun at 500 x g for 5 minutes (Eppendorf Centrifuge 5417R). Cells were washed with ice-cold PBS and centrifuged at 500 x g for 3 minutes. The supernatant was discarded, leaving the cell pellet as dry as possible. PANC-1 cells were subjected to the manufacturer's protocol (Subcellular Protein Fractionation Kit for Cultured Cells, Thermo Fischer Scientific, UK). Briefly, ice-cold cytoplasmic extraction buffer (CEB) containing protease inhibitors was added to the cell pellet and incubated at 4 °C for 10 minutes with gentle mixing, followed by centrifugation at 500 x g for 5 minutes (Eppendorf Centrifuge 5417R). The resultant supernatant (cytoplasmic extract) was transferred to a clean pre-chilled tube. Ice-cold membrane extraction buffer (MEB) containing protease inhibitors was added to the pellet, vortexed for 5 seconds on the

highest setting and incubated at 4 °C for 10 minutes with gentle mixing (Eppendorf ThermoMixer C). Cells were spun at 3000 x g for 5 minutes (Eppendorf Centrifuge 5417R) and supernatant (membrane extract) was transferred to a clean pre-chilled tube. Ice-cold nuclear extraction buffer (NEB) containing protease inhibitors was added to the pellet, vortexed for 15 seconds and incubated at 4 °C for 30 minutes with gentle mixing (Eppendorf ThermoMixer C). Cells were centrifuged at 5000 x g for 5 minutes (Eppendorf Centrifuge 5417R) and supernatant (nuclear extract) was transferred to a clean pre-chilled tube. Given the low volume of each extract, the total volume was transferred to a designated counting tube and radioactivity was recorded using a γ counter (PerkinElmer 2480 Automatic Wizard 2).

2.9. Clonogenic Assays

2.9.1. *In Vitro* Irradiations

Cells were seeded in a 6-well plate 12 h prior to irradiation and left to adhere at 37 °C, 5% CO_2. Prior to irradiation, cells were washed with PBS and the medium was replaced with fresh medium. Cells were taken to the irradiatior in a sterile polystyrene box and irradiated using a [^{137}Cs] laboratory irradiator (IBL 637, CISbio International, France;0.662 MeV γ rays, dose rate of 0.81 Gy·min^{-1}). Following irradiation, cells were returned to the incubator.

2.9.2. Co-Delivery of [^{123}I]I-anti-KRas Macromolecules

Cells were washed with PBS and detached with 3 mL Accutase (Sigma Aldrich, UK) over 15 minutes. Cells were counted using a Countess II Automated Cell Counter and 20x10^3 cells were transferred to a clean 1.5 mL LoBind Eppendorf tube (Eppendorf). Cells were treated in serum-free medium to a final volume of 200 µL and incubated for 1 h at 37 °C, 5% CO_2. Cells were washed with PBS, resuspended in supplemented medium, as previously described, and centrifuged for 5 minutes at 4.2 RPM (VWR™ MicroStar 12).

The resulting supernatant was discarded, and cells were washed 2x with PBS and resuspended in 400 µL of supplemented medium. Each cell suspension (100 µL) was added to 6-well plates containing 2 mL of supplemented medium in each well. Samples were plated in triplicate, and incubated for the appropriate period.

2.9.3. Cell Staining

After 10-15 days of incubation, plates were washed with DPBS (Sigma Aldrich, UK) and stained using 0.01% (w/v) crystal violet for 1 h. Excess stain was removed with gentle washing, and plates were allowed to dry overnight. On the following day, plates were imaged using GelCount™ (Oxford Optronics, UK) and clusters of more than 50 cells were counted as a colony. Figures were analysed using Fiji (NIH, MD, USA).

2.10. *In Vivo* Experiments

2.10.1. Animals and Husbandry

Animal procedures were carried out according to the Scientific Procedures Act 1986 and local ethics reviews. Experiments were carried out within the limits of the Home Office-issued project licence P13B66CD9. C57BL/6 and BALB/c nude mice were purchased from Charles River Laboratories (Kent, UK). Female animals (5 weeks old) were housed in groups of two in specific pathogen-free facilities with temperature control (24 ± 1 °C) and humidity control (55 ± 10 °C) and 12-hour light/dark cycles. Mice were fed ad libitum and had unlimited access to water. Mice were allowed to acclimatise for at least 2 weeks before being entered into experiments. Their health was monitored daily and weight was checked twice weekly and if > 10% weight loss was detected, mice were sacrificed using schedule 1 killing.

2.10.2. Tumour Inoculation

PSN-1 cells were harvested according to the 2D cell culture protocol noted above and diluted in PBS. For each mouse, 2 x 10^6 cells, pre-mixed with Cultrex® (bio-techne, UK),

were injected subcutaneously into the flank of anaesthetised mice (5% isoflurane) using a 23G needle. Tumour size was measured twice weekly using callipers, and tumour volume was calculated according to the following formula: Tumour Volume = (length x width x height)/2. If tumour volume approached or surpassed 1000 mm^3, mice were euthanised using schedule 1 killing.

2.10.3. Treatment

In the case of tumour-bearing models, mice were entered into the experiment when the tumour volume reached approximately 70 mm^3. Tri-cTAT B was delivered intravenously (i.v.) via a tail vein cannula under general anaesthesia. For co-delivery experiments, Tri-cTAT B + [^{123}I]I-anti-KRAS IgG was pre-mixed in a chilled Eppendorf tube and allowed to interact for 10 minutes. The resulting mixture was administered via a tail vein cannula under general anaesthesia. The volume of the injectate was 100 µL and in situations where the volume was less than 50 µL, the experimental treatment was diluted in PBS to a volume of 100 µL prior to injection. Cannulations and i.v. injections were performed by Dr Kel Tan or Dr Gemma Dias.

2.10.4. *In Vivo* Bioluminescence Imaging

Tumour-free mice that received AF488-conjugated Tri-cTAT B were anaesthetised and imaged at 1 h and 4 h post-injection (p.i.) using the IVIS Spectrum imaging system (Perkin Elmer, MA, USA) with 500/520 filters for excitation and emission, respectively. Following the 4 h imaging session, mice were euthanised using schedule 1 killing, and selected organs and tissues were removed and visualised using the IVIS Spectrum imaging system under the same settings. Images were analysed using Aura (Spectral Instruments Imaging, AZ, USA).

2.10.5. SPECT/CT

Tumour-bearing mice administered with Tri-cTAT B + [123I]-anti-KRAS IgG were anaesthetised and scanned at 4 h and 24 h p.i.. For that purpose, mice were placed in a purpose-built cradle and monitored using a respiratory rate and temperature probe. Data were acquired in list mode (gamma spectrum collection from 0-1200 keV) with a single gantry SPECT/PET/CT scanner (VECTor4CT, MILabs, Netherlands) equipped with the HE-UHR-RM collimator containing pinhole apertures of 1.8 mm diameter, using MILabs acquisition software v7.39. Triple-energy-window-based scatter correction was applied for iodine-123. All images were reconstructed with MILabs reconstruction software. Following reconstruction, SPECT and CT data were co-registered followed by CT-based attenuation correction. Image slice displays and maximum intensity projections were generated using pMOD v3.36.

2.10.6. SPEC/CT *Ex Vivo* Biodistribution

After mice were imaged 24 h p.i. *via* SPECT/CT, animals were euthanised using schedule 1 killing and selected organs and tissues were removed and placed in pre-weighed tubes. The radioactivity in each tube was measured using a Hidex Automatic γ counter (Finland) along with a tube containing the injected dose prepared at the time of treatment to enable calculation of the % injected dose. Tubes were reweighed to determine tissue weight to enable calculation of % injected dose per gram.

2.11. Statistical Analysis

Statistical analyses were performed using GraphPad Prism, Version 10.0.2 (GraphPad Software, USA). Statistical significance was determined by unpaired one-way ANOVA performed with Dunnett's or Tukey's post hoc adjustment for multiple comparisons. Survival curves based on clonogenic assays were generated using a log10 scale. Graphs show the mean with standard error of the mean (SEM) to indicate the uncertainty in the

mean calculation. Asterisk symbols are used to denote statistical (P) significance values :*P <0.05, **P<0.01, P<0.001, P<0.0001.

Chapter 3 Synthesis of Tri-cTAT B and Co-Delivery of Anti-KRas Molecules

3.1. Introduction

3.1.1. Novel TAT-derived Cell-Penetrating Peptide

The use of macromolecules is currently limited to extracellular targets. Yet, the intracellular environment hosts many cancer-relevant proteins, which are currently inaccessible to antibodies and other immune agents [240,241]. Despite advances, the intracellular delivery of macromolecules remains a formidable challenge due to the toxicity and limited efficacy of current vehicles. During the past three decades, different approaches have been taken, including the use of viral and non-viral carriers and physical techniques, such as electroporation[242–244]. In addition, during this period, valuable progress in the development of polycationic non-viral carriers, such as polymers, lipid particles and CPPs, has been made[245,246].

Since its discovery in the late 1980s, TAT has been extensively used in the design of intracellular targeted therapies[247,248]. However, ATP-mediated endocytosis and subsequent endosome formation, one of the main mechanisms of CPP transfection, is known to be a hindrance to intracytoplasmic delivery[249–251]. Thus, the concentration of TAT-delivered macromolecules that escape from endosomes is often too low to result in an adequate biological response against intracellular targets.

Recent studies have focused on addressing endosomal entrapment by modifying the structure of CPPs[252,253]. Interestingly, some studies suggested that the cyclization of TAT enhanced the non-endocytic cellular uptake[254,255]. However, these approaches are not

feasible *in vivo* due to the high concentrations needed to achieve a therapeutic effect *in vitro* (> 10μM). Also, the typical dose of clinically approved antibody treatments is 10 $mg \cdot kg^{-1}$, emphasizing the need for carriers that can transfect clinically relevant amounts of macromolecules at the lowest concentration possible[256,257].

To address this problem, the Vallis Lab recently reported a novel TAT-derived CPP that combines the cyclisation of the archetypal TAT (cTAT) with the formation of a multimer construct *via* the conjugation of three copies of cTAT to a tetrakis core structure[258]. *In vitro* studies with this innovative CPP, Tri-cTAT B, revealed the intracellular delivery of functional immunoglobulin G (IgG) antibodies and antibody fragments (Fab) in the cytosol and nuclei of live cells at concentrations as low as 1 μM.

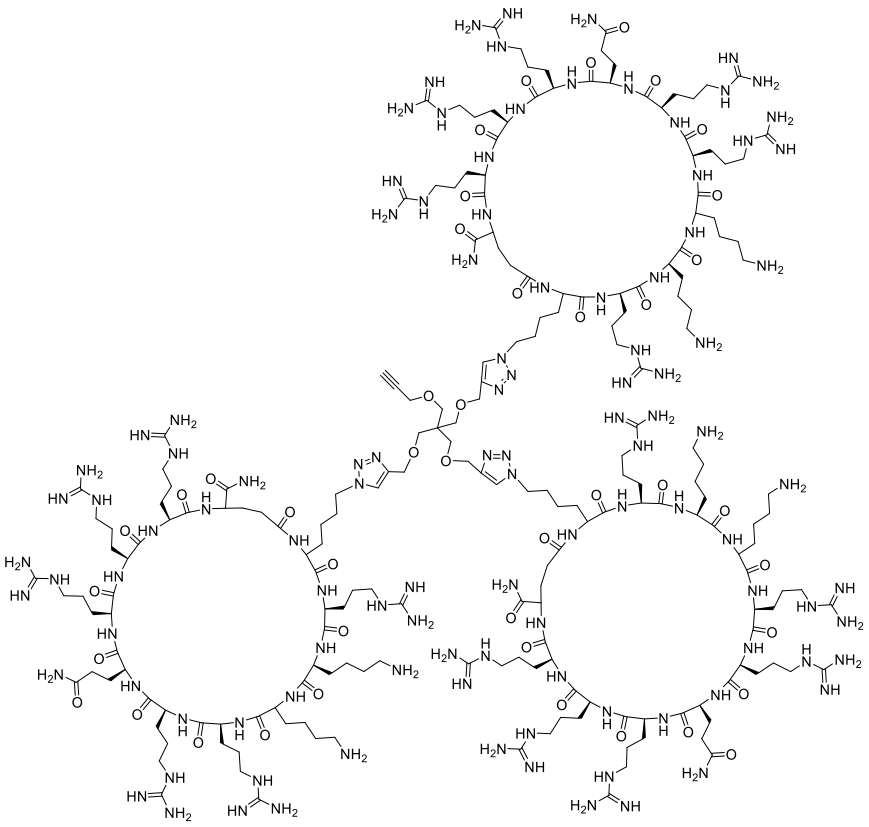


Figure 3.1 – Chemical Structure of Tri-cTAT B. The development of Tri-cTAT B combines the cyclisation of TAT (cTAT) with the addition of three copies of cTAT to a tetrakis core structure, forming a trimeric cell-penetrating peptide (CPP). Overall, approaches enhance the delivery of IgG and other immune molecules with a concentration of Tri-cTAT B as low as 1 μM.

Additionally, based on proximity ligation assays (PLA), the co-delivery of an H2B-AF488 antibody resulted in a significantly higher number of PLA signals per nuclei than control antibodies, suggesting that antibodies co-delivered with Tri-cTAT B retain functionality with the ability to bind target proteins.

3.1.2. Anti-KRas Immune Molecules

The use of small molecules to target KRas has proven difficult to achieve with only two FDA-approved drugs since the 1960s[123,259]. Also, they are both specific to *KRAS p.G12C*, so they are unlikely to have a clinical impact on malignancies with a low incidence of this mutation, including PDAC. The past few years, however, have seen the development of interesting experimental KRas-targeted immunotherapy agents with high specificity and affinity[189,260–263].

Amongst these, DARPin K19 is a potent KRas-specific macromolecule, developed by Professor Terry Rabbitts and colleagues, that binds to an allosteric site encompassing the His95 residue at the helix α3/loop 7/helix α4 interface[188,264]. This interaction prevents KRas nucleotide exchange and dimerisation, thus impairing mutant KRas-effector interactions and downstream signalling. A more recent variant of DARPin K19 is fused to the VHL E3 ligase, resulting in a degrader that induces specific proteolysis of mutant and WT KRas[264]. This has been shown to affect the proliferation of cancer cells expressing mutant KRas *in vitro* and *in vivo,* whilst the viability of WT KRas cells is unaffected.

Rabbitts also reported the development of a single immunoglobulin heavy chain variable domain fragment (scFv), scFv Y6, that binds to the activated form of Ras, preventing the interaction between Ras and effector proteins in the S-I region. Similar to DARPin K19 and DARPin K19-VHL, using scFv Y6 results in the abrogation of proteins activated by KRas, thus limiting the proliferation of mutant KRas cancer cells[265,266].

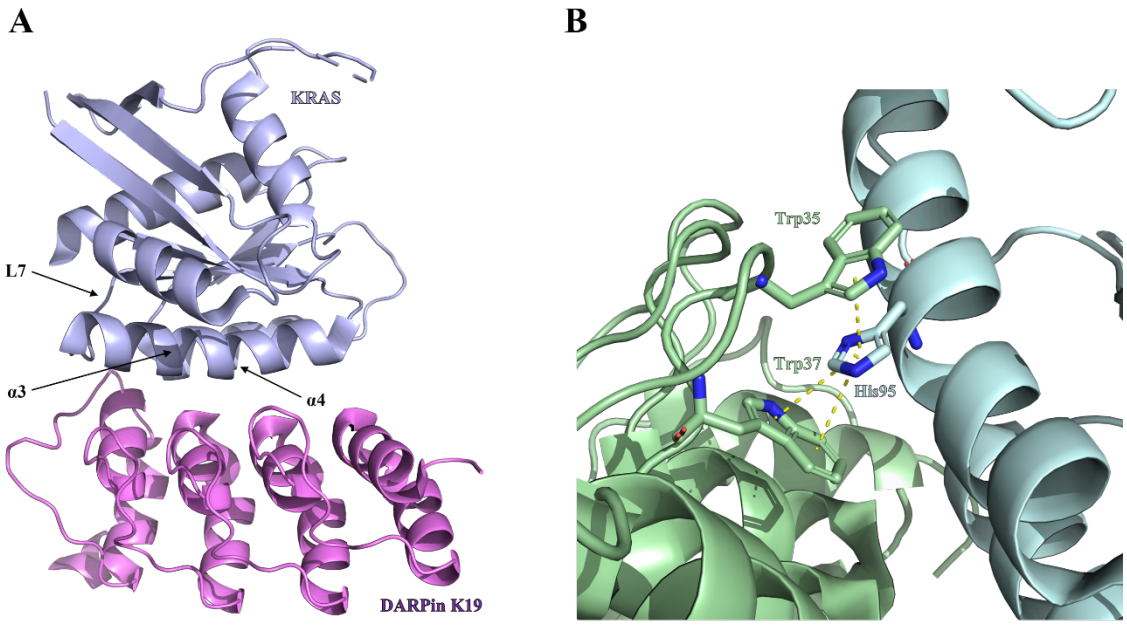


Figure 3.2 - DARPin K19 binds KRas at an allosteric site. (A) X-ray crystal structures of $KRAS^{G12V}$-GDP-bound to DARPin K19 (PDB ID: 6H47), highlighting helix 3 (α3), helix 4 (α4), and loop 7 (L7). **(B)** Binding of DARPin K19 (green) to KRas (light-blue) is based on a sandwich π-π interaction between Trp35 and His95 and a T-shaped π-π interaction between Trp37 and His95.

3.2. Aims

The aims of the research presented in this Chapter were:

- To optimise the synthesis of Tri-cTAT B;
- To assess the uptake of Tri-cTAT B in PDAC cell lines;
- To investigate the co-delivery of anti-KRas immune agents with Tri-cTAT B;
- To study the uptake of Tri-cTAT B and co-delivered anti-KRas macromolecules *in vivo*.

3.3. Results

3.3.1. Synthesis of Tri-cTAT B through Microwave-Assisted Chemistry

The bioconjugation of molecules by copper(I)-catalysed azide-alkyne [3+2] cycloaddition (CuAAC) reactions has proven to be highly useful for the synthesis of complex molecular structures.

Originally, Tri-cTAT B was synthesized following the published method[258]. This included the synthesis around an alkyne functionalised scaffold and the formation of cyclic TAT (cTAT) to match the linear sequence of the HIV TAT peptide (RKKRRQRRR). To include the azide functionality, an azide-modified lysine (K(N3)) residue was added to the N-*terminus*, whilst the cyclisation of the peptide was generated by the addition of a glutamic acid residue to the C-*terminus* for head-to-tail cyclisation to the N-*terminus* to generate K(N_3)RKKRRQRRRE.

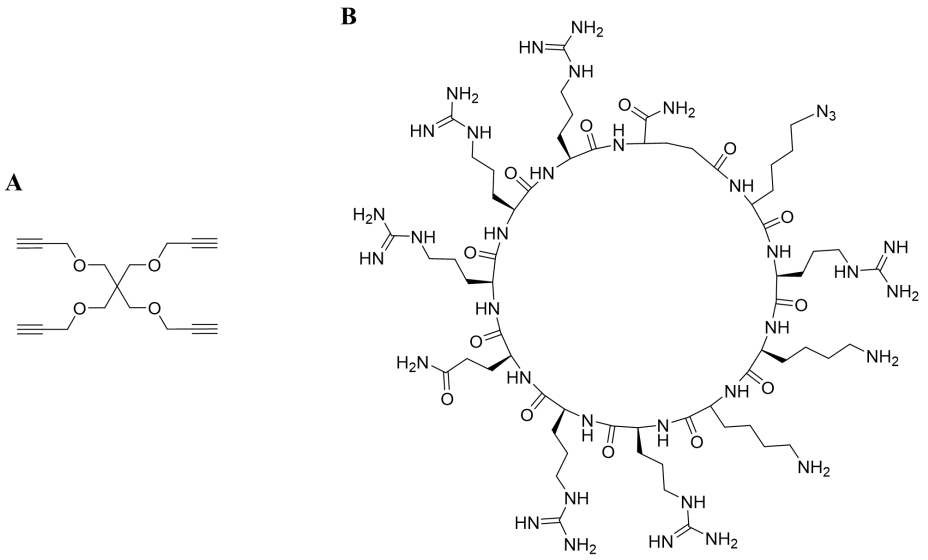


Figure 3.3 - Tri-cTAT B-related chemical structures. (A) Molecular structure of a tetrakis alkyne functionalised scaffold, used for the synthesis of Tri-cTAT B. **(B)** Post-cyclisation structure of the HIV TAT (49-57) peptide with the addition of a functionalised azide-modified lysine.

Following the cyclisation of TAT, Tri-cTAT B was formed *via* CuAAC with an excess of cTAT compared to the tetrakis alkyne functionalised scaffold. Table 3.1 describes the conditions tested for the synthesis of Tri-cTAT B.

Table 3.1 – Cooper(I)-catalysed azide-alkyne [3+2] cycloaddition (CuAAC) conditions

	STOCK					REACTION			
	MW / g·mol^{-1}	**m /mg**	**V / uL**	**[Stock] / mM**		**Eq.**	**m / ug**	**V_{Stock} / uL**	**%**
DMSO	-	-	-	-		-	-	32.00	30
PBS	-	-	-	-		-	-	11.00	10
Tetrakis-Alkyne	288.34	2.8	485.5	20		1	22.39	3.88	3.6
cTAT-Azide	1609.96	13.35	829.2	10		4	500.00	31.06	29
Copper (II) Sulfate	159.61	3.4	213.0	100		4	49.57	3.11	2.9
THTPA	434.50	1.8	27.6	150		20	674.71	10.35	9.7
Sodium Ascorbate	198.11	3.9	196.9	100		8	123.05	6.21	5.8
Aminoguanidine Hydrochloride	110.55	5.5	497.5	100		12	103.00	9.32	8.7

The reaction led to the formation of a mixture of products containing monomers, dimers, and trimers of cTAT (Figure 3.4). However, purification via HPLC allowed the separation of three peaks, whose molecular weight was confirmed *via* liquid chromatography-mass spectrometry (LC-MS) (Figure 3.5A). Despite successful synthesis and purification, the conversion rate of starting material to Tri-cTAT B appeared to be lower than Mono-cTAT B or Di-cTAT B. Further analysis was done by quantifying the area of each peak based on the integration of peaks corresponding to the starting material, Mono-cTAT B, Di-cTAT B, and Tri-cTAT B yielding areas of 49.13%, 14.04%, 32.82%, and 14.04% respectively.

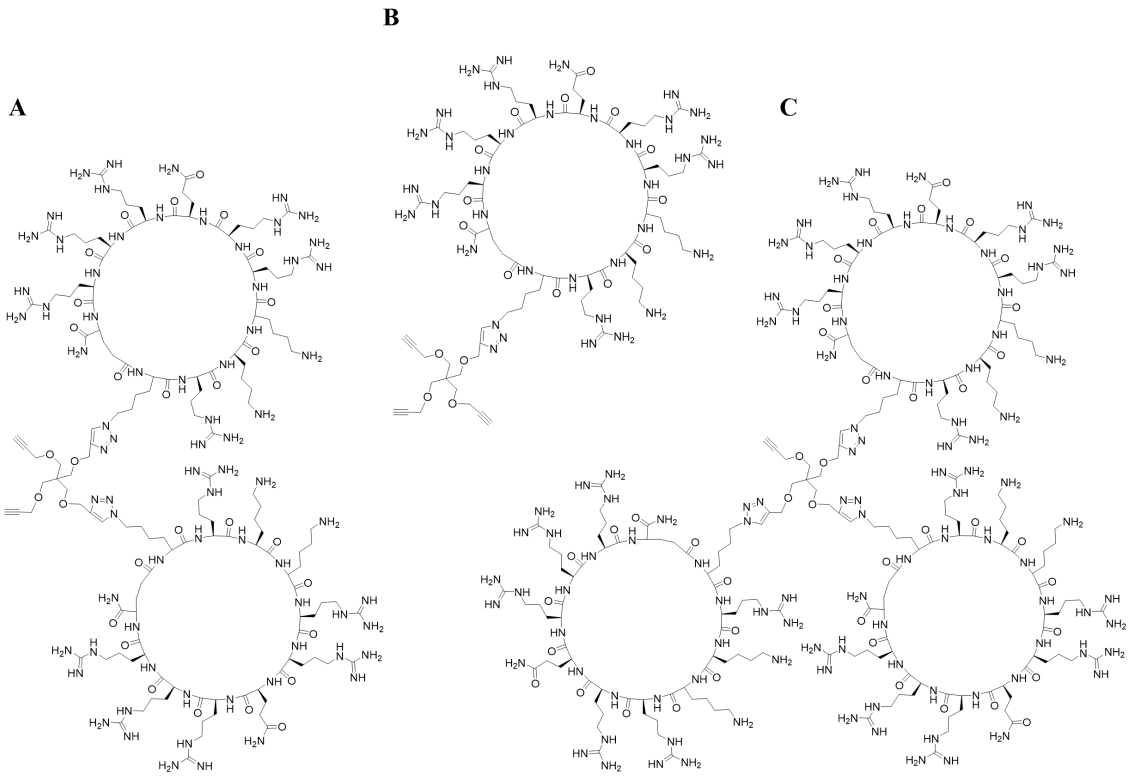
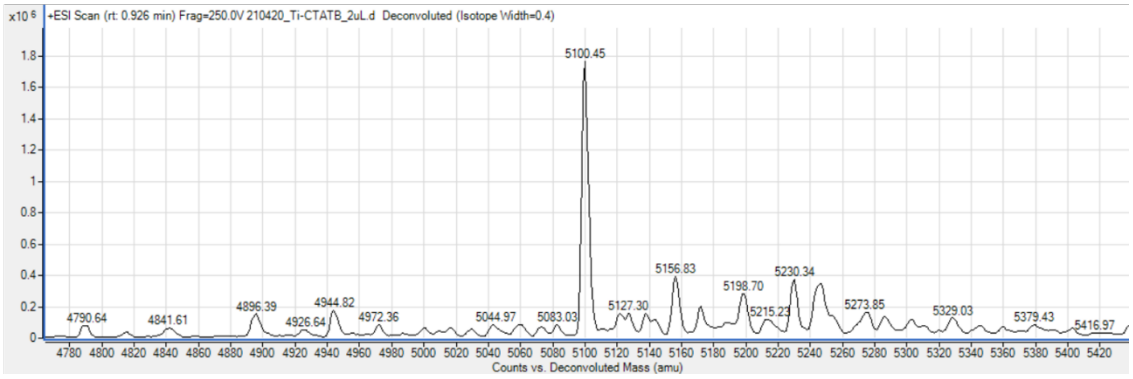
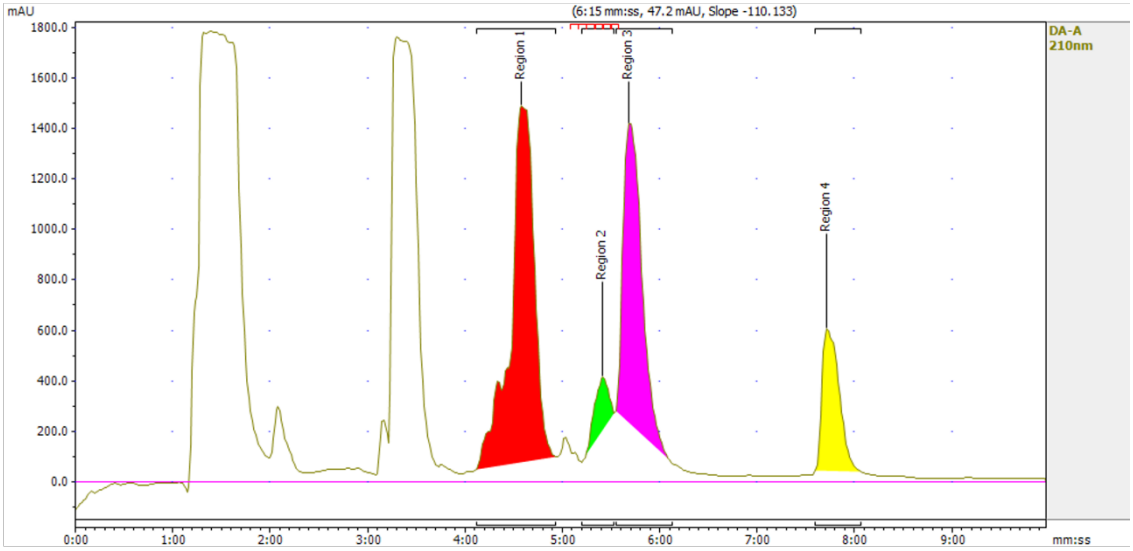


Figure 3.4 - Reaction products. The cooper(I)-catalysed azide-alkyne [3+2] cycloaddition (CuAAC) reaction between a tetrakis alkyne functionalised scaffold and excess of cTAT B results in the synthesis of a mixture of products composed of **(A)** dimers, **(B)** monomers, and **(C)** trimers of cTAT.

A



B

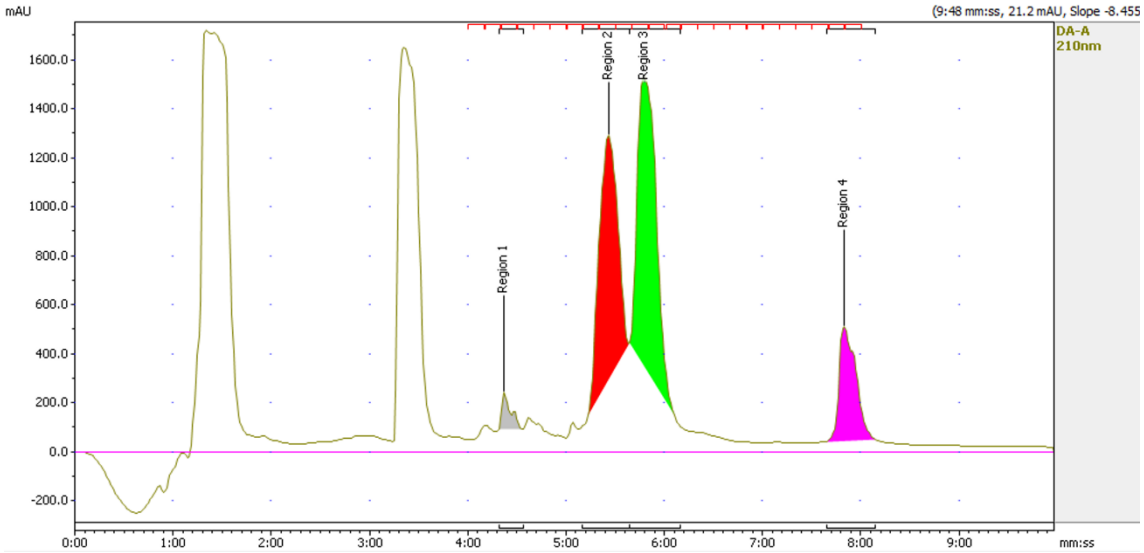


Species	Key	Start	End	%ROI
cTAT B		04:05	04:55	49.13
Mono-cTAT B		07:30	08:00	14.04
Di-cTAT B		05:30	06:05	32.82
Tri-cTAT B		05:10	05:25	4.01

Figure 3.5 - Tri-cTAT B synthesis. (A) Maximum entropy deconvoluted Quadrupole Time-of-Flight Mass Spectrometry (QTOF MS) [ES$^+$] chromatogram confirmed the synthesis of Tri-cTAT B after yielding a molecular weight of 5100.45 g·mol^{-1} against a theoretical molecular weight of 5100.10 g·mol^{-1} for $C_{209}H_{386}N_{108}O_{43}$. **(B)** High-pressure liquid chromatography (HPLC) chromatogram indicates the synthesis of Tri-cTAT B (green), although with a low conversion rate. Quantification of each peak was done by integrating the peaks represented by the starting material (red), Mono-cTAT B (yellow), Di-cTAT B (pink), and Tri-cTAT B (green), indicating a % region of interest (ROI) of Tri-cTAT B of only 4.01%.

As there was poor conversion of starting material to Tri-cTAT B, the first aim was to optimise the synthesis of Tri-cTAT B. To achieve this, alternative conditions to the one outlined in the literature were tried, including modifying the temperature of the reaction and increasing the time of the reaction. Unfortunately, the combination of these changes had little or no effect on the yield of Tri-cTAT B synthesis.

Alternatively, there was evidence suggesting that the use of microwave-assisted synthesis greatly impacted the yield of CuAAC reactions[267–270]. Also, this approach is often described as safer and quicker than conventional synthesis. As a result, the synthesis of Tri-cTAT B was tried *via* microwave-assisted "click" chemistry using the conversion table provided by the manufacturer. Thus, instead of performing the reaction at 50 ºC for 80 minutes, the mixture was allowed to react at 60 ºC for approximately 23 minutes. The chromatography-based analysis provided evidence of an increased conversion rate of the starting material to Tri-cTAT B when comparing conventional CuAAC synthesis to microwave-assisted "click" chemistry. Peak integration of starting material, Mono-cTAT B, Di-cTAT B, and Tri-cTAT B yield areas were 2.74%, 15.54%, 44.70%, and 37.02%, respectively. Thus, the %ROI for Tri-cTAT exhibited a substantial improvement, rising from 4.01% to 37.02%.

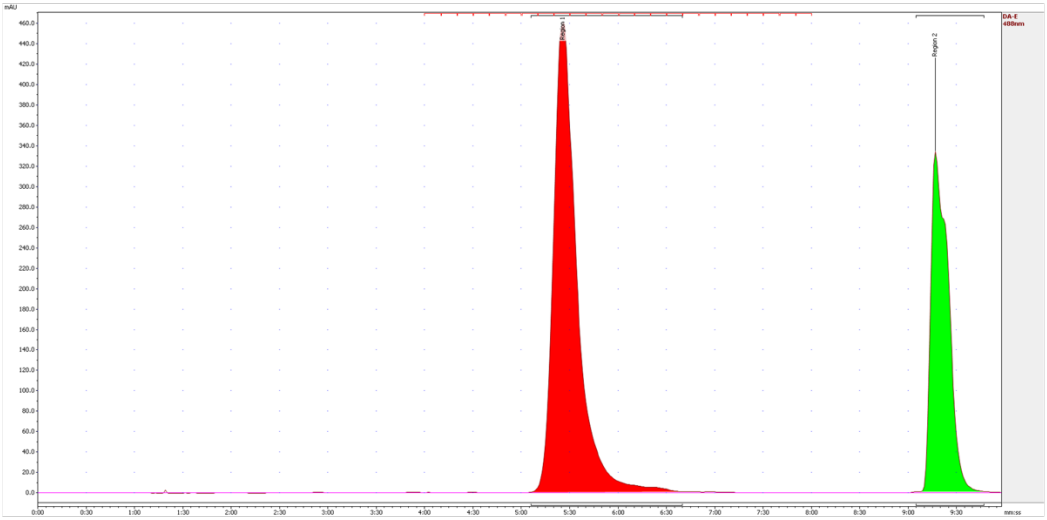


Species	Key	Start	End	%ROI
cTAT B		04:15	04:25	2.74
Mono-cTAT B		07:40	08:10	15.54
Di-cTAT B		05:35	06:05	44.70
Tri-cTAT B		05:10	05:30	37.02

Figure 3.6 – Microwave-assisted "click" chemistry. The use of microwave-assisted "click" chemistry for the synthesis of Tri-cTAT B showed a superior conversion rate compared to the conventional CuAAC synthesis. Based on the analysis of the high-pressure liquid chromatography (HPLC) chromatogram, the area of the peak corresponding to Tri-cTAT B exhibited a substantial increase in the % ROI, rising from 4.01% to 37.02%.

Next, an Alexa Fluor™ 488 Azide (AF488-N_3) fluorophore was added to the last available alkyne functionalised moiety in the tetrakis core. In this case, the covalent attachment of a green fluorophore to Tri-cTAT B was achieved using conventional CuAAC chemistry. Since the reaction proceeded successfully, this step was not explored *via* microwave-assisted "click" chemistry.

A



Species	Key	Start	End	%ROI
Tri-cTAT B-AF488		05:05	06:30	63.46
AlexaFluor™ 488-N_3		09:10	10:00	36.54

B

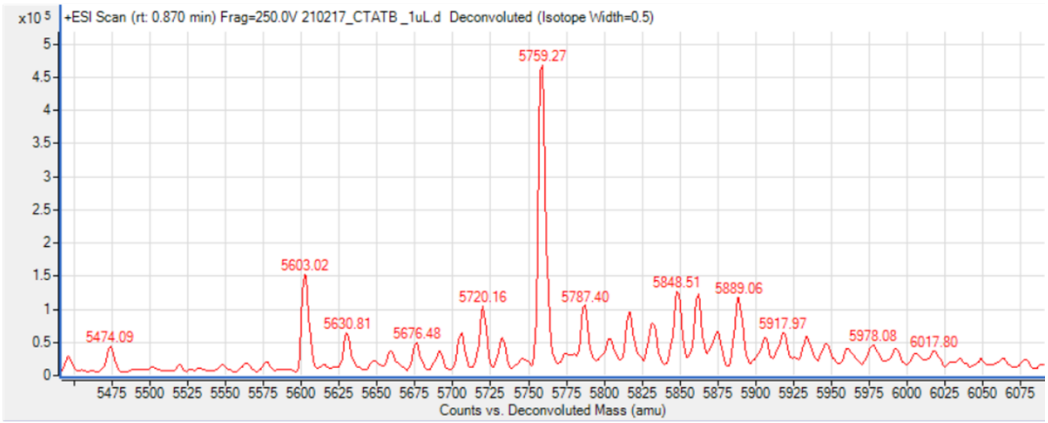


Figure 3.7 - Synthesis of Tri-cTAT B - AlexaFluor™ 488. (A) Labelling efficiency under conventional CuAAC chemistry was determined by high-pressure liquid chromatography (HPLC) analysis at a wavelength of 488 nm, indicating the presence of two distinct chemical structures. HPLC analysis of AlexaFluor™ 488 – N_3 (AF488-N_3) shows one single peak at a retention time between 09:00 and 10:00 (not shown). **(B)** Isolation of the red peak in (A) and analysis *via* maximum entropy deconvoluted Quadrupole Time-of-Flight Mass Spectrometry (QTOF MS) [ES+] yielded a molecular weight of 5759.27 g·mol^{-1} against a theoretical molecular weight of 5758.76 for $C_{236}H_{412}N_{114}O_{53}S_2$.

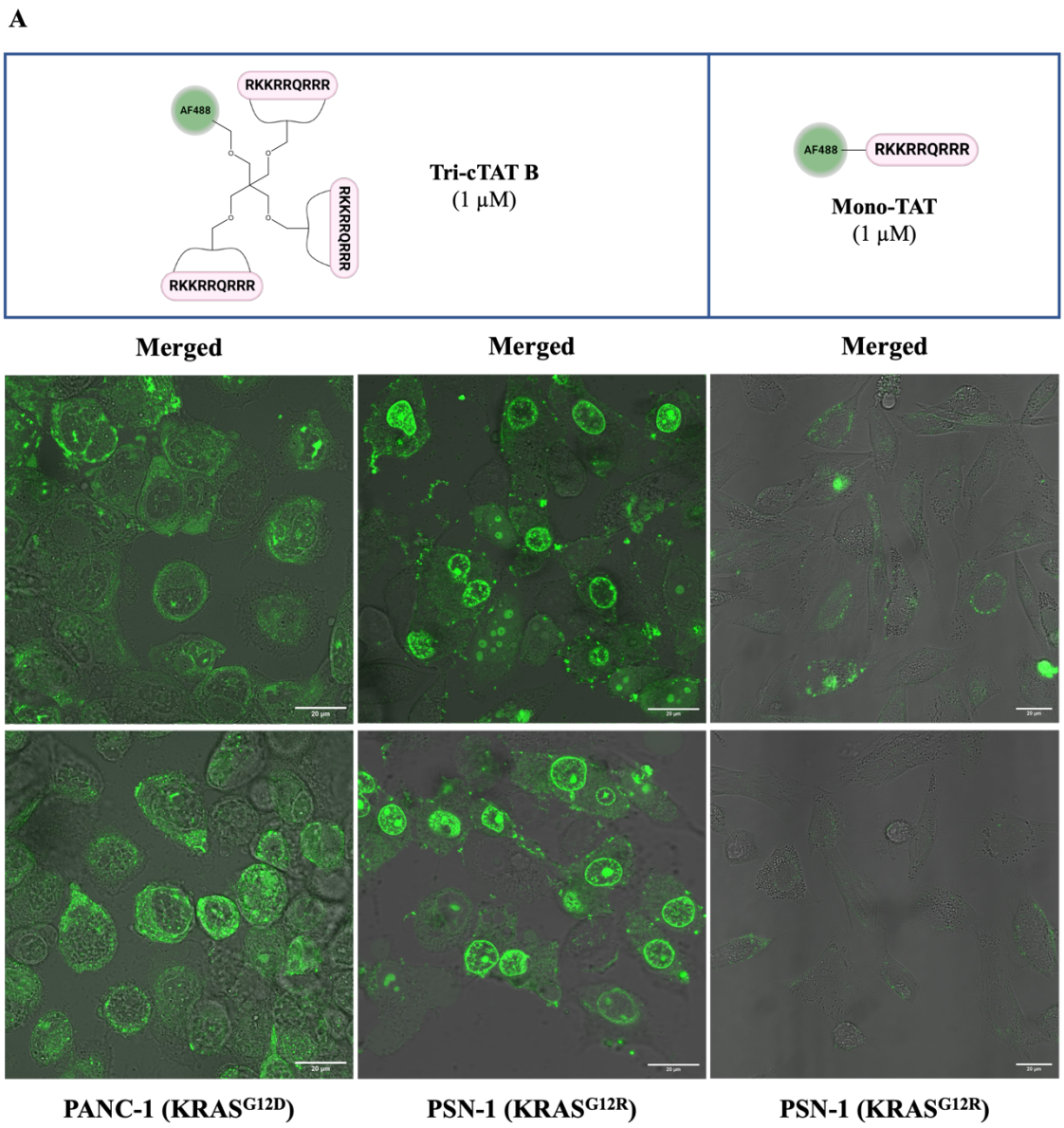
3.3.2. Tri-cTAT B Transfection in PDAC Cell Lines

Following the optimisation of Tri-cTAT B synthesis, the next aim of this thesis was to assemble a panel of KRAS mutant PDAC cell lines and study the ability of Tri-cTAT B to enter these cells. Table 3.2 describes the cell lines used according to the most predominant KRAS mutations in PDAC.

Table 3.2 - PDAC cell lines and respective alterations[271,272]

Cell Line	KRAS Mutation	Additional Alterations
PANC-1	G12D	TP53, CDKN2/p16
AsPC-1	G12D	TP53, CDKN2/p16
PSN-1	G12R	TP53, CDKN2/p16, SMAD4
BxPC-3	WT	TP53, SMAD4

Similar to results published in the literature, the ability of Tri-cTAT B to enter cells was studied at a concentration of 1 μM *via* live-cell confocal microscopy[258]. Consistent with previous data in HeLa and CHO cells, PDAC cells treated with Tri-cTAT B showed a homogeneous internalization, with nearly 85% of cells taking up Tri-cTAT B (Figure 3.8C). Consistent with observations that TAT readily enters the nucleus and accumulates in the nucleoli, homogeneous staining of this organelle was noted, albeit with an average fluorescence intensity that was 2.5-fold higher in PSN-1 than in PANC-1 cells (Figures 3.8B)[273]. Conversely, the uptake of 1 μM Mono-TAT in PSN-1 and PANC-1 cells was limited, with almost no uptake detected and only 12% of transduced cells (Figure 3.8A).


A
AF488
RKKRRQRRR
RKKRRQRRR
RKKRRQRRR
Tri-cTAT B
(1 μM)
AF488
RKKRRQRRR
Mono-TAT
(1 μM)
Merged
Merged
Merged
PANC-1 (KRASG12D)
PSN-1 (KRASG12R)
PSN-1 (KRASG12R)

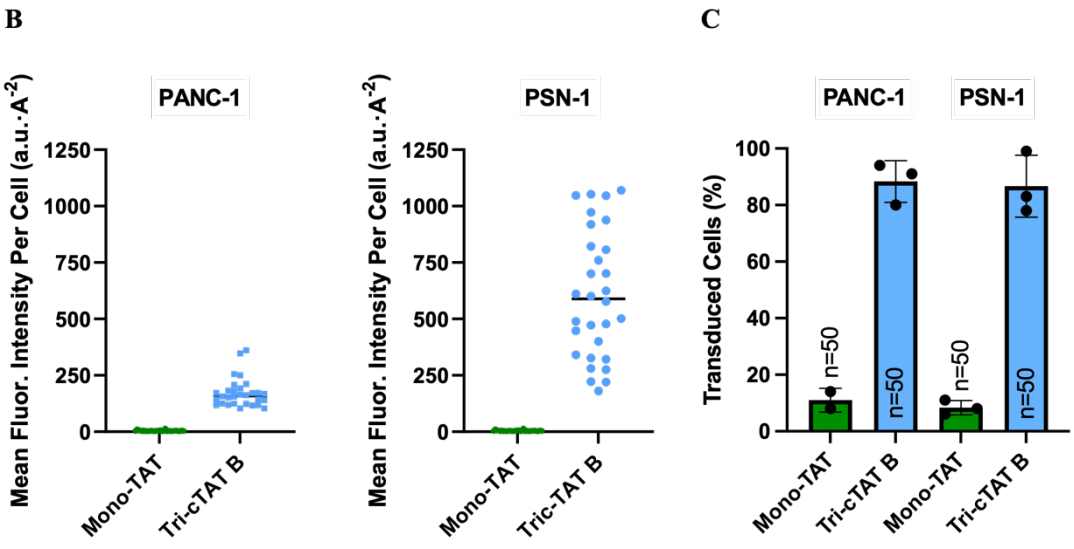

B
PANC-1
PSN-1
Mean Fluor. Intensity Per Cell (a.u.·A-2)
1250
1000
750
500
250
0
Mono-TAT
Tri-cTAT B
Tric-TAT B
C
PANC-1
PSN-1
Transduced Cells (%)
100
80
60
40
20
0
n=50
n=50
n=50
n=50
Mono-TAT
Tri-cTAT B
Mono-TAT
Tri-cTAT B

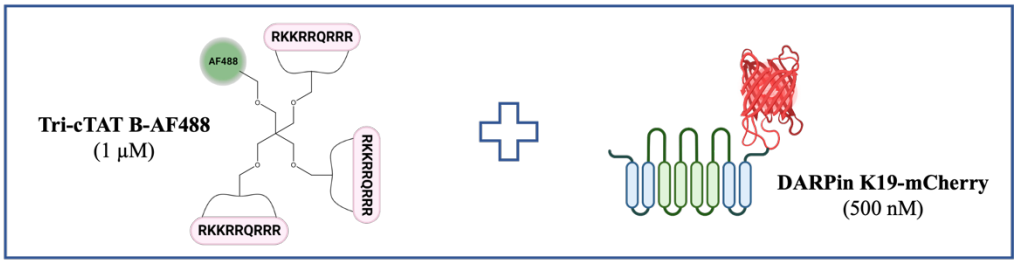
Figure 3.8 - Live-cell confocal microscopy of linear and cyclic TAT trimers in PANC-1 and PSN-1 cells. (A) PANC-1 ($KRas^{G12D}$) and PSN-1 ($KRas^{G12R}$) cells treated with 1 μM Tri-cTAT B result in its accumulation in the cytosol and nucleoli, whilst the uptake of 1 μM linear Mono-TAT in PSN-1 cells is limited and concentrated *in foci* around the cell membrane, indicating endosomal entrapment. Merged images were constructed by superimposing the green channel, representative of Tri-cTAT B-AF488 and the brightfield channel. Scale bars: 20 μm. **(B)** Quantification of the mean fluorescence intensity per cell in cells treated with linear Mono-TAT or cyclic Tri-cTAT B constructs. The number of cells analysed (*n*) is similar across the different treatment groups (n=20). **(C)** Quantification of the percentage of transduced cells (scored as positive when presenting cytoplasmic and nucleolar fluorescence) in cells treated with linear Mono-TAT or cyclic Tri-cTAT B constructs. Data are presented as mean ± SD.

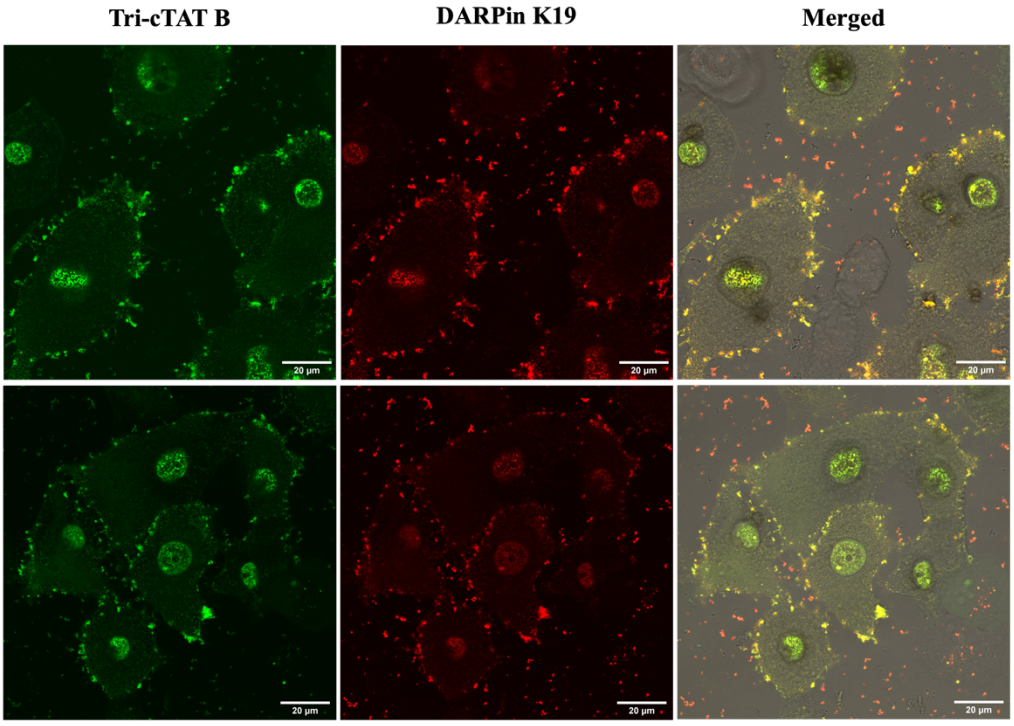
3.3.3. Co-Delivery of Anti-KRas Immune Molecules with Tri-cTAT B

Next, the ability of Tri-cTAT B to co-deliver DARPin K19 or scFv Y6 into PDAC cell lines was investigated. In live cell imaging experiments, Tri-cTAT B was conjugated to AF488 while anti-KRas DARPin K19 and anti-pan-Ras scFv Y6 were coupled with mCherry, enabling the identification of Tri-cTAT B as green and the identification of anti-KRAS macromolecules as red. The concentration of anti-KRas DARPin K19 and anti-pan-Ras scFv Y6 used for *in vitro* studies was determined based on their molecular weight, estimated to be between 45 kDa and 55 kDa. Hence, a concentration of 500 nM was calculated to maintain the ratio of Tri-cTAT B: DARPin K19 or Tri-cTAT B: scFv Y6 to approximately 1: 5.

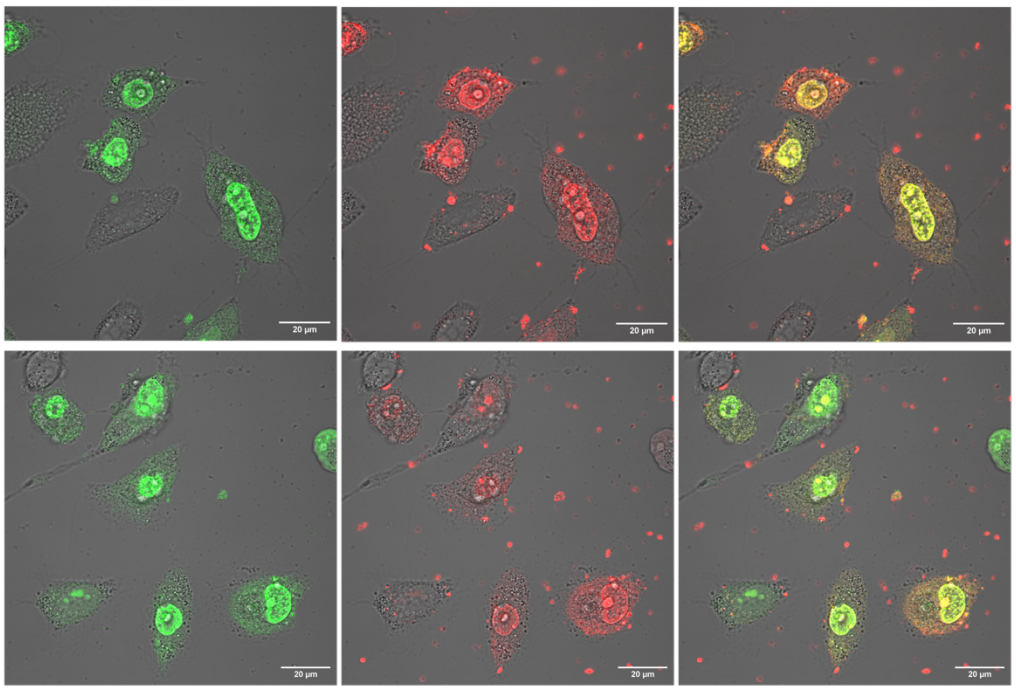
Exposure of PSN-1, PANC-1, and AsPC-1 cells to 500 nM DARPin K19-mCherry and 1 μM Tri-cTAT B-AF488 resulted in successful internalisation based on visible uptake into the cytosol and nucleus (Figure 3.9A and 3.9B, respectively). Consistent with previous observations regarding the intracellular distribution of TAT-based compounds, there was a greater uptake of DARPin K19 in the nucleus and nucleoli compared to the cytoplasm (Figure 3.9C).

A

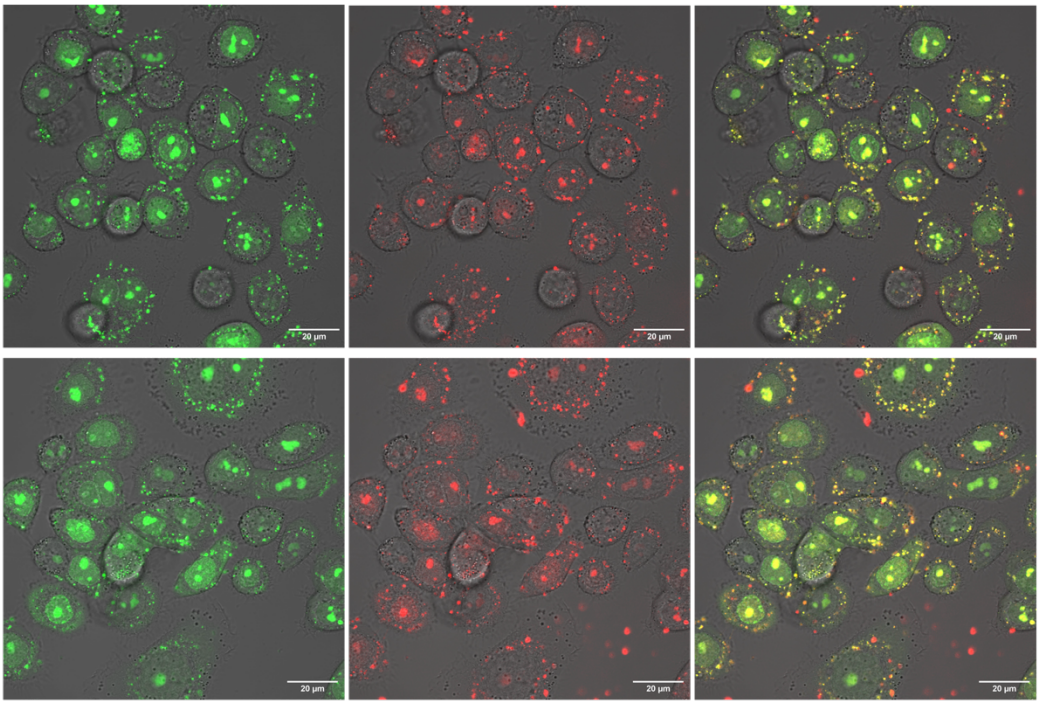




PANC-1 ($KRAS^{G12D}$)

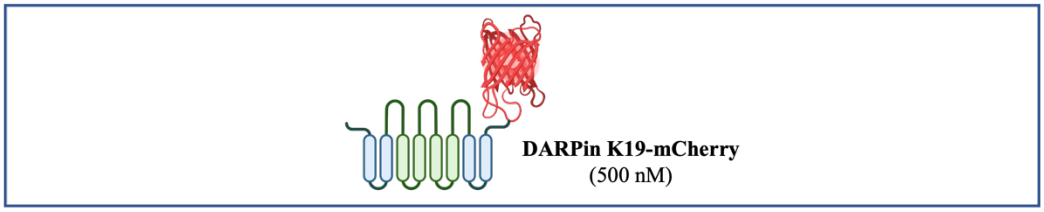


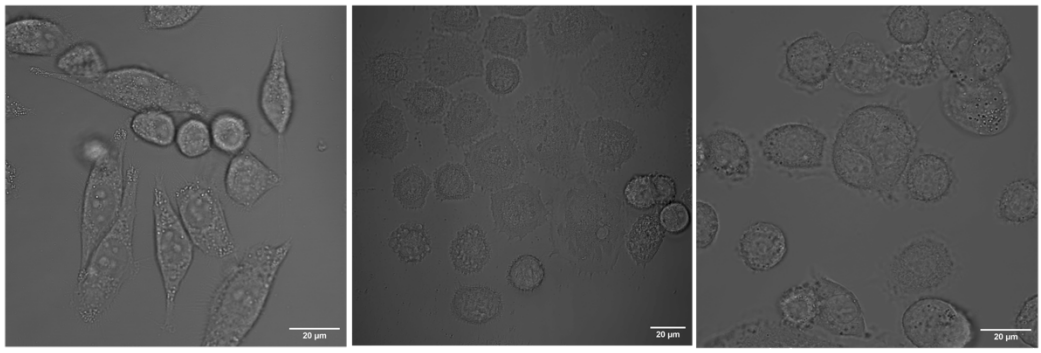
PSN-1 ($KRAS^{G12R}$)



AsPC-1 (KRAS^{G12D})

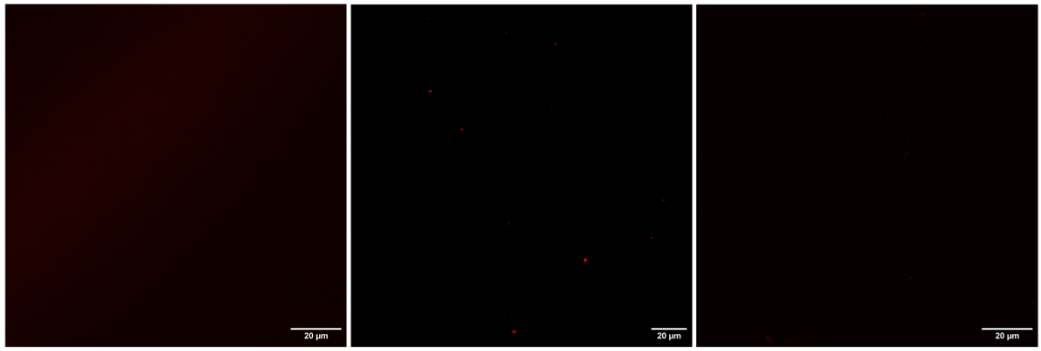
B





Brightfield | Brightfield | Brightfield

DARPin K19 | DARPin K19 | DARPin K19



PSN-1 (KRAS^{G12R}) | PANC-1 (KRAS^{G12D}) | AsPC-1 (KRAS^{G12D})

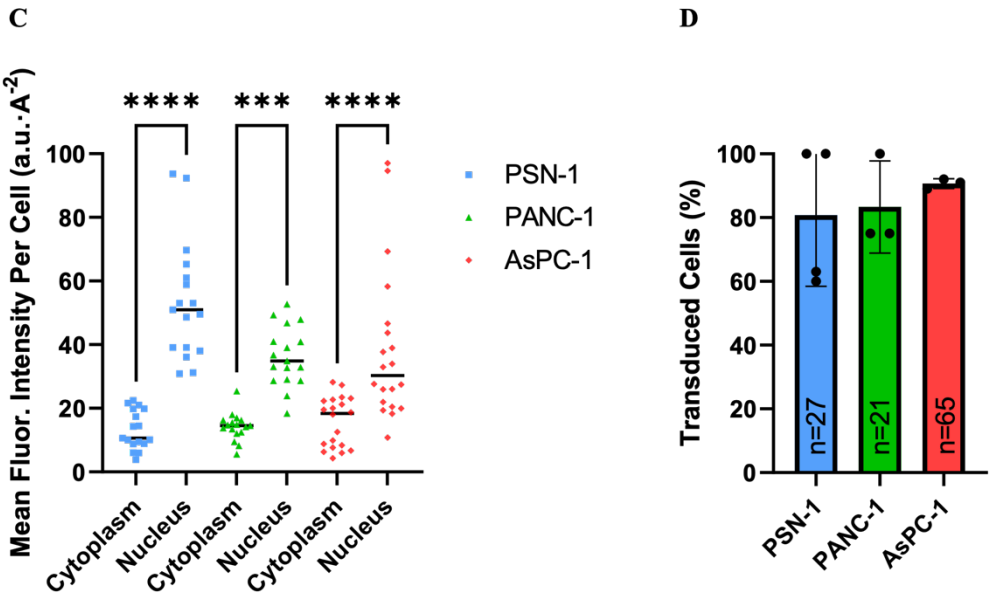
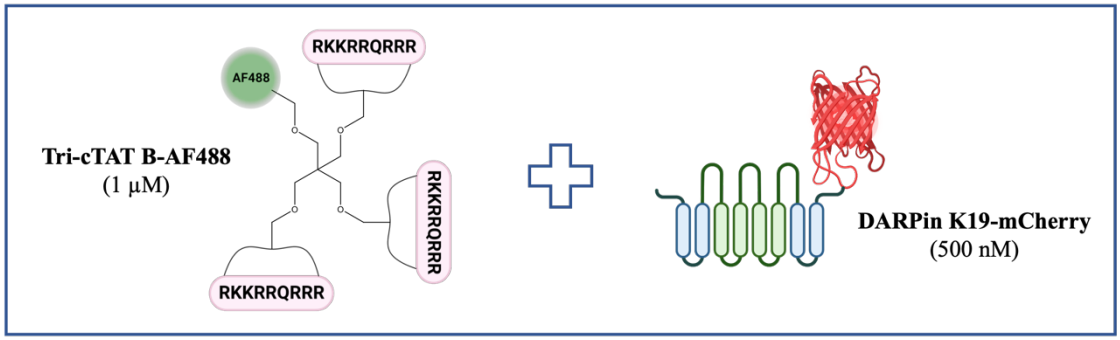


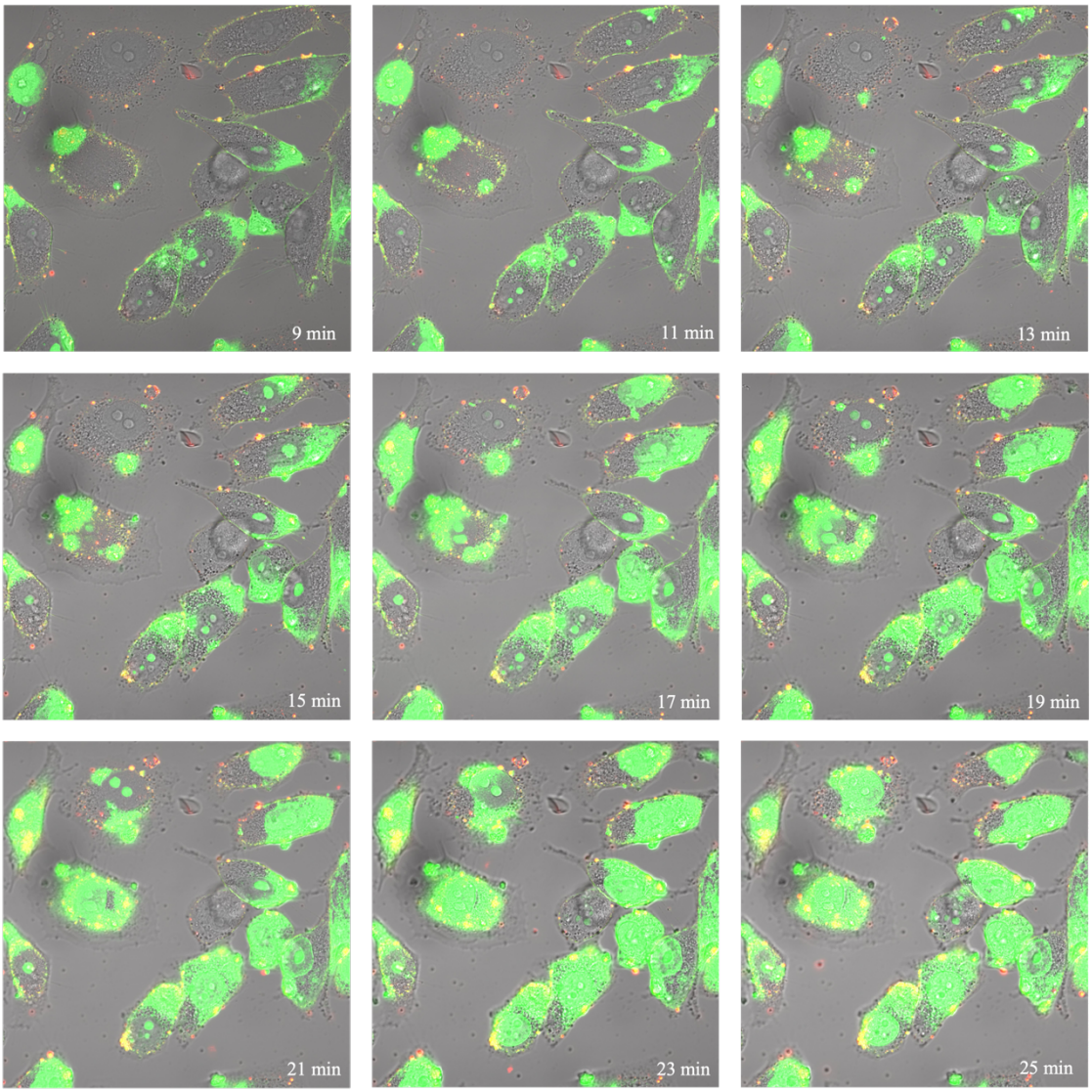
Figure 3.9 – Co-delivery of DARPin K19 in PDAC cell lines using Tri-cTAT B. Post-wash live-cell confocal microscopy images of **(A)** PSN-1, PANC-1 and AsPC-1 cells treated with 500 nM DARPin K19-mCherry (red channel) and 1 µM Tri-cTAT B-AF488 (green channel) for 60 minutes (37 ºC, 5% CO_2). Image **(A)** shows a homogeneous distribution of DARPin K19 in the cytosol and nucleus of cells, whilst the treatment of **(B)** PSN-1, PANC-1, and AsPC-1 cells incubated with 500 nM DARPin K19-mCherry alone (red channel) for 60 min resulted in failure of uptake into the cytosol or nucleus. **(C)** Mean fluorescence intensity of Tri-cTAT B and DARPin K19 in the cytoplasm and nucleus of PSN-1 (n=17), PANC-1 (n=17), and AsPC-1 (n=20) cells. **(D)** Percentage of cells transduced with DARPin K19 (scored as positive when showing homogeneous cytoplasmic and nuclear fluorescence). Data are presented as mean ± SD. One-way ANOVA and Tukey's test were employed in statistical analysis. *P* values: ***$P < 0.01$, ****$P < 0.0001$. Scale bars: 20 µm.

According to mathematical models, the net charge of DARPin K19 reveals a negative charge of -6.75 at pH 7.4, whilst Tri-cTAT B exhibits a positive charge at the same pH, primarily attributed to arginine and lysine residues. As a result, DARPin and Tri-cTAT B form strong electrostatic interactions. Importantly, the uptake of DARPin K19-mCherry was exclusively detected in cells co-treated with Tri-cTAT B, highlighting that the macromolecule does not internalise in the absence of the CPP (Figure 3.9B). Internalisation of DARPin K19 occurred in more than 80% of cells, highlighting the efficiency of Tri-cTAT B in delivering high molecular weight molecules into cells.

Having established the efficacy of Tri-cTAT B in co-delivering DARPin K19 in three PDAC cell lines, the kinetics of internalization of Tri-cTAT B and DARPin K19 was investigated. For this, PSN-1 cells were treated with 500 nM DARPin K19-mCherry and 1 μM Tri-cTAT B-AF488. Live-cell confocal microscopy was used to capture images at intervals of 120 seconds from 9 minutes to 30 minutes. As previously detected in HeLa cells, the presence of Tri-cTAT B and DARPin K19 were detected within the cytoplasm and nucleus of some cells after only 9 minutes (Figure 3.10A). Consistent with previous studies, the interaction between Tri-cTAT B and the cell membrane results in the formation of vesicular structures close to the membrane[258]. In this experiment, these structures, possibly endosomes, are visible as yellow *foci*, indicating the co-localization of Tri-cTAT B and DARPin K19.

A





PSN-1 ($KRAS^{G12R}$)

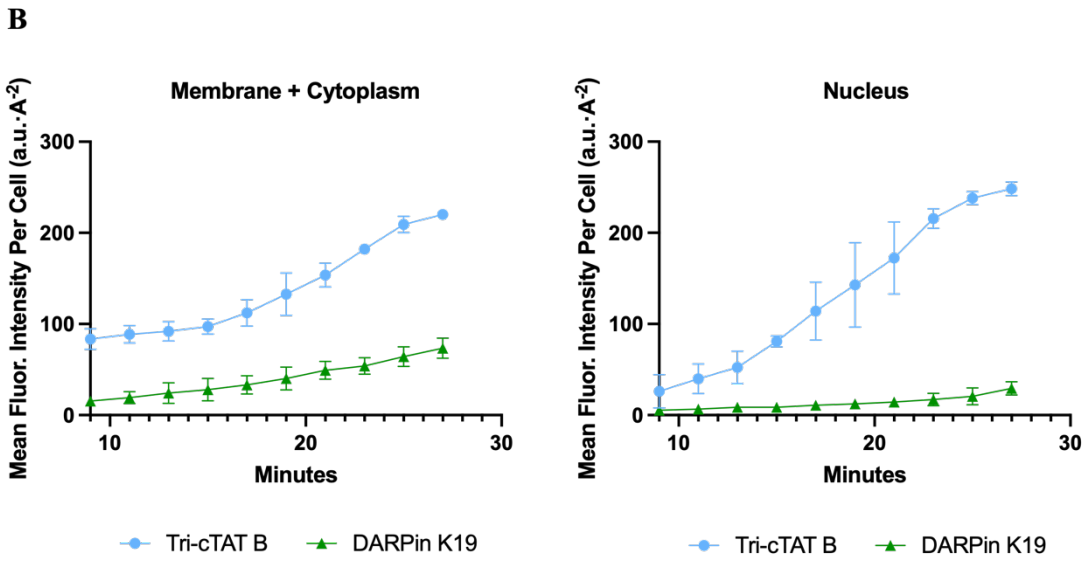


Figure 3.10 – Time-course uptake of DARPin K19 and Tri-cTAT B in PSN-1 cells. (A) Continuous live-cell confocal microscopy of PSN-1 cells treated with 500 nM DARPin K19-mCherry (red) and 1 µM Tri-cTAT B-AF488 (green). Images taken every 120 seconds for 21 minutes show a consistent uptake of Tri-cTAT B and DARPin K19 in the cytoplasm and nucleus, highlighted by the presence of yellow co-localized pixels. **(B)** Quantification of the mean fluorescence intensity of Tri-cTAT B and DARPin K19 over 18 minutes in the membrane + cytoplasm (left-hand side) and the nucleus (right-hand side) of PSN-1 cells (n=3). Data are presented as mean ± SD.

To quantify the internalisation of Tri-cTAT B and DARPin K19 in PSN-1 cells over time, regions of interest (ROIs) corresponding to the nucleus and nucleoli and the cytoplasm and cellular membrane (excluding endosomes) were delineated. Mean fluorescence intensities for each ROI, at all time points, in three cells (n=3) were calculated and plotted in Figure 3.10B. In accordance with images from Figure 3.10A, it is noticeable that there is a clear increase in the average fluorescence intensity for Tri-cTAT B and DARPin K19, observed both in the membrane and nucleus. Quantification of the average fluorescence intensity for Tri-cTAT B in the membrane reveals a modest increase during the first 8 minutes, followed by a steep increase in the subsequent 10 minutes. In the nucleus, Tri-cTAT B exhibits evident accumulation, characterized by a pronounced surge during the first 25 minutes, followed by a gradual increase in the last two time points, indicating a *plateau*. Similarly, the uptake of DARPin K19 in the membrane exhibits a progressive

increase over time, following the same pattern as observed with Tri-cTAT B. However, despite observing an increase in the mean fluorescence intensity of DARPin K19 in the nucleus, this was modest with data suggesting less than a 5-fold increase between minutes 9 and 27.

A closer analysis of the co-localization between the green and red channels suggested the possibility of a fluorescence bleed-through effect. To address this, a comparison of both channels within the same figure was made.

As previously addressed, the co-delivery of anti-KRas macromolecules by Tri-cTAT B lies in their electrostatic interaction. Additionally, due to the positively-charged nature of Tri-cTAT B and negatively-charged DARPin K19, this interaction will likely result in strong co-localized pixels. However, it cannot be assumed that images from different channels would be identical. Consequently, images containing the same ROI from different channels were overlayed, and their co-localization values were estimated based on Pearson's Correlation Coefficient. To exemplify, if two images were identical, they would yield a Pearson's Correlation Coefficient of one, whilst a complete absence of co-localisation would return a value of zero.

Analyses of images of PSN-1, PANC-1 and AsPC-1 cell lines, with internalised DARPin K19-mCherry and Tri-cTAT B-AF488 yielded Pearson's Correlation Coefficients between 0.6 and 0.8. Moreover, a one-way ANOVA analysis comparing a control group (r = 1) with experimental groups indicated statistical differences, confirming variations between images derived using different channels (Figure 3.11A). This suggests a robust interaction between DARPin K19 and Tri-cTAT B, due to the highly correlative but non-identical images from different channels.

In addition, the internalisation of DARPin K19 by Tri-cTAT B within PSN-1 and PANC-1 cells was explored *via* western blotting. For that purpose, cell lysates, previously treated with Tri-cTAT B + DARPin K19, were probed with a specific mCherry monoclonal antibody (Figure 3.11B). Notably, the results were highly consistent with previous data, as a distinct band corresponding to the size of the mCherry-DARPin K19 (45 kDa) was detected in the lysates of PSN-1 and PANC-1 cells that were exposed to Tri-cTAT B plus DARPin K19. In contrast, the control exhibited no detectable band.

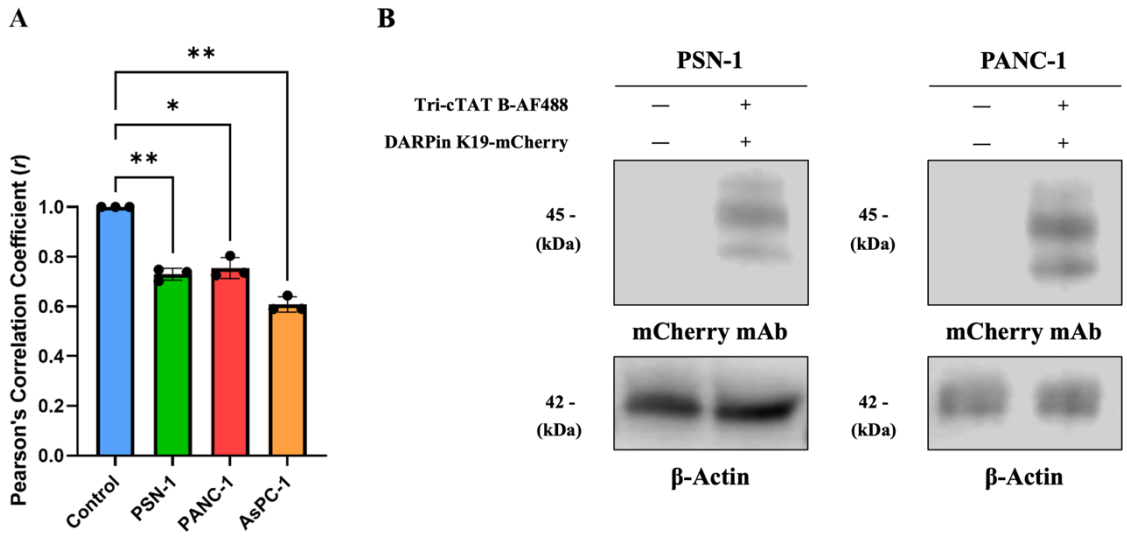


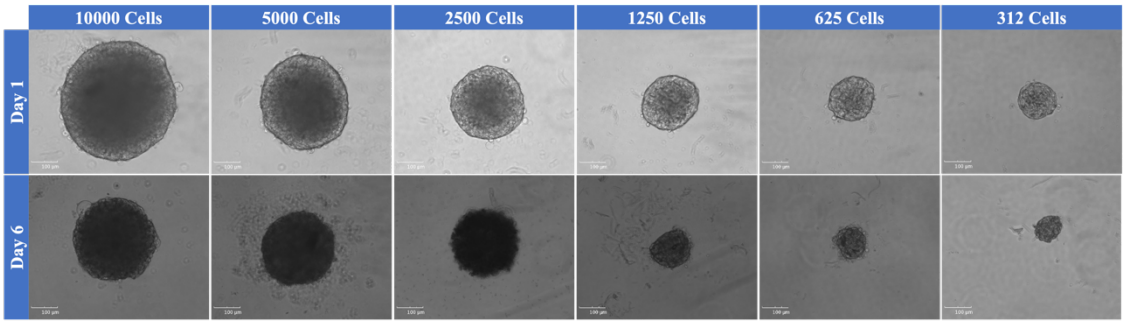
Figure 3.11 – Co-delivery of DARPin K19 confirmed by western blotting. (A) Quantification of the Pearson's Correlation Coefficient between two channels from the same figure indicates a strong correlation between DARPin K19 and Tri-cTAT B but a statistically significant difference between the experimental groups and a control group with an r=1. For each experimental group, three independent figures containing on average eight cells each were analysed. Control groups consisted of the overlay of two identical figures. Data are presented as mean ± SD (n=3). One-way ANOVA and Tukey's test were employed in statistical analysis. P values: *P < 0.02, **P < 0.005. **(B)** Western blot analysis of lysates from PSN-1 and PANC-1 cells exposed to 1 µm Tri-cTAT B-AF488 and 500 nM DARPin K19-mCherry for 60 minutes. Blots were incubated with mCherry monoclonal antibody, indicating the presence of a band corresponding to the size of the mCherry-DARPin K19 (45 kDa) in the experimental group. Lysates from control PSN-1 and PANC-1 cells yielded no detectable band. β-Actin was used as a loading control.

Despite the success in proving the internalisation of macromolecules with Tri-cTAT B in PDAC cell lines, 2D cell culture offers several limitations that can affect the relevance to

and accuracy of mimicking the in vivo cellular environment. These include the lack of physiological relevance since 2D cells grow on a flat surface, not mimicking the complex three-dimensional (3D) tissue architecture. Additionally, in 2D culture, cells are exposed to a homogeneous distribution of nutrients and oxygen, whilst in vivo cells experience concentration gradients of these factors, affecting basic cellular functions. Ultimately, the use of 3D models, including spheroids, represents a versatile model to recapitulate the heterogeneity and pathophysiology of human cancers. Therefore, the potential of Tri-cTAT B to deliver anti-KRAS macromolecules was investigated in 3D spheroids.

For this, PANC-1 cells were seeded in increasing quantities, and their growth was evaluated on day one and day six post-seeding. Within just one day, there was obvious formation of a stable cluster of cells with clearly defined borders (Figure 3.12A). Interestingly, upon evaluating their growth on day six, it was possible to observe a decrease in the diameter of the spheroids compared to day 1, suggesting a denser group of cells (Figure 3.12B). Spheroid viability was evaluated by measuring ATP activity. As expected, larger spheroids, comprising a greater number of cells, yielded a higher luminescence value, indicating a higher ATP activity (Figure 3.12C).

A



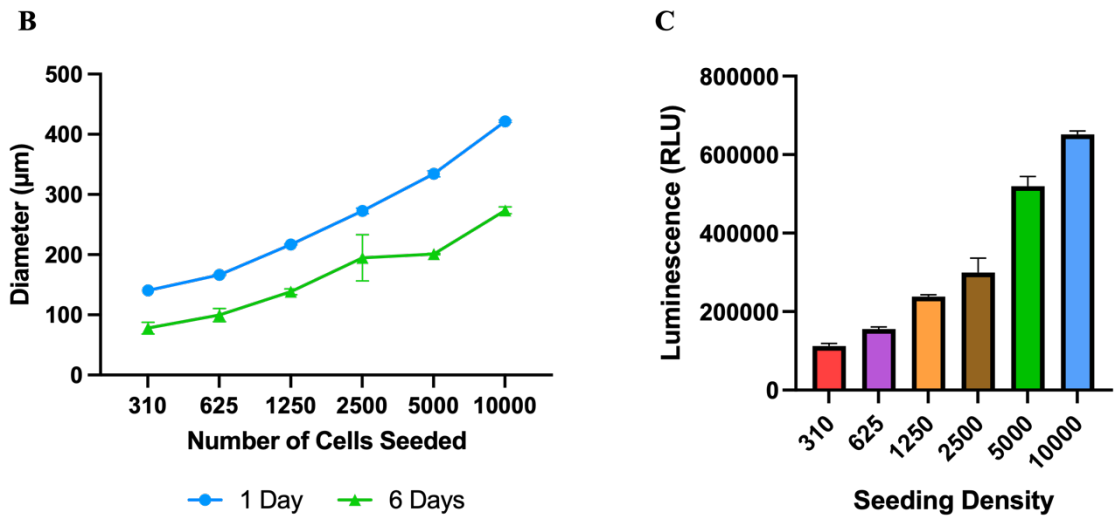
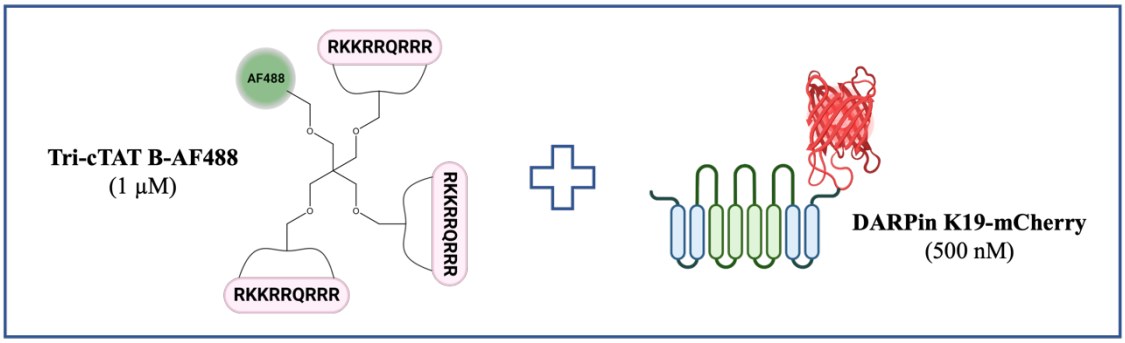


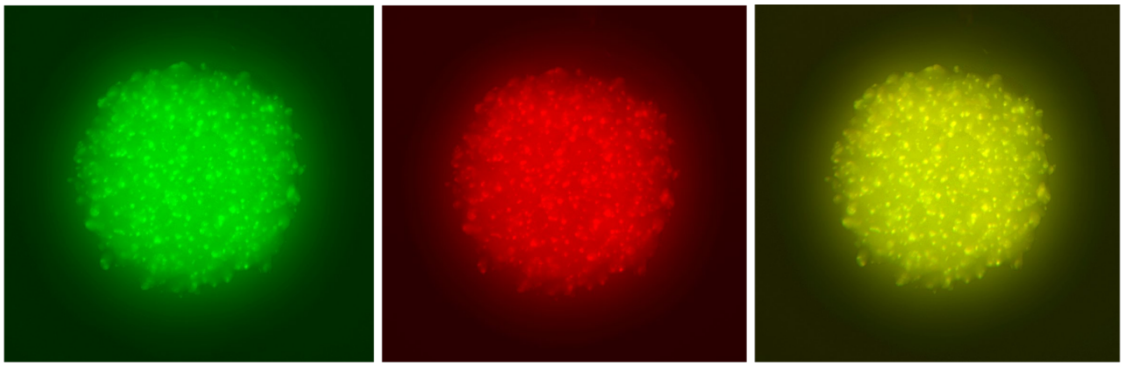
Figure 3.12 – Morphology of PANC-1 spheroids. (A) Evaluation of PANC-1 cell growth at day one and day 6 post-seeding with multiple cell densities. **(B)** Spheroid structures were analysed by measuring their diameter, indicating a decrease in this parameter between day one and day six. **(C)** The viability of each spheroid was assessed on day 6 by quantifying ATP activity through quantification of luminescence. Data are presented as mean ± SD. Scale bars: 100 µM.

To assess whether Tri-cTAT B could internalize macromolecules in 3D cultures, a spheroid with an initial seeding density of 2500 cells and a diameter of around 200 µm was selected. To be consistent, the spheroid was subjected to identical concentrations of Tri-cTAT B-AF488 (1 µM) and DARPin K19-mCherry (500 nM), as well as equivalent incubation periods as employed in 2D cell culture (Figure 3.13).

A



Tri-cTAT B **DARPin K19** **Merged**



B

Tri-cTAT B **DARPin K19**

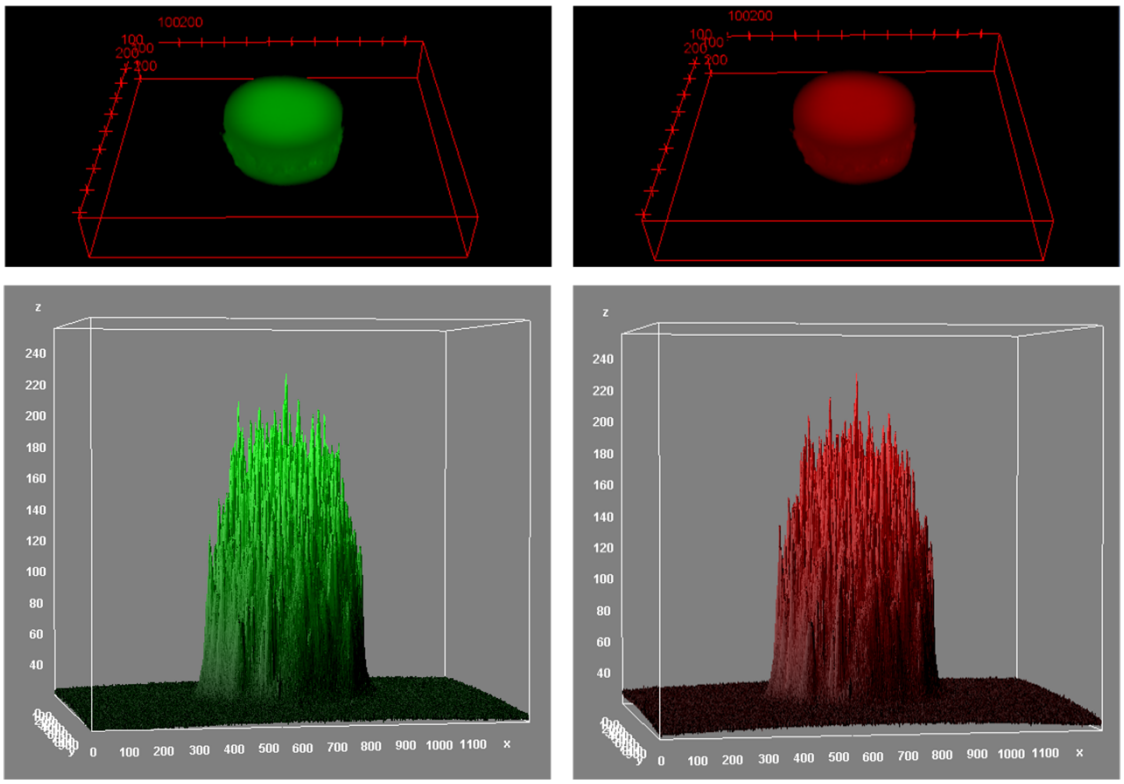


Figure 3.13 – Co-delivery of DARPin K19 in live PANC-1-derived spheroids using Tri-cTAT B. (A) Live-cell confocal microscopy images of PANC-1-derived spheroid treated with 500 nM DARPin K19-mCherry and 1 μM Tri-cTAT B-AF488 for 60 minutes shows a homogeneous distribution of both constructs across its surface. **(B)** PANC-1-derived 3D spheroid structure (top figure) was developed by performing a z-stack analysis based on the assembly of 200 slices of the spheroid taken at intervals of 2 μm across the Z-axis. Overall, the figure shows a well-defined 3D structure with precise borders and dimensions. Fluorophore intensity analysis (bottom) of a slice from the core of the spheroid suggests the presence of DARPin K19-mCherry (red) and Tri-cTAT B-AF488 (green) within the core of the spheroid.

The uptake of Tri-cTAT B and DARPin K19 was studied *via* live-cell confocal microscopy, with results suggesting the co-delivery of DARPin K19-mCherry (red channel) by Tri-cTAT B-AF488 (green channel) (Figure 3.13A). To further study the uptake of Tri-cTAT B and DARPin K19, as well as examine the morphological characteristics of the spheroid, a z-stack analysis was performed. 200 slices of the spheroid were captured at intervals of 2 μm along the Z-axis and subsequently assembled into an image of the 3D structure. Next, the internalisation of Tri-cTAT B and DARPin K19 into the core of the spheroid was explored. To do so, an analysis of the intensity of both fluorophores along the X-axis was performed by selecting a slice from the core of the fluorophore. According to the results, a higher fluorescence intensity along the Z-axis was observed when the X-axis and Y-axis aligned with the centre of the spheroid, suggesting the presence of both fluorophores within the core of the spheroid (Figure 3.13B).

To summarise this section of work, the ability of Tri-cTAT B to co-deliver macromolecules, namely DARPin K19, had been clearly demonstrated in 2D and 3D models. However, as shown in Figure 3.14 and quantified in Figure 3.9D, the uptake of DARPin K19 in PDAC cells is predominantly observed within the nucleus and nucleoli. Yet, KRas is mainly located at the inner leaflet of the cell membrane in a bivalent manner via the C-terminal HVR region and the CAAX motif[104,275]. As a result, it was

hypothesised that this arrangement could result in an off-target phenomenon and thus an inadequate biological effect.

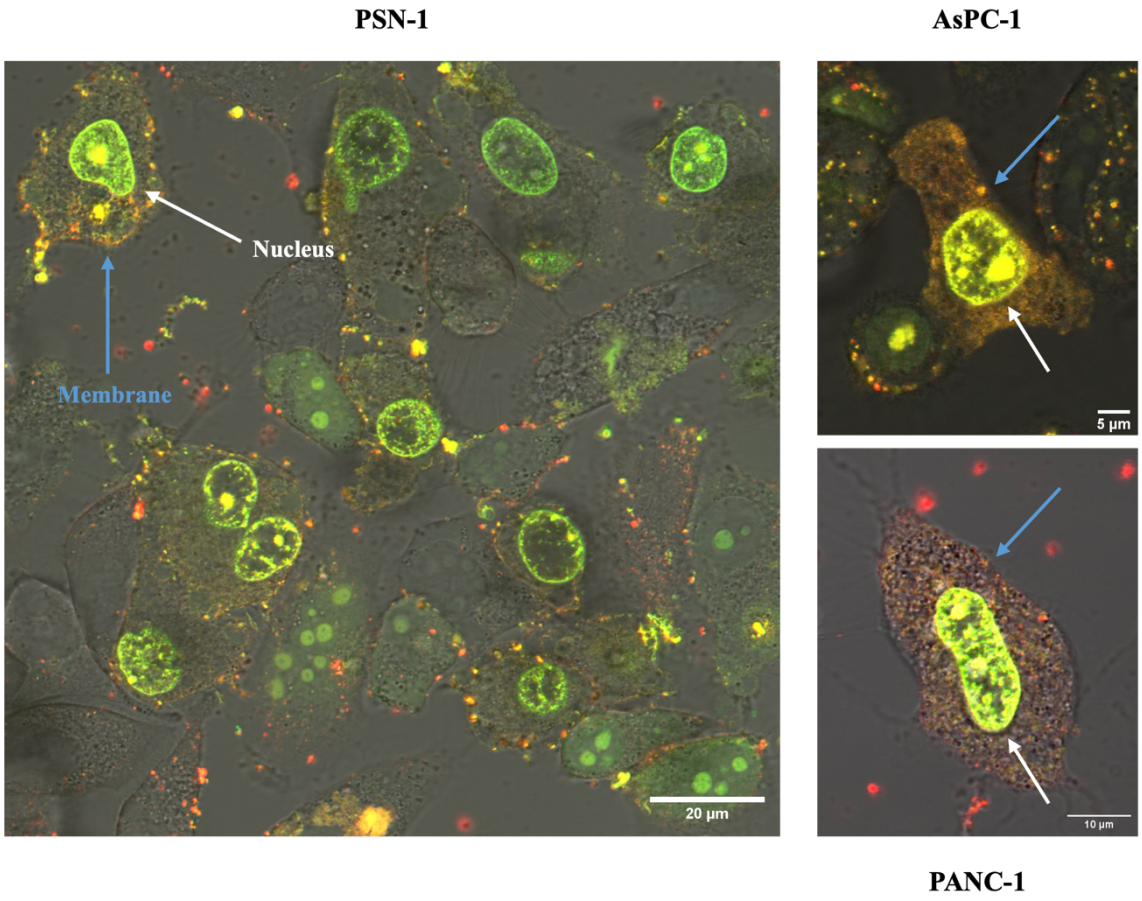


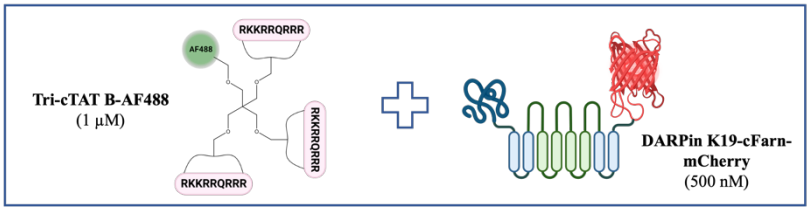
Figure 3.14 – DARPin K19-mCherry accumulation in PDAC cells. Co-delivery of 500 nM DARPin K19-mCherry with 1 µM Tri-cTAT B-AF488 for 60 minutes results in the accumulation of both constructs predominantly in the nucleus of PSN-1, PANC-1 and AsPC-1 cell lines. Images assembled by combining the red channel, representative of DARPin K19, and the green channel, showing Tri-cTAT B. Co-localization in yellow. Scale bars: 5 – 20 µm.

To address this concern, a second generation of DARPin K19 was synthesized by adding a farnesyl moiety to a cysteine residue near the C-terminal CAAX motif of the protein. Based on the literature, the addition of a farnesyl tag is crucial for the subcellular localization of certain proteins by facilitating their association with cellular membranes and allowing them to exert their biological activities within the appropriate cellular compartments[274]. Concomitantly, in collaboration with Professor Terry Rabbitts, the

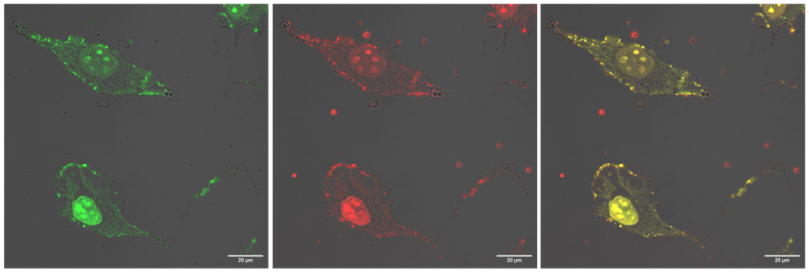
internalization of another anti-KRas macromolecule named anti-pan-Ras scFv Y6 was tested. Similarly to DARPin K19, these macromolecules were entirely developed by the Rabbitts Lab. Anti-KRas macromolecules containing a farnesyl group are designated DARPin K19-cFarn and anti-pan-RAS scFv Y6-cFarn.

Similar to DARPin K19, the uptake of DARPin K19-cFarn-mCherry or scFv Y6-cFarn-mCherry by Tri-cTAT B-AF488 was evaluated using live-cell confocal microscopy. Treatment of PSN-1 and PANC-1 cells with 500 nM DARPin K19-cFarn-mCherry and 1 μM Tri-cTAT B-AF488 for 1 h resulted in a significant redistribution, with a greater accumulation at the cell membrane compared to the unfarnesylated variant (Figure 3.15A). DARPin K19-cFarn and Tri-cTAT B were still detected in the nucleus, but their accumulation at the membrane was also clearly observed. Notwithstanding the natural affinity of TAT towards the nucleus, it was interesting to observe that the redistribution of DARPin K19 to the membrane resulted in the persistent occurrence of strong co-localization. This observation further reinforces the suggestion of physical, charge-mediated interaction between Tri-cTAT B and DARPin K19. Similarly, treatment of PANC-1 and PSN-1 cells with 500 nM scFv Y6-cFarn-mCherry with 1 μM Tri-cTAT B-AF488 for 1 h resulted in their accumulation within the cell membrane (Figure 3.15B). Notably, in PSN-1 cells, signals derived from Tri-cTAT B and scFv Y6-cFarn were exclusively detected in the cell membrane. Following treatment of cells with DARPin K19-cFarn-mCherry or scFv Y6-cFarn-mCherry for 1 h in the absence of Tri-cTAT B there was no detectable internalisation of either protein (Figure 3.15C).

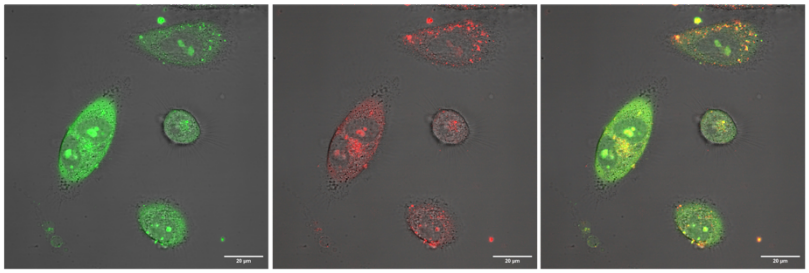
A



Tri-cTAT B | DARPin K19-cFarn | Merged

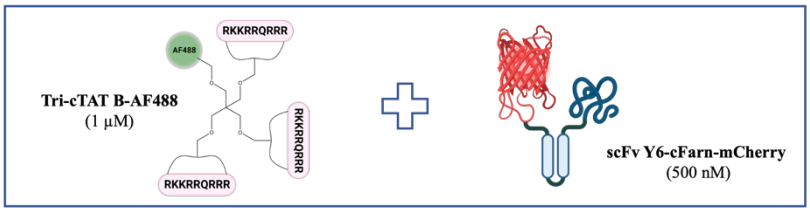


PANC-1 (KRAS^{G12D})

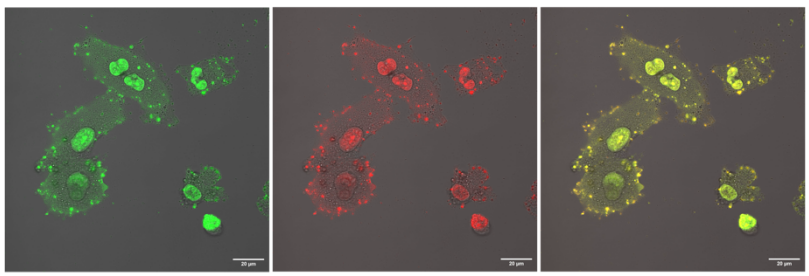


PSN-1 (KRAS^{G12R})

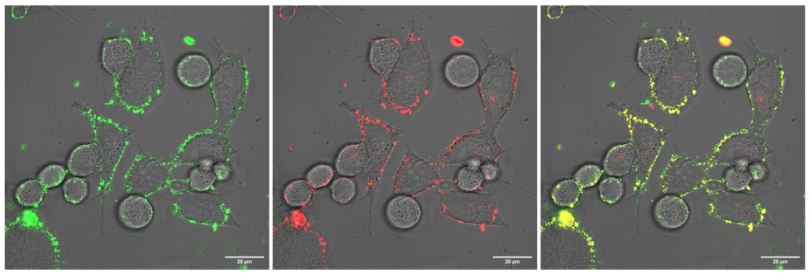
B



Tri-cTAT B | DARPin K19-cFarn | Merged



PANC-1 (KRAS^{G12D})



PSN-1 (KRAS^{G12R})

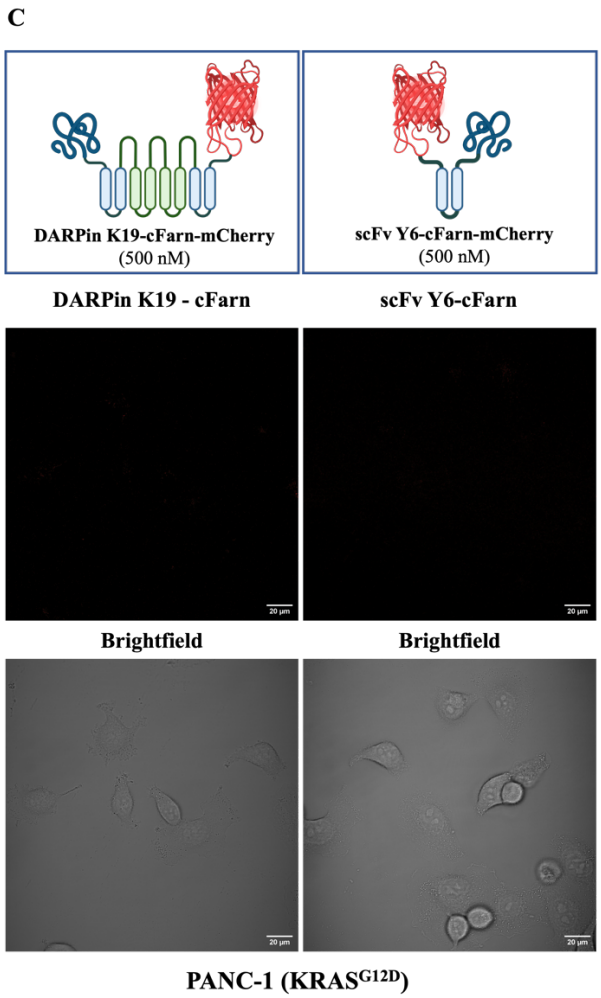
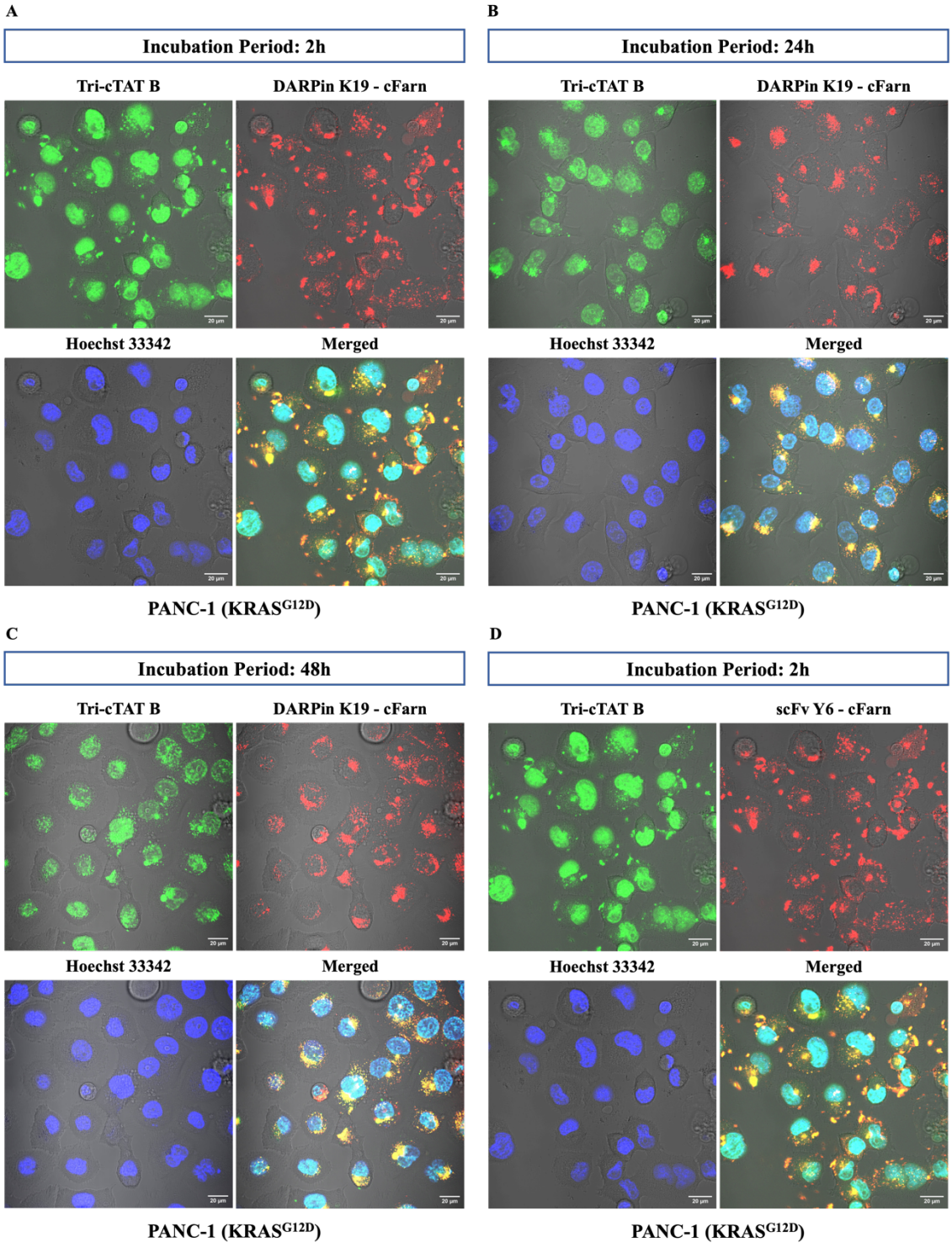


Figure 3.15 - Co-delivery of modified anti-KRas macromolecules in PDAC cell lines using Tri-cTAT B. Post-wash live-cell confocal microscopy images of PSN-1 and PANC-1 cells treated with **(A)** 500 nM DARPin K19-cFarn-mCherry or **(B)** 500 nM scFv Y6-cFarn-mCherry (red channel) and 1 µM Tri-cTAT B-AF488 (green channel) for 1 h. Co-localized pixels are represented in yellow. **(B)** Post-wash live-cell confocal microscopy images of PSN-1 and PANC-1 cells treated with 500 nM DARPin K19-cFarn-mCherry or 500 nM scFv Y6-cFarn-mCherry (red channel) for 1 h shows there is no internalisation in the absence of Tri-cTAT B.

The addition of a farnesyl group to DARPin K19 and scFv Y6 resulted in a stronger association with the cell membrane. Given the known rapid uptake of anti-KRas macromolecules by Tri-cTAT B in PDAC cell lines, an early time point of 1 h had been selected. Longer incubation periods were also investigated to assess the temporal pattern of association between farnesylated anti-KRAS macromolecules and the inner cell membrane. For that purpose, PANC-1 cells were treated with DARPin K19-cFarn-

mCherry or scFv Y6-cFarn-mCherry and Tri-cTAT B-AF488 and images obtained at 2, 24 and 48 h (Figure 3.16).



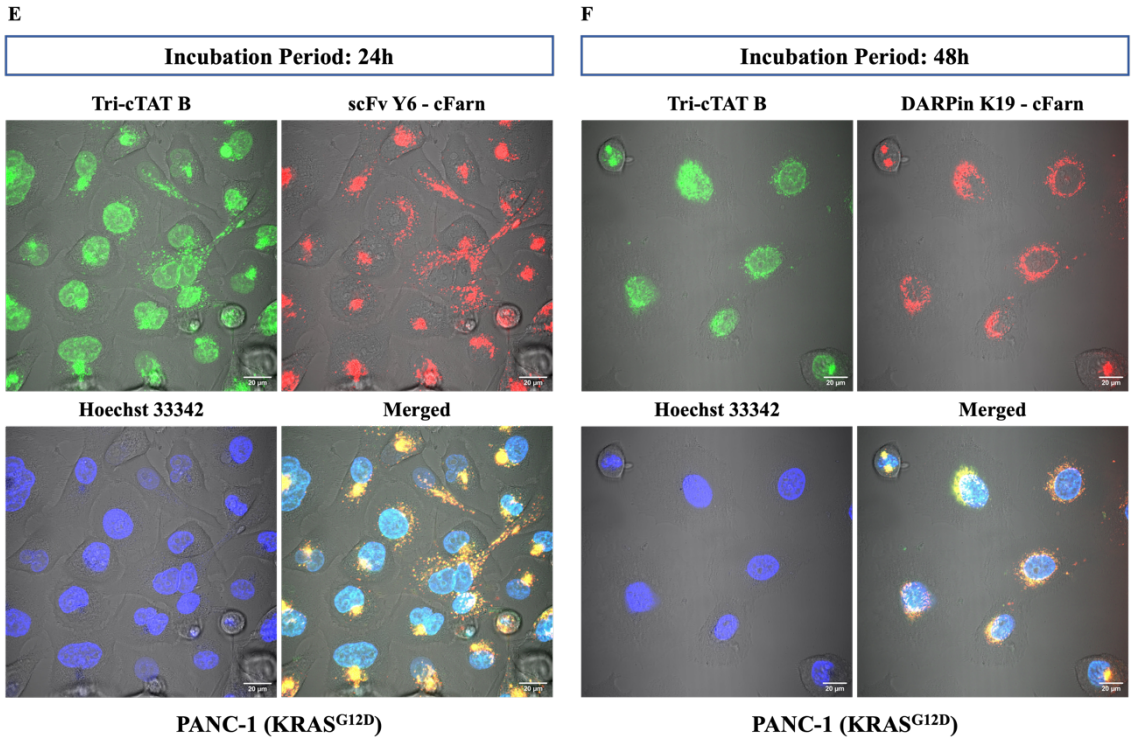


Figure 3.16 - Distribution of farnesylated anti-KRas macromolecules over 48 h. Post-wash live-cell confocal microscopy images of PANC-1 cells treated with **(A), (B),** and **(C)** 500 nM DARPin K19-cFarn-mCherry or **(D), (E),** and **(F)** 500 nM scFv Y6-cFarn-mCherry (red channel) and 1 µM Tri-cTAT B-AF488 (green channel) for 1 h. Confocal microscopy images were taken at **(A)**, **(D)** 2-, **(B)**, **(E)** 24-, and **(C)**, **(F)** 48 h post-treatment show a re-distribution and perinuclear accumulation of farnesylated anti-KRAS macromolecules. Co-localization in yellow and Hoechst 33342 was used as a nuclear stain.

According to the results of immunofluorescence microscopy, a similar re-distribution pattern was observed for both DARPin K19-cFarn-mCherry and scFv Y6-cFarn-mCherry within PANC-1 cells over 48 h. Similar to the observations made at 1 h, there was a clear accumulation of DARPin K19-cFarn or scFv Y6-cFarn at the cell membrane (Figure 3.16A and D). However, after 24 h, a noticeable shift towards the cytoplasm was observed, with limited signal detected in the membrane (Figure 3.16B and E). At 48 h, intense co-localization between DARPin K19-cFarn or scFv Y6-cFarn and Tri-cTAT B

was visible (Figure 3.16C and F). At 48 h, the nuclear signal for DARPin K19-cFarn or scFv Y6-cFarn had diminished, but perinuclear accumulation persisted.

3.3.4. Co-Delivery of Anti-KRas^{G12D} Antibody Interacts with KRas

To determine whether internalised macromolecules retain their ability to bind to the intended epitope, a Duolink® Proximity Ligation Assay (PLA) was employed, enabling the study and quantification of endogenous protein-protein interactions (PPIs) using confocal microscopy.

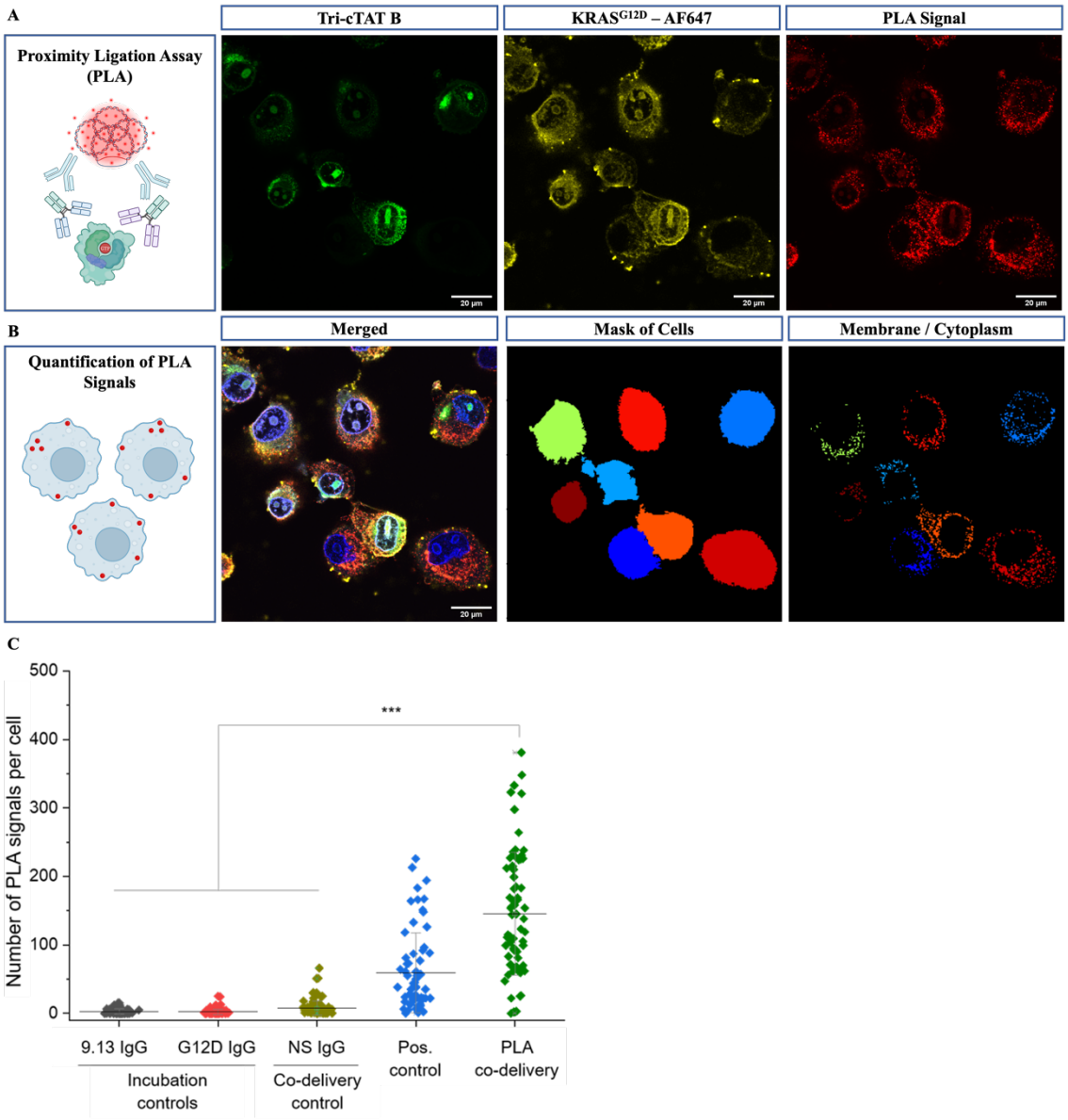
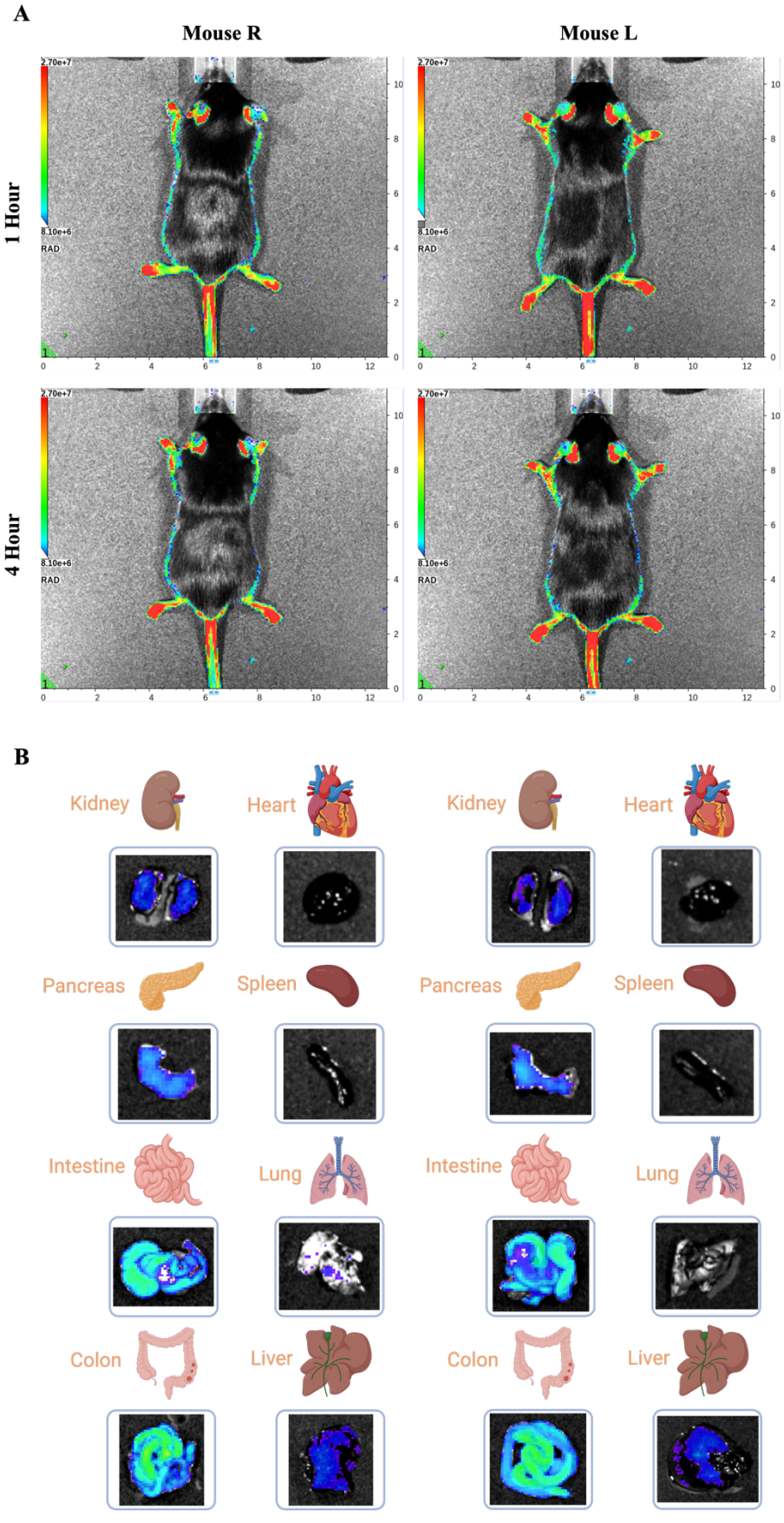


Figure 3.17 - Proximity ligation assay (PLA). PLA was performed in PANC-1 cells using a G12D-AF647 Ras antibody and a 9.13 KRAS antibody. G12D-AF647 (166 nM) was co-delivered into cells using Tri-cTAT B (1 μM, 60 minutes incubation at 37 ˚C, 5% CO_2). Negative controls consisted of Tri-cTAT B-mediated internalisation of rabbit non-specific (ns) antibody (166 nM IgG, 1 μM tri-cTat B, 60 minutes incubation at 37 ˚C, 5% CO_2) and incubation with 9.13 and G12D KRas antibodies after fixation and permeabilization of cells. **(A)** Confocal microscopy images show the distribution of Tri-cTAT B (green), anti-$KRas^{G12D}$-AF647 IgG (yellow), and the detection of PLA signals (red). **(B)** Overlay of the fluorescent channels with Hoechst 33342 and BioTracker™ 400 allowed the quantification of the PLA signals in the cell cytoplasm using CellProfiler and represented using Origin. Data presented as mean ± SD (n=50). One-way ANOVA and Tukey's test were employed in statistical analysis. *P* values: *** $P < 0.001$.

The PLA signal in PANC-1 cells that were treated with Tri-cTAT B-AF488 and anti-KRAS^{G12D} IgG-AF647, followed by anti-KRAS 9.13 IgG, was significantly higher than in cells incubated with either anti-KRas^{G12D} IgG-AF647 or anti-KRAS 9.13 IgG alone (Figure 3.17). Controls were co-delivered non-specific IgG plus Tri-cTAT B, and the incubation of anti-KRAS^{G12D} IgG and anti-KRAS 9.13 IgG after cells were fixed and permeabilized, resulting in a limited number of PLA signals. Overall, this provides evidence that anti-KRas IgG co-delivered Tri-cTAT B is functional, retaining the ability to bind its target epitope.

3.3.5. *In vivo* Uptake of Tri-cTAT B

A preliminary experiment to assess the in vivo biodistribution of Tri-cTAT B was performed. Due to the limited quantity of CPP available, each mouse received 0.5 μM (3.5 μg) of Tri-cTAT B-AF488 instead of the typical 1 μM that was used in previous studies *in vitro*. To evaluate the uptake of Tri-cTAT B-AF488, fluorescence images were taken at 1 h and 4 h post-injection (p.i.), with fluorescence being detected only in the regions where fur is not present and possibly creating a misleading idea about the *in vivo* distribution of Tri-cTAT B-AF488 (Figure 3.18A). At 4 h p.i., the mice were euthanised and organs removed to enable quantification of tracer within each organ (Figure 3.18B and 3.18C). Ex vivo organ uptake revealed a distinct fluorescence signal in the liver, kidney, and pancreas. The highest uptake was detected in the pancreas, whilst the lowest fluorescence signal arose from the spleen. Additionally, the ex vivo uptake of Tri-cTAT B-AF488 was found to be similar in both mice, as indicated by the small error bars in Figure 3.18C. Despite an intense fluorescence signal detected in the intestine and colon, its significance was discarded. The reason for this is that the chow-fed to the animals emits fluorescence at this wavelength. Consequently, any fluorescence detected in organs of the gastrointestinal (GI) tract, including the stomach, intestine, and colon, was not considered for analysis. Statistical analysis involving the uptake of Tri-cTAT B-AF488 was done by comparing the fluorescence signal from the spleen with the other organs of interest.


A
Mouse R
Mouse L
1 Hour
4 Hour
2.70e+7
8.10e+6
RAD
B
Kidney
Heart
Pancreas
Spleen
Intestine
Lung
Colon
Liver

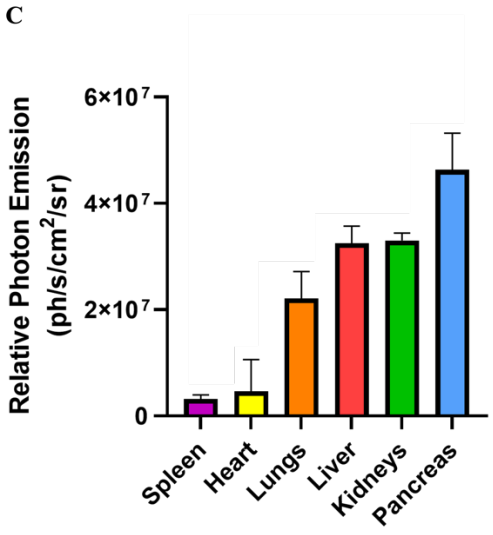


Figure 3.18 - Tri-cTAT B-AF488 distribution *in vivo*. (A) 3.5 µg Tri-cTAT B-AF488 was administered to two C57BL/6 mice *via* the tail vein, and its uptake was studied by using the IVIS Spectrum system operating with 500/ 560 nm excitation/ emission filters at the fluorescence mode. Images were acquired at 1 h and 4 h post-treatment. **(B)** *Ex vivo* biodistribution analysis within different organs of interest shows a modest uptake of Tri-cTAT B-AF488. Since the food administered emits fluorescence at the studied wavelength, the signal detected in the GI tract was disregarded. **(C)** The fluorescence quantification analysis reveals a statistically significant uptake of Tri-cTAT B in the pancreas, kidneys, and liver, as compared to the spleen.

3.4. Discussion

Under normal biological conditions, molecules with a molecular weight of 1 kDa or more do not spontaneously transfer across cell membranes, limiting their uptake into the intracellular environment. However, the intracellular environment hosts many cancer proteins of enormous biological significance, making them valuable targets for the development of therapeutic agents. Since the discovery of the HIV transcription factor TAT in the late 1980s, the use of CPPs has been seen as a viable way to deliver macromolecules into cells without affecting their integrity and function. This chapter explored the optimisation of the synthesis of a novel TAT-derived CPP, Tri-cTAT B, and its uptake in a group of PDAC cell lines harbouring KRAS mutations. Additionally, the ability of Tri-cTAT B to transfect macromolecules with a molecular weight of around 50

kDa in increasingly more complex environments, ranging from 2D to 3D cell culture, was assessed. Finally, the co-delivery of functional anti-KRas antibodies and their subsequent interaction with KRAS was explored. Overall, the objective was to study the potential of Tri-cTAT B as a therapeutic intermediate in delivering potent and specific macromolecules against key cancer-related intracellular targets such as mutant KRas.

3.4.1. Tri-cTAT B Mediates the Delivery of Anti-KRas Macromolecules in Cells

Following the optimisation of the synthesis of Tri-cTAT B, the first aim of this chapter was to evaluate the uptake of Tri-cTAT B and its ability to transfect macromolecules into PDAC cell lines.

As shown in Figures 3.8 and 3.9, Tri-cTAT B successfully transfected DARPin K19-mCherry into PSN-1, PANC-1 and AsPC-1 cells. Importantly, the mean fluorescence intensity of Tri-cTAT B-AF488 was 36- and 136-fold higher in PANC-1 and PSN-1 cells, respectively, than the mean fluorescence intensity of PANC-1 and PSN-1 cells treated with Mono-TAT-AF488. Despite using a different cell line, HeLa, these findings follow the conclusions provided by Tietz and colleagues by showing a 50-fold difference between cells treated with Tri-cTAT B-AF488 and Mono-TAT-AF488[258]. The uptake of Tri-cTAT B and DARPin K19 was detected as early as 9 minutes, which was also consistent with the results reported by Tietz et al.[258].

Comparison with other CPPs reveals that the cyclisation of TAT, along with its subsequent trimeric formation, does enhances the rate of internalisation[275]. Conversely, whereas other TAT-derived CPPs require concentrations exceeding 10 μM, Tri-cTAT B achieves proficient transfection of functional macromolecules at a concentration of 1 μM[253]. At these concentrations, CPPs are often toxic to cells, and given the non-specific targeting of CPPs to tumour cells, their clinical applicability becomes compromised[203]. Hence, the use of Tri-cTAT B emerges as a promising clinical application as it requires

one-tenth of the conventional CPP concentration, mitigating potential cytotoxicity concerns associated with higher doses.

Not surprisingly, live-cell images showed higher uptake of Tri-cTAT B in the nucleus, supporting data that suggests TAT's affinity to accumulate within this organelle[273]. However, data also showed higher uptake of DARPin K19-mCherry in the nucleus, highlighted by the strong colocalisation signal. Aware that the co-delivery of DARPin K19 by Tri-cTAT B is purely based on electrostatic interactions, this result suggests a strong affinity between both constructs. While these observations support similar studies by showing that TAT-derived CPPs are valuable carriers for functional antibodies, the accumulation of DARPin K19 in the nucleus might lead to an inadequate biological effect, given KRas location at the inner leaflet of membranes[258,276].

Alternatively, structural modifications on DARPin K19 and scFv Y6 were pursued by the addition of a farnesyl tag. Equally used by KRas to promote its activation, live-cell images revealed the accumulation of DARPin K19-cFarn-mCherry at the membrane[277]. Although the synthesis of unfarnesylated scFv Y6-mCherry was not pursued, thus impeding comparisons, treatment of cells with scFv Y6-cFarn-mCherry showed a pronounced accumulation on the membrane, particularly highlighted in PSN-1 cells. Interestingly, notwithstanding the translocation of DARPin K19 and scFv Y6 to the membrane, a similar phenomenon involving Tri-cTAT B was seen. Whilst the initial hypothesis aimed at the segregation of both constructs upon cellular internalisation, microscopy figures revealed a continuous interaction between the two, underscoring their robust electrostatic interaction. Nonetheless, the addition of a farnesyl tag proved to be a critical modification, promoting the accumulation of anti-KRas macromolecules in the membrane, supporting findings that highlight their potential to facilitate membrane association[278]. However, longer incubation periods exposed a shift between 2 h and 24 h, implying the binding

affinity between Tri-cTAT B and the nucleus exceeds the anchoring strength exerted by the farnesylated tag. Yet, after 48 h, the signal derived from Tri-cTAT B shifted to the nucleus whilst the signal from farnesylated anti-KRas macromolecules remained on the outer layer of the nuclear membrane. These observations suggest the role of the farnesyl tag in anchoring DARPin K19 and scFv to the nuclear membrane, impeding them from crossing the nuclear membrane. Despite not providing further evidence about this hypothesis, studies show the importance of farnesyl moieties in the lamin protein family by facilitating localisation and retention at the inner nuclear envelope[279]. Furthermore, this allows to hypothesise about the use of this strategy as a viable approach to other internal targets that could be inhibited using organelle-specific modifications of immune molecules.

3.4.2. Tri-cTAT B Enables Intact Co-Delivery of DARPin K19 in 3D Spheroids

Next, the internalisation of DARPin K19 using Tri-cTAT B was explored in PANC-1-derived spheroids (Figure 3.13). Importantly, the use of 3D cell models allowed to evaluate the ability of Tri-cTAT B in transfecting DARPin K19 into more complex systems, allowing to replicate the heterogeneity and pathophysiology of human cancers[280]. Similar to 2D cell models, DARPin K19, in combination with Tri-cTAT B, was readily detected by live-cell microscopy, with further analysis revealing the presence of Tri-cTAT B and DARPin K19 in the spheroid's core. Given the novelty around Tri-cTAT B, their use in spheroids was, for the first time, evaluated in this work, impeding comparisons with other studies. Nonetheless, previous investigations have explored the internalisation of other CPPs, particularly TAT, in spheroids. Similar to 2D models, the uptake of monomeric TAT at low concentrations proves to be inadequate, limiting its use as a macromolecule transporter. In one study, Rahman and colleagues investigated the efficacy of monomeric TAT in human CRC cell line HT-29-derived spheroids, using

incubation periods akin to those employed in this thesis (1 h)[281]. Surprisingly, for a treatment involving 1 μM TAT at 37 °C for 1 h, the authors observed CPP in only 4% of cells. On the other hand, exposure of PANC-1-derived spheroids with Tri-cTAT B at an equivalent concentration to the one used by Rahman and colleagues with TAT revealed the presence of Tri-cTAT B in the whole structure. As previously described for 2D models, efficient TAT transfections are only detected at high concentrations. In this particular study, Rahman *et al*. detected TAT uptake in 77% of cells only when a concentration of 25 μM was used. As previously reported, TAT concentrations greater than 10 μM are anticipated to be toxic for cells, thereby invalidating its application in the clinic[203]. On the other hand, Tri-cTAT B proves to be highly effective, without compromising the viability of non-tumour cells. Although the use of antibodies offers advantages in comparison with small molecules, their large size can be problematic, causing poor tissue/tumour penetrance[282]. However, the internalisation of anti-KRas macromolecules with Tri-cTAT B offers a viable alternative to overcome this problem, at least in small-volume tumours.

3.4.3. Tri-cTAT B Facilitates the Interaction of a KRas^{G12D} IgG with KRas

Following the transfection of functional antibodies in PANC-1 cells, their interaction with KRas was explored using PLA. According to Figure 3.17, the experimental group, composed by the co-delivery of an anti-KRas^{G12D} IgG, exhibited greater PLA signals than the control group ($P<0.001$), comprised by the co-delivery of a non-specific antibody. Additionally, the experimental group yielded higher PLA signals than the positive control. These observations align with the findings of Tietz and colleagues, underscoring that the co-delivery of functional antibodies not only facilitated interaction with its target but also had no detrimental effects on its viability[258]. Importantly, it is essential to note that protein-protein interactions were assessed using an IgG and not DARPin K19 or scFv

Y6. However, based on the nature of the PLA assay, it is imperative to use a structure that can be easily recognised by a secondary antibody. As a suitable secondary antibody for DARPin K19 or scFv Y6 could not be identified, the interaction between an anti-KRas macromolecule and KRas upon internalisation with Tri-cTAT B was conducted using an IgG. Nonetheless, this alternative does not compromise the overall objective of this assay by studying if the internalisation of functional immune molecules with Tri-cTAT B causes their interaction with the target. Importantly, the detection of PLA signals is only possible when the two antibodies are within 40 Å of each other. Consequently, this provides irrefutable evidence about the physical interaction between the co-delivered anti-$KRAS^{G12D}$ IgG and KRas.

3.4.4. Tri-cTAT B Demonstrates Multi-Organ Uptake *In Vivo*

Although *in vitro* technologies have advanced to replicate the pathophysiology of human cancers, *in vivo* models remain an essential part of the drug development process. Amongst other advantages, *in vivo* models allow a comprehensive study of how drugs interact in complex physiological environments, enabling the study of pharmacokinetic and pharmacodynamic properties, as well as drug interactions. Additionally, they offer valuable insights regarding a drug's efficacy and safety before moving to more advanced stages. Consequently, the uptake of Tri-cTAT B *in vivo* was explored (Figure 3.18). Importantly, whilst other studies involved the use of 1 µM Tri-cTAT B, *in vivo* analyses were performed with a concentration of 0.5 µM (3.5 µg) Tri-cTAT B, owing to the limited availability of CPP. However, even at low concentrations, the uptake of Tri-cTAT B was detected in key organs, including the pancreas. Similar to the internalisation of Tri-cTAT B in 3D models, *in vivo* studies with Tri-cTAT B were, for the first time, reported in this thesis, thus impeding comparisons with other studies. Nonetheless, other studies have looked at the efficacy of TAT *in vivo*. Despite Lee and colleagues previously investigating

the uptake of TAT in vivo using [^{125}I], their results demonstrated higher TAT accumulation in organs such as kidneys, liver, lung and heart[283] – coincidentally, the same organs where Tri-cTAT B exhibited a higher presence. Interestingly, the authors do not report any uptake in the pancreas. Similarly, Kim *et al*. described equivalent findings by showing a higher uptake of TAT in the kidneys, liver, lungs and heart[284]. Notably, whilst Lee and colleagues do not report TAT's uptake in the spleen, Kim *et al*. do, aligning with the distribution pattern seen with Tri-cTAT B, albeit to a lower extent. Similar to Lee and colleagues, Kim *et al*. do not describe any uptake in the pancreas. Therefore, these findings collectively suggest that the alterations made to TAT have facilitated its enhanced uptake within the pancreas. On the other hand, both studies report the uptake of TAT in the brain, whereas, with Tri-cTAT B, no detectable uptake within the brain was observed, suggesting that its increased molecular weight might affect the penetration across the blood-brain barrier.

Chapter 4 Biological Effect of the Co-Delivery of Anti-KRas Immune Molecules in PDAC Cancer Cells

4.1. Introduction

In the previous chapter, it was shown that the co-delivery of functional anti-KRas antibodies into PDAC cells is possible with Tri-cTAT B and that their internalisation results in the interaction with KRas proteins. The next part of the research plan was to investigate whether internalisation leads to significant biological responses. To do so, two main objectives were pursued in this chapter: investigating the downregulation of proteins activated by KRas and studying the viability of cells following their treatment with Tri-cTAT B + anti-KRas macromolecules.

As reported by Rabbitts and colleagues, transfection of DARPin K19 through a plasmid containing the macromolecule sequence into HCT116 cells, a colorectal cell line harbouring the $KRAS^{G13D}$ mutation, decreases the phosphorylation of MEK/ERK and PI3K/AKT kinases[261]. Interestingly, DARPin K19 does not affect the downregulation of either of these pathways in cell lines with NRAS or HRAS mutations. Importantly, treatment of MCF-7 cells, a RAS^{WT} cancer cell line, with DARPin K19, results in no significant downregulation of proteins activated by RAS, showing that it has a selective potential towards endogenous mutant KRas.

Similarly, treatment of NIH/3T3 cells, transfected with plasmids expressing mutant $HRAS^{G12V}$, with scFv Y6, resulted in the downregulation of phosphorylated ERK1/2 and AKT kinases[265]. Interestingly, whilst a decrease in the phosphorylation level of ERK and AKT kinases was detected 24 h after cells were treated with DARPin K19-containing plasmid, the same effect was only observed 48 h after cells were treated with scFv Y6-containing plasmid. Nonetheless, even though scFv Y6 shows higher affinity towards KRAS than DARPin K19, it is incorrect in this case to compare the effect of the two since different cell lines were used.

Despite the function of KRas in regulating several cell processes, including cell proliferation, migration, transformation, and survival, *via* signalling pathways and transcription factors, other GTPases are known to have similar functions[45,285]. As a result, the downregulation of KRas in cells whose survival is KRas-independent leads to a resistance mechanism in which cells activate other GTPases to promote tumorigenesis. In PDAC, studies have been focusing on understanding whether cell lines are KRas-dependent or KRas-independent. In 2009, Settleman and colleagues reported a study in which short hairpin RNAs were used to deplete KRas in lung and pancreatic cancer cell lines harbouring KRAS mutations. Based on their findings, Settleman *et al*. developed a

Ras dependency index, showing that while PANC-1 cells ($KRAS^{G12D}$) have a low dependency on KRas for their survival, the survival of CAPAN-1 cells ($KRAS^{G12V}$) is highly KRas-dependent[286]. The development of innovative techniques, such as CRISPR/Cas9, allowed researchers to modify the genome of eukaryotic cells, thus permitting the study of the importance of certain genes, including RAS. Based on a CRISPR/Cas-mediated KRAS knockout, Jacks and colleagues studied the survival of pancreatic cancer cells lacking KRAS. Interestingly, in their report, the authors showed that KRAS knockout in PANC-1 cells led to a dose-dependent effect on the proliferation of cells compared to intact clones of PANC-1 cells[287,288]. Despite strong results, the authors were unable to generate KRAS-deficient clones of several cell lines using CRISPR/Cas-mediated KRAS knockout, including YAPC ($KRAS^{G12V}$), 8902 ($KRAS^{G12V}$), and PSN-1 ($KRAS^{G12R}$).

Alternatively, over the past two decades, researchers have looked to target kinases that are activated by KRas, including MEK, ERK, PI3K, and AKT. However, this approach has proven broadly unsuccessful due to the inhibitory crosstalk between different KRas pathways[115]. Thus, this approach is often seen as a temporary solution. To overcome the crosstalk between the PI3K/AKT and MAPK pathways, scientists started to investigate the possibility of dual-pathway inhibition by using multiple kinase inhibitors. However, so far, these have proven to be unviable due to the toxicity often associated with this approach[116,289].

4.2. Aims

The aims of this part of the project were:

- To study the downregulation of kinases activated by KRAS following the co-delivery of anti-KRAS macromolecules with Tri-cTAT B.

- To investigate whether treatment of PDAC cells with Tri-cTAT B and anti-KRAS macromolecules affects the viability of cells.

4.3. Results

4.3.1. Downregulation of KRas-mediated Kinases

To study whether the co-delivery of anti-KRas macromolecules with Tri-cTAT B results in the downregulation of KRas-mediated proteins, four distinct approaches were tried. Due to the limited quantity of Tri-cTAT B and anti-KRas macromolecules available, this work focuses mainly on the downregulation of phosphorylated ERK (pERK) and briefly on the phosphorylated MEK (pMEK), representing the two main signalling pathways activated by KRas, that is the PI3K/AKT and the MAPK pathways. The multiple experimental conditions that were tested and the various attempts to prove the downregulation of pERK and pMEK are summarised in Table 4.1.

Table 4.1 - Conditions used for the downregulation of KRAS-mediated kinases

Condition 1	Condition 2	Condition 3	Condition 4
1 h in serum-free medium	1 h in serum-free medium + 1 h in supplemented medium	1 h in serum-free medium + 24 h in supplemented medium	24 h in serum-free medium

Whilst treatment of PDAC cells using Conditions 1 or 2 returned no detectable pERK downregulation, treatment of PANC-1 cells using Condition 3 yielded 24 % pERK downregulation (Figure 4.1). As a positive control, SCH772984, a known pERK small-molecule inhibitor, was included.

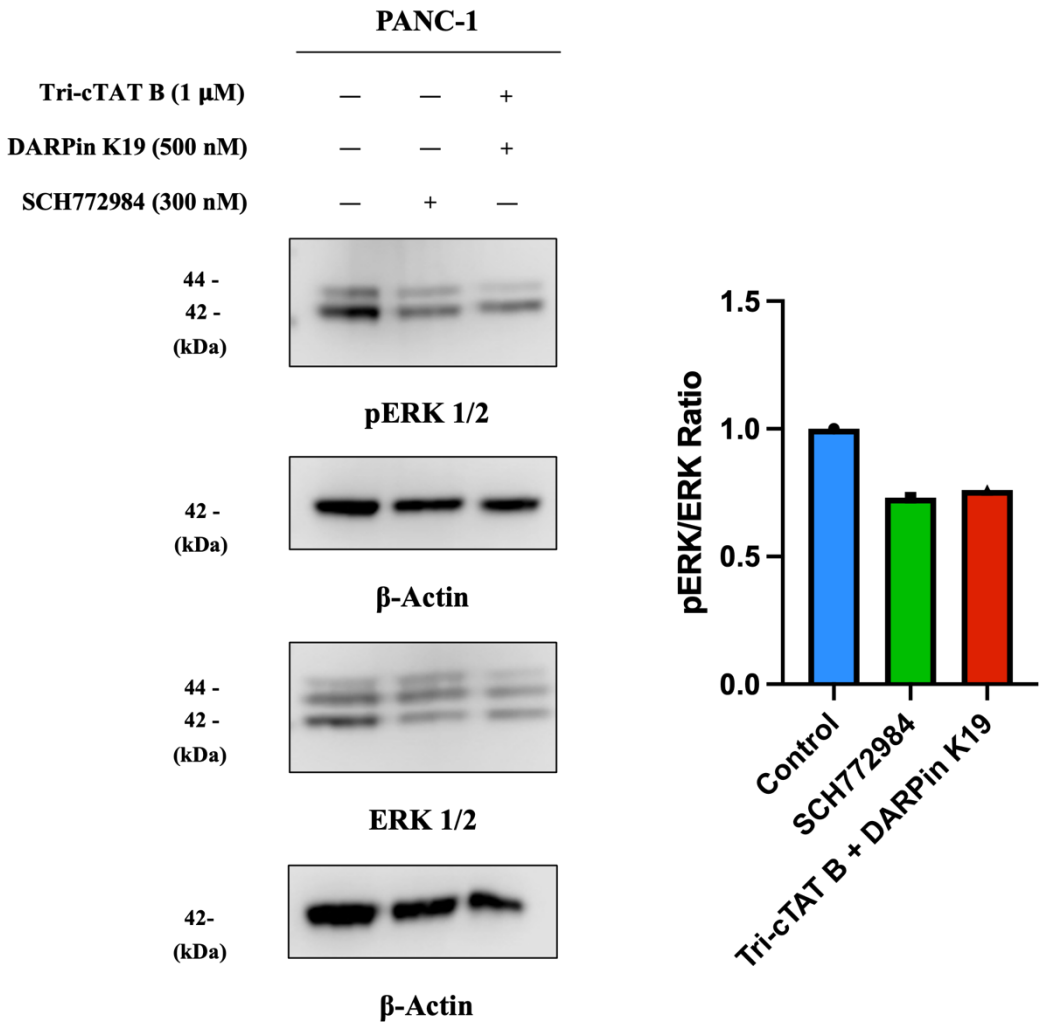


Figure 4.1 – Treatment of PANC-1 cells using Condition 3 causes limited pERK downregulation. Co-delivery of 500 nM DARPin K19 with 1 µM Tri-cTAT B in PANC-1 cells for 1 h, followed by 24 h post-wash incubation resulted in 24% pERK downregulation, compared to the control group. SCH772984 was used as a positive control, and β-Actin as the loading control. Quantification of pERK/ERK bands from the Western Blot were normalised to the control condition.

Despite showcasing for the first time inhibition of kinases activated by KRas, repeat experiments failed to reveal similar results. Thus, a fourth condition was tried by treating cells with equivalent concentrations of Tri-cTAT B and anti-KRas macromolecules but for 24 h in serum-free medium. Given the availability of farnesylated anti-KRAS macromolecules at this point, the downregulation of pERK was also explored by co-delivering DARPin K19-cFarn with Tri-cTAT B (Figure 4.2).

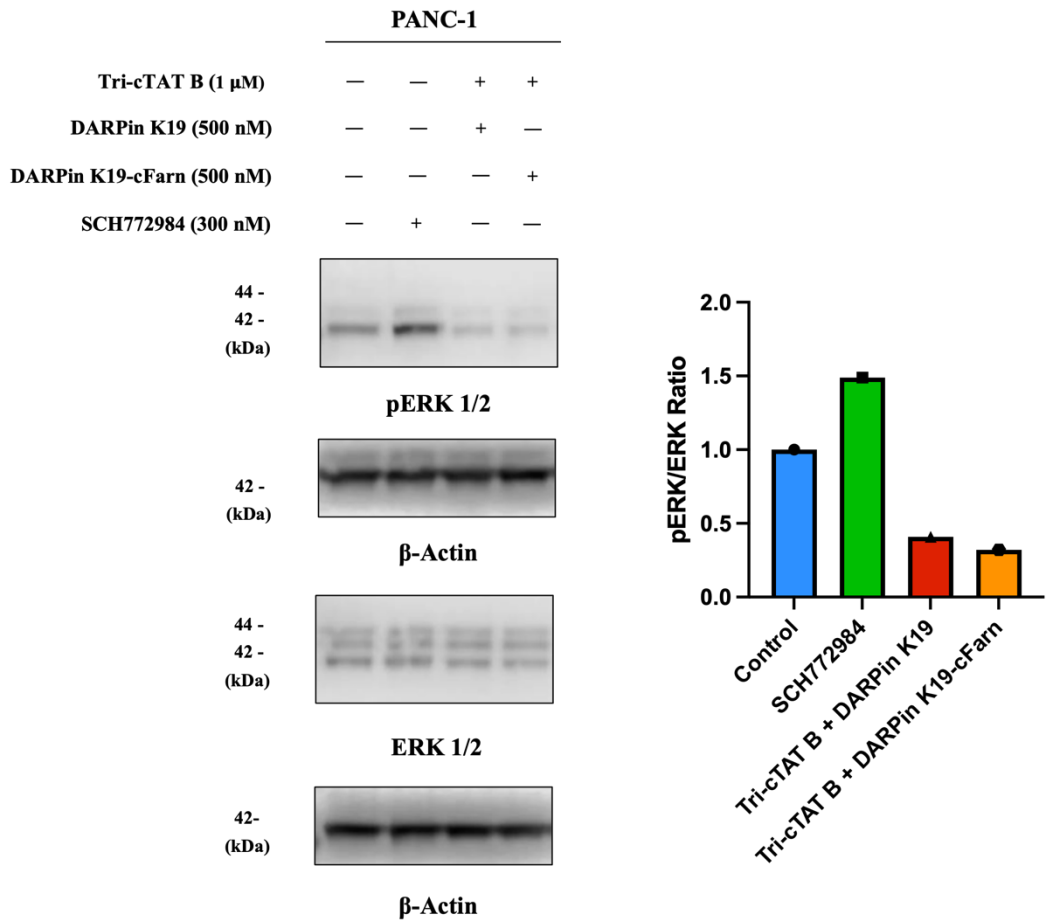


Figure 4.2 - Treatment of PANC-1 cells using Condition 4 reveals extensive pERK downregulation. Co-delivery of 500 nM DARPin K19 or DARPin K19-cFarn with 1 µM Tri-cTAT B in PANC-1 cells for 24 h resulted in 59% and 68% pERK downregulation, respectively. SCH772984 was used as a positive control, and β-Actin as the loading control. Quantification of pERK/ERK bands from the Western Blot were normalised to the control condition.

As depicted in Figure 4.2, co-delivery of DARPin K19 or DARPin K19-cFarn with Tri-cTAT B in PANC-1 cells for 24 h in serum-free medium caused pERK downregulation. Notably, despite live-cell imaging showing a higher accumulation of farnesylated DARPin K19 in the membrane of cells compared to unfarnesylated DARPin K19, the difference in the downregulation of pERK following exposure of cells to these two macromolecules was minimal. Interestingly, pERK was upregulated in the group treated with SCH772984. Due to its known effectiveness in inhibiting pERK, this result was

surprising, and so the treatment of PANC-1 cells with SCH772984 was explored further by using Condition 4 (Figure 4.3).

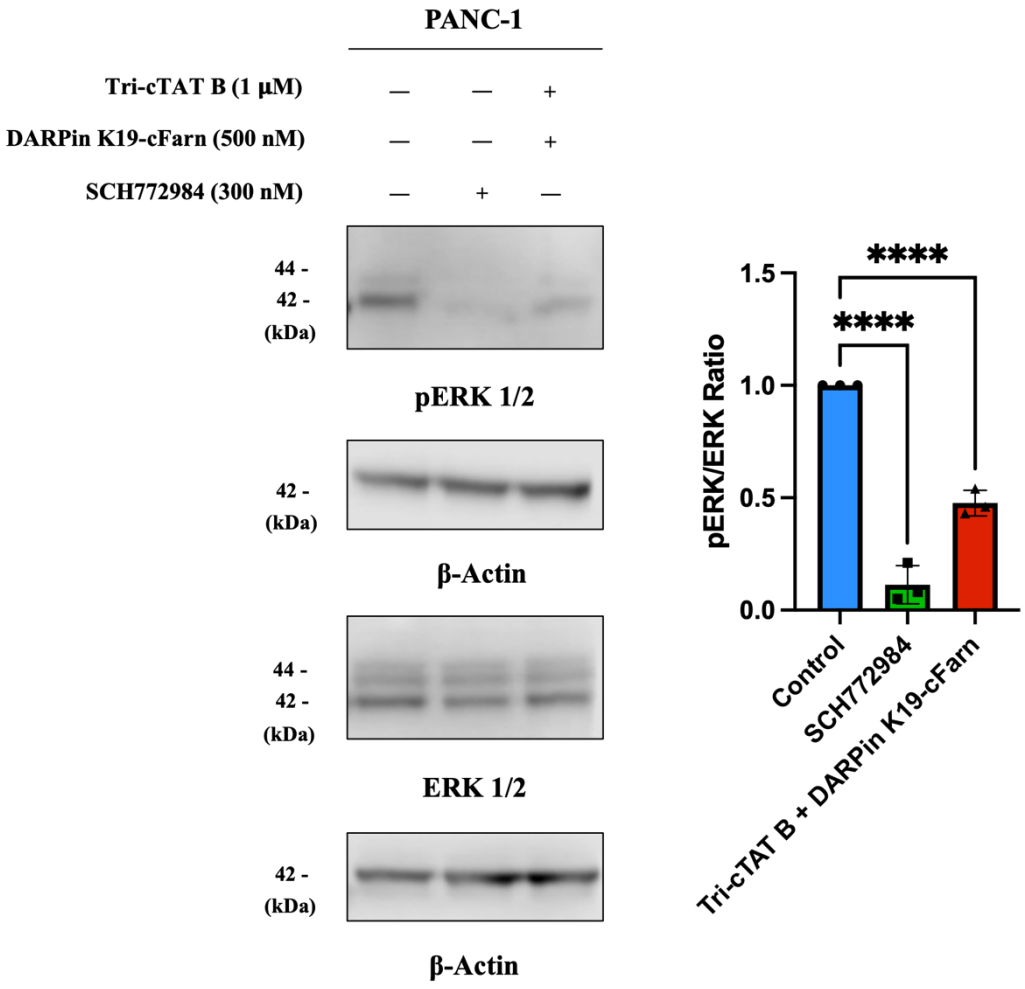
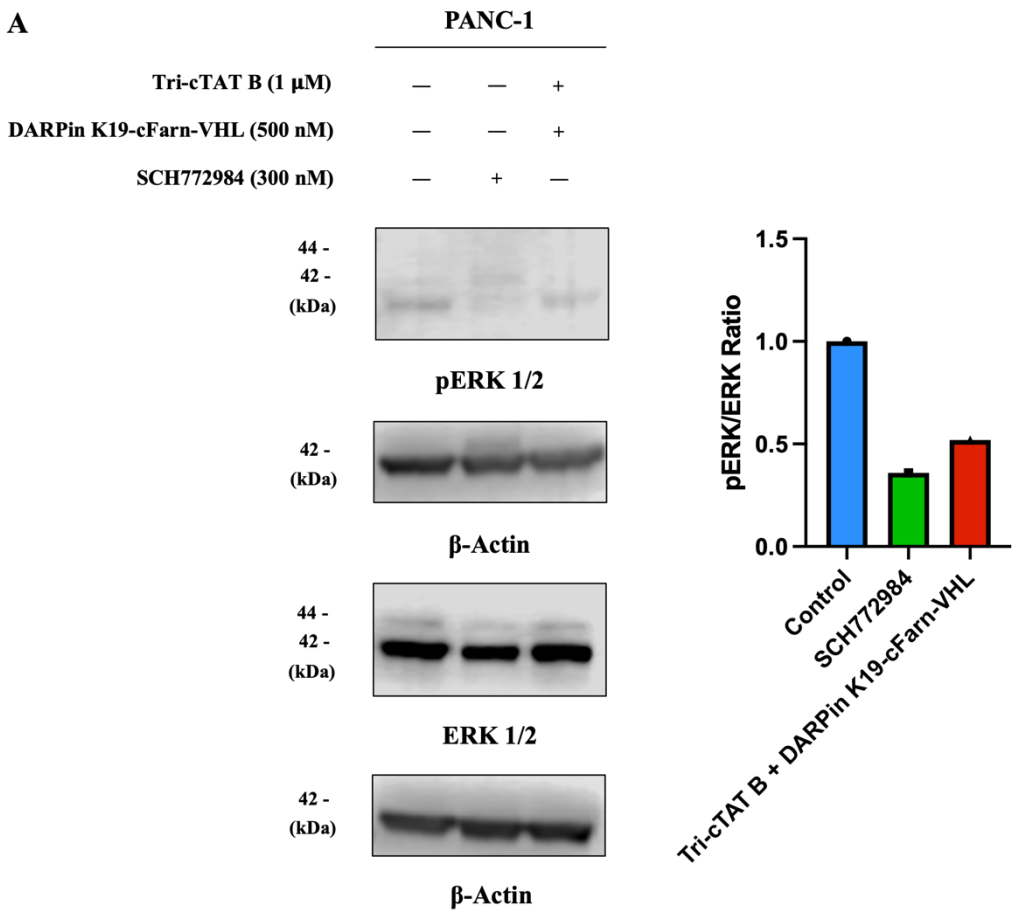


Figure 4.3 - Efficacy of DARPin K19-cFarn in downregulating pERK after 24 h incubation. Co-delivery of 500 nM DARPin K19-cFarn with 1 µM Tri-cTAT B in PANC-1 cells for 24 h resulted in an overall pERK downregulation of 52 ± 5% over three independent experiments (n=3). Quantifications of pERK/ERK bands from the Western Blot were normalised to the control condition. Data are presented as mean ± SD. One-way ANOVA and Tukey's test were employed in statistical analysis. P values: ****$P < 0.0001$.

Similar to data from Figure 4.2, treatment of PANC-1 cells with Tri-cTAT B and DARPin K19-cFarn employing Condition 4 led to the downregulation of pERK. Additionally, an adequate pERK downregulation was detected in the group that was treated with SCH772984. Importantly, the downregulation of pERK was detected in three independent

experiments, with an overall downregulation of 52 ± 5 % (Figure 4.3), indicating the ability of Tri-cTAT B and DARPin K19-cFarn to inhibit the MAPK pathway in PANC-1 cells.

Next, the downregulation of pERK was explored in the presence of a third variant of DARPin K19 that incorporates a farnesyl tag as before and, in addition, a VHL E3 ligase moiety. Due to the limited quantity of DARPin K19-cFarn-VHL, only one experiment involving the downregulation of pERK was performed (Figure 4.4A). Additionally, the downregulation of other KRas-mediated kinases, particularly phosphorylated MEK (pMEK), was explored for the first time (Figure 4.4B).



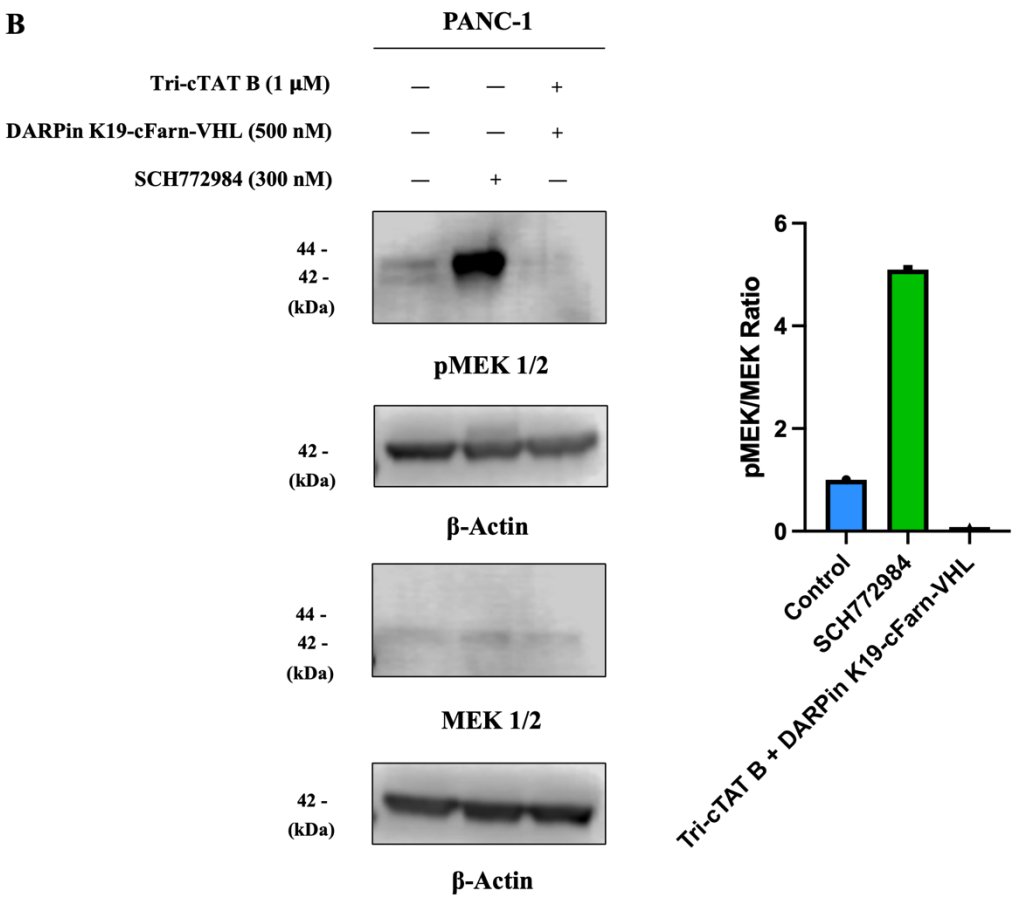


Figure 4.4 - DARPin K19-cFarn-VHL downregulates the MAPK signalling pathway of KRas. Co-delivery of 500 nM of DARPin K19-cFarn-VHL with 1 µM Tri-cTAT B in PANC-1 cells for 24 h led to a **(A)** 48% pERK downregulation and **(B)** 92% pMEK downregulation. For (A), SCH772984 was used as an intended positive control, and for (A) and (B), β-Actin was used as a loading control. Quantification of pERK/ERK and pMEK/MEK bands from the Western Blots were normalised to the control condition.

Similar to DARPin K19 and DARPin K19-cFarn, treatment of PANC-1 cells with Tri-cTAT B and DARPin K19-cFarn-VHL resulted in the downregulation of pERK. Additionally, pMEK expression was reduced, highlighting the ability of this approach to inhibit KRas and subsequently the downregulation of kinases activated by Ras, particularly the MAPK pathway.

Additionally, the downregulation of pERK was explored in lysates of PANC-1 cells, previously treated with Tri-cTAT B and scFv-Y6-cFarn using Condition 4 (Figure 4.5)

Similarly, the availability of scFv Y6-cFarn was limited, allowing only a single experiment.

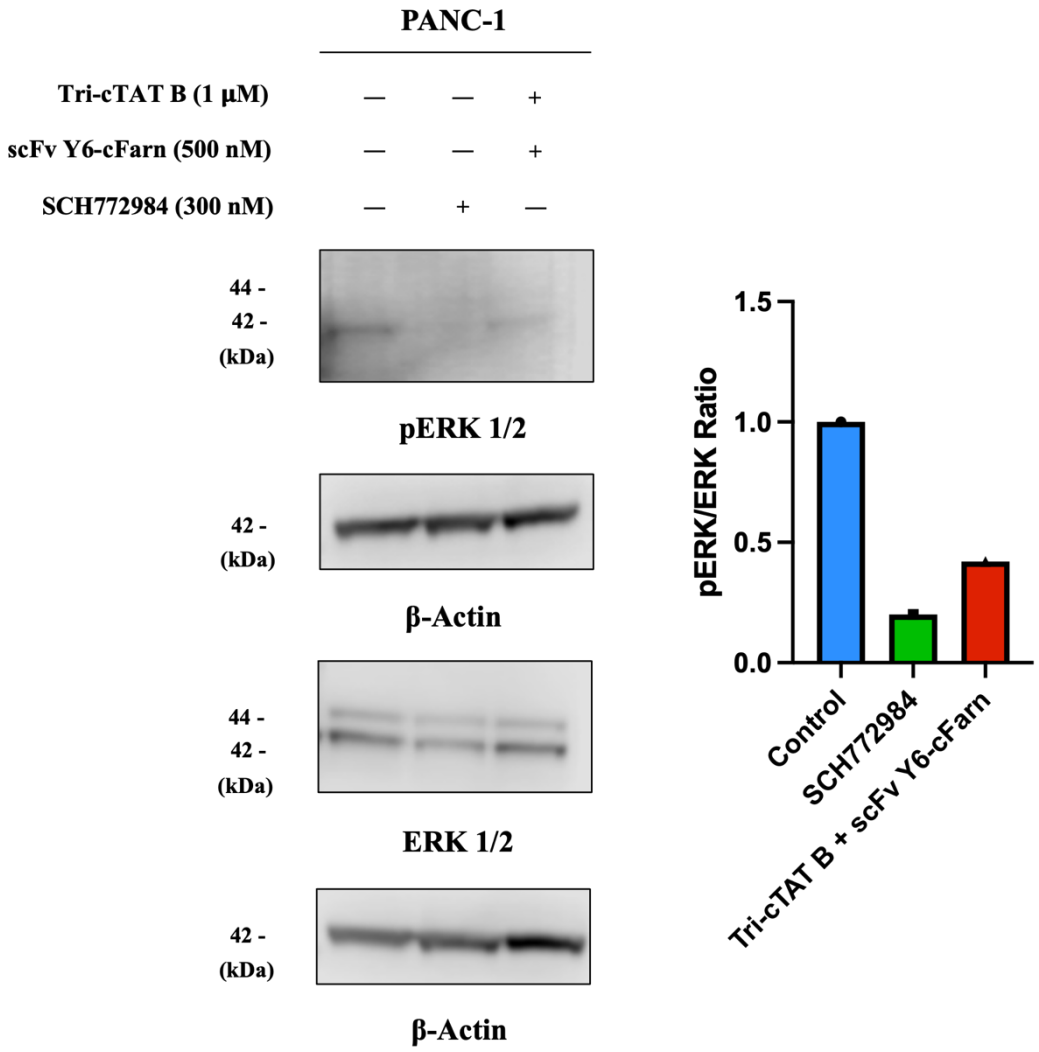
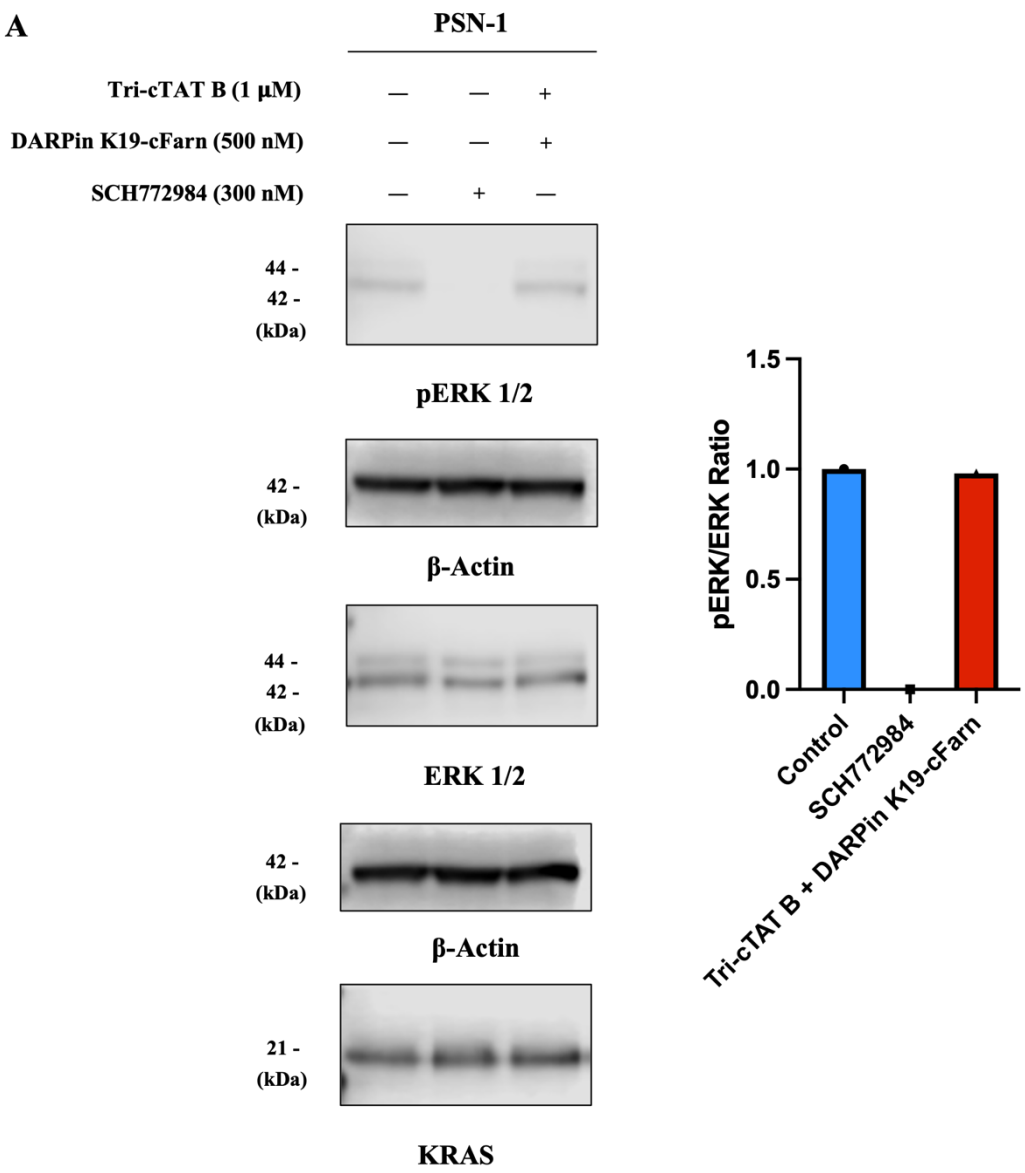


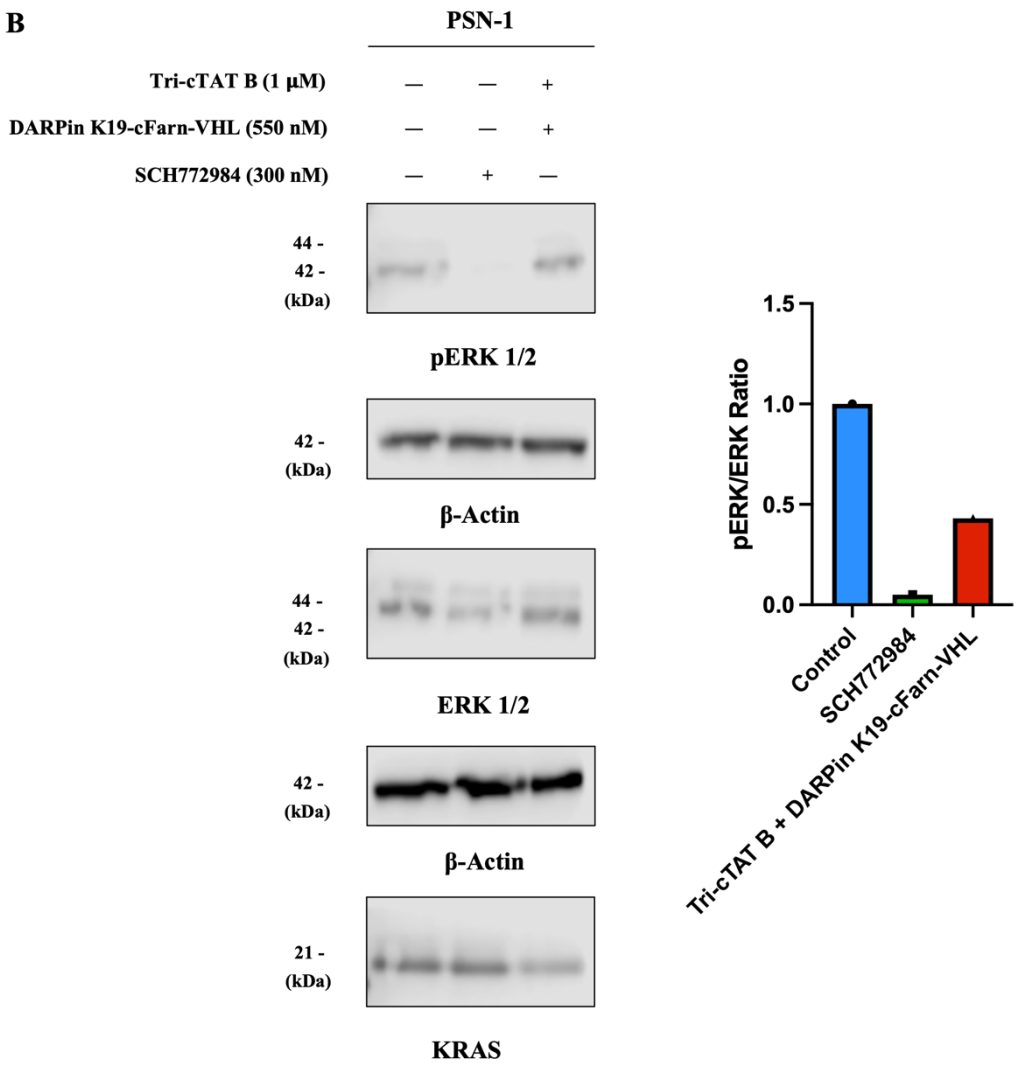
Figure 4.5 – Treatment of PANC-1 cells with scFv-Y6-cFarn reduces pERK expression. Co-delivery of 500 nM of scFv Y6-cFarn with 1 µM Tri-cTAT B in PANC-1 cells using Condition 4 led to downregulation of pERK downregulation by 58%. SCH772984 was used as a positive control and β-Actin as the loading control. Quantification of pERK/ERK bands from the Westerrn Blot were normalised to the control condition.

Having previously shown the downregulation of pERK in PANC-1 cells following the co-delivery of DARPin K19-cFarn or DARPin K19-cFarn-VHL, treatment of PANC-1 cells with scFv Y6-cFarn gave rise to similar results, with pERK downregulation of 58% compared to the control group.

Following the study of the downregulation of pERK and pMEK in PANC-1 cells upon co-delivery of DARPIN K19- and scFv Y6-related macromolecules with Tri-cTAT B, similar effects were explored in PSN-1 cells. To do so, PSN-1 cells were treated with 1 μM Tri-cTAT B and DARPin K19-cFarn (Figure 4.6A) or DARPin K19-cFarn-VHL (Figure 4.5B) or scFv Y6-cFarn (Figure 4.5C) using Condition 4. Similarly to PANC-1 cells, due to the limited amount of anti-KRAS macromolecules available, the downregulation of pERK in PSN-1 cells was assessed in single experiments. In addition to the downregulation of pERK, KRAS expression was also evaluated following the co-delivery of farnesylated anti-KRas macromolecules with Tri-cTAT B.


A
PSN-1
Tri-cTAT B (1 μM) — — +
DARPin K19-cFarn (500 nM) — — +
SCH772984 (300 nM) — + —
44 -
42 -
(kDa)
pERK 1/2
42 -
(kDa)
β-Actin
44 -
42 -
(kDa)
ERK 1/2
42 -
(kDa)
β-Actin
21 -
(kDa)
KRAS
pERK/ERK Ratio
1.5
1.0
0.5
0.0
Control
SCH772984
Tri-cTAT B + DARPin K19-cFarn

(cont.)


B
PSN-1
Tri-cTAT B (1 µM) — — +
DARPin K19-cFarn-VHL (550 nM) — — +
SCH772984 (300 nM) — + —
44 -
42 -
(kDa)
pERK 1/2
42 -
(kDa)
β-Actin
44 -
42 -
(kDa)
ERK 1/2
42 -
(kDa)
β-Actin
21 -
(kDa)
KRAS
pERK/ERK Ratio
1.5
1.0
0.5
0.0
Control
SCH772984
Tri-cTAT B + DARPin K19-cFarn-VHL

(cont.)

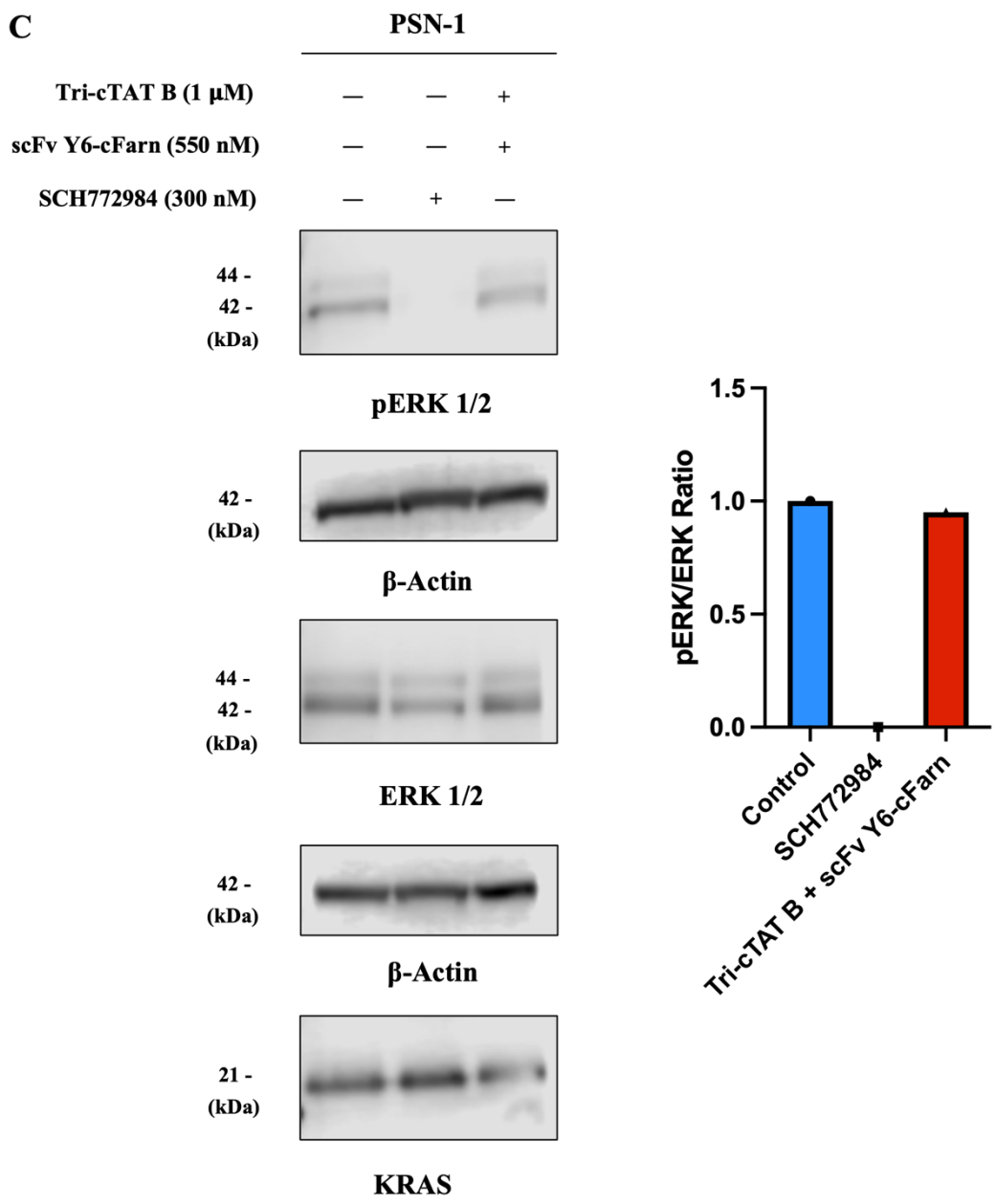


Figure 4.6 – pERK downregulation in PSN-1 cells appears to be limited. Co-delivery of 500 nM of **(A)** DARPin K19-cFarn, **(B)** DARPin K19-cFarn-VHL, or **(C)** scFv Y6-cFarn with 1 µM Tri-cTAT B in PSN-1 cells for 24 h, resulted in limited downregulation of pERK, with the exception of (B), with a pERK inhibition of 54% was observed. SCH772984 was used as a positive control, and β-Actin as the loading control. Quantification of pERK/ERK bands from the Western Blots were normalised to the control condition.

The downregulation of pERK in PSN-1 cells was observed to be limited, with the exception of the combination of Tri-cTAT B and anti-KRas DARPin K19-cFarn-VHL (Figure 4.6B), resulting in a partial decrease in pERK levels. Notably, treatment of PSN-

1 cells with Tri-cTAT B and DARPin K19-cFarn-VHL led to a reduced level of KRas expression, whilst the same effect was not observed in the groups containing an unaltered level of pERK. Interestingly, the downregulation of pERK was complete in the group that was treated with SCH772984, whereas in PANC-1 cells, the fall in pERK expression following exposure to SCH772984 was similar to that achieved using the internalised macromolecules. Despite this study having the limitation of a single experiment per treatment group, these results suggest the resistance of PSN-1 cells to our approach, with the exception of the combination of Tri-cTAT B and anti-KRas DARPin K19-cFarn-VHL.

4.3.2. Downregulation of KRas Affects the Viability of PDAC Cell Lines

Having shown that the co-delivery of anti-KRas macromolecules with Tri-cTAT B results in the downregulation of proteins activated by KRas, particularly pERK and pMEK, the next aim was to investigate whether the viability of cells was affected. To do so, cell viability was determined based on the quantitation of ATP, an indicator of metabolically active cells, *via* luminescence detection.

For consistency, the viability of PANC-1cells was investigated in the same cell lines and using the same controls and treatment conditions that were used in WBA to investigate the downregulation of proteins activated by KRas. These included a negative control (no treatment), a positive control (SCH772984), and an experimental group (Tri-cTAT B + DARPin K19-cFarn). The viability of PANC-1 cells was determined 48 h after cells were treated with the experimental treatment regimen (Figure 4.7).

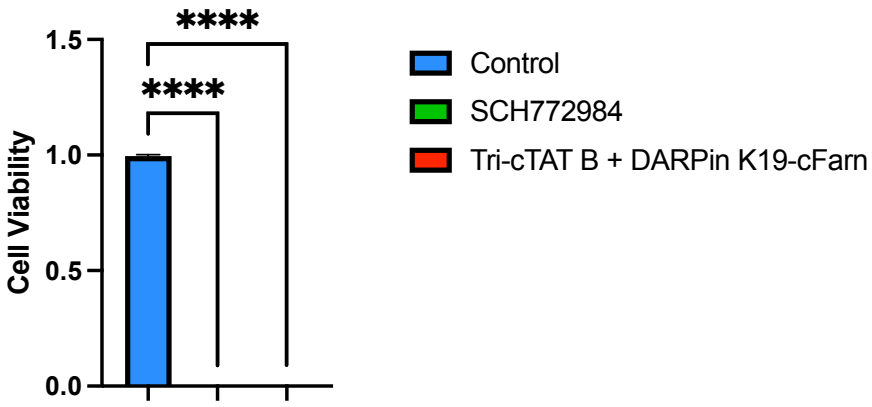


Figure 4.7 - Co-delivery of anti-KRas macromolecules with Tri-cTAT B impairs the viability of PANC-1 cells. Treatment of PANC-1 cells with 1 μM Tri-cTAT B and 500 nM DARPin K19-cFarn for 48 h compromises the viability of cells. The viability of PANC-1 cells was evaluated by measuring the ATP level of each experimental group. SCH772984 was used as a positive control. Quantification of cell viability was calculated by normalising each experimental group to the control group. Each group is composed of two technical replicates (n=2). Data are presented as mean ± SD.

Treatment of PANC-1 cells with Tri-cTAT B + DARPin K19-cFarn for 48 h compromised the viability of cells, whereas the control group showed high luminescence levels, thus indicating the presence of viable cells. Equally, the group that received SCH772984 as a treatment showed no detectable levels of ATP, suggesting the disruption of cell viability. These results suggest that macromolecule-mediated downregulation of phosphorylated ERK and other proteins activated by KRas severely compromises the viability of PANC-1 cells.

To further explore the viability of PDAC cell lines, following the co-delivery of anti-KRAS macromolecules, additional controls and treatment approaches were employed. Based on data from WBA, the downregulation of pERK was limited in PSN-1 cells, suggesting possible resistance to Tri-cTAT B + DARPin K19-cFarn or scFv Y6-cFarn in this cell line. Thus, PSN-1 cells were also tested for viability in the presence of SCH772984 and anti-KRas macromolecules (Figure 4.8).

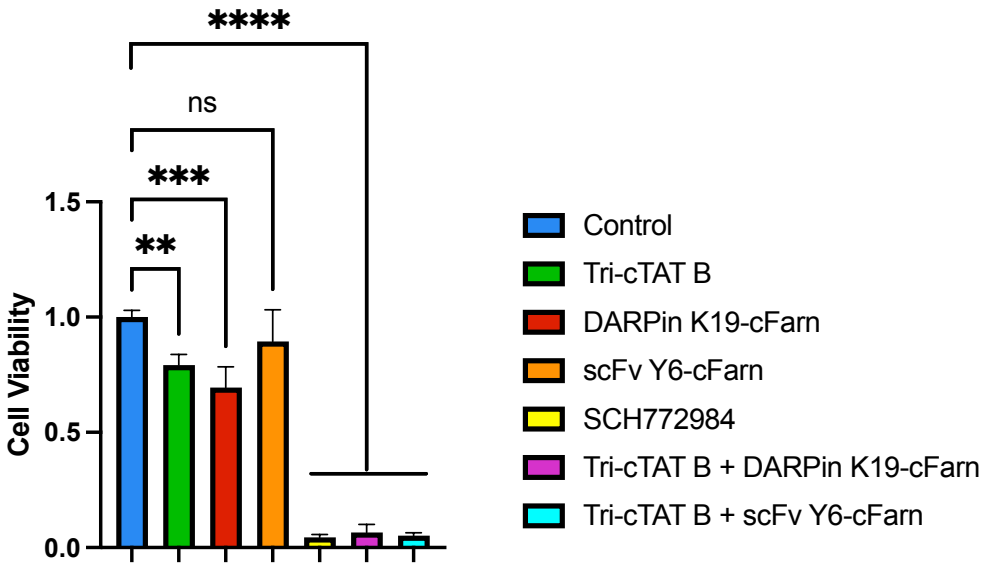


Figure 4.8 - Co-delivery of anti-KRas macromolecules with Tri-cTAT B impairs the viability of PSN-1 cells. Treatment of PSN-1 cells with 1 μM Tri-cTAT B and 500 nM DARPin K19-cFarn or scFv Y6-cFarn for 48 h compromises the viability of cells, whilst treatment with Tri-cTAT B, DARPin K19-cFarn, or scFv Y6-cFarn, alone, had a limited effect in PSN-1 cells. The viability of PSN-1 cells was evaluated by measuring the ATP level of each experimental group. SCH772984 was used as a positive control. Quantification of cell viability was calculated by normalising each experimental group to the control group. Each group is composed of three technical replicates (n=3). Data are presented as mean ± SD. One-way ANOVA and Tukey's test were employed in statistical analysis. P values: ****$P < 0.0001$, *** $P < 0.0004$, ** $P < 0.01$, ns = not significant.

Surprisingly, PSN-1 cell viability was significantly compromised by the co-delivery of DARPin K19-cFarn or scFv Y6-cFarn with Tri-cTAT B (6% and 5%, respectively) compared to the control group, although these macromolecules did not show significant downregulation of KRAS signalling. Equally, treatment of PSN-1 cells with SCH772984 disrupted the viability of cells, resulting in only 4% of cells being viable compared to the control group. Despite affecting the viability of PSN-1 cells to a lower extent than the combination of Tri-cTAT B + anti-KRas macromolecules, treatment of cells with Tri-cTAT B or DARPin K19 statistically affected the viability of cells compared to the control group (80% vs 100%, ** $P < 0.009$ and 75% vs 100%, *** $P < 0.0004$, respectively). Although treatment of PSN-1 cells with scFv Y6-cFarn resulted in a 10%

decrease in cell viability compared to the control group, this difference was not statistically significant.

Next, the same strategy was explored in BxPC-3 cells, a WT KRas PDAC cell line, where the co-delivery of DARPin K19-cFarn or scFv Y6-cFarn would not be expected to comprise the viability of cells, showcasing the premise that these macromolecules are specific for KRas mutations (Figure 4.9)

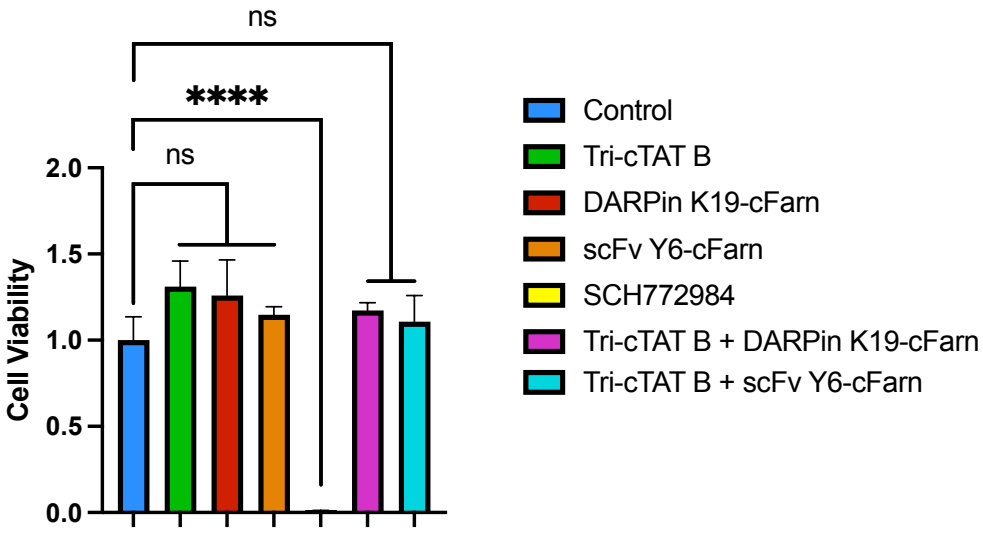


Figure 4.9 - Co-delivery of anti-KRas macromolecules with Tri-cTAT B has no effect on the viability of BxPC-3 cells. Treatment of BxPC-3 cells with 1 μM Tri-cTAT B and 500 nM DARPin K19-cFarn or scFv Y6-cFarn for 48 h does not affect cell viability. Similarly, treatment of BxPC-3 cells Tri-cTAT B, DARPin K19-cFarn, or scFv Y6-cFarn alone, has no effect on cell viability. The viability of BxPC-3 cells was evaluated by measuring the ATP level of each experimental group. SCH772984 was used as a positive control. Quantification of cell viability was calculated by normalising each experimental group to the control group. Each group is composed of three technical replicates (n=3). Data are presented as mean ± SD. One-way ANOVA and Tukey's test were employed in statistical analysis. P values: ****$P < 0.0001$, ns = not significant.

As predicted co-delivery of DARPin K19-cFarn or scFv Y6-cFarn with Tri-cTAT B had no effect on the viability of BxPC-3 cells. Comparison with the control group, yielded cell viability of 117% and 110%, respectively. However, similar to other PDAC cell lines, treatment of BxPC-3 with SCH772984, severely affected viability, compared to the

control group (1% vs 100%). Moreover, this result supports the hypothesis that the co-delivery of engineered mutant-specific anti-KRas macromolecules is only effective in cell lines harbouring a KRas mutation. Moreover, these results suggest that the co-delivery of these molecules is not specific to a particular KRas mutation, broadening their use as a therapeutic approach.

4.3. Discussion

Following the study of the Tri-cTAT B-mediated internalisation of anti-KRas macromolecules and their subsequent interaction with KRas, the focus of this chapter was on an exploration of the resulting downstream biological effects. To do this, two main assays were employed: Western Blot analysis to evaluate the downregulation of KRas-mediated kinases and cell viability assays to understand the consequences of disrupting vital KRas-dependent signalling pathways.

4.3.1. Co-Delivery of Anti-KRas Macromolecules Causes ERK/MEK Suppression

The main objective of this section was to evaluate the downregulation of KRas-mediated kinases, particularly ERK and MEK. However, preliminary experiments were required to explore the optimum experimental conditions to achieve this aim. Consequently, four different experimental conditions were investigated, with differences lying in the incubation period and type of medium.

Initial experiments that used a similar incubation period to the ones used in live-cell confocal microscopy showed no effect on the expression of downstream KRas signalling pathways. Thus, a new alternative was tried by co-delivering anti-KRas macromolecules for 1 h in a serum-free medium, followed by 24 h incubation in a serum-supplemented medium, resulting, for the first time, in downregulation of pERK (Figure 4.1). However, experiments using equivalent conditions carried out to replicate this observation failed to yield similar results. Further work to understand the optimal conditions for incubation of

cells with macromolecules resulted in the selection of incubation for 24 h in serum-free medium. The longer duration of incubation allowed efficient internalisation of anti-KRAS macromolecules and consistent downregulation of KRas signalling. Surprisingly, while WBA revealed pERK downregulation in cells treated with DARPin K19 or DARPin K19-cFarn plus Tri-cTAT B, the positive control, SCH772984, returned no detectable pERK downregulation (Figure 4.2). This is in contrast to the work of Morris *et al*., who showed that exposure of LOX *BRAF*^{V600E} melanoma cells to 300 nM SCH772984 for 24 h abolished pERK expression, although details of the experimental conditions in which cells were treated were omitted[290]. Repeat experiments, in which PANC-1 cells were treated with SCH772984 in serum-free medium for 24 h were conducted, resulting now in the consistent downregulation of pERK. Importantly, three individual experiments involving the co-delivery of DARPin K19-cFarn plus Tri-cTAT B returned similar pERK expression levels, both in the positive control group and in the experimental group (Fig. 4.3). With results being consistent with Condition 4, this suggests that although after 1 h, anti-KRas macromolecules are seen in cells, it might not be enough to cause the downregulation of KRas-mediated proteins. As a result, extended exposure of cells to Tri-cTAT B and anti-KRas macromolecules is needed to cause a detectable biological effect.

Moreover, the use of a third generation of DARPin K19, DARPin K19-cFarn-VHL, yielded a similar level suppression of pERK expression as DARPin K19-cFarn (Figure 4.4A). It was interesting that treatment of PANC-1 cells with DARPin K19-cFarn-VHL revealed complete abrogation of pMEK (Figure 4.4B). However, since the effect of DARPin K19-cFarn on the downregulation of pMEK was not explored, it is not possible to draw a conclusion about the effect of the addition of a VHL moiety on the inhibition of MEK signalling. Notably, pMEK expression was overexpressed in the group treated

with SCH772984. Despite the initial surprise, Wong *et al*. have shown that treatment of melanoma cells with SCH772984 induced the expression of pMEK as early as 24 h post-treatment [291,292]. Similarly, the same result was reported by Jin and colleagues, indicating a potential loss of ERK1/2-mediated negative feedback inhibition in the RAS-RAF-MEK signalling in BON1, QGP-1 and NCI-H727 cell lines[292]. The effect of scFv Y6-cFarn on pERK expression was similar to that of the DARPin 19 variants (Figure 4.5)[265].

While the biological effects of DARPin K19-modified proteins with a farnesylated moiety were for the first time described in this thesis, the Rabbitts Lab has provided extensive analysis on DARPin K19[261]. With multiple cell lines being studied, downregulation of pERK was only noted in HCT116 cells, albeit to a lower extent than when Tri-cTAT B was used to internalise DARPin K19 or DARPin K19-cFarn in PANC-1 cells (75% and 50%, respectively). Similar to DARPin K19, the biological effects of DARPin K19-VHL-modified proteins with a farnesylated tag were for the first time explored in this thesis. However, the authors reported extensive data using an unfarnesylated version of DARPin K19-VHL [264]. Despite using cell lines other than PANC-1, the authors have demonstrated similar pERK and pMEK levels when comparing the treatment of cells with DARPin K19-VHL-containing plasmid and co-delivery of DARPin K19-cFarn-VHL with Tri-cTAT B. However, with regards to the co-delivery of DARPin K19-cFarn-VHL to PANC-1 cells, it is important to note that this result is based on a single experiment, with additional repeats being needed. Nonetheless, when considering the overall biological effect on the treatment of PANC-1 cells with Tri-cTAT B and farnesylated versions of DARPin K19, these affected the expression of pERK by more than 50%, suggesting an improved effect in comparison with the original study[261].

Next, the same endpoints were studied in a second KRas mutant cell line, PSN-1, to test the generalisability of the findings. However, co-delivery of DARPin K19-cFarn, or scFv Y6, showed little to no effect in the downregulation of pERKin this cell line, with values of 5% and 6%, respectively, compared to the control group. In contrast to PANC-1 cells, the insertion of the VHL E3 ligase resulted in the partial depletion of pERK with downregulation of 45%, compared to the control group. Besides pERK and ERK, lysates of PSN-1 cells that were treated with Tri-cTAT B + anti-KRas macromolecules were analysed in WBA using a KRas antibody. Interestingly, KRas expression in cells that were treated with DARPin K19-cFarn or scFv Y6-cFarn remained unchanged, while cells that were treated with DARPin K19-cFarn-VHL led to a decreased expression of KRas, suggesting the addition of a VHL degrader impairs KRAS in PSN-1 cells. Although the mechanism of action was not explored, studies show that E3 ligases engineered on intracellular single domains invoke proteolysis of targets by inducing the depletion of their target via the ubiquitin-proteasome system[293–295].

Based on findings from Rabbitts *et al*., the downregulation of pERK in cells that were treated with DARPin K19 for 24 h was limited, with only HCT116 cells showing a significant reduction[261]. On the other hand, based on equivalent incubation periods, the co-delivery of DARPin K19 or DARPin K19-cFarn with Tri-cTAT B results in pronounced pERK abrogation. In another article by Rabbitts *et al*., it was shown that the addition of VHL E3 ligase to DARPin K19 led to greater downregulation of KRas signalling pathways compared to the unmodified DARPin. Overall, this validates the use of Tri-cTAT B to internalise functional anti-KRas macromolecules by causing the downregulation of KRas-mediated proteins. While both DARPin K19 and scFv Y6 macromolecules show promising results in targeting KRas, scFv Y6 offers an advantage

in comparison with DARPin K19. Alongside its lower molecular weight, it shows a higher affinity towards KRas than DARPin K19[261,266].

4.3.2. Co-Delivery of Anti-KRas Macromolecules Impairs PDAC Cell Viability

Cancer cells have multiple mechanisms to evade inhibition of signalling pathways allowing them to continue to promote tumorigenesis via alternate oncogenes and proteins[297]. As a result, this work not only focussed on targeting KRas but also asked the question of whether inhibiting KRAS resulted in the loss of viability of PDAC cells. To do so, following the treatment of cells with Tri-cTAT B + anti-KRas macromolecules, their viability was assessed by measuring the intrinsic ATP level.

Treatment of PANC-1 cells with Tri-cTAT B and DARPin K19-cFarn for 48 h compromises the survival of PANC-1 cells (Figure 4.7). Notably, these findings contradict the conclusions put forward by Singh *et al*., who reported that PANC-1 cells have a low Ras Dependency Index (RDIs) score[286]. Conversely, studies conducted by Muzudmar and colleagues were consistent with the data presented in this chapter, as they showed that KRas abrogation compromised the viability of PANC-1 cells[287]. In the Muzudmar *et al*. study, KRas knockout clones of PANC-1 cells were generated through CRISPR/Cas9-mediated genome editing, whereas Settleman and colleagues assessed KRas dependency in human tumour cells by RNA interference (RNAi). According to the findings and techniques used in each study, it remains uncertain whether the observed "KRas-independent" phenotype reported by Singh *et al.* resulted from the incomplete inhibitory effects of RNAi, leading to the presence of residual KRas protein that was adequate to sustain cell survival. Data presented in this thesis provide additional evidence that KRas inhibition affects the viability of PANC-1 cells.

PSN-1 cell viability was also evaluated following the co-delivery of anti-KRas macromolecules with Tri-cTAT B (Fig. 4.8). However, based on the previous observation

that pERK downregulation was limited in PSN-1 cells, it was anticipated that their viability would remain unaltered. Additionally, multiple control groups were added, including the treatment of PSN-1 cells with Tri-cTAT B and anti-KRas macromolecules alone. Unexpectedly, the co-delivery of anti-KRas DARPin K19-cFarn with Tri-cTAT B compromised the viability of PSN-1 cells, albeit to a lesser extent than PANC-1 cells. Similarly, treatment of PSN-1 cells with Tri-cTAT B and scFv Y6-cFarn resulted in the depletion of cells, with results disputing data obtained from western blotting. Hence, suggestions were made regarding the potential occurrence of cellular toxicity resulting from KRAS inhibition, albeit mediated through other KRAS-controlled pathways, namely PI3K/AKT. Yet, evidence provided by Hobbs *et al*. quickly rejected this hypothesis by showing that PSN-1 cells are impaired in PI3K/AKT signalling, suggesting that any KRAS biological effect is mainly mediated through the MAPK pathway[221]. To further assess these findings, WBA with lysates derived from PSN-1 cells and incubated with MEK and pMEK antibodies yielded no detectable bands, confirming the findings from Hobbs *et al*. However, it is important to note that in studies whose objective was to assess the downregulation of proteins activated by KRas, treatment of cells was limited to 24 h while the evaluation of cell viability and proliferation was conducted 48 h after cells were exposed to Tri-cTAT B and anti-KRas macromolecules. Without further evidence, it is only possible to hypothesise the downregulation of KRas signalling pathways in PSN-1 cells may occur at a later stage. Notably, the reduction in viability observed is consistent with the literature reports showing that inhibition of KRAS in PSN-1 cells compromises the viability of cells. Whilst Muzudmar and colleagues were able to create multiple clones of PDAC cells following KRAS knockout, they were unable to derive KRAS deficient clones from PSN-1 cells, making it impossible to conclude whether PSN-1 cells can survive following the depletion of KRAS by CRISPR/Cas9-

mediated genome editing[287]. However, Novotny *et al*. reported in 2017 the synthesis of a neo-substrate for farnesyltransferase that prevents the alternative prenylation by geranylgeranyltransferase, resulting in the mislocalisation of oncogenic KRas[296]. The use of this approach in PSN-1 cells interfered with KRas post-translational processing and subsequent cellular localisation, impeding KRas activation and, ultimately, the activation of KRas-mediated kinases, particularly ERK. Overall, this compromised the viability of PSN-1 cells, showcasing KRas-dependency for their survival.

The effects of the co-delivery of engineered anti-KRas macromolecules with Tri-cTAT B were also evaluated in BxPC-3 cells. Based on its KRAS WT nature, co-delivery of DARPin K19-cFarn or scFv Y6-cFarn with Tri-cTAT B caused no effect on cell viability, highlighting the specificity of these anti-KRas macromolecules against mutant KRas cell lines. Alongside offering a more targeted approach than anti-KRas small-molecule inhibitors, DARPin K19-cFarn and scFv Y6 impair the viability of PDAC-derived cells containing two of the most mutated forms of KRas. As a result, this approach offers an advantage by not targeting only one mutation. Consequently, although this thesis was centred on PDAC, the use of DARPin K19-cFarn and scFv Y6 can be easily extrapolated to other tumours containing KRAS mutations, including CRC and NSCLC. Similar to PANC-1 and PSN-1 cells, BxPC-3 cells exposed to either Tri-cTAT B or DARPin K19-cFarn or scFv Y6-cFarn alone showed no loss of viability. This result reinforces the previous finding that Tri-cTAT B is not toxic to cells. The lack of effect of DARPin K19-cFarn or scFv Y6-cFarn is consistent with the findings of live-cell confocal microscopy that showed these constructs do not transfect cells in the absence of a CPP.

Chapter 5 Internalisation of Radiolabelled Anti-KRas Macromolecules for Radionuclide Therapy

5.1. Introduction

Following the internalisation of anti-KRasmacromolecules with Tri-cTAT B, assessed in Chapter 3 and the resultant biological effect investigated in Chapter 4, the primary aim of this chapter was to test the hypotheses that (1) KRas downregulation resulting from internalisation of anti-KRas antibodies would result in radiosensitisation and that (2) this could be exploited therapeutically by simultaneous delivery of an Auger electron-emitting anti-KRas macromolecule variant. To address these hypotheses, the clonogenic survival of PDAC cells that had been exposed to anti-KRas immune molecules followed by external beam radiation was investigated. Radiolabelled variants of anti-KRas macromolecules, including DARPin K19-cFarn and scFv Y6-cFarn, were developed and co-delivered with Tri-cTAT B in preliminary experiments to explore a targeted radionuclide therapy approach.

5.1.1. Targeted Radiation Delivery

Alongside techniques under the umbrella of External Beam Radiotherapy (EBRT), other approaches include the systemic delivery of highly selective radioactive drugs for a more targeted approach than EBRT, limiting possible damage in normal tissues. However, although the intracellular environment of cancer cells holds a significant number of key targets, the use of macromolecule-based radiopharmaceuticals is often dismissed due to their inability to enter cells. As a result, current agents rely on binding proteins present on the external aspect of the plasma membrane. Moreover, although the use of small molecules is not limited by this phenomenon, their use is often abandoned due to off-target events, lacking the specificity that is necessary for radiolabelled drugs. In addition to their therapeutic properties, radiolabelled compounds can often be used as powerful

diagnostic imaging tracers for Single-Photon Emission-Computerised Tomography (SPECT-CT) and Positron Emission Tomography (PET) [297,298].

The potential benefits of targeted radiation delivery have, over the years, led to efforts to develop anti-cancer radiopharmaceuticals, including radioiodine-based pharmaceuticals such as [^{131}I]I-metaiodobenzylguanidine ([^{131}I]I-MIBG) for the treatment of medullary carcinoma of the thyroid, neuroendocrine tumours (NETs), and paediatric neuroblastoma[299–301]. Historically, the radioisotopes of iodine have been a common choice in nuclear medicine for the development of diagnostic and therapeutic agents[302]. Characterised as β- and γ-emitters, the use of radioisotopes of iodine, including [^{123}I], [^{125}I], and [^{131}I], are often employed for peptide and antibody radiolabelling. This family of isotopes offer a half-life ranging from 13.3 h to 60 days, and in addition, the labelling of proteins, antibodies or antibody fragments with radionuclides of iodine forms stable covalent bonds, causing minimal alterations to the protein backbone. Additionally, the chemistry associated with radioiodination of antibodies is well understood as a covalent linkage formed by the halogenation of tyrosine and histidine residues in the presence of chemical or enzymatic oxidants. Unlike iodination, conjugation of other radionuclides to antibodies, including [^{111}In] and [^{177}Lu], requires a chelating agent that provides donor atoms, saturating the coordination sphere of the metal complex, thus stabilising it. Consequently, the use of radionuclides other than iodine involves an extra step critical to the radiolabelling efficacy, making the use of iodine a more straightforward approach to labelling macromolecules. Importantly, [^{123}I] and [^{125}I] are Auger electrons emitting isotopes and exhibit an extremely short range, typically from nanometers to micrometres, which is notably less than the diameter of a single cell[303]. As a result, in order to be effective, therapeutic agents involving radionuclides of [^{123}I] and [^{125}I] need to be internalised. Given the objective of this thesis by internalising radionuclides of anti-KRas

macromolecules, the use of [^{123}I] can be seen as a viable approach. Moreover, studies show that cell membranes are thought to be sensitive to Auger electrons [304]. Based on the location of KRas at the inner leaflet of cell membranes and the accumulation of DARPin K19-cFarn and scFv Y6-cFarn at the membrane of cells, the use of [^{123}I] offers an additional advantage in comparison with other radionuclides. Lastly, [^{123}I] emits γ photons of sufficient energy for SPECT imaging, a valuable characteristic for *in vivo* biodistribution studies[305].

Given the interest in radiolabelling DARPins, previous works highlight the ability to radiolabel DARPins with [^{125}I] were reported[306,307]. In the work reported by Vorobyeva and colleagues, the authors have shown the labelling of DARPin Ec1, targeted to bind the Epithelial Cell Adhesion Molecule (EpCAM), with [^{125}I] using the chloramine-T method[306]. Consisting of a methodology first reported in the 1960s, it offers a stable and straightforward mechanism to label proteins with radionuclides of iodine[308]. By being pH-dependent, the chloramine-T method favours the binding of radionuclides of iodine to tyrosine residues at physiological pH.

5.1.2. External Beam Radiation and Radiosensitisation of Cancer Cells

EBRT is used to effectively treat many types of cancer through the induction of DNA double-strand and single-strand breaks, ultimately affecting cell division and proliferative capacity. However, given the physical, non-molecularly targeted nature of EBRT, the delivery of ionizing radiation, including electrons, photons, protons, and heavy ions, does not distinguish tumour cells from healthy tissues, introducing the possibility of detrimental effects in normal tissues. As with other therapeutic modalities, cancer cells can evade the detrimental consequences of radiation therapy, a process that is associated with multiple biological alterations, including disruption of the cell cycle, avoidance of apoptosis and enhanced DNA repair mechanisms, all of which ultimately cause resistance

to treatment[309–312]. Based on these two characteristics, the therapeutic effect of radiation therapy can be limited. As a result, the development of measures to avoid the irradiation of healthy tissues and radiation resistance are urgently needed. The avoidance of organs at risk has been improved in the current era through the introduction of physical advances, amongst others, by the development of imagining techniques, including imaging-guided radiotherapy (IGRT). Efforts to overcome inherent or acquired radioresistance have included the use of drugs, such as DNA repair inhibitors and antiangiogenics. Drugs that render tumour cells more sensitive to radiation therapy while sparing normal tissues are commonly referred to as radiosensitisers. Due to its importance in the outcome of cancer treatment, over the years many radiosensitisers were developed, including 5-fluorouracil, cisplatin, docetaxel, and molecularly targeted agents such as cetuximab[157,163,171,313]. Other targets can be seen as valuable radiosensitiser targets, including KRas. However, due to the historical challenge of targeting KRas, these approaches have often been abandoned. Nonetheless, findings suggest that the downregulation of KRas signalling pathways, namely the PI3K/mTOR pathway, can lead to tumour radiosensitisation by normalising tumour vasculature[175]. Yet, other studies report that the downregulation of the MAPK/ERK pathway by the MEK inhibitor trametinib equally results in the radiosensitisation of KRAS-mutant NSCLC *in vitro* and *in vivo*[314]. Other studies look for the relationship between KRas and other oncogenes, particularly the hepatocyte growth factor receptor (c-Met). Known to equally activate the PI3K/mTOR and MAPK/ERK pathways, the treatment of cetuximab-resistant mutant KRas-driven CRC cell lines with a c-Met inhibitor, crizotinib, successfully sensitises cancer cells to radiation[315]. However, once again, these approaches look to indirectly target KRas since c-Met is an extracellular target, making it easier to target than KRas. More recently, studies looked to radiosensitise KRas-derived tumours, not by targeting KRas, but by targeting survival

pathways proteins. In this particular study, Tandon *et al.* used pixantrone, an antineoplastic small molecule to target prosurvival proteins, including Ki-67, strictly associated with cell proliferation[316]. The development of the first class of KRas direct inhibitors opened a new window of opportunity, with some articles already advocating their positive effects on the radiosensitisation of KRas-mutant CRC models by inducing G1/S arrest[317]. Others aimed to combine EBRT with KRas and MEK inhibitors (AMG510 and Trametinib, respectively), showing the decrease of radiation-induced PD-L1 expression, mediating immune tolerance[318].

5.2. Aims

The central aim of the research presented in this chapter was to define the rationale and assess the feasibility of using internalising anti-KRas macromolecules as carriers for radionuclide therapy

The specific aims were:

- To develop a protocol for radiolabelling anti-KRas macromolecules with [^{123}I]
- To assess the accumulation and intracellular distribution of [^{123}I]-anti-KRas macromolecules following co-delivery with Tri-cTAT B
- To evaluate the radiosensitivity of PANC-1 cells following the downregulation of KRas signalling
- To conduct a pilot in vivo biodistribution study of [^{123}I]I-anti-KRas macromolecules

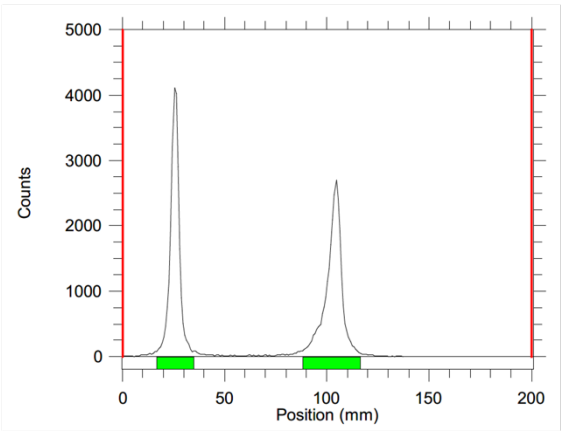
5.3. Results

5.3.1. Radiolabelling of anti-KRas macromolecules with [^{123}I].

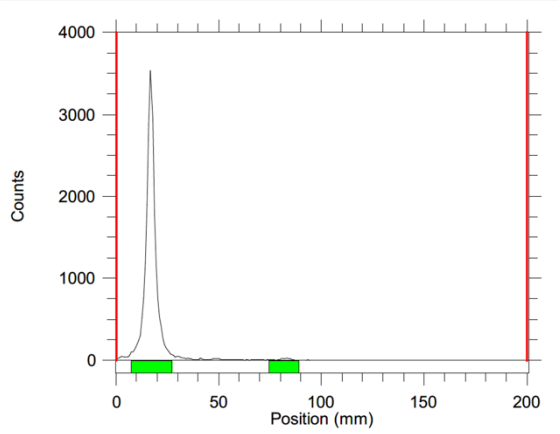
The first aim was to find an appropriate and consistent method for radiolabeling anti-KRAS macromolecules. Based on the presence of several tyrosine residues in the primary structures of DARPin K19 and scFv Y6, initial efforts were made to attempt the

radiolabelling of these constructs using [^{123}I] *via* the Chloramine T method. For that purpose, DARPin K19, DARPin K19-cFarn and scFv Y6 were radiolabelled, and their reaction and purification yields were characterised by Instant Thin Layer Chromatography (iTLC) (Figure 5.1).

Crude

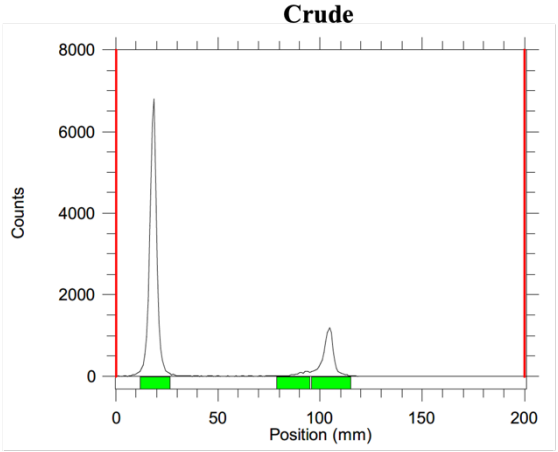


Purified

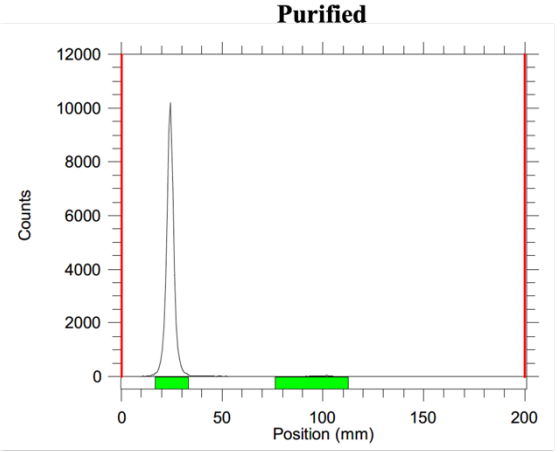


	Condition	Region 1 - Position (mm)	% ROI	Region 2 - Position (mm)	% ROI
[^{123}I]I-DARPin K19	Crude	[10 - 40]	48.3	[80-110]	51.7
	Purified	[10 - 30]	98.9	[80-90]	1.1

Crude

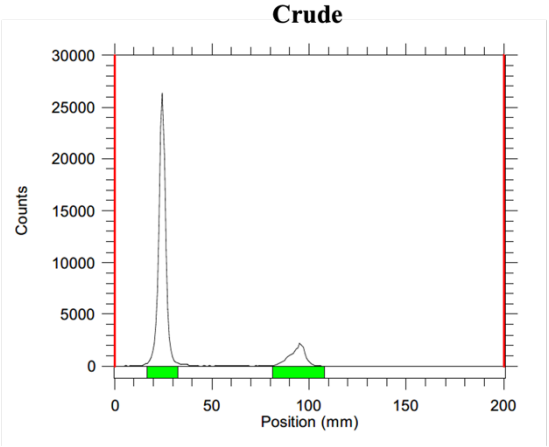


Purified

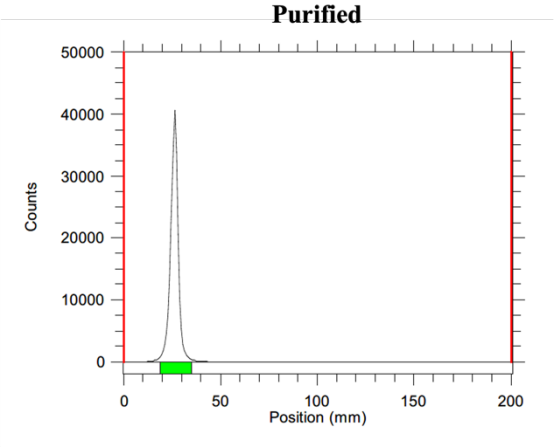


	Condition	Region 1 - Position (mm)	% ROI	Region 2 - Position (mm)	% ROI
[^{123}I]I-DARPin K19-cFarn	Crude	[10 - 30]	77.3	[80-110]	22.7
	Purified	[20 - 30]	98.7	[80-110]	1.3

Crude



Purified



	Condition	Region 1 - Position (mm)	% ROI	Region 2 - Position (mm)	% ROI
[^{123}I]I-scFv Y6-cFarn	Crude	[20 - 30]	84.8	[80-110]	100
	Purified	[20 - 30]	100	0	0

Figure 5.1 - Labelling of anti-KRas macromolecules with [^{123}I]. Radioiodination of DARPin K19, DARPin K19-cFarn and scFv-cFarn with [^{123}I] was achieved using the chloramine T method for protein labelling. Labelling efficiency and purity were determined by instant thin-layer chromatography (iTLC). Purification was performed by molecular weight cut-off (MWCO) filters. Crude iTLC chromatograms reveal two peaks, representative of radiolabelled anti-KRAS macromolecules and excess Na[^{123}I]I. Purification of radiolabelled compounds was only considered with a % region of interest (ROI) ≥ 98%. Radiolabelling of each anti-KRas construct was independently performed at least three times, returning equivalent results.

As depicted in Figure 5.1, iTLC analysis revealed the presence of two peaks, with the first corresponding to the radiolabelled protein and the second being consistent with free Na[^{123}I]I. Given the significant molecular weight difference between [^{123}I]I-anti-KRas macromolecules and Na[^{123}I]I, purification was possible using MWCO membranes yielding satisfactory purity values based on the % ROI on the iTLC chromatogram. Thus, whilst the radiolabelling of DARPin K19 yielded a purity of 98.9%, the radioiodination of DARPin K19-cFarn returned a ROI of 98.7%. The reaction between Na[^{123}I]I and scFv Y6-cFarn produced a purity index of 100%. Although anti-KRAS macromolecules were radiolabelled multiple times, the results were always consistent with the ones highlighted in Figure 5.1. As a quality control, radiolabelled proteins were only used in biological assays where the % ROI was greater than 98%.

5.3.2. Distribution of [^{123}I]I-Anti-KRas Macromolecules in PANC-1 Cells

Following the radiolabelling of anti-KRas macromolecules with [^{123}I], the intracellular distribution of anti-KRas macromolecules, including DARPin K19, DARPin K19-cFarn and scFv Y6-cFarn was explored. For that purpose, [^{123}I]I-anti-KRas macromolecules (1 MBq·μg^{-1}) were co-delivered in PANC-1 cells with Tri-cTAT B, and cell lysates fractionated, allowing the isolation of membrane, cytoplasm, and nuclear fractions (Figure 5.2).

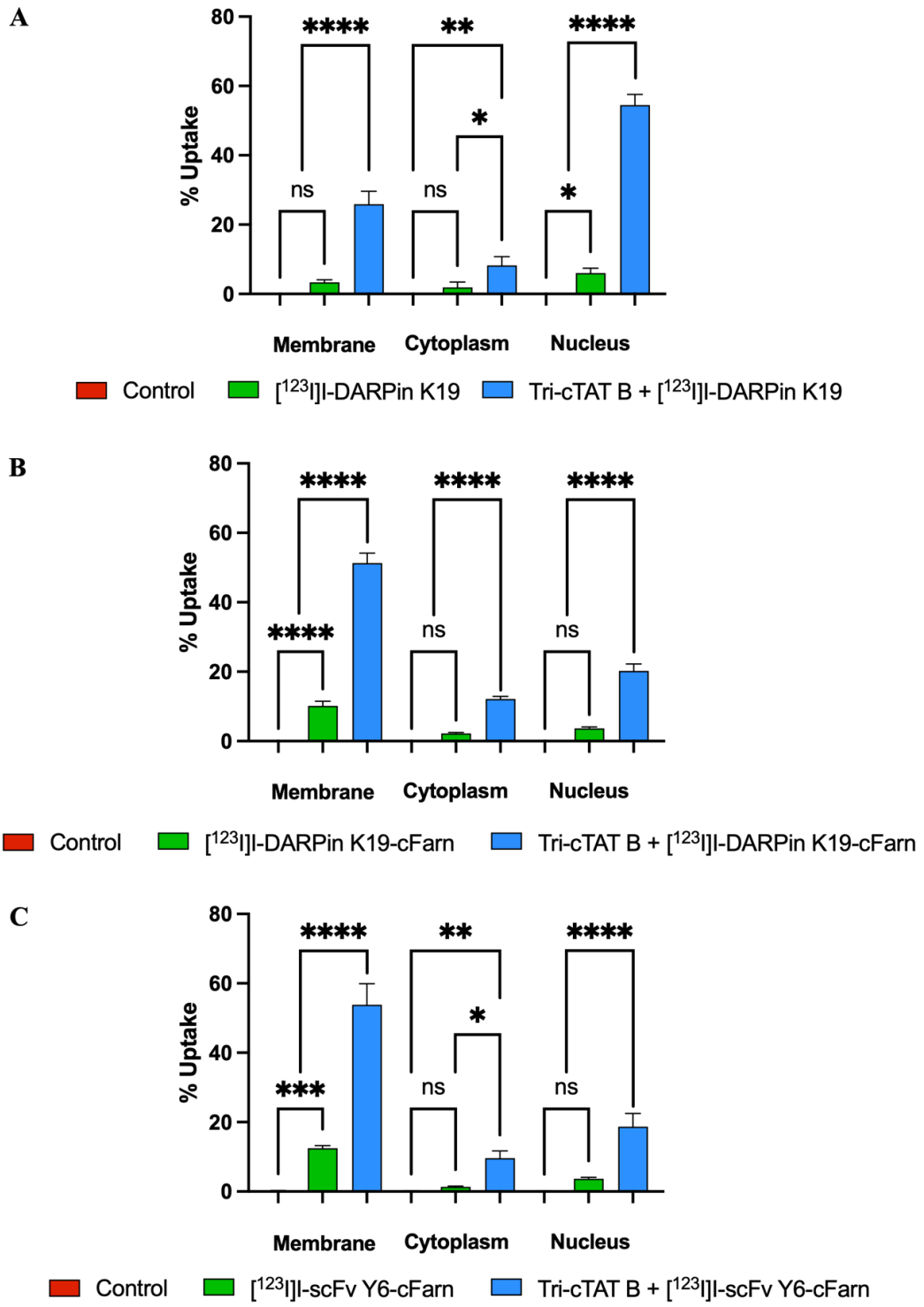


Figure 5.2 - Fractionation of PANC-1 cells. Fractionation of PANC-1 cells was performed following the co-delivery of 1 MBq·μg^{-1} [^{123}I]I-DARPin K19 **(A)**, [^{123}I]I-DARPin K19-cFarn **(B)** or [^{123}I]I-scFv Y6-cFarn **(C)** with 1 μM Tri-cTAT B for 1 h. For each anti-KRAS construct, a group comprised of cells treated only with [^{123}I]I-DARPin K19, [^{123}I]I-DARPin K19-cFarn or [^{123}I]I-scFv-Y6 was also included. PANC-1 cells from each treatment modality were subject to identical protocols, allowing the separation of the membrane, cytoplasm, and nucleus. The radioactivity of each fragment was measured in a γ counter, and the counts per minute (CPM) of each group were normalised to

calculate the % uptake of each treatment modality in the membrane, cytoplasm, and nucleus. Data are presented as mean ± SD. Data indicative of three independent repeats per treatment group (n=3). One-way ANOVA and Tukey's test were employed in statistical analysis. ns: non-significant; *P* values: **P* < 0.03, ***P* < 0.002, ****P* <0.0002, *****P* < 0.0001.

Analysis of Figure 5.2 reveals the internalisation of [^{123}I]I-DARPin K19 was greater in the nucleus (55 ± 3%), followed by the membrane (26 ± 4%) and cytoplasm (8 ± 3%). However, the addition of a farnesyl tag in the structure of DARPin's K19 and subsequent radioiodination led to a redistribution that resulted in a higher uptake in the membrane (51 ± 3%), followed by the nucleus (20 ± 2%) and cytoplasm (12 ± 1%). Despite the inability of DARPin K19 alone to internalise into cells, radioiodination of these constructs and subsequent fractionation of cells revealed a small but statistically significant accumulation of radiation in the nucleus (Figure 5.2A). However, based on iTLC chromatograms (Figure 5.1), the presence of minimal amounts of Na[^{123}I]I is predictable. Given its low molecular weight (145.90 g·mol^{-1}), the intracellular accumulation of Na[^{123}I] is likely to occur, meaning that any detection of radiation in the nucleus and membrane is probably due to Na[^{123}I]I. Similar to [^{123}I]I-DARPin K19-cFarn, the internalisation of [^{123}I]I-scFv Y6-cFarn showed greater accumulation in the membrane (54 ± 6%), followed by the nucleus (19 ± 4%) and cytoplasm (10 ± 2%). As for DARPin K19-cFarn, treatment of PANC-1 cells with [^{123}I]I-scFv Y6-cFarn caused a statistically significant accumulation of radiation in the membrane (Figure 5.2A and 5.2B). Overall, these findings are consistent with the data from live-cell confocal microscopy which showed the co-delivery of DARPin K19-mCherry with Tri-cTAT B resulted in a higher mean fluorescence intensity in the nucleus than in the membrane. However, the addition of a farnesyl tag resulted in the redistribution of the fluorescence towards the cellular membrane. Aware of the difficulty of synthesising these anti-KRAS macromolecules, priority was given to farnesylated constructs. Therefore, experiments were not carried out

with scFv Y6. Nonetheless, based on previous results, it is possible to hypothesise that co-delivery of [^{123}I]I-scFv Y6 would result in a higher accumulation in the nucleus than in the membrane. Moreover, treatment of PANC-1 cells with scFv Y6-cFarn-mCherry or [^{123}I]I-scFv Y6-cFarn led to a similar outcome by showing a higher accumulation in cellular membranes compared to unfarnesylated variants.

To evaluate the quality of cell fractionation, western blotting of different cell fragments is routinely carried out. However, due to the limited availability of the anti-KRas constructs being studied, the protein concentration of cell lysates was very low, limiting their use in western blotting. As an alternative, a control group of PANC-1 cells were subjected to an identical protocol, yielding sufficient protein concentrations of each fragment. These were subsequently analysed using western blotting (Figure 5.2).

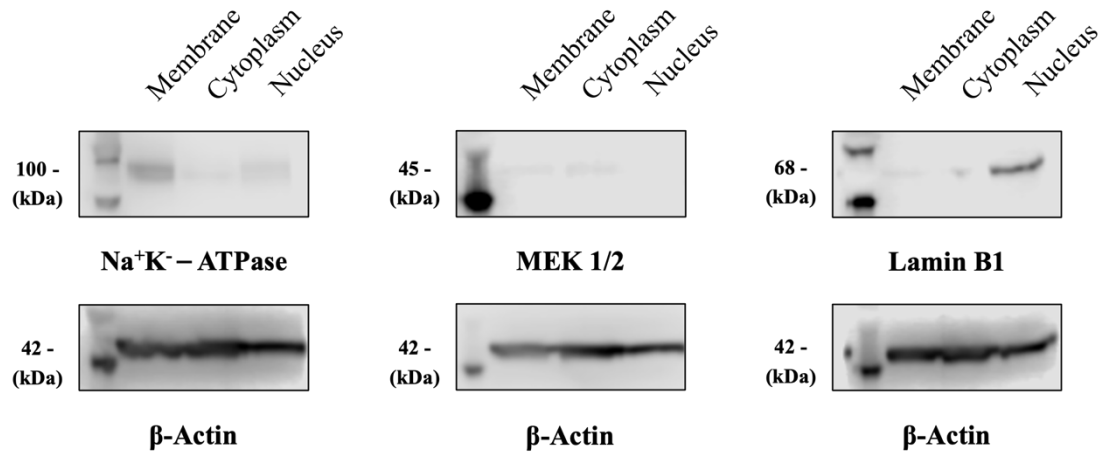


Figure 5.3 – Western blot validation of PANC-1 cell fractionation. Protein fractions derived from cellular structures extracted from PANC-1 cells, including membrane, cytoplasm, and nucleus, were analysed using western blotting. Membranes were probed with target-specific antibodies to verify the efficacy of the fractionation assay. These include Na^+K^- – ATPase (membrane), MEK 1/2 (cytoplasm) and Lamin B1 (nucleus) antibodies. β-Actin is the loading control.

In line with Figure 5.2, these findings suggest the presence of distinct protein bands in the corresponding fractions obtained through cell fractionation. These were particularly clear in the blots incubated with Na^+K^-–ATPase, representative of the transmembrane ion

channel and in blots probed with Lamin-B1, a major structural component of the nuclear lamina. Overall, these results showcase the ability to successfully extract different cellular fractions, thus validating the findings regarding the accumulation and distribution of [^{123}I]I-anti-KRas macromolecules in cells. It is important to note that the results from Figure 5.3 are not the same samples as in Figure 5.2. However, they are both derived from PANC-1 cells, and the protocol and method used in both assays were equivalent, giving great confidence about the separation of cell fractions in the samples used for Figure 5.2.

5.3.3. Intracellular Retention of [^{123}I]I-DARPin K19-cFarn

Following the Tri-cTAT B-mediated internalisation and accumulation of modified anti-KRas macromolecules and the subsequent interaction and downregulation of KRas signalling pathways, this section addresses the retention of [^{123}I]I-DARPin K19-cFarn in PANC-1 and PSN-1 cells following its co-delivery with Tri-cTAT B. After 1 h incubation, cell-associated radioactivity was evaluated after designated post-wash incubation periods (Figure 5.4).

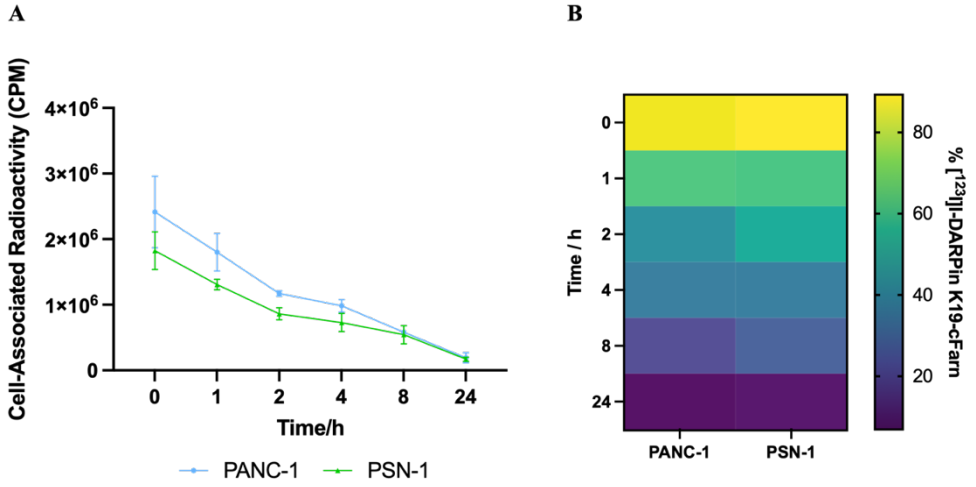


Figure 5.4 - Retention of [^{123}I]I-DARPin K19-cFarn in PANC-1 and PSN-1 cells as a function of time. PANC-1 and PSN-1 cells were incubated in medium containing 1 MBq·µg^{-1} [^{123}I]I-DARPin K19-cFarn plus 1 µM Tri-cTAT B for 1 h. Radioactivity of PANC-1 and PSN-1 cells was measured as counts per minute (CPM) at designated times, 1, 2, 4, 8 and 24 h and values were recorded as a function of time **(A)**. The % [^{123}I]I-DARPin K19-cFarn at each time point was calculated by normalising the value against t_0 **(B)**. The physical decay of [^{123}I] was taken into account for

quantification of CPM at time points other than t_0. Data are presented as mean ± SD. Data indicative of three independent repeats per treatment group (n=3).

The retention of [^{123}I]I-DARPin K19-cFarn following Tri-cTAT B-mediated internalisation was similar in PANC-1 and PSN-1 cells (Figure 5.4). Moreover, the detection of [^{123}I]I-DARPin K19-cFarn was minimal at 24 h with 7 ± 3% and 8 ± 2% of the original (t_0) radioactivity detected in PANC-1 and PSN-1 cells, respectively. A comparison of both cell lines shows the biggest difference was detected 2 h and 8 h post-wash incubation. Whilst at 2 h the % [^{123}I]I-DARPin K19-cFarn was 42 ± 1% for PANC-1 cells, for PSN-1 cells the % [^{123}I]I-DARPin K19-cFarn was 42 ± 6%. At 8 h post-wash incubation, the retention of [^{123}I]I-DARPin K19-cFarn in PANC-1 cells was 21 ± 1% of the original value, whereas for PSN-1 cells the activity of [^{123}I]I-DARPin K19-cFarn detected was 27 ± 4%. Overall, this data highlights the similarity of the retention profile of [^{123}I]I-DARPin K19-cFarn for both PANC-1 and PSN-1 cells.

5.3.4. Cytotoxicity of [^{123}I]I-DARPin K19-cFarn-internalised Macromolecules

Next, the clonogenic survival of PANC-1 cells was explored by co-delivering increasing amounts of [^{123}I]I-DARPin K19-cFarn with Tri-cTAT B. To do so, cell survival was evaluated by clonogenic assays, and the normalised survival fraction was calculated based on the platting efficiency of PANC-1 cells. In addition to vehicle only, the use of Tri-cTAT B alone, [^{123}I]I-DARPin K19-cFarn (1 MBq·μg^{-1}) alone and Tri-cTAT B + non-radiolabelled DARPin K19-cFarn were included as controls (Figure 5.5).

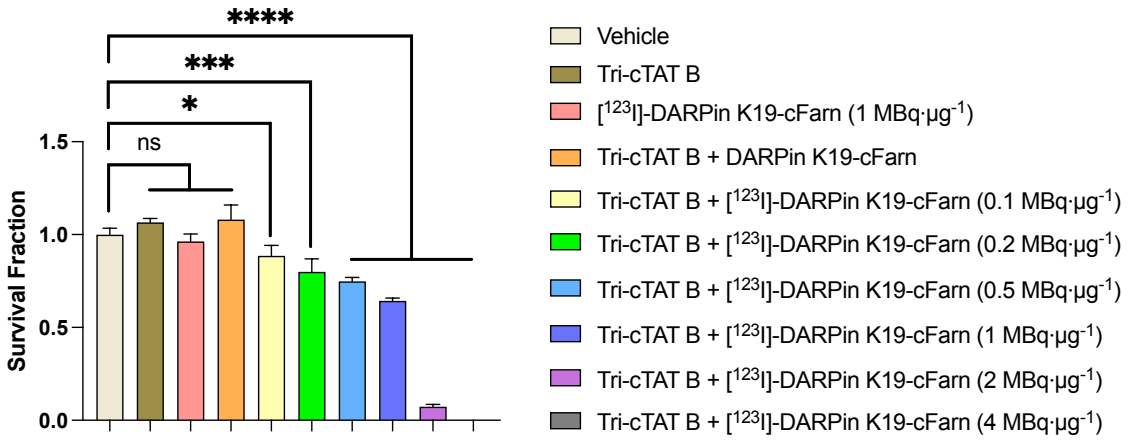


Figure 5.5 - Internalisation of [^{123}I]I-DARPin K19-cFarn impairs the survival of PANC-1 cells. Survival fraction for each treatment group was quantified through the analysis of the respective colonies (Supplementary Information) and based on the platting efficiency of PANC-1 cells. Data are presented as mean ± SD. Data indicative of three independent repeats per treatment group (n=3). One-way ANOVA and Tukey's test were employed in statistical analysis. ns: non-significant; *P* values: **P* < 0.03, ****P* <0.0002, *****P* < 0.0001.

According to Figure 5.5, there is an inverse correlation between the concentration of [^{123}I]I-DARPin K19-cFarn internalised in PANC-1 cells and the resulting survival fraction. Concomitantly, the co-delivery of 0.1, 0.2, 0.5 and 1 MBq·µg^{-1} of [^{123}I]I-DARPin K19-cFarn led to a comparable decrease of colonies, corresponding to a survival fraction of 0.89 ± 0.06, 0.80 ± 0.07, 0.75 ± 0.02, and 0.64 ± 0.02, respectively. However, the transfection of 2 MBq·µg^{-1} of [^{123}I]I-DARPin K19-cFarn produced a steep reduction of colonies corresponding to a survival fraction of 0.07 ± 0.01. Internalisation of 4 MBq·µg^{-1} of [^{123}I]I-DARPin K19-cFarn with Tri-cTAT B yielded no detectable colonies, equivalent to a survival fraction of 0.00 ± 0.00. Treatment of PANC-1 cells with 1 MBq·µg^{-1} of [^{123}I]I-DARPin K19-cFarn in the absence of CPP caused a survival fraction of 0.96 ± 0.04, a statistically non-significant difference compared to the vehicle group. However, co-delivery of 1 MBq·µg^{-1} of [^{123}I]I-DARPin K19-cFarn with Tri-cTAT B compromised the survival of PANC-1 cells by 32%, compared to the control group, resulting in a survival fraction of 0.64 ± 0.02, compared to the vehicle only group. Despite

assessing the sensitivity of PANC-1 cells to internalised radioimmunoconjugates, this result highlights again the importance of Tri-cTAT B for a targeted therapy approach based on the internalisation of anti-KRas macromolecules.

5.3.3. KRas-mediated Radiosensitisation of PANC-1 Cells

Next, the radiosensitisation of PANC-1 cells following the downregulation of KRas-mediated kinases was explored by EBRT. Based on previous findings, PANC-1 cells were treated with Tri-cTAT B and scFv-cFarn, allowing the downregulation of KRas signalling pathways and subsequently exposed to increasing doses of EBRT from 0 to 4 Gy (Figure 5.6).

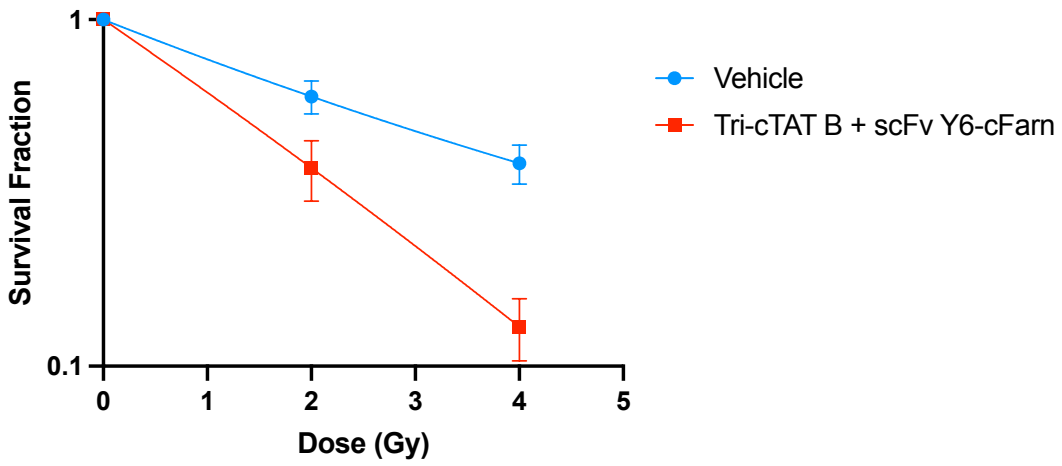


Figure 5.6 – Downregulation of KRas signalling pathways radiosensitises PANC-1 cells. Following treatment of PANC-1 cells with 1 µM Tri-cTAT B + 500 nM scFv y6-cFarn for 24 h, cells were plated into 6-well plates and irradiated with 0, 2 or 4 Gy. Control groups included the irradiation of PANC-1 cells that were not previously treated (vehicle). Survival fraction for each treatment group quantified through the analysis of the respective colonies and based on the plating efficiency of PANC-1 cells. Data are presented as mean ± SD. Data indicative of three independent repeats per treatment group (n=3).

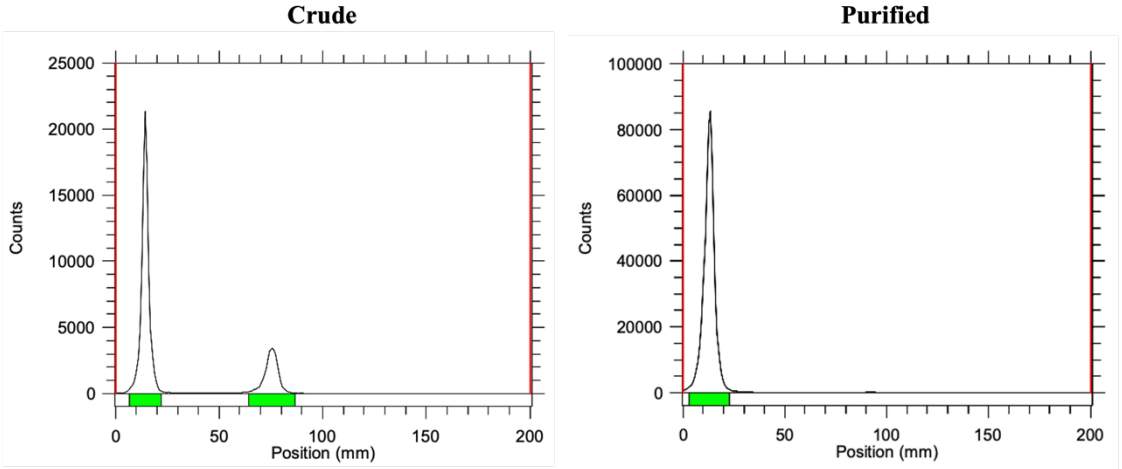
As depicted in Figure 5.6, pre-treatment of PANC-1 cells with Tri-cTAT B and scFv Y6-cFarn caused a lower survival fraction than cells that were only exposed to EBRT. While the vehicle group that received a radiation dose of 2 Gy yielded a survival fraction of 0.60 ± 0.07, the experimental group returned a survival fraction of 0.37 ± 0.07. At 4 Gy, this

difference was even more pronounced, with the vehicle group presenting a survival fraction of 0.39 ± 0.05, whereas the experimental cohort resulted in a survival fraction of 0.13 ± 0.03. In summary, these findings suggest the initial thesis that the downregulation of KRAS signalling pathways results in the radiosensitisation of cancer cells, namely PANC-1 cells.

5.3.4. Evaluation of the Biosdistribution of [^{123}I]I-anti-KRas IgG *in Vivo* by SPECT/CT.

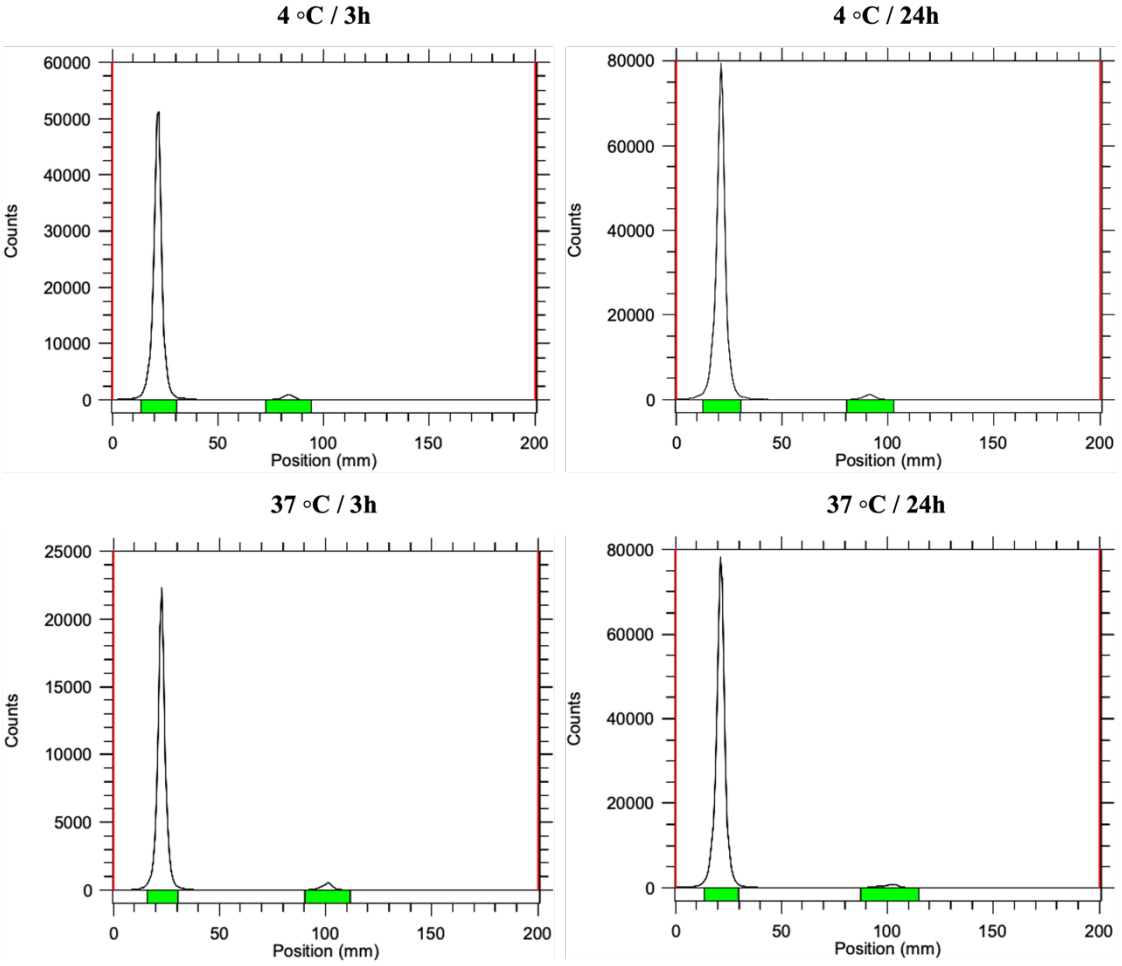
To assess the uptake of anti-KRas macromolecules by Tri-cTAT B in PSN-1 tumour-bearing mice, anti-KRas macromolecules were radiolabelled with [^{123}I]I and their uptake was assessed using SPECT/CT. Due to the large quantity of antibody needed to perform this experiment, the use of DARPin K19-cFarn or scFv Y6-cFarn was not possible at the time of the experiment. Nonetheless, as a proof-of-principle, anti-KRAS IgG was radiolabelled, and its biodistribution was studied following intravenous co-delivery with Tri-cTAT B. A control group composed of one mouse treated with [^{123}I]I-anti-KRas IgG was included. Similar to experiments involving DARPin K19-cFarn or scFv Y6-cFarn, initial experiments included the radiolabelling of anti-KRas IgG with [^{123}I]I. Given previous findings from the retention assay (Figure 5.4), SPECT/CT scanning was performed 3 h and 24 h post-injection (p.i). Moreover, since these involved the uptake of these constructs *in vivo*, a more complex system than *in vitro* models, a serum-stability test of [^{123}I]I-anti-KRas IgG at 37 °C was performed in preparation for the *in vivo* experiment. For this purpose, [^{123}I]I-anti-KRas IgG was incubated at 4 °C or 37 °C for 3 h and 24 h with mouse serum (Figure 5.7).

A

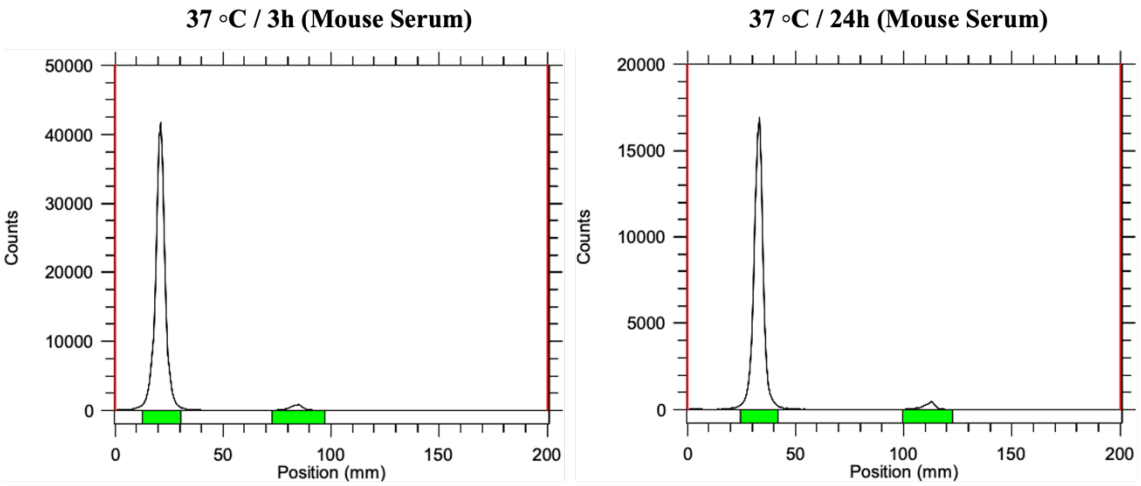


[^{123}I]I-anti-KRAS IgG	Condition	Region 1 - Position (mm)	% ROI	Region 2 - Position (mm)	% ROI
	Crude	[10 - 20]	80	[65-85]	20
	Purified	[0 - 20]	100	n/a	0

B



(cont.)



Condition	Incubation Period / h	Region 1 - Position (mm)	% ROI	Region 2 - Position (mm)	% ROI
4 °C	3	[10 - 30]	97.5	[75-95]	2.5
	24	[10 - 30]	96.3	[90-110]	3.7
37 °C	3	[10 - 30]	97.8	[80-100]	2.2
	24	[10 - 30]	97.9	[90-115]	2.1
37 °C - Mouse Serum	3	[10 - 30]	97.2	[75-95]	2.8
	24	[20 - 40]	96.4	[100 - 120]	3.6

Figure 5.7 - Anti-KRas IgG Radiolabelling and Serum-Stability Assay. (A) iTLC chromatogram representative of the radiolabelling of an anti-KRas IgG with [^{123}I] fusing the chloramine T method for protein labelling. Labelling efficiency and purity were determined by instant thin-layer chromatography (iTLC). Purification was performed by molecular weight cut-off (MWCO) filters. Crude iTLC chromatograms reveal two peaks, representative of radiolabelled anti-KRAS IgG and free Na[^{123}I]. **(B)** Stability of [^{123}I]I-anti-KRas IgG in mouse serum at 37 °C evaluated by iTLC at 3 h and 24 h time-points. Control groups included the incubation of [^{123}I]I-anti-KRas IgG at 3 °C or 37 °C for 3 h or 24 h in PBS. Mouse serum stability of [^{123}I]I-anti-KRas IgG was evaluated by the formation of new ROIs based on iTLC analysis.

Similar to other anti-KRas macromolecules, labelling of anti-KRas IgG with [^{123}I] by the chloramine-T method was straightforward, with initial iTLC chromatograms (Figure 5.7A – Left) showing excess Na[^{123}I]I with a % ROI of 20%. According to Figure 5.7A - Right, purification of [^{123}I]I-anti-KRas IgG returned a peak with a % ROI of 100%. Analysis of [^{123}I]I-anti-KRas IgG incubated at 37 °C for 3 h or 24 h with mouse serum revealed the formation of a second peak with a % ROI of 2.8 and 3.6% accordingly, suggesting a minor deiodination at these time points. However, analysis of iTLC chromatograms from samples incubated at 4 °C or 37 °C for 3 h or 24 h without mouse

serum revealed similar patterns with the development of a second peak with a % ROI between 2.1 and 3.7%. Samples incubated at 37 °C revealed a % ROI corresponding to [^{123}I]I-anti-KRAS IgG of 97.8 and 97.9% for samples incubated at 37 °C for 3 h or 24 h, without mouse serum, and 97.2 and 96.4% for samples incubated at 37 °C for 3 h or 24 h with mouse serum. The % ROI above 96% in both conditions and the evidence that similar peaks were formed without mouse serum, indicates stability of this antibody was sufficient for *in vivo testing*. Nonetheless, it is necessary to remember that this approach is only valid based on the hypothesis that any degradation will result in a radioiodinated construct that can be detected using iTLC chromatography. Following the evaluation of antibody stability in mouse serum, the uptake of [^{123}I]I-anti-KRas IgG with Tri-cTAT B in tumour-bearing BALB/c nude mouse was evaluated and SPECT/CT scan performed at 3 h and 24 h p.i (Figure 5.8).

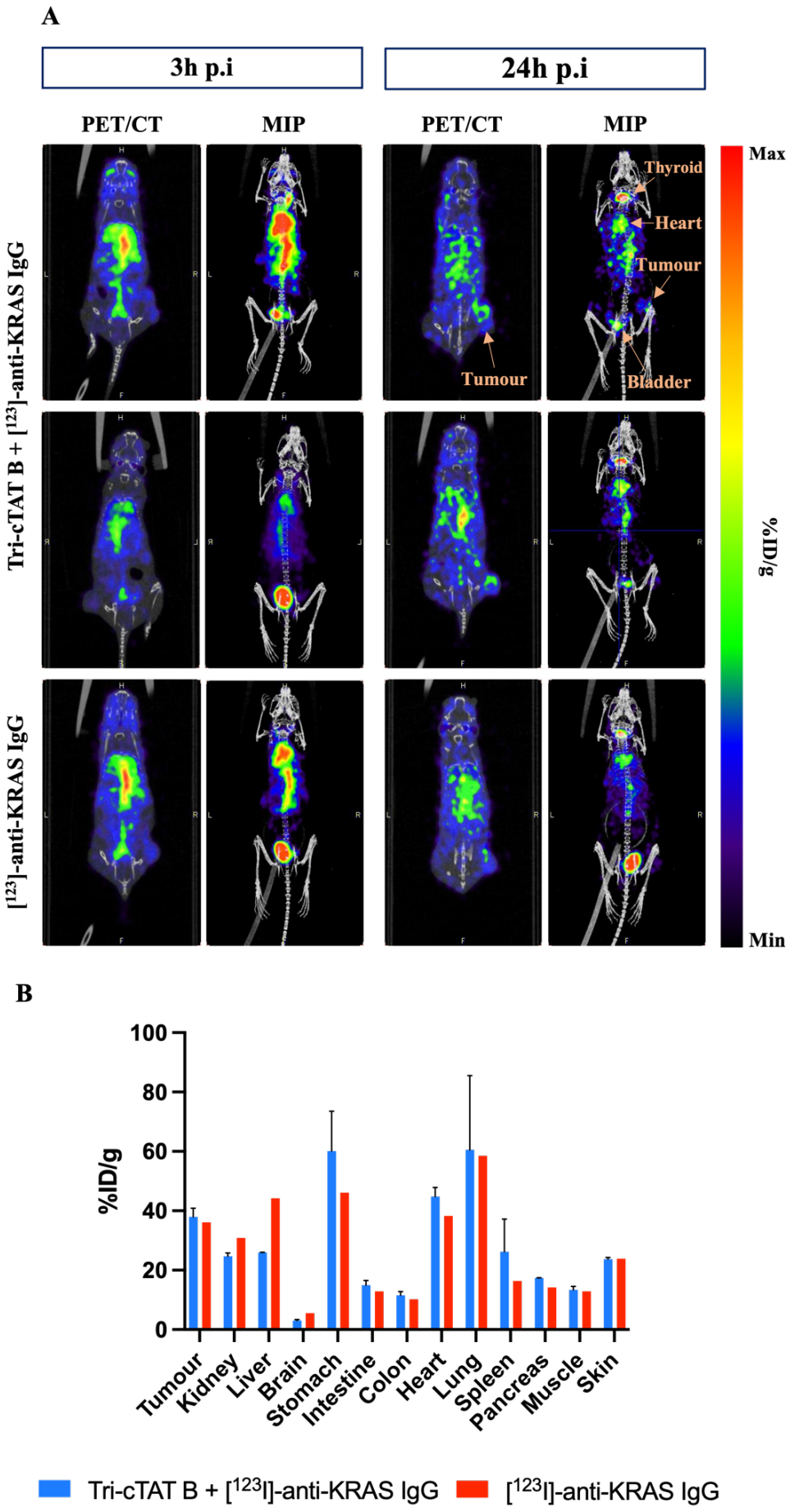

A
3h p.i
24h p.i
PET/CT
MIP
PET/CT
MIP
Thyroid
Heart
Tumour
Tumour
Bladder
Max
Min
%ID/g
Tri-cTAT B + [123]-anti-KRAS IgG
[123]-anti-KRAS IgG
B
%ID/g
100
80
60
40
20
0
Tumour
Kidney
Liver
Brain
Stomach
Intestine
Colon
Heart
Lung
Spleen
Pancreas
Muscle
Skin
Tri-cTAT B + [123I]-anti-KRAS IgG
[123I]-anti-KRAS IgG

Figure 5.8 – *In vivo* imaging of anti-KRas IgG in PSN-1 tumours. (A) Representative PET/CT and Maximum Intensity Projection (MIP) images showing distribution of [^{123}I]I-anti-KRas IgG co-delivered with Tri-cTAT B in PSN-1 mice xenografts, 3 h and 24 h after intravenous administration. **(B)** [^{123}I]I-anti-KRas IgG uptake (%ID/g) in selected tissues after 24 h. Tri-cTAT B + [^{123}I]I-anti-KRas IgG (n=2), [^{123}I]I-anti-KRas IgG (n=1).

Analysis of Figure 5.8 shows the co-delivery of [^{123}I]I-anti-KRas IgG with Tri-cTAT B resulted in a non-specific detection of [^{123}I] in multiple organs and tissues. While higher activities in the tumour were expected, this was not observed. Nonetheless, evaluation of the experimental group treated with Tri-cTAT B + [^{123}I]I-anti-KRas IgG showed that the tumour was the third tissue with a higher presence of [^{123}I]I-anti-KRas IgG with a mean %ID/g of 38%, just behind the lungs and stomach, with a %ID/g of 61 and 60% accordingly. Another objective of this experiment was to evaluate the efficacy of Tri-cTAT B in transfecting macromolecules *in vivo*. However, a comparison between both experimental groups shows only a small difference between the two, with some organs, including the liver, kidneys, and brain, presenting a higher %ID/g in the group treated with [^{123}I]I-anti-KRas IgG than in the group treated with Tri-cTAT B + [^{123}I]I-anti-KRas IgG. Yet, despite the small number of animals limiting the statistical analysis of these findings, for the remaining organs, the %ID/g was greater in the group that received full treatment than in the group that only received [^{123}I]I-anti-KRas IgG, including in the pancreas (17% vs 14%) and in the tumour (38% vs 36%). Interestingly, the lower % ID/g detected was in the brain, suggesting the co-delivery of macromolecules by Tri-cTAT B in the brain is limited by the blood-brain barrier (BBB). Alongside the statistical analysis performed based on data from SPECT/CT scans, it is notorious the high % ID/g in the bladder, implying the excretion of the treatment by urine, hence the higher uptake in the kidneys and in the thyroid, a common target for iodinated compounds.

5.4. Discussion

Following the internalisation of anti-KRas macromolecules by Tri-cTAT B, explored in Chapter 3 and the subsequent biological responses, assessed in Chapter 4, the current chapter introduced the potential for the development of a radionuclide therapeutic to target KRas. In addition, Chapter 5 evaluated whether the downregulation of KRas-mediated kinases affected the radiosensitisation of PANC-1 cells whilst confirming the advantageous effects of inserting a farnesyl moiety into anti-KRas macromolecules.

5.4.1. Radioiodination of Anti-KRas Macromolecules

Initial efforts were made to study the radioiodination of anti-KRas macromolecules using the Chloramine-T method developed by Hunter and colleagues[308]. With radiolabelling reactions taking less than one minute, radioiodination of DARPin K19, DARPin K19-cFarn and scFv Y6-cFarn has proven to be successful (Figure 5.1). Similar to the work provided by Seo *et al*., purification of radiolabelled macromolecules was easily achieved by MWCO centrifugal filters[319]. Hence, this technique, in line with reports from Tolmachev and colleagues, demonstrates the feasibility of effectively labelling high molecular weight constructs, particularly DARPins, with radionuclides of iodine whilet achieving purities exceeding 98%[307].

5.4.2. Radioiodination of Farnesylated Anti-KRas Macromolecules Follows Live-Cell Microscopy Data

Following the radiolabelling of anti-KRas constructs, an alternative method to explore the effect of farnesylation of DARPin K19 and scFv Y6 was tried. Consequently, radiolabelled anti-KRas macromolecules were co-delivered, and their uptake was studied by fractionating PANC-1-derived cell lysates, allowing the separation of the membrane, cytoplasm and nucleus (Figure 5.2). Similar to live-cell confocal microscopy, quantification of [^{123}I]I-DARPin K19 resulted in a higher accumulation in the nucleus,

followed by the membrane and cytoplasm. Nonetheless, consistent with live-cell microscopy data, the insertion of a farnesyl tag caused a relocation of DARPin K19-cFarn to the membrane. Similarly, co-delivery of scFv Y6-cFarn with Tri-cTAT B and subsequent fractionation yielded similar outcomes, revealing a higher activity in the membrane, followed by the nucleus and cytoplasm. Based on studies conducted using DARPin K19, showing its predominant accumulation in the nucleus, the synthesis of scFv Y6 was considered not critical. Thus, the synthesis of scFv Y6-cFarn was given priority, impeding the direct comparison between [^{123}I]I-scFv Y6 and [^{123}I]I-scFv Y6-cFarn. However, based on the comparison between [^{123}I]I-DARPin K19 and [^{123}I]I-DARPin K19-cFarn, it is predictable that similar results would be observed for the scFv counterparts. Overall, these findings reinforce the conclusions from Chapter 3, underlining once again the outcomes achieved by Cox *et al*., highlighting the role of farnesyl moieties promoting membrane localisation[278]. As previously highlighted, the modification of anti-KRas macromolecules with farnesyl moieties validates this approach to other internal targets that could be inhibited using organelle-specific modifications of immune molecules.

5.4.3. Downregulation of KRas-Mediated Kinases Causes Radiosensitisation

Initial experiments included the co-delivery of increasing concentrations of [^{123}I]I-DARPin K19-cFarn with Tri-cTAT B, with biological effects being explored using clonogenic assays (Figure 5.5). Not surprisingly, increasing concentrations of [^{123}I]I-DARPin K19-cFarn resulted in lower survival rates of PANC-1 cells. Notably, treatment of PANC-1 cells with 1 MBq·µg^{-1} [^{123}I]I-DARPin K19-cFarn did not affect the survival of cells in comparison with the vehicle group. However, co-delivery of 1 MBq·µg^{-1} [^{123}I]-DARPin K19-cFarn with Tri-cTAT B statistically compromised the survival of PANC-1 cells ($P<0.0001$). As previously described by Tietz *et al*. and throughout this thesis, these

results support the capacity for Tri-cTAT B to internalise multiple varieties of macromolecules[258]. With regards to this assay, preliminary results highlight the feasibility of developing a valuable radionuclide therapy modality, based on the delivery of targeted compounds in combination with Tri-cTAT B. Importantly, it is vital to confirm the detected toxicity effect is due to the interaction between [^{123}I]I-DARPin K19-cFarn and mutant KRas and not due to the internalisation of a radionuclide. As a result, a similar experiment but in a WT KRas cell line (i.e. BxPC-3) is key and should be addressed in the future.

Next, the radiosensitisation of PANC-1 cells was tested following the downregulation of KRAS-mediated kinases. Thus, following treatment with Tri-cTAT B and scFv Y6-cFarn for 24 h, cells were radiated with increasing doses ranging from 0 Gy to 4 Gy (Figure 5.6). As a control, PANC-1 cells that were not treated with Tri-cTAT B and scFv Y6-cFarn were equally radiated with the same doses of EBRT. Notably, cells that were previously treated with Tri-cTAT B and scFv Y6-cFarn revealed lower survival fractions than cells that were not exposed to Tri-cTAT B and scFv Y6-cFarn. For cells radiated with 4 Gy, samples that were not previously treated yielded a survival fraction of 0.40±0.05, whereas samples that were transfected with Tri-cTAT B and scFv Y6-cFarn returned a survival fraction of 0.12±0.03. Despite these results stemming from what could be deemed as a pilot experiment, it shows *in vitro* what was previously described *in vivo* by Fokas and colleagues, describing that inhibition of PI3K and subsequent EBRT diminished tumour growth, in comparison with EBRT alone[175]. Similar to the internalisation of [^{123}I]I-DARPin K19-cFarn in PDAC cell lines, it is important to compare these results with a control experiment involving a WT KRas cell line. If cells previously treated with Tri-cTAT B + scFv Y6-cFarn and subsequently exposed to radiation yield the same survival fraction as cells that were only exposed to radiation,

then it is irrefutable that downregulation of KRas-mediated kinases causes the radiosensitisation of PDAC cell lines. Nonetheless, these preliminary findings support the hypothesis that targeting KRas may enhance the therapeutic approach in PDAC using EBRT.

5.4.4. Co-Delivery of Anti-KRas IgG *In Vivo* Demonstrates Limited Effects

Finally, the last efforts were made to perform a pilot study regarding the co-delivery of an anti-KRas macromolecule with Tri-cTAT B *in vivo*. Due to the unavailability of DARPin K19-cFarn and scFv Y6-cFarn, a commercially available anti-KRas IgG was used for this experiment. To quantify the uptake of antibody *in vivo*, anti-KRas IgG was radiolabelled with Na[^{123}I], following the same technique as employed for DARPin K19 and scFv Y6 (Figure 5.7A). Moreover, the stability of [^{123}I]I-anti-KRas IgG in mouse serum was explored prior to the delivery *in vivo* (Figure 5.7B). Despite serum-stability assays are generally explored using HPLC, the stability of anti-KRas IgG was explored using iTLC, a similar approach to the one employed by Radaram and colleagues[320]. Notably, iTLC analysis of [^{123}I]I-anti-KRas IgG incubated with mouse serum revealed minimal degradation with a % ROI of 97.2 % and 96.4 % at 3 h and 24 h incubation, respectively. However, comparison with a control group involving the incubation of [^{123}I]I-anti-KRas IgG at 37 °C without mouse serum revealed a similar % ROI, suggesting that any observed degradation was not a result of its interaction with mouse serum. Following the intravenous administration of [^{123}I]I-anti-KRas IgG or Tri-cTAT B and [^{123}I]I-anti-KRas IgG *in vivo*, SPECT/CT images were acquired at 3 h and 24 h p.i., with further *ex vivo* quantification being performed in organs and tissues of interest. Despite the purification of [^{123}I]I-anti-KRas IgG, allowing the separation of Na[^{123}I], an elevated uptake was detected in the thyroid, known to be a target tissue for iodine derivatives[321,322]. Moreover, SPECT images revealed a similar uptake of [^{123}I]I-anti-KRas IgG in both

experimental groups, suggesting the addition of Tri-cTAT B did not enhance the accumulation of [^{123}I]I-anti-KRas IgG in specific tissues. Notably, in neither treatment modalities, no clear uptake of [^{123}I]I-anti-KRas IgG in the tumour was detected, with a higher % ID/g being identified in the bladder, alongside the thyroid. Despite *in vivo* images showing areas where [^{123}I]I-anti-KRas IgG is more predominant, *ex vivo* analysis allows for the quantification of its uptake in specific organs. Interestingly, whilst *in vivo* images showed no tumour uptake, *ex vivo* analysis revealed that after the heart, lung and stomach, the tumour was the fourth tissue with higher uptake. Moreover, *ex vivo* analysis revealed that out of 13 organs and tissues assessed, the group comprised by Tri-cTAT B and [^{123}I]I-anti-KRas IgG yielded higher uptakes than [^{123}I]I-anti-KRas IgG alone in 10 of them, including the tumour. However, this difference was subtle and likely not significant. Whilst the uptake of [^{123}I]I-anti-KRas IgG with Tri-cTAT B *in vivo* was limited, it is important to mention this was a pilot study with optimisations needed. Equally important, as tried by Lee and colleagues with TAT and Tietz *et al.* with Tri-cTAT B, the internalisation of macromolecules into live cells throughout this thesis, was explored simply by incubating Tri-cTAT B with anti-KRAS macromolecules[258,323]. Consequently, the transfection of DARPin K19 and scFv Y6 by Tri-cTAT B was purely based on their electrostatic interaction and not by the formation of a covalent bond. Given the complexity of *in vivo* systems, it is predictable that an electrostatic force between Tri-cTAT B and anti-KRas macromolecules is not strong enough to deliver these macromolecules in vivo and that a covalent bond between the two is mandatory. As a hypothesis, based on the negatively charged nature of serum proteins, it is possible that Tri-cTAT B, known to be highly positively charged, loses interaction with anti-KRas macromolecules, limiting its delivery in target tissues[324]. Although studies suggest that co-delivery of macromolecules is beneficial given their stability in physiological buffer

and lack of toxicity, these are mainly studied *in vitro*, thus limiting their applicability in the clinic[325]. Yet, other studies indicate that covalent attachment of cargo molecules to CPPs leads to greater efficacy than non-conjugated approaches[326,327]. With multiple conjugation techniques available, including through the formation of amide, maleimide, disulfide or triazole bonds, each strategy provides different characteristics that must be weighed when considered[328].

Chapter 6 Concluding Remarks

6.1. Synopsis

The development of new therapies for KRas mutant tumours remains an urgent necessity. Despite clear advancements over the last decade, since the discovery of KRAS in 1964 and its importance in promoting tumourigenesis, only two small-molecule drugs have been approved for clinical use. Nonetheless, their use is limited to NSCLC[124,329,330], and there have been early reports of the emergence of resistance to these agents Moreover, PDAC diagnosis continues to be seen as a death sentence, with little to no effective treatment available. Despite its involvement in other types of tumours, KRas is considered a hallmark in PDAC with mutations being detected in 90-95% of cases, and thus being considered the most Ras-addicted of all cancers[102]. Moreover, although PDAC development involves the mutation of multiple genes, including TP53, SMAD4 and CDKN2A/p16, KRas is the main trigger of this stepwise genetic transition[23]. As a result, this thesis has focused on the investigation of a viable treatment for mutant KRas-based cancers using PDAC models.

Given the challenges of targeting KRas, particularly the affinity of GDP and GTP towards the protein and the lack of deep pockets, methods other than small molecule drug approaches have been explored[331]. As an alternative, this work explored the use of anti-

KRas immune molecules, yielding high affinities for the intended epitopes and thus limiting the development of off-target events. Specifically, this work investigated the use of macromolecules developed by the Rabbitts Group, including DARPin K19 and scFv Y6. A major drawback of antibody-based therapies, despite their potentially transformative impact as treatments for specific cancers, is that their targeting capabilities are restricted to extracellular proteins, owing to their inability to cross cellular membranes. Thus, in this project an innovative TAT-derived cell-penetrating peptide was used, to explore the possibility of transfecting DARPin K19 and scFv Y6 into live cells. Consistent with studies provided by Tietz *et al.*, the structural modification of TAT greatly enhanced its uptake, as well as the transfection of macromolecules, in comparison to its original linear and monomeric structure. Once in cells, the biological effect of DARPin K19 and scFv Y6 was explored, mainly by western blotting and cell viability assays. Whilst initial evidence showed an off-target event, consistent with the translocation of macromolecules to the nucleus by TAT-derived CPPs, the addition of a farnesyl tag resulted in preferential accumulation at the inner leaflet of the cell membrane. These results were confirmed either by live-cell confocal microscopy or by fractionation of cellular structures following their treatment and quantified using [^{123}I]I-anti-KRas macromolecules. Next, the biological effect of this structural modification was explored, with western blotting data revealing the downregulation of pERK in PANC-1 cells with DARPin K19-cFarn, DARPin K19-cFarn-VHL and scFv Y6-cFarn. Moreover, transfection of DARPin K19-cFarn-VHL by Tri-cTAT B in PANC-1 cells caused full abrogation of the pMEK signal. Nonetheless, the downregulation of pERK in PSN-1 cells was limited with only DARPin K19-cFarn-VHL, showing pronounced pERK downregulation. Analysis of cell viability following the treatment of PANC-1 cells with DARPin K19-cFarn or scFv Y6-cFarn exhibited complete impairment of cell viability,

suggesting that inhibition of KRAS and subsequent inhibition of KRAS-mediated kinases compromises the viability of cells. Not surprisingly, treatment of cells with Tri-cTAT B, DARPin K19-cFarn or scFv Y6-cFarn alone caused little to no biological effect. Interestingly, despite the observations made in PSN-1 cells using western blotting, treatment of cells with DARPin K19-cFarn or scFv Y6-cFarn equally compromised the viability of cells. However, while for WBA, PSN-1 cells were exposed to Tri-cTAT B and DARPin K19-cFarn or scFv Y6-cFarn for 24 h, for cell viability assays, PSN-1 cells were treated for 48 h. As a result, this suggests that to detect abrogation of KRas-mediated kinases, longer incubation periods for PSN-1 cells are required. Similar to PANC-1 cells, treatment of PSN-1 cells with Tri-cTAT B, DARPin K19-cFarn or scFv Y6-cFarn revealed no biological effect. Importantly, transfection of DARPin K19-cFarn or scFv Y6-cFarn by Tri-cTAT B in BxPC-3 cells revealed no cell viability impairment. Hence this confirms the initial hypothesis showing that albeit not specific for a particular KRas mutation, DARPin K19 and scFv Y6 only bind mutant forms of KRas.

Next, this thesis explored its main objective by studying the possibility of developing a radiation-based approach for the treatment of KRas-mutant PDAC. Based on evidence showing that downregulation of KRas-mediated kinases causes the radiosensitisation of cancer cells, a similar approach was tried. To do so, following the treatment of PANC-1 cells with Tri-cTAT B and scFv Y6-cFarn, cells were subject to doses of radiation using EBRT and their survival capacity was explored via clonogenic assays. Consequently, the experimental group that was treated beforehand with Tri-cTAT B and scFv Y6-cFarn, revealed a lower survival than cells that were exposed to EBRT only, suggesting that KRas inhibition promotes the radiosensitisation of cells. Additionally, the development of an anti-KRAS radionuclide therapy, a more targeted approach, was tried. Following the radiolabelling of DARPin K19-cFarn with [^{123}I], increasing concentrations of [^{123}I]I-

DARPin K19-cFarn were delivered with Tri-cTAT B in PANC-1 cells and their survival was explored. Not surprisingly, increasing concentrations caused lower cell survival, highlighting the capacity of Tri-cTAT B to internalise anti-KRas radionuclides. Importantly, treatment of PANC-1 cells with 1 MBq·µg-1 of [^{123}I]I-DARPin K19-cFarn did not affect the viability of cells, whereas the use of Tri-cTAT B with 1 MBq·µg-1 of [^{123}I]I-DARPin K19-cFarn reduced the survival of cells. Given the capacity to specifically deliver macromolecules into tumour cells, these findings suggest a valuable approach to target mutant KRas cells.

Finally, as a proof-of-principle, this work explored the co-delivery of a radiolabelled anti-KRas macromolecule *in vivo* in tumour-bearing mice with Tri-cTAT B. Since the availability of DARPin K19-cFarn or scFv Y6-cFarn was limited, a commercial anti-KRas IgG was used. However, SPECT images showed little to no difference between the group that received Tri-cTAT B and [^{123}I]I-anti-KRas IgG and the control group that was exposed to [^{123}I]I-anti-KRas IgG. As previously mentioned, throughout this thesis, the delivery of anti-KRas macromolecules by Tri-cTAT B was only performed in a non-covalent manner, promoting the formation of electrostatic interactions between both. Yet, *in vivo* environments are more complex than *in vitro*, with the mouse serum containing multiple highly negatively charged proteins, including albumin. Given the highly positively charged nature of Tri-cTAT B, it is possible there was a loss of the interaction between the CPP and [^{123}I]I-anti-KRas IgG before reaching the tumour, thus limiting its delivery in targeted tissues.

6.2. Study Limitations

Despite strong findings, this thesis presents limitations that should be addressed to strengthen its significance in the pre-clinical development of PDAC therapies. With the majority of this thesis focused on the transfection of DARPin K19- and scFv Y6-related

macromolecules into PDAC cells, it is assumed that any biological effect detected confirms the interaction between transfected DARPin K19 or scFv Y6 macromolecules and KRas. However, no study involving the interaction between DARPin K19 or scFv Y6 following its internalisation with Tri-cTAT B was pursued. Yet, this thesis explored the interaction of a Tri-cTAT B-internalised anti-KRas^{G12D} IgG with KRas via PLA, assuming that if the interaction was detected, then a similar effect would be expected with DARPin K19 or scFv Y6.

With regards to the *in vivo* internalisation of Tri-cTAT B, it is important to acknowledge that the concentration used was suboptimal. Consequently, this had not allowed to thoroughly study the capacity of Tri-cTAT B *in vivo*. Additionally, while *ex vivo* analysis permitted Tri-cTAT B's quantification in organs of interest, comparisons of *in vivo* uptake at 1 h and 4 h p.i. returned no detectable fluorescence, presumably due to the fur of the animal model. Equally, the internalisation of anti-KRas macromolecules *in vivo* offered limited conclusions. However, this was a pilot study that clearly requires further optimisation. Similar to the PLA assay, this experiment involved the use of another macromolecule than DARPin K19 or scFv Y6. Yet, given the shortage of DARPin K19 and scFv Y6 at the time of this experiment, no other alternative was possible. Moreover, based on previous reports, it was anticipated a need for a covalent bond between Tri-cTAT B and [^{123}I]I-anti-KRas IgG for a satisfactory delivery in tissues of interest.

Given the central focus on investigating the biological effects of co-delivered anti-KRas macromolecules and their potential to enhance the radiosensitivity of PDAC cancer cells, key limitations were considered. Despite showing strong evidence about the downregulation of pERK in PANC-1, this study only investigated one KRas-mediated signalling pathway. Yet, only pERK was properly assessed with a pilot study being done on pMEK. As a result, it would be critical to expand this study to other KRas-mediated

pathways, particularly the PI3K/AKT/mTOR pathway. Importantly, while this thesis has demonstrated the downregulation of KRas-mediated kinases in cell lines harbouring two of the most prevalent KRas mutations in PDAC, it only looked for a single cell line for each distinct mutant form of KRas. Additionally, it should be expanded to other KRas mutations, including cell lines harbouring G12V mutations. Still on this line, this thesis has shown clear evidence that the co-delivery of farnesylated anti-KRas macromolecules with Tri-cTAT B impairs the viability of PANC-1 and PSN-1 cells. Yet, this was only demonstrated 48 h post-treatment, with other time-points being needed to identify the rate at which this effect is detected.

Ultimately, the objective of this thesis was to demonstrate whether the downregulation of KRas-mediated kinases caused the radiosensitisation of PDAC cells. Alongside exploring this event with the internalisation of [^{123}I]I-DARPin K19-cFarn by Tri-cTAT B, the same phenomena were evaluated with EBRT. Notably, radiosensitisation was detected in both approaches, although only in PANC-1 cells in a single experiment with three technical repeats. Yet, these results support the main aim of this thesis by showing that KRas disruption influences the radiosensitivity of PDAC cells.

Aware of the incredible effort made by the Rabbits Lab, one of the main limitations of this work was the limited availability of DARPin K19- and scFv Y6-related macromolecules. With various anti-KRas constructs being explored, including DARPin K19, DARPin K19-cFarn, DARPin K19-cFarn-VHL and scFv Y6-cFarn, assays were many times performed based on the available construct, resulting in trying to balance the rationale of each experiment accordingly. On the other hand, assays involving the study of biological effects using western blotting and clonogenic assays are typically performed in 6- and 12-well plates. As a result, these often require higher quantities of material to

follow the conditions used in other assays that require less working volumes (i.e. live-cell confocal microscopy).

6.3. Future Perspectives

According to the limitations previously described, additional pre-clinical studies are required to consider this approach as a viable method for the treatment of PDAC. With the ultimate goal of employing this technique in vivo, previous experiments have shown that the covalent attachment between Tri-cTAT B and anti-KRAS macromolecules is critical. As a result, before the submission of this thesis, different approaches were being explored. Considering Tri-cTAT B contains a tetrakis core with an available alkyne tag, the primary goal is to link an NHS-PEG_X-N_3 linker by CuAAC chemistry. Next, given the presence of tyrosine residues in the primary structure of DARPin K19 and scFv Y6 macromolecules, Tri-cTAT B-PEG_X-NHS can be covalently attached to these based on the NHS tag present in the linker. Importantly, this will form an amide bond that can be promptly cleaved through various enzymatic and non-enzymatic processes within cells, allowing the separation between Tri-cTAT B-PEG_X and DARPin K19 or scFv Y6 once inside cells [332–334].

While the internalisation of anti-KRas macromolecules was explored, the study of its subsequent biological effects was limited. As a result, western blotting is still required to understand the downregulation of KRAS-mediated kinases other than pERK. Although incubation periods were limited to 1 h and 24 h, others are needed to understand the optimal incubation period. Furthermore, a dose-dependent study is imperative to comprehend the ideal concentration of anti-KRAS macromolecules necessary to detect KRas downregulation. While a concentration of 500 nM was employed, based on the findings from Tietz *et al*., different immune molecules present different bindings affinities, ultimately varying the concentrations required[258]. Importantly, if considering

the co-delivery of anti-KRas macromolecules with Tri-cTAT B, it is fundamental to understand their interactions. With efforts made to optimise the downregulation of pERK, questions about the interaction between Tri-cTAT B and DARPin K19- or scFv Y6-related macromolecules arose. To exemplify, it was previously mentioned the electrostatic nature between both constructs. However, no further evidence is provided in this sense. Therefore, throughout this thesis, it was hypothesised whether electrostatic binding between both constructs occurred always in the same location or if it varied. With WBA suggesting different pERK expressions using equivalent conditions, it could be possible that Tri-cTAT B interacts with DARPin K19 and scFv Y6 in a location that is essential to interact with KRAS, thus impeding it. To further explore this, the use of x-ray crystallography is planned to evaluate the location where Tri-cTAT B interacts with DARPin K19 or scFv Y6 and more importantly, if these interactions occur in the same place. Nonetheless, the covalent linkage between Tri-cTAT B and anti-KRAS macromolecules would eliminate this need, albeit it would be necessary to understand the location of the bond, particularly in the cargo molecule.

Regarding the radiosensitisation of PDAC cell lines, this was only explored in PANC-1 with scFv Y6-cFarn. Despite more independent repeats are required, the use of other cell lines is mandatory to show that these events are not dependent on the model used but that any mutant KRAS model will yield similar effects. Importantly, it is equally vital to include control models. Thus, it would be valuable to show that treatment of BxPC-3 cells with Tri-cTAT B and DARPin K19-cFarn or scFv Y6-cFarn and subsequent radiation would cause equivalent cell survival than radiation alone. With the ultimate aim of developing a targeted anti-KRas radionuclide, other experiments are required. Importantly, this thesis has shown that co-delivery of [^{123}I]I-DARPin K19 by Tri-cTAT B causes cell toxicity. However, it is vital to understand if the co-delivery of a non-

specific radiolabelled antibody causes similar cell toxicity. If not, this represents a valuable step for the development of a dual approach therapy, since the internalisation of DARPin K19-cFarn and consequent downregulation of KRAS radiosensitises cells, whilst [^{123}I] promotes the delivery of targeted radiation.

With mostly *in vitro* assays being explored in serum-free medium, questions may arise regarding the feasibility of employing this technique *in vivo*. Nonetheless, it is important to note that although serum proteins might interact with Tri-cTAT B, limiting their delivery, a pilot *ex vivo* internalisation revealed the internalisation of Tri-cTAT B in organs of interest, including the pancreas. With additional *in vitro* work required, *in vivo* experiments are vital for the next stage in developing anti-KRas-based therapies. Alongside a thorough evaluation of the pharmacodynamic and pharmacokinetic properties of Tri-cTAT B and anti-KRas macromolecules *in vivo*, it is imperative to study its accumulation and survival in tumour-bearing models. Similarly, it is vital to compare these with a control group exposed to Tri-cTAT B and a non-specific IgG. Following the accumulation of [^{123}I]I-anti-KRas macromolecules in tumour-bearing models, its biological effect must be explored, including the downregulation of KRas-mediated kinases and radiosensitisation effect. Importantly, *in vitro* assays have revealed that Tri-cTAT B lacks specificity to tumour cells. Therefore, future studies should consider the addition of a tumour-seeking ligand to restrict the delivery of anti-KRas macromolecules into tumour cells. To exemplify, cancer cells exhibit various extracellular markers, including glycoproteins with altered glycan expression, representing a valuable hypothesis[335]. Nonetheless, it is important to remember that Tri-cTAT B is not toxic to cells. Moreover, considering that DARPin K19-cFarn and scFv Y6-cFarn yielded no biological effect on BxPC-3 cells, their uptake by non-tumour cells would not represent any harm.

Lastly, this thesis has considered the development of a therapeutic approach to KRas-derived PDAC. However, it is also possible to consider this approach as a technique to detect KRas mutations, potentially serving as a diagnostic tracer. As previously mentioned, the development of PDAC involves a stepwise genetic transition in which KRas mutations are the first event. Additionally, nearly a decade can pass between the onset of KRas mutations and PDAC. As a result, for individuals with specific risk factors, the early detection of KRas mutations prior to the development of PDAC could serve as a valuable indicator for the potential occurrence of PDAC. Yet, based on today's approach to detecting PDAC using CT, the frequent exposure of patients with early-detected KRas mutations to radiation might represent a limitation of this approach to detecting premalignant pancreas.

To conclude, this thesis had the objective of showing the ability of Tri-cTAT B to internalise macromolecules in cells, promoting their interaction with intracellular targets, particularly KRas. Following their internalisation, this work shows that the capacity to downregulate KRas-mediated pathways vital to promote cell division and proliferation of cancer cells. Given the downregulation of KRas-mediated kinases, namely pERK and pMEK, the viability of cells was shown to be compromised, whereas treatment of BxPC-3 resulted in no biological effect. To further develop a concise therapeutic approach, the sensitisation of PANC-1 cells was tried, suggesting that downregulation of pERK and pMEK results in their radiosensitisation. As an alternative to promote the development of a targeted therapeutic approach anti-KRas macromolecules were radiolabelled with [^{123}I] and successfully internalised into PANC-1 cells, compromising their viability. Overall, this thesis demonstrates a feasible approach to target PDAC, a disease that despite much effort, continues to be highly lethal, mainly due to KRas.

Chapter 7 Bibliography

1. Röder, P. V., Wu, B., Liu, Y. & Han, W. Pancreatic regulation of glucose homeostasis. *Exp Mol Med* **48,** (2016).

2. World Cancer Research Fund. Worldwide cancer data. *World Cancer Research Fund* at <https://www.wcrf.org/cancer-trends/worldwide-cancer-data/>

3. Cancer Research UK. Pancreatic cancer statistics. *Cancer Research UK* at <https://www.cancerresearchuk.org/health-professional/cancer-statistics/statistics-by-cancer-type/pancreatic-cancer>

4. Cancer Research UK. Pancreatic cancer incidence trends over time. (2021). at <https://www.cancerresearchuk.org/health-professional/cancer-statistics/statistics-by-cancer-type/pancreatic-cancer/incidence#heading-Two>

5. Cancer Research UK. Pancreatic cancer incidence by age . (2021). at <https://www.cancerresearchuk.org/health-professional/cancer-statistics/statistics-by-cancer-type/pancreatic-cancer/incidence#heading-One>

6. Mukhopadhyay, S., Vander Heiden, M. G. & McCormick, F. The metabolic landscape of RAS-driven cancers from biology to therapy. *Nat Cancer* **2,** 271–283 (2021).

7. Gullo, L., Pezzilli, R. & Morselli-Labate, A. M. Diabetes and the risk of pancreatic cancer. *New England Journal of Medicine* **331,** 81–84 (1994).

8. Toriola, A. T., Stolzenberg-Solomon, R., Dalidowitz, L., Linehan, D. & Colditz, G. Diabetes and pancreatic cancer survival: A prospective cohort-based study. *Br J Cancer* **111,** 181–185 (2014).

9. Wang, S., Zheng, Y., Yang, F., Zhu, L., Zhu, X. Q., Wang, Z. F., Wu, X. L., Zhou, C. H., Yan, J. Y., Hu, B. Y., Kong, B., Fu, D. L., Bruns, C., Zhao, Y., Qin, L. X. & Dong, Q. Z. The molecular biology of pancreatic adenocarcinoma: translational challenges and clinical perspectives. *Signal Transduct Target Ther* **6,** Preprint at https://doi.org/10.1038/s41392-021-00659-4 (2021)

10. Zhang, S., Wang, C., Huang, H., Jiang, Q., Zhao, D., Tian, Y., Ma, J., Yuan, W., Sun, Y., Che, X., Zhang, J., Chen, H., Zhao, Y., Chu, Y., Zhang, Y. & Chen, Y. Effects of alcohol drinking and smoking on pancreatic ductal adenocarcinoma mortality: A retrospective cohort study consisting of 1783 patients. *Sci Rep* **7,** (2017).

11. Singhi, A. D., Koay, E. J., Chari, S. T. & Maitra, A. Early Detection of Pancreatic Cancer: Opportunities and Challenges. *Gastroenterology* **156,** 2024–2040 (2019).

12. Iacobuzio-Donahue, C. A. Genetic evolution of pancreatic cancer: Lessons learnt from the pancreatic cancer genome sequencing project. *Gut* **61,** 1085–1094 Preprint at https://doi.org/10.1136/gut.2010.236026 (2012)

13. Almoguera, C., Shibata, D., Forrester, K., Martin, J., Arnheim, N. & Perucho, M. Most Human Carcinomas of the Exocrine Pancreas Contain Mutant c-K-ras Genes. *Cell* **53,** 549–554 (1988).

14. Caldas, C., Hahn, S. A., Da Costa, L. T., Redston, M., Schutte, M., Seymour, A. B., Weinstein, C. L., Hruban, R. H., Yeo, C. J. & Kern, S. E. Frequent somatic mutations and homozygous deletions of the p16 (MTS1) gene in pancreatic adenocarcinoma. *Nat Genet* **8,** 27–32 (1994).

15. Schutte, M., Hruban, R. H., Geradts, J., Maynard, R., Hilgers, W., Rabindran, S. K., Moskaluk, C. A., Hahn, S. A., Schwarte-Waldhoff, I., Schmiegel, W., Baylin, S. B., Kern, S. E. & Herman, J. G. Abrogation of the Rb/p16 Tumor-suppressive Pathway in Virtually All Pancreatic Carcinomas. *Cancer Res* **57,** 3126–3130 (1997).

16. Redston, M. S., Caldas, C., Seymour, A. B., Hruban, R. H., da Costa, L., Yeo, C. J. & Kern, S. E. p53 Mutations in Pancreatic Carcinoma and Evidence of Common Involvement of Homocopolymer Tracts in DNA Microdeletions. *Cancer Res* **54,** 3025–3033 (1994).

17. Hahn, S. A., Schutte, M., Hoque, A. T. M. S., Moskaluk, C. A., da Costa, L. T., Rozenblum, E., Weinstein, C. L., Fischer, A., Yeo, C. J., Hruban, R. H. & Kern, S. E. DPC4, A Candidate Tumor Suppressor Gene at Human Chromosome 18q21.1. *Science (1979)* **271,** 350–353 (1996).

18. Schubbert, S., Shannon, K. & Bollag, G. Hyperactive Ras in developmental disorders and cancer. *Nat Rev Cancer* **7,** 295–308 Preprint at https://doi.org/10.1038/nrc2109 (2007)

19. Raycroft, L., Wu, H. & Lozano, G. Transcriptional Activation by Wild-Type But Not Transforming Mutants of the p53 Anti-Oncogene. *Science (1979)* **249,** 1049–1051 (1990).

20. Goh, A. M., Coffill, C. R. & Lane, D. P. The role of mutant p53 in human cancer. *Journal of Pathology* **223,** 116–126 (2011).

21. Kim, W. Y. & Sharpless, N. E. The Regulation of INK4/ARF in Cancer and Aging. *Cell* **127,** 265–275 (2006).

22. Massagué, J. TGFβ in Cancer. *Cell* **134,** 215–230 (2008).

23. Moskaluk, C. A., Hruban, R. H. & Kern, S. E. p16 and K-ras Gene Mutations in the Intraductal Precursors of Human Pancreatic Adenocarcinoma. *Cancer Res* **57,** 2140–2143 (1997).

24. DiGiuseppe, J. A., Redston, M. S., Yeo, C. J., Kern, S. E. & Hruban, R. H. Communication p53-Independent Expression of the Cyclin-Dependent Kinase Inhibitor p21 in Pancreatic Carcinoma. *American Journal of Pathology* **147,** (1995).

25. Wilentz, R. E., Iacobuzio-Donahue, C. A., Argani, P., McCarthy, D. M., Parsons, J. L., Yeo, C. J., Kern, S. E. & Hruban, R. H. Loss of Expression of Dpc4 in Pancreatic Intraepithelial Neoplasia: Evidence That DPC4 Inactivation Occurs Late in Neoplastic Progression 1. *Cancer Res* **60,** 2002–2006 (2000).

26. Park, W., Chawla, A. & O'Reilly, E. M. Pancreatic Cancer: A Review. *JAMA - Journal of the American Medical Association* **326,** 851–862 (2021).

27. Stapley, S., Peters, T. J., Neal, R. D., Rose, P. W., Walter, F. M. & Hamilton, W. The risk of pancreatic cancer in symptomatic patients in primary care: A large case-control study using electronic records. *Br J Cancer* **106,** 1940–1944 (2012).

28. Kardon, D. E., Thompson, L. D. R., Przygodzki, R. M. & Heffess, C. S. Adenosquamous Carcinoma Of The Pancreas: A Clinicopathologic Series Of 25 Cases. *Modern Pathology* **14,** 443–451 (2001).

29. Brody, J. R., Costantino, C. L., Potoczek, M., Cozzitorto, J., McCue, P., Yeo, C. J., Hruban, R. H. & Witkiewicz, A. K. Adenosquamous carcinoma of the pancreas harbors KRAS2, DPC4 and TP53 molecular alterations similar to pancreatic ductal adenocarcinoma. *Modern Pathology* **22,** 651–659 (2009).

30. Madura, J. A., Jarman, B. T., Doherty, M. G., Yum, M.-N. & Howard, T. J. Adenosquamous Carcinoma of the Pancreas. *JAMA - Journal of the American Medical Association* **134,** 599–603 (1999).

31. Madura, J. A. Adenosquamous Carcinoma of the Pancreas. *Archives of Surgery* **134,** 599–603 (1999).

32. Boyd, C. A., Benarroch-Gampel, J., Sheffield, K. M., Cooksley, C. D. & Riall, T. S. 415 Patients with Adenosquamous Carcinoma of the Pancreas: A Population-Based Analysis of Prognosis and Survival. *Journal of Surgical Research* **174,** 12–19 (2012).

33. Shi, Y., Wang, X., Wu, W., Xie, J., Jin, J., Peng, C., Deng, X., Chen, H. & Shen, B. Prognostic Analysis and Influencing Serum Biomarkers of Patients With Resectable Pancreatic Adenosquamous Cancer. *Front Oncol* **10,** (2021).

34. Hruban, R. H. & Fukushima, N. Pancreatic adenocarcinoma: Update on the surgical pathology of carcinomas of ductal origin and panins. *Modern Pathology* **20,** 61–70 (2007).

35. Benninger, R. K. P. & Kravets, V. The physiological role of β-cell heterogeneity in pancreatic islet function. *Nat Rev Endocrinol* **18,** 9–22 Preprint at https://doi.org/10.1038/s41574-021-00568-0 (2022)

36. Yao, J. C., Eisner, M. P., Leary, C., Dagohoy, C., Phan, A., Rashid, A., Hassan, M. & Evans, D. B. Population-based study of islet cell carcinoma. *Ann Surg Oncol* **14,** 3492–3500 (2007).

37. Brooks, J. C., Shavelle, R. M. & Vavra-Musser, K. N. Life expectancy in pancreatic neuroendocrine cancer. *Clin Res Hepatol Gastroenterol* **43,** 88–97 (2019).

38. Sakamoto, H., Attiyeh, M. A., Gerold, J. M., Makohon-Moore, A. P., Hayashi, A., Hong, J., Kappagantula, R., Zhang, L., Melchor, J. P., Reiter, J. G., Heyde, A., Bielski, C. M., Penson, A. V., Gönen, M., Chakravarty, D., O'reilly, E. M., Wood, L. D., Hruban, R. H., Nowak, M. A., Socci, N. D., Taylor, B. S. & Iacobuzio-Donahue, C. A. The evolutionary origins of recurrent pancreatic cancer. *Cancer Discov* **10,** 792–805 (2020).

39. Walter, F. M., Mills, K., Mendonça, S. C., Abel, G. A., Basu, B., Carroll, N., Ballard, S., Lancaster, J., Hamilton, W., Rubin, G. P. & Emery, J. D. Symptoms and patient factors associated with diagnostic intervals for pancreatic cancer (SYMPTOM pancreatic study): a prospective cohort study. *Lancet Gastroenterol Hepatol* **1,** 298–306 (2016).

40. Rawla, P., Sunkara, T. & Gaduputi, V. Epidemiology of Pancreatic Cancer: Global Trends, Etiology and Risk Factors. *World J Oncol* **10,** 10–27 (2019).

41. American Cancer Society. Pancreatic Cancer Stages. *American Cancer Society* at <https://www.cancer.org/cancer/pancreatic-cancer/detection-diagnosis-staging/staging.html#written_by>

42. Conroy, T., Hammel, P., Hebbar, M., Ben Abdelghani, M., Wei, A. C., Raoul, J.-L., Choné, L., Francois, E., Artru, P., Biagi, J. J., Lecomte, T., Assenat, E., Faroux, R., Ychou, M., Volet, J., Sauvanet, A., Breysacher, G., Di Fiore, F., Cripps, C., Kavan, P., Texereau, P., Bouhier-Leporrier, K., Khemissa-Akouz, F., Legoux, J.-L., Juzyna, B., Gourgou, S., O'Callaghan, C. J., Jouffroy-Zeller, C., Rat, P., Malka, D., Castan, F. & Bachet, J.-B. FOLFIRINOX or Gemcitabine as Adjuvant Therapy for Pancreatic Cancer. *New England Journal of Medicine* **379,** 2395–2406 (2018).

43. De Vita, F., Ventriglia, J., Febbraro, A., Laterza, M. M., Fabozzi, A., Savastano, B., Petrillo, A., Diana, A., Giordano, G., Troiani, T., Conzo, G., Galizia, G., Ciardiello, F. & Orditura, M. NAB-paclitaxel and gemcitabine in metastatic pancreatic ductal adenocarcinoma (PDAC): From clinical trials to clinical practice. *BMC Cancer* **16,** (2016).

44. Miyabayashi, K., Ijichi, H., Mohri, D., Tada, M., Yamamoto, K., Asaoka, Y., Ikenoue, T., Tateishi, K., Nakai, Y., Isayama, H., Morishita, Y., Omata, M., Moses, H. L. & Koike, K. Erlotinib prolongs survival in pancreatic cancer by blocking gemcitabine-induced MAPK signals. *Cancer Res* **73,** 2221–2234 (2013).

45. Buscail, L., Bournet, B. & Cordelier, P. Role of oncogenic KRAS in the diagnosis, prognosis and treatment of pancreatic cancer. *Nat Rev Gastroenterol Hepatol* **17,** 153–168 Preprint at https://doi.org/10.1038/s41575-019-0245-4 (2020)

46. Palta, M., Godfrey, D., Goodman, K. A., Hoffe, S., Dawson, L. A., Dessert, D., Hall, W. A., Herman, J. M., Khorana, A. A., Merchant, N., Parekh, A., Patton, C., Pepek, J. M., Salama, J. K., Tuli, R. & Koong, A. C. Radiation Therapy for Pancreatic Cancer: Executive Summary of an ASTRO Clinical Practice Guideline. *Pract Radiat Oncol* **9,** 322–332 (2019).

47. Harvey, J. J. An Unidentified Virus which causes the Rapid Production of Tumours in Mice. *Nature* **204,** 1104–1105 (1964).

48. W H Kirsten & L A Mayer. Morphologic responses to a murine erythroblastosis virus. *J Natl Cancer Inst.* **39,** 311–315 (1967).

49. Peters RL, Rabstein LS, VanVleck R, Kelloff GJ & Huebner RJ. Naturally occurring sarcoma virus of the BALB/cCr mouse. *J Natl Cancer Inst.* **53,** 1725–1729 (1974).

50. Rasheed, S., Gardner, M. B. & Huebner, R. J. In vitro isolation of stable rat sarcoma viruses. *Proceedings of the National Academy of Sciences* **75,** 2972–2976 (1978).

51. Ellis, R. W., Defeo, D., Shih, T. Y., Gonda\, M. A., Young\, H. A., Tsuchida, N., Lowy, D. R. & Scolnick, E. M. *The p21 src genes of Harvey and Kirsten sarcoma viruses originate from divergent members of a family of normal vertebrate genes*. *Nature* **292,** (1981).

52. Der, C. J., Krontiris, T. G. & Cooper, G. M. Transforming genes of human bladder and lung carcinoma cell lines are homologous to the ras genes of Harvey and Kirsten sarcoma viruses. *Proc. Natl. Acad. Sci. USA* **79,** 3637–3640 (1982).

53. Hall, A., Marshall, C. J., Spurr, N. K. & Weiss, R. A. Identification of transforming gene in two human sarcoma cell lines as a new member of the ras gene family located on chromosome 1. *Nature* **303,** 397–400 (1983).

54. Shimizu, K., Goldfarb, M., Perucho, M. & Wiglert, M. *Isolation and preliminary characterization of the transforming gene of a human neuroblastoma cell line (DNA-mediated gene transfer/human oncogene/tiINA suppressor)*. *Proc. Natl Acad. Sci. USA* **80,** (1983).

55. Reddy, E. P., Reynolds, R. K., Santos, E. & Barbacid, E. A point mutation is responsible for the acquisition of transforming properties by the T24 human bladder carcinoma oncogene. *Nature* **300,** 149–152 (1982).

56. Tabin, C. J., Bradley, S. M., Bargmann, C. I. & Weinberg, R. A. Mechanism of activation of a human oncogene. *Nature* **300,** 143–149 (1982).

57. Taparowsky, E., Suard, Y., Fasano, O., Shimizu, K., Goldfarb, M. & Wigler, M. Activation of the T24 bladder carcinoma transforming gene is linked to a single amino acid change. *Nature* **300,** 762–765 (1982).

58. Land, H., Parada, L. F. & Weinberg, R. A. Tumorigenic conversion of primary embryo fibroblasts requires at least two cooperating oncogens. *Nature* **304,** 596–602 (1983).

59. Newbold, R. F. & Overell, R. W. Fibroblast immortality is a prerequisite for transformation by EJ c-Ha-ras oncogene. *Nature* **304,** 648–651 (1983).

60. Ruley, H. E. Adenovirus early region 1A enables viral and cellular transforming genes to transform primary cells in culture. *Nature* **304,** 602–606 (1983).

61. Santos, E., Martin-Zanca, D., Reddy, E. P., Pierotti, M. A., Porta, G. Della & Barbacid, M. Malignant Activation of a K-ras Oncogene in Lung Carcinoma but Not in Normal Tissue of the Same Patient. *Science (1979)* **223,** 661–664 (1984).

62. Bos, J. L., Fearon, E. R., Hamiltont, S. R., Verlaan-De Vries, M., van Boom, J. H., Van der Eb, A. J. & Vogelstein, B. Prevalence of ras gene mutations in human colorectal cancers. *Nature* **327,** 293–297 (1987).

63. Forrester, K., Almoguera, C., Han, K., Grizzle, W. E. & Perucho, M. Detection of high incidence of K-ras oncogenes during human colon tumorigenesis. *Nature* **327,** 298–303 (1987).

64. Parks, W. P. & Scolnick, E. M. In Vitro Translation of Harvey Murine Sarcoma Virus RNA. *J Virol* **22,** 711–719 (1977).

65. Shih, T. Y., Weeks, M. 0, Young, H. A. & Scolnick, E. M. p21 of Kirsten Murine Sarcoma Virus Is Thermolabile in a Viral Mutant Temperature Sensitive for the Maintenance of Transformation. *J Virol* **31,** 546–556 (1970).

66. Hurley, J. B., Simon, M. I., Teplow, D. B., Robishaw, J. D. & Gilman, A. G. Homologies Between Signal Transducing G Proteins and ras Gene Products. *Science (1979)* **226,** 860–862 (1984).

67. Willingham, M. C., Pastan, I., Shih, T. Y. & Scolnickjr, E. M. Localization of the SK Gene Product of the Harvey Strain of MSV to Plasma Membrane of Transformed Cells by Electron Microscopic lmmunocytochemistry. *Cell* **19,** 1005–1014 (1980).

68. Kamata, T. & Feramisco, J. R. Epidermal growth factor stimulates guanine nucleotide binding activity and phosphorylation of ras oncogene proteins. *Nature* **310,** 147–150 (1984).

69. Trahey, M. & McCormick, F. A Cytoplasmic Protein Stimulates Normal N-ras p21 GTPase, but Does Not Affect Oncogenic Mutants. *Science (1979)* **238,** 542–545 (1987).

70. Wolfman, A. & Macara, I. G. A Cytosolic Protein Catalyzes the Release of GDP from p21ras. *Science (1979)* **248,** 67–69 (1990).

71. Bowtell, D., Fu, P., Simon, M. & Senior, P. Identification of murine homologues of the Drosophila Son of sevenless gene: Potential activators of ras. *Proc. Natl. Acad. Sci. USA* **89,** 6511–6515 (1992).

72. Shou, C., Farnsorth, C. L., Neel, B. G. & Feig, L. A. Molecular cloning of cDNAs encoding a guanine-nucleotide-releasing factor for Ras p21. *Nature* **358,** 351–354 (1992).

73. Wei, W., Mosteller, R. D., Sanyal, P., Gonzales, E., Mckinney, D., Dasgupta, C., Peng, L., Liu, B.-X. & Broek, D. Identification of a mammalian gene structurally and functionally related to the CDC25 gene of Saccharomyces cerevisiae. *Proc. Natl. Acad. Sci. USA* **89,** 7100–7104 (1992).

74. McCormick, F. How receptors turn Ras on. *Nature* **363,** 15–16 (1993).

75. Matuoka, K., Shibata, M., Yamakawa, A. & Takenawa, T. Cloning of ASH, a ubiquitous protein composed of one Src homology region (SH) 2 and two SH3 domains, from human and rat cDNA libraries. *Proc. Natl. Acad. Sci. USA* **89,** 9015–9019 (1992).

76. Moodie, S. A., Willumsen, B. M., Weber, M. J. & Wolfman, A. Complexes of Ras.GTP with Raf-1 and Mitogen-Activated Protein Kinase Kinase. *Science (1979)* **260,** 1658–1661 (1993).

77. Warne, P. H., Viciana, P. R. & Downward, J. Direct interaction of Ras and the amino-terminal region of Raf-1 in vitro. *Nature* **364,** 352–355 (1993).

78. Zhang, X.-F., Settleman, J., Kyriakis, J. M., Takeuchi-Suzuki, E., Elledge, S. J., Marshall, M. S., Bruder, J. T., Rapp, U. R. & Avruch, J. Normal and oncogenic p21'as proteins bind to the amino-terminal regulatory domain of c-Raf-1. *Nature* **364,** 308–313 (1993).

79. Vojtek, A. B., Hollenberg, S. M. & Cooper, J. A. Mammalian Ras Interacts Directly with the Serine/Threonine Kinase Raf. *Cell* **74,** 205–214 (1993).

80. Leevers, S. J., Paterson, H. F. & Marshall, C. J. Requirement for Ras in Raf activation is overcome by targeting Raf to the plasma membrane. *Nature* **369,** 411–414 (1994).

81. Marais, R., Light, Y., Paterson, H. F. & Marshall, C. J. Ras recruits Raf-1 to the plasma membrane far activation by tyrosine phosphorylation. *EMBO J* **14,** 3136–3145 (1995).

82. Pruitt, K. & Der, C. J. Ras and Rho regulation of the cell cycle and oncogenesis. *Cancer Lett* **171,** 1–10 (2001).

83. Yordy, J. S. & Muise-Helmericks, R. C. Signal transduction and the Ets family of transcription factors. *Oncogene* **19,** 6503–6513 (2000).

84. Rodriguez-Viciana, P., Warne, P. H., Dhandt, R., Vanhaesebroeck, B., Gout, I., Fry, M. J., Waterfieldtt, M. D. & Downward, J. Phosphatidylinositol-3-OH kinase as a direct target of Ras. *Nature* **370,** 527–532 (1994).

85. Pacold, M. E., Suire, S., Perisic, O., Lara-Gonzalez, S., Davis, C. T., Walker, E. H., Hawkins, P. T., Stephens, L., Eccleston, J. F. & Williams, R. L. Crystal Structure and Functional Analysis of Ras Binding to Its Effector Phosphoinositide 3-Kinase γ. *Cell* **103,** 931–943 (2000).

86. Datta, S. R., Brunet, A. & Greenberg, M. E. Cellular survival: a play in three Akts. *Genes Dev* **13,** 2905–2927 (1999).

87. Lambert, J. M., Lambert, Q. T., Reuther, G. W., Malliri, A., Siderovski, D. P., Sondek, J., Collard, J. G. & Der, C. J. Tiam1 mediates Ras activation of Rac by a PI(3)K-independent mechanism. *Nat Cell Biol* **4,** 621–625 (2002).

88. Malliri, A., van der Kammen, R. A., Clark, K., van der Valk, M., Michiels, F. & Collard, J. G. Mice deficient in the Rac activator Tiam1 are resistant to Ras-induced skin tumours. *Nature* **417,** 867–871 (2002).

89. De Ruiter, N. D., Burgering, B. M. T. & Bos, J. L. Regulation of the Forkhead Transcription Factor AFX by Ral-Dependent Phosphorylation of Threonines 447 and 451. *Mol Cell Biol* **21,** 8225–8235 (2001).

90. Kelley, G. G., Reks, S. E., Ondrako, J. M. & Smrcka, A. V. Phospholipase Cε: A novel Ras effector. *EMBO Journal* **20,** 743–754 (2001).

91. De Vos, A. M., Tong, L., Milburn, M. V., Matias, P. M., Jancarik, J., Noguchi, S., Nishimura, S., Miura, K., Ohtsuka, Ei. & Kim, S.-H. Three-Dimensional Structure of an Oncogene Protein: Catalytic Domain of Human c-H-ras p21. *Science (1979)* **239,** 888–893 (1988).

92. Pai, E. F., Kabsch, W., Krengel, U., Holmes, K. C., John, J. & Wittinghofer, A. Structure of the guanine-nucleotide-binding domain of the Ha-ras oncogene product p21 in the triphosphate conformation. *Nature* **341,** 209–214 (1989).

93. Krengel, U., Schlichting, I., Scherer, A., Schumann, R., Frech, M., John, J., Kabsch, W., Pai, E. F. & Wittinghofer, A. Three-Dimensional Structures of H-ras p21 Mutants: Molecular Basis for Their Inability to Function As Signal Switch Molecules. *Cell* **62,** 539–548 (1990).

94. Tong, L., de Vos, A. M., Milburn, M. V. & Kim, S.-H. Crystal Structures at 2.2 Å Resolution of the Catalytic Domains of Normal ras Protein and an Oncogenic Mutant Complexed with GDP. *J. Mol. Biol* **217,** 503–516 (1991).

95. Scheffzek, K., Ahmadian, M. R., Kabsch, W., Wiesmü, L., Lautwein, A., Schmitz, F. & Wittinghofer, A. The Ras-RasGAP Complex: Structural Basis for GTPase Activation and Its Loss in Oncogenic Ras Mutants. *Science (1979)* **277,** 333–338 (1997).

96. Wittinghofer, A. & Vetter, I. R. Structure-function relationships of the G domain, a canonical switch motif. *Annu Rev Biochem* **80,** 943–971 (2011).

97. Welman, A., Burger, M. M. & Hagmann, J. Structure and function of the C-terminal hypervariable region of K-Ras4B in plasma membrane targetting and transformation. *Oncogene* **19,** 4582–4591 (2000).

98. Ostrem, J. M., Peters, U., Sos, M. L., Wells, J. A. & Shokat, K. M. K-Ras(G12C) inhibitors allosterically control GTP affinity and effector interactions. *Nature* **503,** 548–551 (2013).

99. Prior, I. A., Hood, F. E. & Hartley, J. L. The frequency of ras mutations in cancer. *Cancer Res* **80,** 2669–2974 (2020).

100. Siegel, R. L., Miller, K. D., Wagle, N. S. & Jemal, A. Cancer statistics, 2023. *CA Cancer J Clin* **73,** 17–48 (2023).

101. Prior, I. A., Lewis, P. D. & Mattos, C. A comprehensive survey of ras mutations in cancer. *Cancer Res* **72,** 2457–2467 Preprint at https://doi.org/10.1158/0008-5472.CAN-11-2612 (2012)

102. Waters, A. M. & Der, C. J. KRAS: The critical driver and therapeutic target for pancreatic cancer. *Cold Spring Harb Perspect Med* **8,** (2018).

103. Vaclova, T., Chakraborty, A., Sherwood, J., Ross, S., Carroll, D., Barrett, J. C., Downward, J. & de Bruin, E. C. Concomitant KRAS mutations attenuate sensitivity of non-small cell lung cancer cells to KRAS G12C inhibition. *Sci Rep* **12,** (2022).

104. Hancock, J. F., Paterson, H. & Marshall, C. J. A polybasic domain or palmitoylation is required in addition to the CAAX motif to localize p21ras to the plasma membrane. *Cell* **63,** 133–139 (1990).

105. Van Cutsem, E., van de Velde, H., Karasek, P., Oettle, H., Vervenne, W. L., Szawlowski, A., Schoffski, P., Post, S., Verslype, C., Neumann, H., Safran, H., Humblet, Y., Perez Ruixo, J., Ma, Y. & Von Hoff, D. Phase III trial of gemcitabine plus tipifarnib compared with gemcitabine plus placebo in advanced pancreatic cancer. *Journal of Clinical Oncology* **22,** 1430–1438 (2004).

106. Rao, S., Cunningham, D., de Gramont, A., Scheithauer, W., Smakal, M., Humblet, Y., Kourteva, G., Iveson, T., Andre, T., Dostalova, J., Illes, A., Belly, R., Perez-Ruixo, J. J., Park, Y. C. & Palmer, P. A. Phase III double-blind placebo-controlled study of farnesyl transferase inhibitor R115777 in patients with refractory advanced colorectal cancer. *Journal of Clinical Oncology* **22,** 3950–3957 (2004).

107. Rowell, C. A., Kowalczyk, J. J., Lewis, M. D. & Garcia, A. M. Direct demonstration of geranylgeranylation and farnesylation of Ki-Ras in vivo. *Journal of Biological Chemistry* **272,** 14093–14097 (1997).

108. Whyte, D. B., Kirschmeier, P., Hockenberry, T. N., Nunez-Oliva, I., James, L., Catino, J. J., Bishop, W. R. & Pai, J. K. K- and N-Ras are geranylgeranylated in cells treated with farnesyl protein transferase inhibitors. *Journal of Biological Chemistry* **272,** 14459–14464 (1997).

109. Lobell, R. B., Liu, D., Buser, C. A., Davide, J. P., DePuy, E., Hamilton, K., Koblan, K. S., Lee, Y., Mosser, S., Motzel, S. L., Abbruzzese, J. L., Fuchs, C. S., Rowinsky, E. K., Rubin, E. H., Sharma, S., Deutsch, P. J., Mazina, K. E., Morrison, B. W., Wildonger, L., Yao, S.-L. & Kohl, N. E. Preclinical and Clinical Pharmacodynamic Assessment of L-778,123, a Dual

Inhibitor of Farnesyl:Protein Transferase and Geranylgeranyl:Protein Transferase Type-I. *Mol Cancer Ther* **1,** 747–758 (2002).

110. DeSolms, S. J., Ciccarone, T. M., MacTough, S. C., Shaw, A. W., Buser, C. A., Ellis-Hutchings, M., Fernandes, C., Hamilton, K. A., Huber, H. E., Kohl, N. E., Lobell, R. B., Robinson, R. G., Tsou, N. N., Walsh, E. S., Graham, S. L., Beese, L. S. & Taylor, J. S. Dual protein farnesyltransferase-geranylgeranyltransferase-I inhibitors as potential cancer chemotherapeutic agents. *J Med Chem* **46,** 2973–2984 (2003).

111. Bergo, M. O., Lieu, H. D., Gavino, B. J., Ambroziak, P., Otto, J. C., Casey, P. J., Walker, Q. M. & Young, S. G. On the physiological importance of endoproteolysis of CAAX proteins. Heart-specific Rce1 knockout mice develop a lethal cardiomyopathy. *Journal of Biological Chemistry* **279,** 4729–4736 (2004).

112. Karreth, F. A., Frese, K. K., DeNicola, G. M., Baccarini, M. & Tuveson, D. A. C-Raf is required for the initiation of lung cancer by K-Ras G12D. *Cancer Discov* **1,** 128–136 (2011).

113. Blasco, R. B., Francoz, S., Santamaría, D., Cañamero, M., Dubus, P., Charron, J., Baccarini, M. & Barbacid, M. C-Raf, but Not B-Raf, Is Essential for Development of K-Ras Oncogene-Driven Non-Small Cell Lung Carcinoma. *Cancer Cell* **19,** 652–663 (2011).

114. Eser, S., Reiff, N., Messer, M., Seidler, B., Gottschalk, K., Dobler, M., Hieber, M., Arbeiter, A., Klein, S., Kong, B., Michalski, C. W., Schlitter, A. M., Esposito, I., Kind, A. J., Rad, L., Schnieke, A. E., Baccarini, M., Alessi, D. R., Rad, R., Schmid, R. M., Schneider, G. & Saur, D. Selective requirement of PI3K/PDK1 signaling for kras oncogene-driven pancreatic cell plasticity and cancer. *Cancer Cell* **23,** 406–420 (2013).

115. Zimmermann, S. & Moelling, K. Phosphorylation and Regulation of Raf by Akt (Protein Kinase B). *Science (1979)* **286,** 1741–1744 (1999).

116. Shimizu, T., Tolcher, A. W., Papadopoulos, K. P., Beeram, M., Rasco, D. W., Smith, L. S., Gunn, S., Smetzer, L., Mays, T. A., Kaiser, B., Wick, M. J., Alvarez, C., Cavazos, A., Mangold, G. L. & Patnaik, A. The clinical effect of the dual-targeting strategy involving PI3K/AKT/mTOR and RAS/MEK/ERK pathways in patients with advanced cancer. *Clinical Cancer Research* **18,** 2316–2325 (2012).

117. The Lancet Oncology. Undruggable KRAS—time to rebrand? *Lancet Oncol* **22,** 289 Preprint at https://doi.org/10.1016/S1470-2045(21)00091-7 (2021)

118. John, J., Sohmen, R., Feuerstein, J., Linke, R., Wittinghofer, A. & Goody, R. S. Kinetics of Interaction of Nucleotides with Nucleotide-Free H-ras p21. *Biochemistry* **29,** 6058–6065 (1990).

119. Patricelli, M. P., Janes, M. R., Li, L. S., Hansen, R., Peters, U., Kessler, L. V., Chen, Y., Kucharski, J. M., Feng, J., Ely, T., Chen, J. H., Firdaus, S. J., Babbar, A., Ren, P. & Liu, Y. Selective inhibition of oncogenic KRAS output with small molecules targeting the inactive state. *Cancer Discov* **6,** 316–329 (2016).

120. Janes, M. R., Zhang, J., Li, L. S., Hansen, R., Peters, U., Guo, X., Chen, Y., Babbar, A., Firdaus, S. J., Darjania, L., Feng, J., Chen, J. H., Li, S., Li, S., Long, Y. O., Thach, C., Liu, Y., Zarieh, A., Ely, T., Kucharski, J. M., Kessler, L. V., Wu, T., Yu, K., Wang, Y., Yao, Y., Deng, X., Zarrinkar, P. P., Brehmer, D., Dhanak, D., Lorenzi, M. V., Hu-Lowe, D., Patricelli, M.

P., Ren, P. & Liu, Y. Targeting KRAS Mutant Cancers with a Covalent G12C-Specific Inhibitor. *Cell* **172,** 578-589.e17 (2018).

121. Canon, J., Rex, K., Saiki, A. Y., Mohr, C., Cooke, K., Bagal, D., Gaida, K., Holt, T., Knutson, C. G., Koppada, N., Lanman, B. A., Werner, J., Rapaport, A. S., San Miguel, T., Ortiz, R., Osgood, T., Sun, J. R., Zhu, X., McCarter, J. D., Volak, L. P., Houk, B. E., Fakih, M. G., O'Neil, B. H., Price, T. J., Falchook, G. S., Desai, J., Kuo, J., Govindan, R., Hong, D. S., Ouyang, W., Henary, H., Arvedson, T., Cee, V. J. & Lipford, J. R. The clinical KRAS(G12C) inhibitor AMG 510 drives anti-tumour immunity. *Nature* **575,** 217–223 (2019).

122. Skoulidis, F., Li, B. T., Dy, G. K., Price, T. J., Falchook, G. S., Wolf, J., Italiano, A., Schuler, M., Borghaei, H., Barlesi, F., Kato, T., Curioni-Fontecedro, A., Sacher, A., Spira, A., Ramalingam, S. S., Takahashi, T., Besse, B., Anderson, A., Ang, A., Tran, Q., Mather, O., Henary, H., Ngarmchamnanrith, G., Friberg, G., Velcheti, V. & Govindan, R. Sotorasib for Lung Cancers with KRAS p.G12C Mutation . *New England Journal of Medicine* **384,** 2371–2381 (2021).

123. Hallin, J., Engstrom, L. D., Hargi, L., Calinisan, A., Aranda, R., Briere, D. M., Sudhakar, N., Bowcut, V., Baer, B. R., Ballard, J. A., Burkard, M. R., Fell, J. B., Fischer, J. P., Vigers, G. P., Xue, Y., Gatto, S., Fernandez-Banet, J., Pavlicek, A., Velastagui, K., Chao, R. C., Barton, J., Pierobon, M., Baldelli, E., Patricoin, E. F., Cassidy, D. P., Marx, M. A., Rybkin, I. I., Johnson, M. L., Ignatius, S. H., Lito, P., Papadopoulos, K. P., Jänne, P. A., Olson, P. & Christensen, J. G. The KRASG12C inhibitor MRTX849 provides insight toward therapeutic susceptibility of KRAS-mutant cancers in mouse models and patients. *Cancer Discov* **10,** 54–71 (2020).

124. Awad, M. M., Liu, S., Rybkin, I. I., Arbour, K. C., Dilly, J., Zhu, V. W., Johnson, M. L., Heist, R. S., Patil, T., Riely, G. J., Jacobson, J. O., Yang, X., Persky, N. S., Root, D. E., Lowder, K. E., Feng, H., Zhang, S. S., Haigis, K. M., Hung, Y. P., Sholl, L. M., Wolpin, B. M., Wiese, J., Christiansen, J., Lee, J., Schrock, A. B., Lim, L. P., Garg, K., Li, M., Engstrom, L. D., Waters, L., Lawson, J. D., Olson, P., Lito, P., Ou, S.-H. I., Christensen, J. G., Jänne, P. A. & Aguirre, A. J. Acquired Resistance to KRAS G12C Inhibition in Cancer . *New England Journal of Medicine* **384,** 2382–2393 (2021).

125. Wang, X., Allen, S., Blake, J. F., Bowcut, V., Briere, D. M., Calinisan, A., Dahlke, J. R., Fell, J. B., Fischer, J. P., Gunn, R. J., Hallin, J., Laguer, J., Lawson, J. D., Medwid, J., Newhouse, B., Nguyen, P., O'Leary, J. M., Olson, P., Pajk, S., Rahbaek, L., Rodriguez, M., Smith, C. R., Tang, T. P., Thomas, N. C., Vanderpool, D., Vigers, G. P., Christensen, J. G. & Marx, M. A. Identification of MRTX1133, a Noncovalent, Potent, and Selective KRASG12DInhibitor. *J Med Chem* **65,** 3123–3133 (2022).

126. Whiteside, T. L. The tumor microenvironment and its role in promoting tumor growth. *Oncogene* **27,** 5904–5912 Preprint at https://doi.org/10.1038/onc.2008.271 (2008)

127. Friedl, P. & Alexander, S. Cancer invasion and the microenvironment: Plasticity and reciprocity. *Cell* **147,** 992–1009 Preprint at https://doi.org/10.1016/j.cell.2011.11.016 (2011)

128. Altorki, N. K., Markowitz, G. J., Gao, D., Port, J. L., Saxena, A., Stiles, B., McGraw, T. & Mittal, V. The lung microenvironment: an important regulator of tumour growth and metastasis. *Nat Rev Cancer* 9–31 (2019). doi:10.1038/s41568

129. Karamitopoulou, E. Tumour microenvironment of pancreatic cancer: immune landscape is dictated by molecular and histopathological features. *Br J Cancer* **121,** 5–14 Preprint at https://doi.org/10.1038/s41416-019-0479-5 (2019)

130. Balkwill, F. & Mantovani, A. Inflammation and cancer: back to Virchow? *The Lancet* **357,** 539–545 (2001).

131. Kitajima, S., Thummalapalli, R. & Barbie, D. A. Inflammation as a driver and vulnerability of KRAS mediated oncogenesis. *Semin Cell Dev Biol* **58,** 127–135 Preprint at https://doi.org/10.1016/j.semcdb.2016.06.009 (2016)

132. Carvalho, P. D., Guimarães, C. F., Cardoso, A. P., Mendonça, S., Costa, Â. M., Oliveira, M. J. & Velho, S. KRAS oncogenic signaling extends beyond cancer cells to orchestrate the microenvironment. *Cancer Res* **78,** 7–14 Preprint at https://doi.org/10.1158/0008-5472.CAN-17-2084 (2018)

133. Taniguchi, K. & Karin, M. IL-6 and related cytokines as the critical lynchpins between inflammation and cancer. *Semin Immunol* **26,** 54–74 Preprint at https://doi.org/10.1016/j.smim.2014.01.001 (2014)

134. Zhang, Y., Yan, W., Collins, M. A., Bednar, F., Rakshit, S., Zetter, B. R., Stanger, B. Z., Chung, I., Rhim, A. D. & Di Magliano, M. P. Interleukin-6 is required for pancreatic cancer progression by promoting MAPK signaling activation and oxidative stress resistance. *Cancer Res* **73,** 6359–6374 (2013).

135. Sparmann, A. & Bar-Sagi, D. Ras-induced interleukin-8 expression plays a critical role in tumor growth and angiogenesis. *Cancer Cell* **6,** 447–458 (2004).

136. Sunaga, N., Imai, H., Shimizu, K., Shames, D. S., Kakegawa, S., Girard, L., Sato, M., Kaira, K., Ishizuka, T., Gazdar, A. F., Minna, J. D. & Mori, M. Oncogenic KRAS-induced interleukin-8 overexpression promotes cell growth and migration and contributes to aggressive phenotypes of non-small cell lung cancer. *Int J Cancer* **130,** 1733–1744 (2012).

137. Liou, G. Y., Döppler, H., Necela, B., Edenfield, B., Zhang, L., Dawson, D. W. & Storz, P. Mutant KRAS–induced expression of ICAM-1 in pancreatic acinar cells causes attraction of macrophages to expedite the formation of precancerous lesions. *Cancer Discov* **5,** 52–63 (2015).

138. Watterson, A. & Coelho, M. A. Cancer immune evasion through KRAS and PD-L1 and potential therapeutic interventions. *Cell Communication and Signaling* **21,** Preprint at https://doi.org/10.1186/s12964-023-01063-x (2023)

139. Coelho, M. A., de Carné Trécesson, S., Rana, S., Zecchin, D., Moore, C., Molina-Arcas, M., East, P., Spencer-Dene, B., Nye, E., Barnouin, K., Snijders, A. P., Lai, W. S., Blackshear, P. J. & Downward, J. Oncogenic RAS Signaling Promotes Tumor Immunoresistance by Stabilizing PD-L1 mRNA. *Immunity* **47,** 1083-1099.e6 (2017).

140. Glorieux, C., Xia, X., He, Y. Q., Hu, Y., Cremer, K., Robert, A., Liu, J., Wang, F., Ling, J., Chiao, P. J. & Huang, P. Regulation of PD-L1 expression in K-ras-driven cancers through ROS-mediated FGFR1 signaling. *Redox Biol* **38,** (2021).

141. Smakman, N., Veenendaal, L. M., Van Diest, P., Bos, R., Offringa, R., Borel Rinkes, I. H. M. & Kranenburg, O. Dual effect of KrasD12 knockdown on tumorigenesis: Increased immune-mediated tumor clearance and abrogation of tumor malignancy. *Oncogene* **24,** 8338–8342 (2005).

142. Zhang, Z., Rohweder, P. J., Ongpipattanakul, C., Basu, K., Bohn, M. F., Dugan, E. J., Steri, V., Hann, B., Shokat, K. M. & Craik, C. S. A covalent inhibitor of K-Ras(G12C) induces MHC class I presentation of haptenated peptide neoepitopes targetable by immunotherapy. *Cancer Cell* **40,** 1060-1069.e7 (2022).

143. Zdanov, S., Mandapathil, M., Eid, R. A., Adamson-Fadeyi, S., Wilson, W., Qian, J., Carnie, A., Tarasova, N., Mkrtichyan, M., Berzofsky, J. A., Whiteside, T. L. & Khleif, S. N. Mutant KRAS conversion of conventional T cells into regulatory T cells. *Cancer Immunol Res* **4,** 354–365 (2016).

144. Bayne, L. J., Beatty, G. L., Jhala, N., Clark, C. E., Rhim, A. D., Stanger, B. Z. & Vonderheide, R. H. Tumor-Derived Granulocyte-Macrophage Colony-Stimulating Factor Regulates Myeloid Inflammation and T Cell Immunity in Pancreatic Cancer. *Cancer Cell* **21,** 822–835 (2012).

145. Liao, W., Overman, M. J., Boutin, A. T., Shang, X., Zhao, D., Dey, P., Li, J., Wang, G., Lan, Z., Li, J., Tang, M., Jiang, S., Ma, X., Chen, P., Katkhuda, R., Korphaisarn, K., Chakravarti, D., Chang, A., Spring, D. J., Chang, Q., Zhang, J., Maru, D. M., Maeda, D. Y., Zebala, J. A., Kopetz, S., Wang, Y. A. & DePinho, R. A. KRAS-IRF2 Axis Drives Immune Suppression and Immune Therapy Resistance in Colorectal Cancer. *Cancer Cell* **35,** 559-572.e7 (2019).

146. Morgan, M. A. & Lawrence, T. S. Molecular pathways: Overcoming radiation resistance by targeting DNA damage response pathways. *Clinical Cancer Research* **21,** 2898–2904 (2015).

147. Khanna, K. K., Lavin, M. F., Jackson, S. P. & Mulhern, T. D. ATM, a central controller of cellular responses to DNA damage. *Cell Death and Differetiation* **8,** 1052–1065 (2001).

148. Bartek, J. & Lukas, J. Chk1 and Chk2 kinases in checkpoint control and cancer. *Cancer Cell* **3,** 421–429 (2003).

149. Jeggo, P. A. & Löbrich, M. DNA double-strand breaks: Their cellular and clinical impact? *Oncogene* **26,** 7717–7719 (2007).

150. Bonner, W. M., Redon, C. E., Dickey, J. S., Nakamura, A. J., Sedelnikova, O. A., Solier, S. & Pommier, Y. γH2AX and cancer. *Nat Rev Cancer* **8,** 957–967 (2008).

151. Lieber, M. R. The mechanism of double-strand DNA break repair by the nonhomologous DNA end-joining pathway. *Annu Rev Biochem* **79,** 181–211 Preprint at https://doi.org/10.1146/annurev.biochem.052308.093131 (2010)

152. Huang, R. X. & Zhou, P. K. DNA damage response signaling pathways and targets for radiotherapy sensitization in cancer. *Signal Transduct Target Ther* **5,** (2020).

153. Connell, P. P. & Hellman, S. Advances in radiotherapy and implications for the next century: A historical perspective. *Cancer Res* **69,** 383–392 (2009).

154. Longo, D. L. Recent Developments in Radiotherapy. *N Engl J Med* **377,** 1065–1075 (2017).

155. Rutman, R. J., Cantarow, A. & Paschkis, K. E. Studies in 2-Acetylaminofluorene Carcinogenesis III. The Utilization of Uracil-2-C14 by Preneoplastic Rat Liver and Rat Hepatoma. *Cancer Res* **14,** 119–123 (1954).

156. Longley, D. B., Harkin, D. P. & Johnston, P. G. 5-Fluorouracil: Mechanisms of action and clinical strategies. *Nat Rev Cancer* **3,** 330–338 (2003).

157. Moertel, C., Childs, D. S. Jr., Reitemeier, R. J., Colby, M. Y. Jr. & Holbrook, M. Combined 5-Fluorouracil and Supervoltage Radiation Therapy of Locally Unresectable Gastrointestinal Cancer. *The Lancet* **294,** 865–867 (1969).

158. Danenberg, P. V. Thymidylate Synthetase- A Target Enzyme in Cancer Chemotherapy. *Biochim Biophys Acta* **473,** 73–92 (1977).

159. Burris, H. A., Moore, M. J., Andersen, J., Green, M. R., Rothenberg, M. L., Modiano, M. R., Cripps, M. C., Portenoy, R. K., Storniolo, A. M., Tarassoff, P., Nelson, R., Dorr, F. A., Stephens, C. D. & Von Hoff, D. D. Improvements in Survival and Clinical Benefit with Gemcitabine as First-Line Therapy for Patients with Advanced Pancreas Cancer: A Randomized Trial. *Journal of Clinical Oncology* **15,** 2403–2413 (1997).

160. Lawrence, T. S., Chang, E. Y., Hahn, T. M., Hertel, L. W. & Shewach, D. S. Radiosensitization of Pancreatic Cancer Cells by 2',2'-Difluoro-2'-deoxycytidine. *Int. J. Radiation Oncology Biol. Phys* **34,** 867–872 (1996).

161. Rosenberg, B., Van Camp, L. & Krigas, T. Inhibition of Cell Division in Escherichia coli by Electrolysis Products from a Platinum Electrode. *Nature* **205,** 698–699 (1965).

162. Kelland, L. The resurgence of platinum-based cancer chemotherapy. *Nat Rev Cancer* **7,** 573–584 (2007).

163. Huang, H., Zhu, L., Reid, B. R., Drobny, G. P. & Hopkins, P. B. Solution Structure of a Cisplatin-Induced DNA Interstrand Cross-Link. *Science (1979)* **270,** 1842–1845 (1995).

164. Wilson, G. D., Bentzen, S. M. & Harari, P. M. Biologic basis for combining drugs with radiation. *Semin Radiat Oncol* **16,** 2–9 (2006).

165. Tang, C., Livingston, M. J., Safirstein, R. & Dong, Z. Cisplatin nephrotoxicity: new insights and therapeutic implications. *Nat Rev Nephrol* **19,** 53–72 (2023).

166. Ciardiello, F. & Tortora, G. A Novel Approach in the Treatment of Cancer: Targeting the Epidermal Growth Factor Receptor 1. *Clinical Cancer Research* **7,** 2958–2970 (2001).

167. Shepherd, F. A., Rodrigues Pereira, J., Ciuleanu, T., Tan, E. H., Hirsh, V., Thongprasert, S., Campos, D., Maoleekoonpiroj, S., Smylie, M., Martins, R., van Kooten, M., Dediu, M., Findlay, B., Tu, D., Johnston, D., Bezjak, A., Clark, G., Santabárbara, P. & Seymour, L. Erlotinib in Previously Treated Non-Small-Cell Lung Cancer. *New England Journal of Medicine* **353,** (2005).

168. Goldstein, N. I., Prewett, M., Zuklys, K., Rockwell, P. & Mendelsohn, J. Biological Efficacy of a Chimeric Antibody to the Epidermal Growth Factor Receptor in a Human Tumor Xenograft Model. *Clinical Cancer Research* **1,** 1311–1318 (1995).

169. Cunningham, D., Humblet, Y., Siena, S., Khayat, D., Bleiberg, H., Santoro, A., Bets, D., Mueser, M., Harstrick, A., Verslype, C., Chau, I. & Van Cutsem, E. Cetuximab

Monotherapy and Cetuximab plus Irinotecan in Irinotecan-Refractory Metastatic Colorectal Cancer. *New England Journal of Medicine* **351,** 337–345 (2004).

170. Bonner, J. A., Harari, P. M., Giralt, J., Cohen, R. B., Jones, C. U., Sur, R. K., Raben, D., Baselga, J., Spencer, S. A., Zhu, J., Youssoufian, H., Rowinsky, E. K. & Ang, K. K. Radiotherapy plus cetuximab for locoregionally advanced head and neck cancer: 5-year survival data from a phase 3 randomised trial, and relation between cetuximab-induced rash and survival. *Lancet Oncol* **11,** 21–28 (2010).

171. Bonner, J. A., Harari, P. M., Giralt, J., Azarnia, N., Shin, D. M., Cohen, R. B., Jones, C. U., Sur, R., Raben, D., Jassem, J., Ove, R., Kies, M. S., Baselga, J., Youssoufian, H., Amellal, N., Rowinsky, E. K. & Ang, K. K. Radiotherapy plus Cetuximab for Squamous-Cell Carcinoma of the Head and Neck. *New England Journal of Medicine* **354,** 567–578 (2006).

172. Matheson, C. J., Backos, D. S. & Reigan, P. Targeting WEE1 Kinase in Cancer. *Trends Pharmacol Sci* **37,** 872–881 (2016).

173. Morgan, M. A., Parsels, L. A., Maybaum, J. & Lawrence, T. S. Improving the efficacy of chemoradiation with targeted agents. *Cancer Discov* **4,** 280–291 (2014).

174. Lee, Y. Y., Cho, Y. J., Shin, S. won, Choi, C., Ryu, J. Y., Jeon, H. K., Choi, J. J., Hwang, J. R., Choi, C. H., Kim, T. J., Kim, B. G., Bae, D. S., Park, W. & Lee, J. W. Anti-Tumor Effects of Wee1 Kinase Inhibitor with Radiotherapy in Human Cervical Cancer. *Sci Rep* **9,** (2019).

175. Fokas, E., Im, J. H., Hill, S., Yameen, S., Stratford, M., Beech, J., Hackl, W., Maira, S. M., Bernhard, E. J., McKenna, W. G. & Muschel, R. J. Dual inhibition of the PI3K/mTOR pathway increases tumor radiosensitivity by normalizing tumor vasculature. *Cancer Res* **72,** 239–248 (2012).

176. Köhler, G. & Milstein, G. Continuous cultures of fused cells secreting antibody of predefined specificity. *Nature* **256,** 495–497 (1975).

177. Mullard, A. FDA approves 100th monoclonal antibody product. *Nat Rev Drug Discov* **20,** 491–495 (2021).

178. Hansel, T. T., Kropshofer, H., Singer, T., Mitchell, J. A. & George, A. J. T. The safety and side effects of monoclonal antibodies. *Nat Rev Drug Discov* **9,** 325–338 (2010).

179. Reichert, J. M. & Dewitz, M. C. Anti-infective monoclonal antibodies: perils and promise of development. *Nat Rev Drug Discov* **5,** 191–195 (2006).

180. Reichert, J. M., Rosensweig, C. J., Faden, L. B. & Dewitz, M. C. Monoclonal antibody successes in the clinic. *Nat Biotechnol* **23,** 1073–1078 (2005).

181. Bradley, R., Braybrooke, J., Gray, R., Hills, R., Liu, Z., Peto, R., Davies, L., Dodwell, D., McGale, P., Pan, H., Taylor, C., Anderson, S., Gelber, R., Gianni, L., Jacot, W., Joensuu, H., Moreno-Aspitia, A., Piccart, M., Press, M., Romond, E., Slamon, D., Suman, V., Berry, R., Boddington, C., Clarke, M., Davies, C., Duane, F., Evans, V., Gay, J., Gettins, L., Godwin, J., James, S., Liu, H., MacKinnon, E., Mannu, G., McHugh, T., Morris, P., Read, S., Straiton, E., Wang, Y., Crown, J., de Azambuja, E., Delaloge, S., Fung, H., Geyer, C., Spielmann, M., Valagussa, P., Albain, K., Arriagada, R., Bartlett, J., Bergsten-Nordström, E., Bliss, J., Brain, E., Carey, L., Coleman, R., Cuzick, J., Davidson, N., Del Mastro, L., Di

Leo, A., Dignam, J., Dowsett, M., Ejlertsen, B., Francis, P., Gnant, M., Goetz, M., Goodwin, P., Halpin-Murphy, P., Hayes, D., Hill, C., Jagsi, R., Janni, W., Loibl, S., Mamounas, E. P., Martín, M., Mukai, H., Nekljudova, V., Norton, L., Ohashi, Y., Pierce, L., Poortmans, P., Raina, V., Rea, D., Regan, M., Robertson, J., Rutgers, E., Spanic, T., Sparano, J., Steger, G., Tang, G., Toi, M., Tutt, A., Viale, G., Wang, X., Whelan, T., Wilcken, N., Wolmark, N., Cameron, D., Bergh, J., Pritchard, K. I. & Swain, S. M. Trastuzumab for early-stage, HER2-positive breast cancer: a meta-analysis of 13 864 women in seven randomised trials. *Lancet Oncol* **22,** 1139–1150 (2021).

182. Chapman, A. P., Antoniw, P., Spitali, M., West, S., Stephens, S. & King, D. J. Therapeutic antibody fragments with prolonged in vivo half-lives. *Nat Biotechnol* **17,** 780–783 (1999).

183. Lander, E. S., Linton, L. M., Birren, B., Nusbaum, C., Zody, M. C., Baldwin, J., Devon, K., Dewar, K., Doyle, M., FitzHugh, W., Funke, R., Gage, D., Harris, K., Heaford, A., Howland, J., Kann, L., Lehoczky, J., LeVine, R., McEwan, P., McKernan, K., Meldrim, J., Mesirov, J. P., Miranda, C., Morris, W., Naylor, J., Raymond, C., Rosetti, M., Santos, R., Sheridan, A., Sougnez, C., Stange-Thomann, N., Stojanovic, N., Subramanian, A., Wyman, D., Rogers, J., Sulston, J., Ainscough, R., Beck, S., Bentley, D., Burton, J., Clee, C., Carter, N., Coulson, A., Deadman, R., Deloukas, P., Dunham, A., Dunham, I., Durbin, R., French, L., Grafham, D., Gregory, S., Hubbard, T., Humphray, S., Hunt, A., Jones, M., Lloyd, C., McMurray, A., Matthews, L., Mercer, S., Milne, S., Mullikin, J. C., Mungall, A., Plumb, R., Ross, M., Shownkeen, R., Sims, S., Waterston, R. H., Wilson, R. K., Hillier, L. W., McPherson, J. D., Marra, M. A., Mardis, E. R., Fulton, L. A., Chinwalla, A. T., Pepin, K. H., Gish, W. R., Chissoe, S. L., Wendl, M. C., Delehaunty, K. D., Miner, T. L., Delehaunty, A., Kramer, J. B., Cook, L. L., Fulton, R. S., Johnson, D. L., Minx, P. J., Clifton, S. W., Hawkins, T., Branscomb, E., Predki, P., Richardson, P., Wenning, S., Slezak, T., Doggett, N., Cheng, J.-F., Olsen, A., Lucas, S., Elkin, C., Uberbacher, E., Frazier, M., Gibbs, R. A., Muzny, D. M., Scherer, S. E., Bouck, J. B., Sodergren, E. J., Worley, K. C., Rives, C. M., Gorrell, J. H., Metzker, M. L., Naylor, S. L., Kucherlapati, R. S., Nelson, D. L., Weinstock, G. M., Sakaki, Y., Fujiyama, A., Hattori, M., Yada, T., Toyoda, A., Itoh, T., Kawagoe, C., Watanabe, H., Totoki, Y., Taylor, T., Weissenbach, J., Heilig, R., Saurin, W., Artiguenave, F., Brottier, P., Bruls, T., Pelletier, E., Robert, C., Wincker, P., Rosenthal, A., Platzer, M., Nyakatura, G., Taudien, S., Rump, A., Smith, D. R., Doucette-Stamm, L., Rubenfield, M., Weinstock, K., Lee, H. M., Dubois, J., Yang, H., Yu, J., Wang, J., Huang, G., Gu, J., Hood, L., Rowen, L., Madan, A., Qin, S., Davis, R. W., Federspiel, N. A., Abola, A. P., Proctor, M. J., Roe, B. A., Chen, F., Pan, H., Ramser, J., Lehrach, H., Reinhardt, R., McCombie, W. R., de la Bastide, M., Dedhia, N., Blöcker, H., Hornischer, K., Nordsiek, G., Agarwala, R., Aravind, L., Bailey, J. A., Bateman, A., Batzoglou, S., Birney, E., Bork, P., Brown, D. G., Burge, C. B., Cerutti, L., Chen, H.-C., Church, D., Clamp, M., Copley, R. R., Doerks, T., Eddy, S. R., Eichler, E. E., Furey, T. S., Galagan, J., Gilbert, J. G. R., Harmon, C., Hayashizaki, Y., Haussler, D., Hermjakob, H., Hokamp, K., Jang, W., Johnson, L. S., Jones, T. A., Kasif, S., Kaspryzk, A., Kennedy, S., Kent, W. J., Kitts, P., Koonin, E. V., Korf, I., Kulp, D., Lancet, D., Lowe, T. M., McLysaght, A., Mikkelsen, T., Moran, J. V., Mulder, N., Pollara, V. J., Ponting, C. P., Schuler, G., Schultz, J., Slater, G., Smit, A. F. A., Stupka, E., Szustakowki, J., Thierry-Mieg, D., Thierry-Mieg, J., Wagner, L., Wallis, J., Wheeler, R., Williams, A., Wolf, Y. I., Wolfe, K. H., Yang, S.-P., Yeh, R.-F., Collins, F., Guyer, M. S., Peterson, J., Felsenfeld, A., Wetterstrand, K. A., Myers, R. M., Schmutz, J., Dickson, M., Grimwood, J., Cox, D. R., Olson, M. V., Kaul, R., Raymond, C., Shimizu, N., Kawasaki, K., Minoshima, S., Evans, G.

A., Athanasiou, M., Schultz, R., Patrinos, A. & Morgan, M. J. Initial sequencing and analysis of the human genome. *Nature* **409,** 860–921 (2001).

184. Plückthun, A. Designed ankyrin repeat proteins (DARPins): Binding proteins for research, diagnostics, and therapy. *Annu Rev Pharmacol Toxicol* **55,** 489–511 Preprint at https://doi.org/10.1146/annurev-pharmtox-010611-134654 (2015)

185. Stumpp, M. T., Binz, H. K. & Amstutz, P. DARPins: A new generation of protein therapeutics. *Drug Discov Today* **13,** 695–701 (2008).

186. Mullard, A. FDA rejects first DARPin. *Nat Rev Drug Discov* **19,** 501–501 (2020).

187. Kessler, D., Gmachl, M., Mantoulidis, A., Martin, L. J., Zoephel, A., Mayer, M., Gollner, A., Covini, D., Fischer, S., Gerstberger, T., Gmaschitz, T., Goodwin, C., Greb, P., Häring, D., Hela, W., Hoffmann, J., Karolyi-Oezguer, J., Knesl, P., Kornigg, S., Koegl, M., Kousek, R., Lamarre, L., Moser, F., Munico-Martinez, S., Peinsipp, C., Phan, J., Rinnenthal, J., Sai, J., Salamon, C., Scherbantin, Y., Schipany, K., Schnitzer, R., Schrenk, A., Sharps, B., Siszler, G., Sun, Q., Waterson, A., Wolkerstorfer, B., Zeeb, M., Pearson, M., Fesik, S. W. & McConnell, D. B. Drugging an undruggable pocket on KRAS. *Proc Natl Acad Sci U S A* **116,** 15823–15829 (2019).

188. Bery, N., Legg, S., Debreczeni, J., Breed, J., Embrey, K., Stubbs, C., Kolasinska-Zwierz, P., Barrett, N., Marwood, R., Watson, J., Tart, J., Overman, R., Miller, A., Phillips, C., Minter, R. & Rabbitts, T. H. KRAS-specific inhibition using a DARPin binding to a site in the allosteric lobe. *Nat Commun* **10,** (2019).

189. Douglass, J., Hsiue, E. H.-C., Mog, B. J., Hwang, M. S., DiNapoli, S. R., Pearlman, A. H., Miller, M. S., Wright, K. M., Azurmendi, P. A., Wang, Q., Paul, S., Schaefer, A., Skora, A. D., Molin, M. D., Konig, M. F., Liu, Q., Watson, E., Li, Y., Murphy, M. B., Pardoll, D. M., Bettegowda, C., Papadopoulos, N., Gabelli, S. B., Kinzler, K. W., Vogelstein, B. & Zhou, S. Bispecific antibodies targeting mutant RAS neoantigens. *Sci Immunol* **6,** 5515 (2021).

190. Uhlén, M., Fagerberg, L., Hallström, B. M., Lindskog, C., Oksvold, P., Mardinoglu, A., Sivertsson, Å., Kampf, C., Sjöstedt, E., Asplund, A., Olsson, I. M., Edlund, K., Lundberg, E., Navani, S., Szigyarto, C. A. K., Odeberg, J., Djureinovic, D., Takanen, J. O., Hober, S., Alm, T., Edqvist, P. H., Berling, H., Tegel, H., Mulder, J., Rockberg, J., Nilsson, P., Schwenk, J. M., Hamsten, M., Von Feilitzen, K., Forsberg, M., Persson, L., Johansson, F., Zwahlen, M., Von Heijne, G., Nielsen, J. & Pontén, F. Tissue-based map of the human proteome. *Science (1979)* **347,** (2015).

191. Matsson, P. & Kihlberg, J. How Big Is Too Big for Cell Permeability? *J Med Chem* **60,** 1662–1664 (2017).

192. Bestman, J. E., Ewald, R. C., Chiu, S. L. & Cline, H. T. In vivo single-cell electroporation for transfer of DNA and macromolecules. *Nat Protoc* **1,** 1267–1272 (2006).

193. Chow, Y. T., Chen, S., Wang, R., Liu, C., Kong, C. W., Li, R. A., Cheng, S. H. & Sun, D. Single cell transfection through precise microinjection with quantitatively controlled injection volumes. *Sci Rep* **6,** (2016).

194. Frankel, A. D. & Pabo, C. O. Cellular Uptake of the Tat Protein from Human lmmunodeficiency Virus. *Cell* **55,** 1189–1193 (1988).

195. Green, M. & Loewenstein, P. M. Autonomous Functional Domains of Chemically Synthesized Human lmmunodeficiency Virus Tat Trans-Activator Protein. *Cell* **55,** 1179–188 (1988).

196. Derossi, D., Joliot, A. H., Chassaing, G. & Prochiantz, A. The third helix of the Antennapedia homeodomain translocates through biological membranes. *Journal of Biological Chemistry* **269,** 10444–10450 (1994).

197. Magzoub, M. & Gräslund, A. Cell-penetrating peptides: Small from inception to application. *Q Rev Biophys* **37,** 147–195 (2004).

198. Gräslund, A., Madani, F., Lindberg, S., Langel, Ü. & Futaki, S. Mechanisms of cellular uptake of cell-penetrating peptides. *Journal of Biophysics* (2011). doi:10.1155/2011/414729

199. Rothbard, J. B., Jessop, T. C., Lewis, R. S., Murray, B. A. & Wender, P. A. Role of membrane potential and hydrogen bonding in the mechanism of translocation of guanidinium-rich peptides into cells. *J Am Chem Soc* **126,** 9506–9507 (2004).

200. Åmand, H. L., Rydberg, H. A., Fornander, L. H., Lincoln, P., Nordén, B. & Esbjörner, E. K. Cell surface binding and uptake of arginine- and lysine-rich penetratin peptides in absence and presence of proteoglycans. *Biochim Biophys Acta Biomembr* **1818,** 2669–2678 (2012).

201. Wender, P. A., Mitchell, D. J., Pattabiraman, K., Pelkey, E. T., Steinman, L. & Rothbard, J. B. The design, synthesis, and evaluation of molecules that enable or enhance cellular uptake: Peptoid molecular transporters. *Proc. Natl. Acad. Sci. USA* **97,** 13003–13008 (2000).

202. Nakase, I., Niwa, M., Takeuchi, T., Sonomura, K., Kawabata, N., Koike, Y., Takehashi, M., Tanaka, S., Ueda, K., Simpson, J. C., Jones, A. T., Sugiura, Y. & Futaki, S. Cellular uptake of arginine-rich peptides: Roles for macropinocytosis and actin rearrangement. *Molecular Therapy* **10,** 1011–1022 (2004).

203. Cardozo, A. K., Buchillier, V., Mathieu, M., Chen, J., Ortis, F., Ladrière, L., Allaman-Pillet, N., Poirot, O., Kellenberger, S., Beckmann, J. S., Eizirik, D. L., Bonny, C. & Maurer, F. Cell-permeable peptides induce dose- and length-dependent cytotoxic effects. *Biochim Biophys Acta Biomembr* **1768,** 2222–2234 (2007).

204. Taylor, B. N., Mehta, R. R., Yamada, T., Lekmine, F., Christov, K., Chakrabarty, A. M., Green, A., Bratescu, L., Shilkaitis, A., Beattie, C. W. & Das Gupta, T. K. Noncationic peptides obtained from azurin preferentially enter cancer cells. *Cancer Res* **69,** 537–546 (2009).

205. Yamada, T., Mehta, R. R., Lekmine, F., Christov, K., King, M. L., Majumdar, D., Shilkaitis, A., Green, A., Bratescu, L., Beattie, C. W. & Das Gupta, T. K. A peptide fragment of azurin induces a p53-mediated cell cycle arrest in human breast cancer cells. *Mol Cancer Ther* **8,** 2947–2958 (2009).

206. Mehta, R. R., Yamada, T., Taylor, B. N., Christov, K., King, M. L., Majumdar, D., Lekmine, F., Tiruppathi, C., Shilkaitis, A., Bratescu, L., Green, A., Beattie, C. W. & Das Gupta, T. K. A cell penetrating peptide derived from azurin inhibits angiogenesis and tumor growth

by inhibiting phosphorylation of VEGFR-2, FAK and Akt. *Angiogenesis* **14,** 355–369 (2011).

207. Martín, I., Teixidó, M. & Giralt, E. Design, Synthesis and Characterization of a New Anionic Cell-Penetrating Peptide: SAP(E). *ChemBioChem* **12,** 896–903 (2011).

208. Simeoni, F., Morris, M. C., Heitz, F. & Divita, G. Insight into the mechanism of the peptide-based gene delivery system MPG: Implications for delivery of siRNA into mammalian cells. *Nucleic Acids Res* **31,** 2717–2724 (2003).

209. Donovan, M. A., Lutz, H., Yimer, Y. Y., Pfaendtner, J., Bonn, M. & Weidner, T. LK peptide side chain dynamics at interfaces are independent of secondary structure. *Physical Chemistry Chemical Physics* **19,** 28507–28511 (2017).

210. Oehlke, J., Scheller, A., Wiesner, B., Krause, E., Beyermann, M., Klauschenz, E., Melzig, M. & Bienert, M. Cellular uptake of an α-helical amphipathic model peptide with the potential to deliver polar compounds into the cell interior non-endocytically. *Biochim Biophys Acta* **1414,** 127–139 (1998).

211. Jobin, M. L., Blanchet, M., Henry, S., Chaignepain, S., Manigand, C., Castano, S., Lecomte, S., Burlina, F., Sagan, S. & Alves, I. D. The role of tryptophans on the cellular uptake and membrane interaction of arginine-rich cell penetrating peptides. *Biochim Biophys Acta Biomembr* **1848,** 593–602 (2015).

212. Bechara, C., Pallerla, M., Zaltsman, Y., Burlina, F., Alves, I. D., Lequin, O. & Sagan, S. Tryptophan within basic peptide sequences triggers glycosaminoglycan- dependent endocytosis. *FASEB Journal* **27,** 738–749 (2013).

213. Liu, X., Cao, R., Wang, S., Jia, J. & Fei, H. Amphipathicity Determines Different Cytotoxic Mechanisms of Lysine- or Arginine-Rich Cationic Hydrophobic Peptides in Cancer Cells. *J Med Chem* **59,** 5238–5247 (2016).

214. Schmid, S. L. & Carter, L. L. ATP Is Required for Receptor-mediated Endocytosis in Intact Cells. *J Cell Biol* **111,** 2307–2318 (1990).

215. Robinson, M. S., Watts, C. & Zerial, M. Membrane Dynamics in Endocytosis. *Cell* **84,** 13–21 (1996).

216. Doherty, G. J. & McMahon, H. T. Mechanisms of endocytosis. *Annu Rev Biochem* **78,** 857–902 (2009).

217. Underhill, D. M. & Goodridge, H. S. Information processing during phagocytosis. *Nat Rev Immunol* **12,** 492–502 (2012).

218. Arandjelovic, S. & Ravichandran, K. S. Phagocytosis of apoptotic cells in homeostasis. *Nat Immunol* **16,** 907–917 (2015).

219. Swanson, J. A. Shaping cups into phagosomes and macropinosomes. *Nat Rev Mol Cell Biol* **9,** 639–649 (2008).

220. Mercer, J. & Helenius, A. Virus entry by macropinocytosis. *Nat Cell Biol* **11,** 510–520 (2009).

221. Hobbs, G. A., Baker, N. M., Miermont, A. M., Thurman, R. D., Pierobon, M., Tran, T. H., Anderson, A. O., Waters, A. M., Diehl, J. N., Papke, B., Hodge, R. G., Klomp, J. E., Goodwin, C. M., DeLiberty, J. M., Wang, J., Ng, R. W. S., Gautam, P., Bryant, K. L., Esposito, D., Campbell, S. L., Petricoin, E. F., Simanshu, D. K., Aguirre, A. J., Wolpin, B. M., Wennerberg, K., Rudloff, U., Cox, A. D. & Der, C. J. Atypical KRASG12R mutant is impaired in PI3K signaling and macropinocytosis in pancreatic cancer. *Cancer Discov* **10,** 104–123 (2020).

222. Traub, L. M. Regarding the amazing choreography of clathrin coats. *PLoS Biol* **9,** (2011).

223. Merrifield, C. J., Feldman, M. E., Wan, L. & Almers, W. Imaging actin and dynamin recruitment during invagination of single clathrin-coated pits. *Nat Cell Biol* **4,** 691–698 (2002).

224. Nabi, I. R. & Le, P. U. Caveolae/raft-dependent endocytosis. *Journal of Cell Biology* **161,** 673–677 Preprint at https://doi.org/10.1083/jcb.200302028 (2003)

225. Mayor, S. & Pagano, R. E. Pathways of clathrin-independent endocytosis. *Nat Rev Mol Cell Biol* **8,** 603–612 (2007).

226. Munro, S. Lipid Rafts: Elusive or Illusive? *Cell* **115,** 377–388 (2003).

227. Sarrazin, S., Lamanna, W. C. & Esko, J. D. Heparan sulfate proteoglycans. *Cold Spring Harb Perspect Biol* **3,** 1–33 (2011).

228. Christianson, H. C. & Belting, M. Heparan sulfate proteoglycan as a cell-surface endocytosis receptor. *Matrix Biology* **35,** 51–55 (2014).

229. Yamashiro, D. J., Fluss, S. R. & Maxfield, F. R. Acidification of Endocytic Vesicles by an ATP-dependent Proton Pump. *J Cell Biol* **97,** 929–934 (1983).

230. Hu, Y. B., Dammer, E. B., Ren, R. J. & Wang, G. The endosomal-lysosomal system: From acidification and cargo sorting to neurodegeneration. *Transl Neurodegener* **4,** (2015).

231. El-Sayed, A., Khalil, I. A., Kogure, K., Futaki, S. & Harashima, H. Octaarginine- and octalysine-modified nanoparticles have different modes of endosomal escape. *Journal of Biological Chemistry* **283,** 23450–23461 (2008).

232. Nishi, K. & Saigo, K. Cellular internalization of green fluorescent protein fused with herpes simplex virus protein VP22 via a lipid raft-mediated endocytic pathway independent of caveolae and Rho family GTPases but dependent on dynamin and Arf6. *Journal of Biological Chemistry* **282,** 27503–27517 (2007).

233. Du Rietz, H., Hedlund, H., Wilhelmson, S., Nordenfelt, P. & Wittrup, A. Imaging small molecule-induced endosomal escape of siRNA. *Nat Commun* **11,** (2020).

234. Afonin, S., Frey, A., Bayerl, S., Fischer, D., Wadhwani, P., Weinkauf, S. & Ulrich, A. S. The cell-penetrating peptide TAT(48-60) induces a non-lamellar phase in DMPC membranes. *ChemPhysChem* **7,** 2134–2142 (2006).

235. Mishra, A., Gordon, V. D., Yang, L., Coridan, R. & Wong, G. C. L. HIV TAT forms pores in membranes by inducing saddle-splay curvature: Potential role of bidentate hydrogen bonding. *Angewandte Chemie - International Edition* **47,** 2986–2989 (2008).

236. Herce, H. D., Garcia, A. E., Litt, J., Kane, R. S., Martin, P., Enrique, N., Rebolledo, A. & Milesi, V. Arginine-rich peptides destabilize the plasma membrane, consistent with a pore formation translocation mechanism of cell-penetrating peptides. *Biophys J* **97,** 1917–1925 (2009).

237. Yandek, L. E., Pokorny, A., Florén, A., Knoelke, K., Langel, Ü. & Almeida, P. F. F. Mechanism of the cell-penetrating peptide transportan 10 permeation of lipid bilayers. *Biophys J* **92,** 2434–2444 (2007).

238. Mueller, J., Kretzschmar, I., Volkmer, R. & Boisguerin, P. Comparison of cellular uptake using 22 CPPs in 4 different cell lines. *Bioconjug Chem* **19,** 2363–2374 (2008).

239. Richard, J. P., Melikov, K., Vives, E., Ramos, C., Verbeure, B., Gait, M. J., Chernomordik, L. V. & Lebleu, B. Cell-penetrating peptides: A reevaluation of the mechanism of cellular uptake. *Journal of Biological Chemistry* **278,** 585–590 (2003).

240. Carter, P. J. & Lazar, G. A. Next generation antibody drugs: Pursuit of the 'high-hanging fruit'. *Nat Rev Drug Discov* **17,** 197–223 (2018).

241. Verdine, G. L. & Walensky, L. D. The challenge of drugging undruggable targets in cancer: Lessons learned from targeting BCL-2 family members. *Clinical Cancer Research* **13,** 7264–7270 (2007).

242. Kang, S., Kim, K. H. & Kim, Y. C. A novel electroporation system for efficient molecular delivery into Chlamydomonas reinhardtii with a 3-dimensional microelectrode. *Sci Rep* **5,** (2015).

243. Ghosh, S. & Banerjee, M. A smart viral vector for targeted delivery of hydrophobic drugs. *Sci Rep* **11,** (2021).

244. Kreitz, J., Friedrich, M. J., Guru, A., Lash, B., Saito, M., Macrae, R. K. & Zhang, F. Programmable protein delivery with a bacterial contractile injection system. *Nature* (2023). doi:10.1038/s41586-023-05870-7

245. Peraro, L. & Kritzer, J. A. Emerging Methods and Design Principles for Cell-Penetrant Peptides. *Angewandte Chemie International Edition* **57,** 11868–11881 (2018).

246. Brooks, H., Lebleu, B. & Vivès, E. Tat peptide-mediated cellular delivery: Back to basics. *Adv Drug Deliv Rev* **57,** 559–577 Preprint at https://doi.org/10.1016/j.addr.2004.12.001 (2005)

247. Green, M. & Loewenstein, P. M. Autonomous functional domains of chemically synthesized human immunodeficiency virus tat trans-activator protein. *Cell* **55,** 1179–1188 (1988).

248. Frankel, A. D. & Pabo, C. O. Cellular uptake of the tat protein from human immunodeficiency virus. *Cell* **55,** 1189–1193 (1988).

249. Brock, R. The uptake of arginine-rich cell-penetrating peptides: Putting the puzzle together. *Bioconjug Chem* **25,** 863–868 (2014).

250. Fawell, S., Seery, J., Daikh, Y., Moore, C., Chen, L. L., Pepinsky, B. & Barsoum, J. Tat-mediated delivery of heterologous proteins into cells. *Proceedings of the National Academy of Sciences* **91,** 664–668 (1994).

251. Cornelissen, B., Kersemans, V., Darbar, S., Thompson, J., Shah, K., Sleeth, K., Hill, M. A. & Vallis, K. A. Imaging DNA damage in vivo using γH2AX-targeted immunoconjugates. *Cancer Res* **71,** 4539–4549 (2011).

252. Dougherty, P. G., Sahni, A. & Pei, D. Understanding Cell Penetration of Cyclic Peptides. *Chem Rev* **119,** 10241–10287 (2019).

253. Patel, S. G., Sayers, E. J., He, L., Narayan, R., Williams, T. L., Mills, E. M., Allemann, R. K., Luk, L. Y. P., Jones, A. T. & Tsai, Y. H. Cell-penetrating peptide sequence and modification dependent uptake and subcellular distribution of green florescent protein in different cell lines. *Sci Rep* **9,** 1–9 (2019).

254. Lättig-Tünnemann, G., Prinz, M., Hoffmann, D., Behlke, J., Palm-Apergi, C., Morano, I., Herce, H. D. & Cardoso, M. C. Backbone rigidity and static presentation of guanidinium groups increases cellular uptake of arginine-rich cell-penetrating peptides. *Nat Commun* **2,** (2011).

255. Nischan, N., Herce, H. D., Natale, F., Bohlke, N., Budisa, N., Cardoso, M. C. & Hackenberger, C. P. R. Covalent attachment of cyclic TAT peptides to GFP results in protein delivery into live cells with immediate bioavailability. *Angewandte Chemie - International Edition* **54,** 1950–1953 (2015).

256. Ascierto, P. A., Del Vecchio, M., Robert, C., Mackiewicz, A., Chiarion-Sileni, V., Arance, A., Lebbé, C., Bastholt, L., Hamid, O., Rutkowski, P., McNeil, C., Garbe, C., Loquai, C., Dreno, B., Thomas, L., Grob, J. J., Liszkay, G., Nyakas, M., Gutzmer, R., Pikiel, J., Grange, F., Hoeller, C., Ferraresi, V., Smylie, M., Schadendorf, D., Mortier, L., Svane, I. M., Hennicken, D., Qureshi, A. & Maio, M. Ipilimumab 10 mg/kg versus ipilimumab 3 mg/kg in patients with unresectable or metastatic melanoma: a randomised, double-blind, multicentre, phase 3 trial. *Lancet Oncol* **18,** 611–622 (2017).

257. Sun, Y., Revach, O. yam, Anderson, S., Kessler, E. A., Wolfe, C. H., Jenney, A., Mills, C. E., Robitschek, E. J., Davis, T. G. R., Kim, S., Fu, A., Ma, X., Gwee, J., Tiwari, P., Du, P. P., Sindurakar, P., Tian, J., Mehta, A., Schneider, A. M., Yizhak, K., Sade-Feldman, M., LaSalle, T., Sharova, T., Xie, H., Liu, S., Michaud, W. A., Saad-Beretta, R., Yates, K. B., Iracheta-Vellve, A., Spetz, J. K. E., Qin, X., Sarosiek, K. A., Zhang, G., Kim, J. W., Su, M. Y., Cicerchia, A. M., Rasmussen, M. Q., Klempner, S. J., Juric, D., Pai, S. I., Miller, D. M., Giobbie-Hurder, A., Chen, J. H., Pelka, K., Frederick, D. T., Stinson, S., Ivanova, E., Aref, A. R., Paweletz, C. P., Barbie, D. A., Sen, D. R., Fisher, D. E., Corcoran, R. B., Hacohen, N., Sorger, P. K., Flaherty, K. T., Boland, G. M., Manguso, R. T. & Jenkins, R. W. Targeting TBK1 to overcome resistance to cancer immunotherapy. *Nature* **615,** 158–167 (2023).

258. Tietz, O., Cortezon-Tamarit, F., Chalk, R., Able, S. & Vallis, K. A. Tricyclic cell-penetrating peptides for efficient delivery of functional antibodies into cancer cells. *Nat Chem* **14,** 284–293 (2022).

259. Canon, J., Rex, K., Saiki, A. Y., Mohr, C., Cooke, K., Bagal, D., Gaida, K., Holt, T., Knutson, C. G., Koppada, N., Lanman, B. A., Werner, J., Rapaport, A. S., San Miguel, T., Ortiz, R., Osgood, T., Sun, J. R., Zhu, X., McCarter, J. D., Volak, L. P., Houk, B. E., Fakih, M. G., O'Neil, B. H., Price, T. J., Falchook, G. S., Desai, J., Kuo, J., Govindan, R., Hong, D. S., Ouyang, W., Henary, H., Arvedson, T., Cee, V. J. & Lipford, J. R. The clinical KRAS(G12C) inhibitor AMG 510 drives anti-tumour immunity. *Nature* **575,** 217–223 (2019).

260. Kauke, M. J., Traxlmayr, M. W., Parker, J. A., Kiefer, J. D., Knihtila, R., McGee, J., Verdine, G., Mattos, C. & Dane Wittrup, K. An engineered protein antagonist of K-Ras/B-Raf interaction. *Sci Rep* **7,** (2017).

261. Bery, N., Legg, S., Debreczeni, J., Breed, J., Embrey, K., Stubbs, C., Kolasinska-Zwierz, P., Barrett, N., Marwood, R., Watson, J., Tart, J., Overman, R., Miller, A., Phillips, C., Minter, R. & Rabbitts, T. H. KRAS-specific inhibition using a DARPin binding to a site in the allosteric lobe. *Nat Commun* **10,** 2607 (2019).

262. Khan, I., Spencer-Smith, R. & O'Bryan, J. P. Targeting the α4–α5 dimerization interface of K-RAS inhibits tumor formation in vivo. *Oncogene* **38,** 2984–2993 (2019).

263. Röth, S., Macartney, T. J., Konopacka, A., Chan, K. H., Zhou, H., Queisser, M. A. & Sapkota, G. P. Targeting Endogenous K-RAS for Degradation through the Affinity-Directed Protein Missile System. *Cell Chem Biol* **27,** 1151-1163.e6 (2020).

264. Bery, N., Miller, A. & Rabbitts, T. A potent KRAS macromolecule degrader specifically targeting tumours with mutant KRAS. *Nat Commun* **11,** (2020).

265. Tanaka, T. & Rabbitts, T. H. Interfering with RAS-effector protein interactions prevent RAS-dependent tumour initiation and causes stop-start control of cancer growth. *Oncogene* **29,** 6064–6070 (2010).

266. Tanaka, T., Williams, R. L. & Rabbitts, T. H. Tumour prevention by a single antibody domain targeting the interaction of signal transduction proteins with RAS. *EMBO Journal* **26,** 3250–3259 (2007).

267. Appukkuttan, P., Dehaen, W., Fokin, V. V. & Van Der Eycken, E. A microwave-assisted click chemistry synthesis of 1,4-disubstituted 1,2,3-triazoles via a copper(I)-catalyzed three-component reaction. *Org Lett* **6,** 4223–4225 (2004).

268. Bouillon, C., Meyer, A., Vidal, S., Jochum, A., Chevolot, Y., Cloarec, J. P., Praly, J. P., Vasseur, J. J. & Morvan, F. Microwave assisted 'click' chemistry for the synthesis of multiple labeled-carbohydrate oligonucleotides on solid support. *Journal of Organic Chemistry* **71,** 4700–4702 (2006).

269. Kappe, C. O. & Eycken, E. Van Der. Click chemistry under non-classical reaction conditions. *Chem Soc Rev* **39,** 1280–1290 (2010).

270. Gawande, M. B., Shelke, S. N., Zboril, R. & Varma, R. S. Microwave-assisted chemistry: Synthetic applications for rapid assembly of nanomaterials and organics. *Acc Chem Res* **47,** 1338–1348 (2014).

271. Moore, P. S., Sipos, B., Orlandini, S., Sorio, C., Real, F. X., Lemoine, N. R., Gress, T., Bassi, C., Klöppel, G., Kalthoff, H., Ungefroren, H., Löhr, M. & Scarpa, A. Genetic profile of 22 pancreatic carcinoma cell lines. *Virchows Archiv* **439,** 798–802 (2001).

272. Deer, E. L., González-Hernández, J., Coursen, J. D., Shea, J. E., Ngatia, J., Scaife, C. L., Firpo, M. A. & Mulvihill, S. J. Phenotype and Genotype of Pancreatic Cancer Cell Lines. *Pancreas* **39,** 425–435 (2010).

273. Vivès, E., Brodin, P. & Lebleu, B. A Truncated HIV-1 Tat Protein Basic Domain Rapidly Translocates through the Plasma Membrane and Accumulates in the Cell Nucleus. *Journal of Biological Chemistry* **272,** 16010–16017 (1997).

274. Zhou, Y., Prakash, P., Liang, H., Cho, K. J., Gorfe, A. A. & Hancock, J. F. Lipid-Sorting Specificity Encoded in K-Ras Membrane Anchor Regulates Signal Output. *Cell* **168,** 239-251.e16 (2017).

275. Ruan, G., Agrawal, A., Marcus, A. I. & Nie, S. Imaging and Tracking of Tat Peptide-Conjugated Quantum Dots in Living Cells: New Insights into Nanoparticle Uptake, Intracellular Transport, and Vesicle Shedding. *J Am Chem Soc* **129,** 14759–14766 (2007).

276. Nori, A., Jensen, K. D., Tijerina, M., Kopečková, P. & Kopeček, J. Tat-Conjugated Synthetic Macromolecules Facilitate Cytoplasmic Drug Delivery To Human Ovarian Carcinoma Cells. *Bioconjug Chem* **14,** 44–50 (2003).

277. Dharmaiah, S., Bindu, L., Tran, T. H., Gillette, W. K., Frank, P. H., Ghirlando, R., Nissley, D. V., Esposito, D., McCormick, F., Stephen, A. G. & Simanshu, D. K. Structural basis of recognition of farnesylated and methylated KRAS4b by PDEδ. *Proceedings of the National Academy of Sciences* **113,** (2016).

278. Cox, A. D., Der, C. J. & Philips, M. R. Targeting RAS Membrane Association: Back to the Future for Anti-RAS Drug Discovery? *Clinical Cancer Research* **21,** 1819–1827 (2015).

279. Dittmer, T. A. & Misteli, T. The lamin protein family. *Genome Biol* **12,** 222 (2011).

280. Zanoni, M., Cortesi, M., Zamagni, A., Arienti, C., Pignatta, S. & Tesei, A. Modeling neoplastic disease with spheroids and organoids. *J Hematol Oncol* **13,** 97 (2020).

281. Ur Rahman, A., Khan, S. & Khan, M. Transport of trans-activator of transcription (TAT) peptide in tumour tissue model: evaluation of factors affecting the transport of TAT evidenced by flow cytometry. *Journal of Pharmacy and Pharmacology* **72,** 519–530 (2020).

282. Lee, H. T., Lee, J. Y., Lim, H., Lee, S. H., Moon, Y. J., Pyo, H. J., Ryu, S. E., Shin, W. & Heo, Y.-S. Molecular mechanism of PD-1/PD-L1 blockade via anti-PD-L1 antibodies atezolizumab and durvalumab. *Sci Rep* **7,** 5532 (2017).

283. Lee, H. J. & Pardridge, W. M. Pharmacokinetics and Delivery of Tat and Tat-Protein Conjugates to Tissues in Vivo. *Bioconjug Chem* **12,** 995–999 (2001).

284. Young Kim, H., Young Yum, S., Jang, G. & Ahn, D.-R. Discovery of a non-cationic cell penetrating peptide derived from membrane-interacting human proteins and its potential as a protein delivery carrier. *Sci Rep* **5,** 11719 (2015).

285. Dong, Y., Tu, R., Liu, H. & Qing, G. Regulation of cancer cell metabolism: oncogenic MYC in the driver's seat. *Signal Transduct Target Ther* **5,** 124 (2020).

286. Singh, A., Greninger, P., Rhodes, D., Koopman, L., Violette, S., Bardeesy, N. & Settleman, J. A Gene Expression Signature Associated with "K-Ras Addiction" Reveals Regulators of EMT and Tumor Cell Survival. *Cancer Cell* **15,** 489–500 (2009).

287. Muzumdar, M. D., Chen, P.-Y., Dorans, K. J., Chung, K. M., Bhutkar, A., Hong, E., Noll, E. M., Sprick, M. R., Trumpp, A. & Jacks, T. Survival of pancreatic cancer cells lacking KRAS function. *Nat Commun* **8,** 1090 (2017).

288. Ran, F. A., Hsu, P. D., Wright, J., Agarwala, V., Scott, D. A. & Zhang, F. Genome engineering using the CRISPR-Cas9 system. *Nat Protoc* **8,** 2281–2308 (2013).

289. Brown, W. S., McDonald, P. C., Nemirovsky, O., Awrey, S., Chafe, S. C., Schaeffer, D. F., Li, J., Renouf, D. J., Stanger, B. Z. & Dedhar, S. Overcoming Adaptive Resistance to KRAS and MEK Inhibitors by Co-targeting mTORC1/2 Complexes in Pancreatic Cancer. *Cell Rep Med* **1,** 100131 (2020).

290. Morris, E. J., Jha, S., Restaino, C. R., Dayananth, P., Zhu, H., Cooper, A., Carr, D., Deng, Y., Jin, W., Black, S., Long, B., Liu, J., DiNunzio, E., Windsor, W., Zhang, R., Zhao, S., Angagaw, M. H., Pinheiro, E. M., Desai, J., Xiao, L., Shipps, G., Hruza, A., Wang, J., Kelly, J., Paliwal, S., Gao, X., Babu, B. S., Zhu, L., Daublain, P., Zhang, L., Lutterbach, B. A., Pelletier, M. R., Philippar, U., Siliphaivanh, P., Witter, D., Kirschmeier, P., Bishop, W. R., Hicklin, D., Gilliland, D. G., Jayaraman, L., Zawel, L., Fawell, S. & Samatar, A. A. Discovery of a Novel ERK Inhibitor with Activity in Models of Acquired Resistance to BRAF and MEK Inhibitors. *Cancer Discov* **3,** 742–750 (2013).

291. Wong, D. J., Robert, L., Atefi, M. S., Lassen, A., Avarappatt, G., Cerniglia, M., Avramis, E., Tsoi, J., Foulad, D., Graeber, T. G., Comin-Anduix, B., Samatar, A., Lo, R. S. & Ribas, A. Antitumor activity of the ERK inhibitor SCH722984 against BRAF mutant, NRAS mutant and wild-type melanoma. *Mol Cancer* **13,** 194 (2014).

292. Jin, X.-F., Spöttl, G., Maurer, J., Nölting, S. & Auernhammer, C. J. Antitumoral Activity of the MEK Inhibitor Trametinib (TMT212) Alone and in Combination with the CDK4/6 Inhibitor Ribociclib (LEE011) in Neuroendocrine Tumor Cells In Vitro. *Cancers (Basel)* **13,** 1485 (2021).

293. Fulcher, L. J., Macartney, T., Bozatzi, P., Hornberger, A., Rojas-Fernandez, A. & Sapkota, G. P. An affinity-directed protein missile system for targeted proteolysis. *Open Biol* **6,** 160255 (2016).

294. Caussinus, E., Kanca, O. & Affolter, M. Fluorescent fusion protein knockout mediated by anti-GFP nanobody. *Nat Struct Mol Biol* **19,** 117–121 (2012).

295. Bery, N., Keller, L., Soulié, M., Gence, R., Iscache, A.-L., Cherier, J., Cabantous, S., Sordet, O., Lajoie-Mazenc, I., Pedelacq, J.-D., Favre, G. & Olichon, A. A Targeted Protein Degradation Cell-Based Screening for Nanobodies Selective toward the Cellular RHOB GTP-Bound Conformation. *Cell Chem Biol* **26,** 1544-1558.e6 (2019).

296. Novotny, C. J., Hamilton, G. L., McCormick, F. & Shokat, K. M. Farnesyltransferase-Mediated Delivery of a Covalent Inhibitor Overcomes Alternative Prenylation to Mislocalize K-Ras. *ACS Chem Biol* **12,** 1956–1962 (2017).

297. Sgouros, G., Bodei, L., McDevitt, M. R. & Nedrow, J. R. Radiopharmaceutical therapy in cancer: clinical advances and challenges. *Nat Rev Drug Discov* **19,** 589–608 (2020).

298. Crișan, G., Moldovean-Cioroianu, N. S., Timaru, D.-G., Andrieș, G., Căinap, C. & Chiș, V. Radiopharmaceuticals for PET and SPECT Imaging: A Literature Review over the Last Decade. *Int J Mol Sci* **23,** 5023 (2022).

299. Connell, J. M. C., Hilditch, T. E., Elliott, A. & Semple, P. F. 131I-MIBG and Medullary Carcinoma of the Thyroid. *The Lancet* **324,** 1273–1274 (1984).

300. Bomanji, J. B., Wong, W., Gaze, M. N., Cassoni, A., Waddington, W., Solano, J. & Ell, P. J. Treatment of Neuroendocrine Tumours in Adults with 131I-MIBG Therapy. *Clin Oncol* **15,** 193–198 (2003).

301. Hoefnagel, C. A., De Kraker, J., Valdés Olmos, R. A. & Voûte, P. A. 131I-MIBG as a first-line treatment in high-risk neuroblastoma patients. *Nucl Med Commun* **15,** 712–717 (1994).

302. Haisma, H. J., Hilgers, J. & Zurawski Jr, V. R. Iodination of Monoclonal Antibodies for Diagnosis and Radiotherapy Using a Convenient One Vial Method. *The Journal of Nuclear Medicine* **27,** 1890–1895 (1986).

303. Ku, A., Facca, V. J., Cai, Z. & Reilly, R. M. Auger electrons for cancer therapy – a review. *EJNMMI Radiopharm Chem* **4,** 27 (2019).

304. Pouget, J.-P., Santoro, L., Raymond, L., Chouin, N., Bardiès, M., Bascoul-Mollevi, C., Huguet, H., Azria, D., Kotzki, P.-O., Pèlegrin, M., Vivès, E. & Pèlegrin, A. Cell Membrane is a More Sensitive Target than Cytoplasm to Dense Ionization Produced by Auger Electrons. *Radiat Res* **170,** 192–200 (2008).

305. Nosrati, Z., Esquinas, P. L., Rodríguez-Rodríguez, C., Tran, T., Maharaj, A., Saatchi, K. & Häfeli, U. O. Simultaneous SPECT imaging with 123I and 125I - a practical approach to assessing a drug and its carrier at the same time with dual imaging. *Int J Pharm* **606,** 120884 (2021).

306. Vorobyeva, A., Konovalova, E., Xu, T., Schulga, A., Altai, M., Garousi, J., Rinne, S. S., Orlova, A., Tolmachev, V. & Deyev, S. Feasibility of Imaging EpCAM Expression in Ovarian Cancer Using Radiolabeled DARPin Ec1. *Int J Mol Sci* **21,** 3310 (2020).

307. Deyev, S. M., Vorobyeva, A., Schulga, A., Abouzayed, A., Günther, T., Garousi, J., Konovalova, E., Ding, H., Gräslund, T., Orlova, A. & Tolmachev, V. Effect of a radiolabel biochemical nature on tumor-targeting properties of EpCAM-binding engineered scaffold protein DARPin Ec1. *Int J Biol Macromol* **145,** 216–225 (2020).

308. Hunter, W. M. & Greenwood, F. C. Preparation of Iodine-131 Labelled Human Growth Hormone of High Specific Activity. *Nature* **194,** 495–496 (1962).

309. Tang, L., Wei, F., Wu, Y., He, Y., Shi, L., Xiong, F., Gong, Z., Guo, C., Li, X., Deng, H., Cao, K., Zhou, M., Xiang, B., Li, X., Li, Y., Li, G., Xiong, W. & Zeng, Z. Role of metabolism in cancer cell radioresistance and radiosensitization methods. *Journal of Experimental & Clinical Cancer Research* **37,** 87 (2018).

310. Fernald, K. & Kurokawa, M. Evading apoptosis in cancer. *Trends Cell Biol* **23,** 620–633 (2013).

311. Begg, K. & Tavassoli, M. Inside the hypoxic tumour: reprogramming of the DDR and radioresistance. *Cell Death Discov* **6,** 77 (2020).

312. Huang, R.-X. & Zhou, P.-K. DNA damage response signaling pathways and targets for radiotherapy sensitization in cancer. *Signal Transduct Target Ther* **5,** 60 (2020).

313. Patil, V. M., Noronha, V., Menon, N., Singh, A., Ghosh-Laskar, S., Budrukkar, A., Bhattacharjee, A., Swain, M., Mathrudev, V., Nawale, K., Balaji, A., Peelay, Z., Alone, M., Pathak, S., Mahajan, A., Kumar, S., Purandare, N., Agarwal, A., Puranik, A., Pendse, S., Reddy Yallala, M., Sahu, H., Kapu, V., Dey, S., Choudhary, J., Krishna, M. R., Shetty, A., Karuvandan, N., Ravind, R., Rai, R., Jobanputra, K., Chaturvedi, P., Pai, P. S., Chaukar, D., Nair, S., Thiagarajan, S. & Prabhash, K. Results of Phase III Randomized Trial for Use of

Docetaxel as a Radiosensitizer in Patients With Head and Neck Cancer, Unsuitable for Cisplatin-Based Chemoradiation. *Journal of Clinical Oncology* **41,** 2350–2361 (2023).

314. Tao, Z., Le Blanc, J. M., Wang, C., Zhan, T., Zhuang, H., Wang, P., Yuan, Z. & Lu, B. Coadministration of Trametinib and Palbociclib Radiosensitizes KRAS-Mutant Non–Small Cell Lung Cancers In Vitro and In Vivo. *Clinical Cancer Research* **22,** 122–133 (2016).

315. Cuneo, K. C., Mehta, R. K., Kurapati, H., Thomas, D. G., Lawrence, T. S. & Nyati, M. K. Enhancing the Radiation Response in KRAS Mutant Colorectal Cancers Using the c-Met Inhibitor Crizotinib. *Transl Oncol* **12,** 209–216 (2019).

316. Tripathi, P., Soni, R., Antra & Tandon, V. Pixantrone confers radiosensitization in KRAS mutated cancer cells by suppression of radiation-induced prosurvival pathways. *Free Radic Biol Med* **190,** 351–362 (2022).

317. Lv, T., Wang, Y. & Zhang, Z. AMG-510 Plus Cetuximab Enhance Radiosensitivity in KRAS p.G12C Mutant Colorectal Carcinoma Cell Lines via Increasing Apoptosis and Inducing G1/S Arrest. *International Journal of Radiation Oncology*Biology*Physics* **111,** 237–238 (2021).

318. Zheng, Y., Liu, Y., Zhang, F., Su, C., Chen, X., Zhang, M., Sun, M., Sun, Y. & Xing, L. Radiation combined with KRAS-MEK inhibitors enhances anticancer immunity in KRAS-mutated tumor models. *Translational Research* **252,** 79–90 (2023).

319. Seo, J. W., Ingham, E. S., Mahakian, L., Tumbale, S., Wu, B., Aghevlian, S., Shams, S., Baikoghli, M., Jain, P., Ding, X., Goeden, N., Dobreva, T., Flytzanis, N. C., Chavez, M., Singhal, K., Leib, R., James, M. L., Segal, D. J., Cheng, R. H., Silva, E. A., Gradinaru, V. & Ferrara, K. W. Positron emission tomography imaging of novel AAV capsids maps rapid brain accumulation. *Nat Commun* **11,** 2102 (2020).

320. Radaram, B., Glazer, S. E., Yang, P., Li, C.-W., Hung, M.-C., Gammon, S. T., Alauddin, M. & Piwnica-Worms, D. Evaluation of 89Zr-Labeled Anti-PD-L1 Monoclonal Antibodies Using DFO and Novel HOPO Analogues as Chelating Agents for Immuno-PET. *ACS Omega* **8,** 17181–17194 (2023).

321. DANIEL, P. M., GALE, M. M. & PRATT, O. E. Advantages of Iodine-125 for Studying Thyroid Function in Experimental Animals. *Nature* **196,** 1065–1066 (1962).

322. Farebrother, J., Zimmermann, M. B. & Andersson, M. Excess iodine intake: sources, assessment, and effects on thyroid function. *Ann N Y Acad Sci* nyas.14041 (2019). doi:10.1111/nyas.14041

323. Lee, Y.-J., Erazo-Oliveras, A. & Pellois, J.-P. Delivery of Macromolecules into Live Cells by Simple Co-incubation with a Peptide. *ChemBioChem* **11,** 325–330 (2010).

324. Rügheimer, L., Hansell, P. & Wolgast, M. Determination of the charge of the plasma proteins and consequent Donnan equilibrium across the capillary barriers in the rat microvasculature. *Acta Physiologica* **194,** 335–339 (2008).

325. Morris, M. C., Depollier, J., Mery, J., Heitz, F. & Divita, G. A peptide carrier for the delivery of biologically active proteins into mammalian cells. *Nat Biotechnol* **19,** 1173–1176 (2001).

326. Meyer-Losic, F., Nicolazzi, C., Quinonero, J., Ribes, F., Michel, M., Dubois, V., de Coupade, C., Boukaissi, M., Chéné, A.-S., Tranchant, I., Arranz, V., Zoubaa, I., Fruchart, J.-S., Ravel, D. & Kearsey, J. DTS-108, A Novel Peptidic Prodrug of SN38: In vivo Efficacy and Toxicokinetic Studies. *Clinical Cancer Research* **14,** 2145–2153 (2008).

327. Meyer-Losic, F., Quinonero, J., Dubois, V., Alluis, B., Dechambre, M., Michel, M., Cailler, F., Fernandez, A.-M., Trouet, A. & Kearsey, J. Improved Therapeutic Efficacy of Doxorubicin through Conjugation with a Novel Peptide Drug Delivery Technology (Vectocell). *J Med Chem* **49,** 6908–6916 (2006).

328. Kim, G. C., Cheon, D. H. & Lee, Y. Challenge to overcome current limitations of cell-penetrating peptides. *Biochimica et Biophysica Acta (BBA) - Proteins and Proteomics* **1869,** 140604 (2021).

329. Dunnett-Kane, V., Nicola, P., Blackhall, F. & Lindsay, C. Mechanisms of Resistance to KRASG12C Inhibitors. *Cancers (Basel)* **13,** 151 (2021).

330. Liu, J., Kang, R. & Tang, D. The KRAS-G12C inhibitor: activity and resistance. *Cancer Gene Ther* **29,** 875–878 (2022).

331. Nagasaka, M., Li, Y., Sukari, A., Ou, S.-H. I., Al-Hallak, M. N. & Azmi, A. S. KRAS G12C Game of Thrones, which direct KRAS inhibitor will claim the iron throne? *Cancer Treat Rev* **84,** 101974 (2020).

332. Fu, H., Shi, K., Hu, G., Yang, Y., Kuang, Q., Lu, L., Zhang, L., Chen, W., Dong, M., Chen, Y. & He, Q. Tumor-Targeted Paclitaxel Delivery and Enhanced Penetration Using TAT-Decorated Liposomes Comprising Redox-Responsive Poly(Ethylene Glycol). *J Pharm Sci* **104,** 1160–1173 (2015).

333. Xie, Y., Ding, Y., Sun, D., Wang, G., Yang, H., Xu, H., Wang, Z. & Chen, J. An efficient PEGylated liposomal nanocarrier containing cell-penetrating peptide and pH-sensitive hydrazone bond for enhancing tumor-targeted drug delivery. *Int J Nanomedicine* 6199 (2015). doi:10.2147/IJN.S92519

334. Koren, E., Apte, A., Jani, A. & Torchilin, V. P. Multifunctional PEGylated 2C5-immunoliposomes containing pH-sensitive bonds and TAT peptide for enhanced tumor cell internalization and cytotoxicity. *Journal of Controlled Release* **160,** 264–273 (2012).

335. Stowell, S. R., Ju, T. & Cummings, R. D. Protein Glycosylation in Cancer. *Annual Review of Pathology: Mechanisms of Disease* **10,** 473–510 (2015).